

**DEVELOPMENT OF A REGIONAL NUMERICAL WEATHER
PREDICTION MODEL FOR THE TROPICS WITH AN
EMPHASIS ON THE PARAMETERIZATION OF
LAND - SURFACE PROCESSES**

by

ASHU P. DASTOOR

PHY
1989
D
DAS
DEV

TH
PHY 1989/1 D
D262d



**DEPARTMENT OF PHYSICS
INDIAN INSTITUTE OF TECHNOLOGY KANPUR**

JULY, 1989

**DEVELOPMENT OF A REGIONAL NUMERICAL WEATHER
PREDICTION MODEL FOR THE TROPICS WITH AN
EMPHASIS ON THE PARAMETERIZATION OF
LAND - SURFACE PROCESSES**

A Thesis Submitted
in Partial Fulfilment of the Requirements
for the Degree of

DOCTOR OF PHILOSOPHY

by

ASHU P. DASTOOR

to the

**DEPARTMENT OF PHYSICS
INDIAN INSTITUTE OF TECHNOLOGY KANPUR**

JULY 1989

DEVELOPMENT OF A REGIONAL NUMERICAL WEATHER PREDICTION MODEL FOR THE TROPICS WITH AN EMPHASIS ON THE PARAMETERIZATION OF LAND - SURFACE PROCESSES

**A Thesis Submitted
in Partial Fulfilment of the Requirements
for the Degree of**

DOCTOR OF PHILOSOPHY

by

ASHU P. DASTOOR

to the

**DEPARTMENT OF PHYSICS
INDIAN INSTITUTE OF TECHNOLOGY KANPUR**

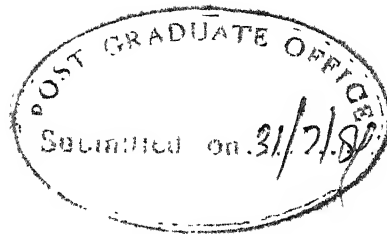
JULY, 1989

13 JUL 1990

CENTRAL LIBRARY
I.I.T. KANPUR

No. A.1.08476

PHY-1989-D-DAS-DEV



C E R T I F I C A T E

This is to certify that the thesis, "Development of a Regional Numerical Weather Prediction Model for the Tropics with an Emphasis on the Parameterization of Land-Surface Processes" submitted by Ms. Ashu P. Dastoor in partial fulfillment of the degree of the Doctor of Philosophy to the Indian Institute of Technology Kanpur, is a record of bonafide research work carried out under our supervision. The results embodied in this thesis have not been submitted to any other Institute or University for the award of a degree.

A handwritten signature in dark ink, appearing to read "V.K. Deshpande".

Prof V.K. Deshpande
Department of Physics
Indian Institute of Technology
Kanpur

A handwritten signature in dark ink, appearing to read "Y. Ramanathan".

Prof. Y. Ramanathan
Department of Physics
Indian Institute of Technology
Kanpur

ACKNOWLEDGMENTS

This work is an evidence of the abundant love of my LORD and SAVIOUR JESUS CHRIST for me. Had He not carried me through this work continually encouraging, guiding and providing strength at every step this thesis would not have materialized.

I wish to earnestly thank Prof Y. Ramanathan for sharing his knowledge and experience in the subject with due guidance and help in carrying out this research work. I am thankful to Profs. V.K. Deshpande and R. Ramachandran for their interest, support and cooperation in completing the work.

The computational work reported in this thesis was carried out under a joint program between the Indian Institute of Technology, Kanpur, and Florida State University, Florida under a grant NSF-INT-87113958. The computations were carried out on the CRAY X-MP/48 computer of the National Center for Atmospheric Research, Boulder, Colorado, which is sponsored by the National Science Foundation.

I wish to express my profound gratitude to Prof. T.N. Krishnamurti for providing guidance and support at the Department of Meteorology, FSU, where the major part of the research work was completed. Also, I thank Arun Kumar, Glenn Daughenbaugh, Kevin Ingles, D. Oosterhof, K.S. Yap, Dr H.S. Bedi, K. Kuma, Janie Nall, Rosemarie, Sara and Atunya among others whose cooperation and help is well appreciated and acknowledged.

The cooperation of Firoz Alam and staff, Physics Department is also acknowledged.

Words cannot express my gratitude to my husband, Praveen, for introducing me to this subject in the first place, sharing my burden and contributing in carrying out this research work. His sacrificial participation is priceless. I am grateful to my parents for providing me the support and opportunity for higher education with constant encouragement throughout. I also owe my gratitude to my parents-in-law for their moral and spiritual support and encouragement. I also very specially acknowledge Al & Bea Wilson, John and Carla Wilson and Judy Hefren for their care and support. May God bless them all abundantly.

Ashu P. Dastoor

TABLE OF CONTENTS

	page
LIST OF FIGURES	vii
LIST OF TABLES	xv
LIST OF ACRONYMS	xvi
LIST OF SYMBOLS	xvii
SYNOPSIS	xix
CHAPTER 1 INTRODUCTION	1
CHAPTER 2 DYNAMICAL FRAMEWORK OF THE REGIONAL MODEL	9
2.1 Vertical and Horizontal Discretization	9
2.2 Equations of Motion	11
2.3 The Integration Scheme	13
2.4 Initialization	33
2.4.1 Formulation	34
2.4.2 Procedure	38
2.5 Boundary Conditions	40
CHAPTER 3 PARAMETERIZATION OF PHYSICAL PROCESSES	44
3.1 Parameterization of Large Scale Condensation	45
3.2 Parameterization of Shallow Convection	46
3.3 Parameterization of Deep Moist Convection	48

3.4	Parameterization of Surface Fluxes	52
3.5	Parameterization of Fluxes above the Surface Layer	59
3.6	Shortwave Radiation	60
3.7	Longwave Radiation	71
3.8	Surface Energy Balance	84
3.9	Orography	85
CHAPTER 4	PREDICTION OF THE LANDFALL OF A TROPICAL STORM	88
4.1	Observational Aspects of the Landfall	90
4.2	Prediction of the Landfall	99
4.3	Rainfall Prediction	105
CHAPTER 5	PARAMETERIZATION OF GROUND WETNESS	114
5.1	The Parameterization Scheme	118
5.2	Results and Discussion of the Parameterization	125
CHAPTER 6	SENSITIVITY OF RAINFALL PREDICTION TO GROUND WETNESS AND RESOLUTION	157
6.1	Rainfall Prediction at 1° Latitude/Longitude Resolution	164
6.2	Rainfall Prediction at 0.5° Latitude/Longitude Resolution	164
CHAPTER 7	CONCLUSION	173
REFERENCES		177

LIST OF FIGURES

Fig. No.	Caption	Page
1	Vertical discretization of the model.	10
2	Horizontal discretization (Arakawa c type grid).	12
3	Flow diagram of the initialization procedure.	39
4	Spectral energy curve of solar radiation at sea level and extrapolated outside the atmosphere, as given by Pettit (1951). The darkened areas represent gaseous absorption in the atmosphere.	61
5	Percent of the solar flux absorbed as a function of ozone amount for two spectral regions.	67
6	IR spectral ranges for H ₂ O, CO ₂ and O ₃ parameterized in the radiation code. Dashed area represents the band centers (for the H ₂ O and CO ₂) and shaded areas are the band wings. Note that CO ₂ (15 μ m band) and O ₃ (9.6 μ m band) overlap with the H ₂ O.	73
7	(a) Earth's albedo field for the summer season and (b) Sea surface temperature used in the model.	86
8	Observed track of the tropical cyclone based on the Guam summaries.	89
9	a, b, c and d: Horizontal motion field on the $\sigma = 0.85$ surface based on the observed wind analysis starting May 11 1979 00 UTC to May 12 1979 1200 UTC.	92
9	e, f and g: Horizontal motion field on the $\sigma = 0.85$ surface based on the observed wind analysis starting May 13 1979 00 UTC to May 14 1979 00 UTC.	93
10	a, b, c and d: Horizontal motion field on the $\sigma = 0.5$ surface based on the observed wind analysis starting May 11 1979 00 UTC to May 12 1979 1200 UTC.	94
10	e, f and g: Horizontal motion field on the $\sigma = 0.5$ surface based on the observed wind analysis starting May 13 1979 00 UTC to May 14 1979 00 UTC.	95

11	a, b, c and d: Horizontal motion field on the $\sigma = 0.25$ surface based on the observed wind analysis starting May 11 1979 00 UTC to May 12 1979 1200 UTC.	97
11	e, f and g: Horizontal motion field on the $\sigma = 0.25$ surface based on the observed wind analysis starting May 13 1979 00 UTC to May 14 1979 00 UTC.	97
12	a, b and c: Predicted horizontal motion field on the $\sigma = 0.85$ surface starting May 11 1979 1200 UTC to May 12 1979 1200 UTC.	98
12	d, e and f: Predicted horizontal motion field on the $\sigma = 0.85$ surface starting May 13 1979 00 UTC to May 14 1979 00 UTC.	100
13	a, b and c: Predicted horizontal motion field on the $\sigma = 0.5$ surface starting May 11 1979 1200 UTC to May 12 1979 1200 UTC.	101
13	d, e and f: Predicted horizontal motion field on the $\sigma = 0.5$ surface starting May 13 1979 00 UTC to May 14 1979 00 UTC.	103
14	a, b and c: Predicted horizontal motion field on the $\sigma = 0.25$ surface starting May 11 1979 1200 UTC to May 12 1979 1200 UTC.	104
14	d, e and f: Predicted horizontal motion field on the $\sigma = 0.25$ surface starting May 13 1979 00 UTC to May 14 1979 00 UTC.	105
15	Accumulated 24 hour rainfall for May 11 1979 00 UTC to May 12 1979 00 UTC. (a) Observed, (b) Predicted using terrain field interpolated from 2.5° lat/long grid to $.9375^\circ$ lat/long grid, (c) Predicted using terrain field interpolated from a high resolution U.S. Navy data.	110
16	Accumulated 24 hour rainfall for May 12 1979 00 UTC to May 13 1979 00 UTC. (a) Observed, (b) Predicted using terrain field interpolated from 2.5° lat/long grid to $.9375^\circ$ lat/long grid, (c) Predicted using terrain field interpolated from a high resolution U.S. Navy data.	111
17	Accumulated 24 hour rainfall for May 13 1979 00 UTC to May 14 1979 00 UTC. (a) Observed, (b) Predicted using terrain field interpolated from 2.5° lat/long grid to $.9375^\circ$ lat/long grid, (c) Predicted using terrain field interpolated from a high resolution U.S. Navy data.	112

- 18 (a) Average (May 11 1979 00 UTC - May 13 1979 12 UTC) surface latent heat flux (watts/m^2) calculated from moisture budget analysis, (b) the corresponding average surface temperature T_g ($^{\circ}\text{K}$), (c) Model predicted average (May 11 1979 00 UTC - May 13 1979 12 UTC) surface latent heat flux (watts/m^2) calculated using similarity theory and ground wetness based on albedo, (d) the corresponding average surface temperature predicted by the model. 126
- 19 a, b and c: Average GW parameter maps for the subperiod 1 (May 11 1979 00 UTC - May 13 1979 12 UTC). It ranges from 0 for dry land to 1 for saturated land. (a) calculated from moisture budget analysis, (b) and (c) are calculated respectively by the expressions given by (5.4) and (5.5). 128
- 20 a, b and c: Average GW parameter maps for the subperiod 2 (May 14 1979 00 UTC - May 16 1979 12 UTC). It ranges from 0 for dry land to 1 for saturated land. (a) calculated from moisture budget analysis, (b) and (c) are calculated respectively by the expressions given by (5.4) and (5.5). 129
- 21 a, b and c: Average GW parameter maps for the subperiod 3 (June 20 1979 00 UTC - June 22 1979 12 UTC). It ranges from 0 for dry land to 1 for saturated land. (a) calculated from moisture budget analysis, (b) and (c) are calculated respectively by the expressions given by (5.4) and (5.5). 130
- 22 a, b and c: Average GW parameter maps for the subperiod 4 (June 23 1979 00 UTC - June 25 1979 12 UTC). It ranges from 0 for dry land to 1 for saturated land. (a) calculated from moisture budget analysis, (b) and (c) are calculated respectively by the expressions given by (5.4) and (5.5). 131
- 23 a, b and c: Average GW parameter maps for the subperiod 5 (June 26 1979 00 UTC - June 28 1979 12 UTC). It ranges from 0 for dry land to 1 for saturated land. (a) calculated from moisture budget analysis, (b) and (c) are calculated respectively by the expressions given by (5.4) and (5.5). 132
- 24 a, b and c: Three-day average observed rainfall rates (mm/day) derived from a mix of raingauge and satellite based estimates for the period (a) May 11 1979 00 UTC - May 14 1979 00 UTC, (b) May 14 1979 00 UTC - May 17 1979 00 UTC, (c) June 20 1979 00 UTC - June 23 1979 00 UTC. 133

- 24 d and e: Three-day average observed rainfall rates (mm/day) derived from a mix of raingauge and satellite based estimates for the period (d) June 23 1979 00 UTC - June 26 1979 00 UTC, (e) June 26 1979 00 UTC - June 29 1979 00 UTC. 134
- 25 a, b, c and d: Average surface latent heat flux (watts/m²) for the subperiod 1 (May 11 1979 00 UTC - May 13 1979 12 UTC) calculated from (a) moisture budget analysis, (b) similarity theory and GW from moisture budget analysis, (c) similarity theory and GW from expression (5.4), (d) similarity theory and GW from expression (5.5). 135
- 26 a, b, c and d: Average surface latent heat flux (watts/m²) for the subperiod 2 (May 14 1979 00 UTC - May 16 1979 12 UTC) calculated from (a) moisture budget analysis, (b) similarity theory and GW from moisture budget analysis, (c) similarity theory and GW from expression (5.4), (d) similarity theory and GW from expression (5.5). 136
- 27 a, b, c and d: Average surface latent heat flux (watts/m²) for the subperiod 3 (June 20 1979 00 UTC - June 22 1979 12 UTC) calculated from (a) moisture budget analysis, (b) similarity theory and GW from moisture budget analysis, (c) similarity theory and GW from expression (5.4), (d) similarity theory and GW from expression (5.5). 137
- 28 a, b, c and d: Average surface latent heat flux (watts/m²) for the subperiod 4 (June 23 1979 00 UTC - May 25 1979 12 UTC) calculated from (a) moisture budget analysis, (b) similarity theory and GW from moisture budget analysis, (c) similarity theory and GW from expression (5.4), (d) similarity theory and GW from expression (5.5). 138
- 29 a, b, c and d: Average surface latent heat flux (watts/m²) for the subperiod 5 (June 26 1979 00 UTC - June 28 1979 12 UTC) calculated from (a) moisture budget analysis, (b) similarity theory and GW from moisture budget analysis, (c) similarity theory and GW from expression (5.4), (d) similarity theory and GW from expression (5.5). 139
- 30 a, b, c and d: Average surface temperature (°K) for the subperiod 1 (May 11 1979 00 UTC - May 13 1979 12 UTC). (a) Calculated from moisture budget analysis, (b) calculated using surface latent heat flux shown in figure 25 (b), (c) calculated using surface latent heat flux shown in figure 25 (c), (d) calculated using surface latent heat flux shown in figure 25 (d). 140

- 31 a, b, c and d: Average surface temperature ($^{\circ}\text{K}$) for the subperiod 2 (May 14 1979 00 UTC - May 16 1979 12 UTC). (a) Calculated from moisture budget analysis, (b) calculated using surface latent heat flux shown in figure 26 (b), (c) calculated using surface latent heat flux shown in figure 26 (c), (d) calculated using surface latent heat flux shown in figure 26 (d). 141
- 32 a, b, c, and d: Average surface temperature ($^{\circ}\text{K}$) for the subperiod 3 (June 20 1979 00 UTC - June 22 1979 12 UTC). (a) Calculated from moisture budget analysis, (b) calculated using surface latent heat flux shown in figure 27 (b), (c) calculated using surface latent heat flux shown in figure 27 (c), (d) calculated using surface latent heat flux shown in figure 27 (d). 142
- 33 a, b, c and d: Average surface temperature ($^{\circ}\text{K}$) for the subperiod 4 (June 23 1979 00 UTC - June 25 1979 12 UTC). (a) Calculated from moisture budget analysis, (b) calculated using surface latent heat flux shown in figure 28 (b), (c) calculated using surface latent heat flux shown in figure 28 (c), (d) calculated using surface latent heat flux shown in figure 28 (d). 143
- 34 a, b, c and d: Average surface temperature ($^{\circ}\text{K}$) for the subperiod 5 (June 26 1979 00 UTC - June 28 1979 12 UTC). (a) Calculated from moisture budget analysis, (b) calculated using surface latent heat flux shown in figure 29 (b), (c) calculated using surface latent heat flux shown in figure 29 (c), (d) calculated using surface latent heat flux shown in figure 29 (d). 144
- 35 a, b, and c: Comparison of average surface latent heat flux (watts/m^2) calculated from 1. moisture budget analysis; 2. similarity analysis and GW from moisture budget analysis; 3. similarity analysis and GW from expression (5.4); 4. similarity analysis and GW from expression (5.5). These comparisons are for four domains defined as I. $12.2^{\circ} - 38.4^{\circ}\text{N}$, $45.9^{\circ} - 66.6^{\circ}\text{E}$, II. $2.8^{\circ} - 21.6^{\circ}\text{N}$, $66.6^{\circ} - 91.9^{\circ}\text{E}$ III. $21.6^{\circ} - 38.4^{\circ}\text{N}$, $66.6^{\circ} - 91.9^{\circ}\text{E}$ IV. $12.2^{\circ} - 38.4^{\circ}\text{N}$, $91.9^{\circ} - 113.4^{\circ}\text{E}$. (a) Subperiod 1, (b) Subperiod 2, (c) Subperiod 3. 146
- 36 a and b: Comparison of average surface latent heat flux (watts/m^2) calculated from 1. moisture budget analysis, 2. similarity analysis and GW from moisture budget analysis; 3. similarity analysis and GW from expression (5.4); 4. similarity analysis and GW from expression (5.5). These comparisons are for four domains defined as I. $12.2^{\circ} - 38.4^{\circ}\text{N}$, $45.9^{\circ} - 66.6^{\circ}\text{E}$, II. $2.8^{\circ} - 21.6^{\circ}\text{N}$, $66.6^{\circ} - 91.9^{\circ}\text{E}$ III. $21.6^{\circ} - 38.4^{\circ}\text{N}$, $66.6^{\circ} - 91.9^{\circ}\text{E}$ IV. $12.2^{\circ} - 38.4^{\circ}\text{N}$, $91.9^{\circ} - 113.4^{\circ}\text{E}$. (a) Subperiod 4, (b) Subperiod 5. 147

- 37 a, b and c: Average GW calculated from the GW expression given by (5.24). This is based on the regression analysis of GW estimates from moisture budget analysis with the parameters past 24 hour rainfall, surface temperature, albedo and terrain. (a) Subperiod 1 (May 11 1979 00 UTC - May 13 1979 12 UTC), (b) Subperiod 2 (May 14 1979 00 UTC - May 16 1979 12 UTC), (c) Subperiod 3 (June 20 1979 00 UTC - June 22 1979 12 UTC). 148
- 38 a and b: Average GW calculated from the GW expression given by (5.24). This is based on the regression analysis of GW estimates from moisture budget analysis with the parameters past 24 hour rainfall, surface temperature, albedo and terrain. (a) Subperiod 4 (June 23 1979 00 UTC - June 25 1979 12 UTC), (b) Subperiod 5 (June 26 1979 00 UTC - June 28 1979 12 UTC). 149
- 39 a, b, c and d: Maps showing GW at 12 hours interval as predicted by the model using new GW parameterization for (a) May 11 1979 00 UTC, (b) May 11 1979 12 UTC, (c) May 12 1979 00 UTC, and (d) May 12 1979 12 UTC. 150
- 40 a, b, and c: Maps showing GW at 12 hours interval as predicted by the model using new GW parameterization for (a) May 13 1979 00 UTC, (b) May 13 1979 12 UTC, and (c) May 14 1979 00 UTC. 151
- 41 (a) Average latent heat flux (watts/m^2) for May 11 1979 00 UTC - May 13 1979 12 UTC predicted by the model using new GW parameterization. Shaded areas show the high values of latent heat flux. (b) Average (May 11 1979 00 UTC - May 13 1979 12 UTC) surface temperature ($^{\circ}\text{K}$) as predicted by the model in the above mentioned experiment. 153
- 42 (a) and (b) are time series of model predicted rainfall using new GW parameterization for two grid points located at 31.9°N , 71.3°E and 23.4°N , 79.7°E respectively; (c) and (d) are the time series of model predicted GW for the above mentioned experiment at the same two grid points. 154
- 43 (a) and (b) are time series of model predicted surface temperature ($^{\circ}\text{K}$) using old GW parameterization for two grid points located at 31.9°N , 71.3°E and 23.4°N , 79.7°E respectively; (c) and (d) are the time series of model predicted surface temperature ($^{\circ}\text{K}$) using new GW parameterization for the above mentioned grid points. 155

- 44 (a) and (b). Time series of surface latent heat flux (watts/m^2) using old GW parameterization for two grid points located at 31.9°N , 71.3°E and 23.4°N , 79.7°E respectively, (c) and (d) are the time series of model predicted surface latent heat flux using new GW parameterization for the above mentioned grid points. 156
- 45a Satellite photograph showing the cloud cover at 10:00 am local time over India for May 12, 1979. 158
- 45b Satellite photograph showing the cloud cover at 10:00 am local time over India for May 13, 1979. 159
- 46 Accumulated 24 hour observed rainfall derived from raingauge data. Raingauge data has been averaged over 1 degree lat/long squares. (a) For the period May 11 1979 00 UTC to May 12 1979 00 UTC (b) For the period May 12 1979 00 UTC to May 13 1979 00 UTC. 161
- 47 Accumulated 24 hour predicted rainfall for the period May 11 1979 00 UTC to May 12 1979 00 UTC. Model resolution is $.9375^\circ$ lat/long. (a) From a control experiment using old GW parameterization (b) From a sensitivity experiment using new GW parameterization. 165
- 48 Accumulated 24 hour predicted rainfall for the period May 12 1979 00 UTC to May 13 1979 00 UTC. Model resolution is $.9375^\circ$ lat/long. (a) From a control experiment using old GW parameterization (b) From a sensitivity experiment using new GW parameterization. 166
- 49 Accumulated 24 hour predicted rainfall for the period May 11 1979 00 UTC to May 12 1979 00 UTC. Model resolution is $.46875^\circ$ lat/long. Rainbands are highlighted by solid lines. (a) From a control experiment using old GW parameterization (b) from a sensitivity experiment using new GW parameterization. 167
- 50 Accumulated 24 hour predicted rainfall for the period May 12 1979 00 UTC to May 13 1979 00 UTC. Model resolution is $.46875^\circ$ lat/long. Rainbands are highlighted by solid lines. (a) From a control experiment using old GW parameterization (b) From a sensitivity experiment using new GW parameterization. 168
- 51 The difference in 24 hour predicted rainfall between model forecasts using old and new GW parameterization for $.46875^\circ$ lat/long resolution for the period (a) May 11 1979 00 UTC to May 12 1979 00 UTC and (b) May 12 1979 00 UTC to May 13 1979 00 UTC. The shaded regions indicate rainfall with new GW > rainfall with old GW. 170

52

Accumulated 24 hour predicted rainfall for the period May 12 1979 00 UTC to May 13 1979 00 UTC. Model resolution is $.46875^\circ$ lat/long. (a) From a control experiment using old GW parameterization (b) From a sensitivity experiment using new GW parameterization. This figure is same as figure 50 a, b but the contouring interval is 25 mm/day.

172

LIST OF TABLES

Table No.	Description	Page
1	Outline of regional models	3
2	Discrete probability distribution of water vapor absorption coefficients, from Davies 1982.	65
3	Parameters for the absorption due to water vapor molecular line from Chou, 1984.	77
4	Parameters for the band-center region and the band-wing regions for CO ₂ (15 μ m band).	78
5	The regression coefficient, $10^4 \times \alpha(w,u)$, for computing the transmission functions.	81
6	The regression coefficient, $10^6 \times \beta(w,u)$, for computing the transmission functions.	81
7	The "Planck weighted" transmission function, $10^3 \times \tau(w,u; 250^\circ\text{K})$, in the water vapor spectral regions.	81
8	The regression coefficients of GW	124

LIST OF ACRONYMS

AMTEX	Airmass Transformation Experiment
ATEX	Atlantic Tropical Experiment
DMSP	Defense Meteorology Satellite Program
ECMWF	European Center for Medium Range Weather Forecast
FGGE	First GARP Global Experiment
FSU	Florida State University
GATE	GARP Atlantic Tropical Experiment
GCM	General Circulation Model
GLAS	Goddard Laboratory of Atmospheric Sciences
GOES	U.S. Operational Geostationary Satellite
GW	Ground Wetness
IR	Infra-Red
JMA	Japan Meteorological Agency
LCL	Lifting condensation level
MONEX	Monex experiment
NCAR	National Center for Atmospheric Research
NMC	National Meteorological Center
NTP	Normal Temperature and Pressure
NWP	Numerical Weather Prediction
SST	Sea surface temperature
TIROS N	U.S. Operational Polar Orbiting Satellite
UCLA	University of California at Los Angeles
UTC	Coordinated Universal Time

LIST OF SYMBOLS

σ	dimensionless vertical coordinate
p	pressure
p_s	pressure at the earth's surface
x	x-coordinate
y	y-coordinate
t	time
λ	longitude, positive eastward from Greenwich
ϕ	latitude, positive northward from equator
u	x-component of wind vector
v	y-component of wind vector
$\dot{\sigma}$	(= $d\sigma/dt$) vertical velocity in sigma coordinate
f	(= $2 \Omega \sin\phi$) Coriolis parameter
Ω	earth's rotation rate
a	earth's radius
g	acceleration due to gravity
z	height
R	specific gas constant (for dry air)
T	temperature
F_x	x-component of momentum flux convergence
F_y	y-component of momentum flux convergence
κ	= R/C_p
C_p	specific heat (for dry air) at constant pressure
H	heating (cooling) term due to all the physical processes
θ	potential temperature
θ_s	potential temperature along saturated moist adiabat
q	specific humidity
q_s	saturation specific humidity
E	moisture convergence and source (sink) term due to all the physical processes
\vec{V}	horizontal wind vector
σ_T	σ coordinate value at the top of the model

α	specific volume
π	$= \left[\frac{p}{1000} \right]^\kappa$
$(\bar{})$	vertical average operator
	$= \frac{1}{1-\sigma_T} \int_{\sigma_T}^1 () d\sigma$
$(\)^*$	horizontal average over model domain
$(\)'$	departure from horizontal average
z_s	surface topography
P	$(= gz_s + RT \ln p_s)$ model parameter
γ	static stability parameter
L	latent heat of vaporization
e	vapor pressure
e_s	saturation vapor pressure
ρ	density of air
ω	vertical velocity in mb s ⁻¹
ζ	relative vertical vorticity
P_T	pressure at cloud top
P_B	pressure at cloud base
k	Von Karman Constant
z_o	roughness parameter
R_i	Richardson number
F_M	surface flux of momentum
F_S	surface flux of heat
F_L	surface flux of moisture
C_D	drag coefficient
C_H	exchange coefficient for heat
C_q	exchange coefficient for moisture
l	mixing length
τ	optical thickness
μ_o	cosine of the solar zenith angle
S_o	solar constant
u_*	friction velocity
θ_*	characteristic temperature scale
q_*	characteristic humidity scale

SYNOPSIS

Development of a Regional Numerical Weather Prediction Model
for the Tropics with an Emphasis on the Parameterization
of Land-Surface Processes

A Thesis Submitted
In Partial Fulfillment of the Requirements
For the Degree of
DOCTOR OF PHILOSOPHY

by

ASHU P. DASTOOR

to the

DEPARTMENT OF PHYSICS
INDIAN INSTITUTE OF TECHNOLOGY KANPUR
JULY 1989

In recent years regional fine mesh models have gained an important place alongwith global models both in operational numerical weather prediction and meteorological research. Compared to global models, the horizontal resolution in these models can be increased with ease, to provide detailed numerical guidance for the region of interest. Also these models are particularly relevant to work on the development of physical parameterization schemes.

The motivation for this study is the development of one such regional weather prediction model with an emphasis on certain aspects of the land surface processes. The thesis has seven chapters. Salient features of various regional models currently in use all over the world for operational and research purposes are briefly reviewed in the introductory chapter. This provides a perspective to the performance of the model discussed in this study.

The second chapter contains a detailed description of the dynamical framework of the model. The domain chosen for the model is in the summer monsoon region from 45°E to 114.4°E West-east and 9.4°S to 39.4°N South-north. The horizontal resolution for control runs is 1° lat/long which is reduced to 0.5° for sensitivity experiments. In the vertical the model uses the sigma ($\sigma = p/p_s$; $p_s \equiv$ surface pressure) coordinate system in which the earth's surface with orographic features is a coordinate surface $\sigma = 1$. The non-linear horizontal advection is computed by the semi-Lagrangian advection scheme that controls non-linear computational instability. The time-differencing is based on a semi-implicit breakdown in which the linear terms responsible for the excitation of gravity waves only are treated implicitly while the slower Rossby modes are handled explicitly. The semi-implicit casting of the time-differencing is known to provide computational efficiency over a fully explicit treatment. An Arakawa C grid for the horizontal lattice structure ensures rapid adjustment between mass and flow fields i.e. geostrophic balance in higher latitudes. The forecast variables are not determined directly but through a model defined variable whose evaluation requires the solution of a three dimensional Helmholtz equation. Using a similarity transformation this three dimensional equation is reduced to a system of two dimensional equations which is solved by the fast fourier transform method. The model uses a dynamic initialization scheme. This scheme involves one time step forward integration of the model with all the physical processes included. It is followed by a number of cycles of forward-backward integration while keeping the non-linear tendencies fixed. Two options of fixed and time dependent lateral boundary conditions are currently available in the model.

The physical processes in the model are described in the third chapter. They include a comprehensive state of the art parameterization of the surface fluxes through the similarity theory, definition of a planetary boundary layer, cumulus convection through a version of Kuo's method, a band model radiative transfer and cloud model radiative feedback processes, solution of surface energy balance equation and the use of the envelope orography.

Details of the case study chosen for the control and sensitivity experiments are given in chapter 4. The landfall of a tropical cyclone containing spiral rainbands in its cloud cover and precipitation patterns is chosen for the study. This cyclone formed in the southern Bay of Bengal during early May 1979, moved northwest to the east coast of southern India where it made its landfall around 12 May 1979. The model was initialized with the FGGE III-b data sets for 11 May 1979 00 UTC, and integrated for 72 hours. The forecast circulation features compared very well with the observations. The storm track was realistic. However the rainfall rates were poorly predicted.

One of the crucial parameters of the land surface processes in estimating the surface fluxes of moisture in the model is the ground wetness/surface soil moisture variable, which is empirically specified. This is recognized as an area of weakness in the current modelling effort, leading to erroneous forecast of rainfall rates. Chapter 5 highlights this problem and gives details of a new parameterization scheme based on carefully designed moisture budget studies. A detailed analysis of the new scheme is made and the results of its impact on the estimation of various surface parameters are compared with the old scheme. A major improvement in the surface moisture

flux estimation is noticed. The forecasts show improvement in the rainfall rates and spatial positions of rainfall regions compared to observations. However there is scope for improvement around the storm region. In the next chapter sensitivity experiments for evaluating the role of horizontal resolution are discussed. Two different horizontal resolutions ($1^{\circ} \times 1^{\circ}$; $0.5^{\circ} \times 0.5^{\circ}$) are chosen for prediction with the old and new parameterization schemes for the ground wetness. These experiments are found useful in assessing the model capability in resolving the details of the complex geometry of the observed precipitation patterns from the new improved parameterization scheme for the ground wetness. Considerable improvement was noticed in the forecasts when the resolution was halved to 0.5° in both the spatial positioning of the rainfall region and the amount of rainfall around the storm region. The final chapter summarises the important conclusions.

Thus, the study shows the development of a regional numerical weather prediction model for use in the tropics. In a case study of the landfall of a tropical cyclone, the model predicted reasonably well the storm track and the rainbands of the cyclone as it made the landfall. With the incorporation of a new parameterization scheme for the ground wetness, the model also predicted realistic rainfall rates over the storm region, at the same time enhancing the accuracy of the geometry of the spiral rainbands compared to observations.

CHAPTER 1

INTRODUCTION

In the tropics mesoscale systems dominate the regional weather and are often part of larger systems like tropical storms. Hence mesoscale models are useful for tropical weather prediction. There are basically two types of mesoscale models. There are those that make use of horizontal resolutions of the order of 50 km or larger and can resolve mesoscale phenomenon whose scale is of the order of a few hundred km, these are quasi-static models. There is also a considerable current research interest in nonhydrostatic mesoscale models that use a horizontal resolution of less than 5 km. The latter are usually designed to study the life cycle and detailed mechanisms of individual mesoscale systems. The present study covers the former class of quasistatic regional mesoscale models. These models are usually as sophisticated as any of the well known global models in terms of their handling of dynamical and thermodynamical processes. The global models are evolving very rapidly with a substantial increase in horizontal resolution. The performance of the high resolution global model has reached a level where one is frequently asking whether a very high resolution global model might be the appropriate mesoscale (quasistatic type) model since it doesn't have to face the problem of lateral boundary conditions. In the coming years perhaps we would be able to answer this question.

Several promising mesoscale regional models have emerged in

recent years that deal with the prediction of heavy rainfall. Table 1 contains a brief summary of some of these regional models. This table, in three parts provides an outline of the *NCAR/Penn State, JMA, NMC, French, ECMWF regional models and the FSU regional model presented in this thesis. This summary includes the horizontal and vertical discretization, time differencing schemes, the lateral boundary conditions, initialization, the diffusion terms and physical processes (surface processes, planetary boundary layer, cumulus parameterization, radiative transfer) and domain of application.

While superficially, the mesoscale prediction models may appear as mere refined versions of limited-area, primitive equation, numerical weather prediction models for the synoptic and large scale, the forecast accuracies of these models are however to a greater extent constrained by limitations imposed by (a) numerical difficulties related to finite differencing and lateral boundary conditions, (b) adequacy of parameterization of subgrid scale physical processes, (c) uncertainties in the model's initial conditions and (d) inherent predictability of atmospheric mesoscale circulations. In the tropics invariably one of the major limitations of mesoscale models initialized through synoptic and subsynoptic scale data is that they show limited skill in simulating the spatial and temporal distribution of precipitation fields despite well predicted flow patterns. This could be attributed to slow spin-up of mesoscale circulations in the model initialized with synoptic and subsynoptic-scale data and inadequate representation of surface latent heat fluxes. In the present

* List of acronyms is given on page xvi.

Table 1 (a) OUTLINE OF REGIONAL MODELS

Model	Horizontal & Vertical Discretization	Time-Differencing Scheme	Lateral Boundary Conditions
NCAR/Penn State limited area model	The model variables are staggered in the vertical and horizontal. In horizontal Arakawa B grid (Arakawa & Lamb, 1977) is used. In vertical 16 σ levels are used where the resolution is higher in PBL. For the horizontal grid Polar stereo graphic, Lambert Conformal or Mercator map projection is used.	Explicit scheme developed by Brown and Campana (1978) is used. A frequency filter (Asselin, 1972) is applied to all prognostic variables.	Five types of lateral boundary conditions can be used. 1) Fixed 2) Time-dependent 3) Time-dependent and inflow/outflow dependent 4) Sponge 5) Relaxation
JMA Tokyo Regional Spectral model	Spectral representation in horizontal using a modified double Fourier series. The series composes of the orthogonal double Fourier series with mirror boundary conditions and additional bases to specify fluxes across the boundary. In vertical, finite differencing is carried out on 16 equispaced σ levels.	Semi-implicit scheme is used for integrating the momentum, thermodynamic equation and continuity equation. Time integration of moisture field is carried out by the leap frog scheme.	Time-dependent b.c.s are prescribed by the global model forecast. Boundary relaxation is performed using a forward time-differencing scheme.
NMC The Nested Grid Model	In the forecast three grid resolutions are used. Stereographic coordinates and Eliassen staggering is used in horizontal. In vertical, discretization suggested by Arakawa (Arakawa <i>et al.</i> 1974) is used.	The time integration scheme is a two-step second-order Lax-Wendroff process (Phillips, 1962; Lax and Wendroff, 1964). It uses the Eliassen time staggering variables (Eliassen, 1956).	At the equator symmetric boundary conditions are chosen.
The French Weather Service Limited Area Model	An Arakawa C-type grid is used. Horizontal discretization is adapted from Sadourny (1975) and Burridge & Haseler (1977). In vertical 15 unevenly spaced σ levels are used where resolution is higher in PBL.	Leap-frog time integration scheme is used. Linear part of the gravity term is treated semi-implicitly. Vertical advection and diffusion terms are treated implicitly.	Fixed large-scale boundary conditions are used. Boundary relaxation proposed by Davies (1976) is used and is treated implicitly.
ECMWF Limited Area Model	Fields are staggered in horizontal as well as in vertical. Arakawa c-type grid is used in horizontal.	Semi-implicit time-stepping scheme is used following Robert <i>et al.</i> (1972). It is based on a time centered scheme.	Time-dependent b.c.s derived either from a previous global forecast or from analyses given at intervals of a few hours. Boundary relaxation technique suggested by Davies (1976) is used for smoothing
FSU Limited Area Model	Fields are staggered in horizontal as well as in vertical. Arakawa c-grid (Mesinger & Arakawa, 1976) is used in horizontal.	A one-step semi-Lagrangian advection (Mathur, 1983) and a semi-implicit time differencing scheme is used.	Model has an option of two types of boundary conditions. 1) Fixed boundary conditions 2) Time-dependent

Model	Initialization	PHYSICAL PROCESSES	
		Horizontal Diffusion	Surface Parameters
NCAR/ Penn State limited area model	Vertical mode initialization scheme developed by Errico (1986).	A second order diffusion near lateral boundaries and fourth-order diffusion inside the domain is used.	Ground surface temperature is computed from a surface-energy budget following the "force restore" slab model developed by Blackadar (Zhang & Anthes, 1982). Fixed ground moisture is used. Surface fluxes are calculated either Bulk-aerodynamically following Deardorff (1972) or using similarity theory.
JMA Tokyo Regional Spectral model	Nonlinear normal mode initialization is used.	Horizontal diffusion is done by linear fourth order Laplacian.	Daily analysed sea surface temperature. Ground surface temperature calculated with 3 ground layers. Fixed ground moisture is used. Surface fluxes are calculated by similarity theory following the scheme given by Louis.
NMC The Nested grid Model	Initialized fields are extracted from globally nonlinear normal mode initialized data.	None	Ground surface temperature is not calculated. No ground hydrology is done. Heat and moisture surface fluxes are not calculated over land. Surface fluxes are calculated Bulk-aerodynamically.
The French Weather Service Limited Area Model	Non-linear normal mode initialization is used.	Fourth order horizontal diffusion.	Ground surface temperature is computed by surface energy budget using a slab model. Similarly ground wetness is computed dynamically using slab model of two layers. Surface fluxes are calculated by stability dependent scheme given by Louis et al. (1981).
ECMWF Limited Area Model	Non-linear normal mode initialization.	Linear fourth order horizontal diffusion.	Ground surface temperature is computed by a slab model. Stability dependent surface fluxes are calculated using similarity theory (Louis, 1979).
FSU Limited area Model	Dynamic normal mode initialization proposed by Sugi (1986).	Linear second order horizontal diffusion.	Ground surface temperature is computed by surface energy balance. Surface fluxes are computed using similarity theory.

¹ In three cases namely stable, mechanically-driven turbulence and forced convection the prognostic variables above the surface layer are computed from k-theory. In the fourth case of free-convection above the surface layer a mixed layer is considered where the vertical mixing is visualized as taking place between the lowest layer and each layer in the mixed layer. Above this layer k-theory is used.

Model	PHYSICAL PROCESSES			Domain
	PBL	Cumulus Parameterization	Radiation	
NCAR/ Penn State limited area model	Vertical eddy fluxes are either calculated Bulk-aerodynamically or using high resolution Blackadar PBL model (Zhang & Anthes, 1982). The atmosphere stratification is divided into four categories based on bulk Richardson number. ¹	A modified Kuo scheme (Anthes, 1977) is used. Dry convective adjustment is also carried out.	Short wave & long wave radiation parameterized. For short wave transmissivity multiple reflection (Benjamin, 1983) is used. Clear-air transmissivities, back scattering coefficients and longwave emissivity are functions of path length and precipitable water. Cloud effects are included following Benjamin, 1983.	Variable domain but poles not included.
Spectral model	ty and shear dependent eddy viscosity coefficients are used.	tion of rain is included.	temperature.	
NMC The Nested grid Model	Eddy fluxes in the vertical are computed using austausch form.	A modified KUO scheme is used. Large scale saturation adjustment is done.	Same as FSU.	Hemispheric model.
The French Weather Service Limited Area Model	Vertical diffusion of fluxes is done using K-theory according to Louis et al. (1981).	Parameterization of deep convection by Bougeault (1985) and Geleyn (1985) and super-saturation are included. Evaporation of rain is also allowed.	Simple radiative transfer scheme is used. Water vapor is the only active constituent for emission & absorption. Emissivity and absorptivity are parameterized by Lepas et al. (1979). Effect of clouds is also included.	Domain centered on Western Europe.
ECMWF Limited Area Model	Eddy fluxes are calculated on the basis of the mixing length theory. Stability and wind shear dependent diffusion coefficients are used.	Kuo-74 cumulus model, supersaturation large scale condensation and non-convective cloud parameterization are included. Evaporation of rain is included.	Radiation parameterization is done following Geleyn and Hollingsworth (1979). Gaseous absorption of H ₂ O CO ₂ and O ₃ is included using band model theory. Cloudy sky is also parameterized.	An arbitrary rectangle but cannot contain a pole or cover a complete zone.
FSU Limited area Model	For the vertical eddy fluxes there are two options: 1) vertical structure based on GATE. 2) K-theory, where diffusion coefficient depends on the mixing length, vertical wind shear and stability of the atmosphere.	The model includes parameterization of deep moist convection following Krishnamurti et al. (1983a), shallow convection (Tiedke, 1984) and large-scale condensation.	Long-wave radiation parameterization based on Harshvardhan and Corsetti (1984); includes effects of water vapor, CO ₂ , O ₃ and clouds. Short-wave radiation scheme is similar to UCLA/GLAS GCM as described by Davies (1982).	Variable domain but poles not included.

work we attempt to provide a realistic representation of the surface latent heat fluxes to overcome the aforementioned inadequacy through the development of a new ground wetness parameterization.

The objectives of the present study are:

- (i) Development of a high resolution regional weather prediction model for the tropics.
- (ii) Assess the performance of the model in predicting the land-fall of a tropical storm.
- (iii) Formulate a procedure to find the initial values of ground wetness and thereafter develop a ground wetness parameterization scheme which includes the effects of precipitation and other land-surface processes in its specification during the integration.
- (iv) Assess the impact of improved ground wetness parameterization in estimating the surface latent heat fluxes and surface temperature.
- (v) Conduct sensitivity experiments to see the impact of improved ground wetness parameterization on rainfall prediction for the same tropical storm as (ii) at resolutions ($1^{\circ} \times 1^{\circ}$) and ($\frac{1}{2}^{\circ} \times \frac{1}{2}^{\circ}$).

The present model is considerably enhanced in the dynamical, physical and initialization aspects. Specifically this model has been designed for studies at very high resolution towards the examination of heavy rainfall events. The model utilizes the usual sigma frame as the vertical coordinate and permits the use of steep mountains. A one

step semi-Lagrangian advection (based on Mathur, 1983) and a semi-implicit time differencing scheme provide the basic framework for this model. The finite differencing grid utilizes the Arakawa c-grid (see Mesinger and Arakawa, 1976). This grid is staggered along the horizontal and the vertical coordinates. Fourth order finite differences are used in the formulation of most of the dynamics and physics of the model. The domain chosen for the present study is -9.4°S to 39.4°N and 45°E to 114.4°E .

The tropical cyclone is an integral part of the weather activity in most tropical ocean basins. Its influence extends into the extratropics. Their evolution has been a subject of interest for decades. During the pre-monsoon period of 1979, when the cross equatorial flow was weak, a tropical depression in the Bay of Bengal on May 4, intensified into a hurricane on May 8, and eventually made landfall on the southeast coast of India causing a major disaster. Recently a numerical study of the genesis of this storm using a fine resolution ($\frac{1}{4}^{\circ} \times \frac{1}{4}^{\circ}$) regional model has been conducted by Tuleya (1988). It is of interest and importance to see the capability of the present regional model in forecasting the landfall of this tropical storm.

An important area deserving further work relates to the proper treatment of fluxes of latent heat at the earth's surface. An important factor in the surface latent heat flux estimation is the parameterization of ground wetness. In climate modelling significant impact of this parameter on the precipitation predictions has been demonstrated by many investigators such as: Yamakazi (1989), Rind

(1984) and several others. Nearly all the regional models outlined in table 1 including the present FSU regional model use very simple parameterization of the ground wetness. These formulations do not provide the changes in ground wetness due to precipitation and many other land surface processes. Therefore we propose a new ground wetness parameterization scheme to remove these deficiencies to some extent. This method makes use of observed measures of vertically integrated humidity budgets to provide a database for the surface humidity fluxes. These, in turn, are used to derive a statistical parameterization for the ground wetness. This parameterization is then used in very high resolution modelling experiments.

CHAPTER 2

DYNAMICAL FRAMEWORK OF THE REGIONAL MODEL

2.1 Vertical and Horizontal Discretization:

The dimensionless σ coordinate is used in the vertical:

$$\sigma = \frac{p}{p_s} \quad (2.1)$$

where p is the pressure and p_s is the pressure at the earth's surface. A list of useful symbols is given on page xvii.

The vertical extent of the model ranges from $\sigma=\sigma_T$ at top of the model to $\sigma=1$ at the earth's surface. There are N layers in the vertical. The thickness of each layer, measured by $\Delta\sigma$, is uniform. Fig. 1 shows the vertical discretization of the model, in which,

$$N = 9 \text{ and } \sigma_T = 0.1. \quad (2.2)$$

Variables u , v , q , and T are defined at the centre of σ layers (dashed levels). The vertical velocity σ and z are defined at the layer interfaces (solid levels).

Arakawa C type grid is used for the horizontal discretization. This appears to be very well suited for the representation of divergence and for the formulation of a Helmholtz's equation which

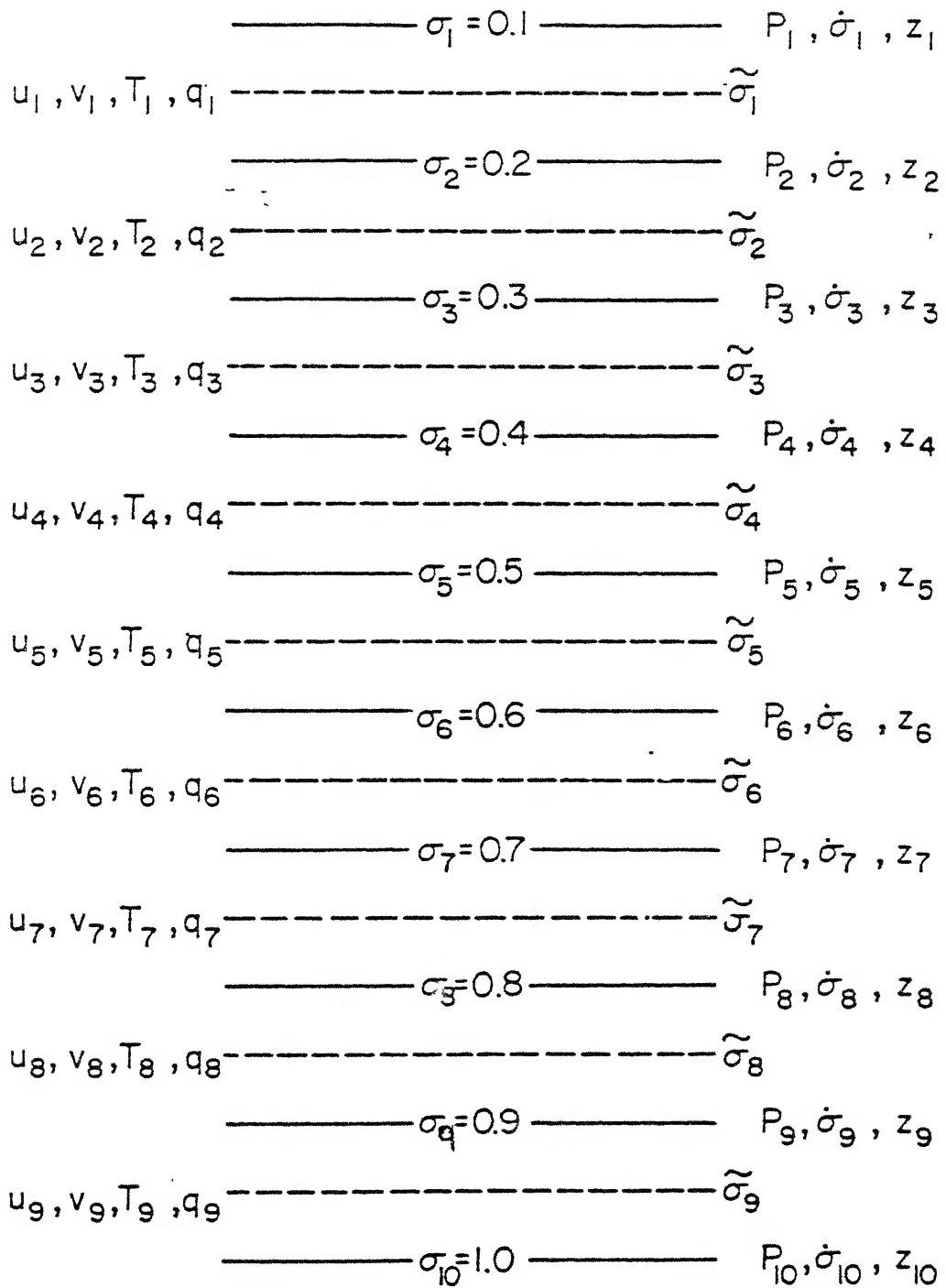


Figure 1: Vertical discretization of the model.

arises in the use of the semi-implicit time integration scheme (McGregor and Leslie, 1977).

The variable representation on the staggered grid are shown in fig. 2. Other thermodynamic variables such as q and T are defined on top of z . σ and $\ln p_s$ are also located at these points.

2.2 Equations of motion:

The governing equations for a semi-Lagrangian formulation in the σ coordinate system are written as follows:

$$\frac{Du}{Dt} = -\dot{\sigma} \frac{\partial u}{\partial \sigma} + v(f + \frac{u}{a} \tan \phi) - g \frac{\partial z}{\partial x} - RT \frac{\partial \ln p_s}{\partial x} + F_x \equiv r_1 \quad (2.3)$$

$$\frac{Dv}{Dt} = -\dot{\sigma} \frac{\partial v}{\partial \sigma} - u(f + \frac{u}{a} \tan \phi) - g \frac{\partial z}{\partial y} - RT \frac{\partial \ln p_s}{\partial y} + F_y \equiv r_2 \quad (2.4)$$

Thermodynamic equation

$$\frac{DT}{Dt} = -\dot{\sigma} \frac{\partial T}{\partial \sigma} + \kappa T \left[\frac{\dot{\sigma}}{\sigma} + \frac{D \ln p_s}{Dt} \right] + H/C_p \quad (2.5)$$

Mass continuity equation

$$\frac{D \ln p_s}{Dt} = -\frac{\partial \dot{\sigma}}{\partial \sigma} - \nabla \cdot \vec{V} \quad (2.6)$$

Moisture continuity equation

$$\frac{Dq}{Dt} = -\dot{\sigma} \frac{\partial q}{\partial \sigma} + E \quad (2.7)$$

Equations (2.3)-(2.7) form the prognostic equations of the model.

To close the system of equations (2.3)-(2.7), the following diagnostic equations are used

Hydrostatic equation

$$\frac{\partial z}{\partial \sigma} = -\frac{RT}{g\sigma} = -\frac{C_p \theta}{g} \frac{\partial \pi^k}{\partial \sigma} \quad (2.8)$$

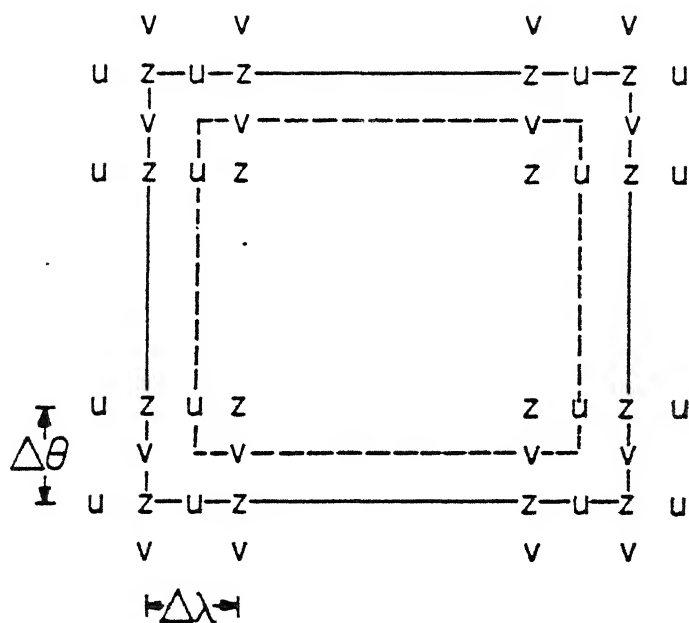


Figure 2: Horizontal discretization (Arakawa c type grid).

Equation of state

$$\alpha = \frac{RT}{p} = \frac{RT}{\sigma p_s} \quad (2.9)$$

The quantity π^K in equation (2.8) is obtained from the Poisson equation:

$$\frac{T}{\theta} = \pi^K = \left[\frac{p}{1000} \right]^K \quad (2.10)$$

The operator $\frac{D}{Dt}$ in equations (2.3)-(2.7), which represents the horizontal Lagrangian operator, can be expressed, in spherical polar coordinate system as

$$\frac{D}{Dt} () = \frac{\partial}{\partial t} () + \frac{u}{a \cos \phi} \frac{\partial}{\partial \lambda} () + \frac{v}{a} \frac{\partial}{\partial \phi} () \quad (2.11)$$

or, in Cartesian coordinate system as

$$\frac{D}{Dt} () = \frac{\partial}{\partial t} () + u \frac{\partial}{\partial x} () + v \frac{\partial}{\partial y} () \quad (2.12)$$

2.3 The Integration Scheme

A one step, second order, semi-Lagrangian advection scheme is used to integrate the model. A special feature of this scheme is that it accounts for time changes of dependent variables and advecting velocity over the trajectory traced by the parcel in time step Δt . The inclusion of this formulation of the advective processes is expected to give better prediction of the phase and amplitude of rapidly developing disturbances as is generally the case in tropics. From a physical point of view it is a direct approach. To make this scheme economical this scheme is coupled to the semi-implicit time integration scheme.

Equations (2.3) to (2.7) are transformed into a form suitable for

the semi-Lagrangian semi-implicit formalism using the following definitions:

$$F^* = \frac{\iint F \cos\phi \, d\lambda d\phi}{\iint \cos\phi \, d\lambda d\phi}, \quad (2.13)$$

the horizontal average over the model domain.

$$F' = F - F^* \quad (2.14)$$

the deviation of the variable from its mean.

Combining the thermodynamic energy equation (2.5) and the mass continuity equation (2.6), a model parameter P is defined as

$$P = gz + RT^* \ln p_s \quad (2.15)$$

so at the earth's surface,

$$P_s = gz_s + RT_s^* \ln p_s \quad (2.16)$$

where z_s and T_s^* are the surface topography and area averaged surface temperature, respectively.

A static stability parameter γ is defined by the relation

$$\gamma = \frac{R}{\sigma} \left[\frac{\kappa T}{\sigma} - \frac{\partial T}{\partial \sigma} \right] \quad (2.17)$$

a horizontal area averaged static stability is given by,

$$\gamma^* = \frac{R}{\sigma} \left[\frac{\kappa T^*}{\sigma} - \frac{\partial T^*}{\partial \sigma} \right] \quad (2.18)$$

and the deviation is expressed by

$$\gamma' = \gamma - \gamma^* \quad (2.19)$$

Upon applying (2.13)-(2.19) to (2.3)-(2.5) and (2.7) the latter can be written as

$$\begin{aligned} \frac{Du}{Dt} &= -\sigma \frac{\partial u}{\partial \sigma} + v(f + \frac{u}{a} \tan\phi) - g \frac{\partial z}{\partial x} - R(T^* + T') \frac{\partial \ln p_s}{\partial x} + F_x \\ &= -\sigma \frac{\partial u}{\partial \sigma} + v(f + \frac{u}{a} \tan\phi) - \frac{\partial}{\partial x} (gz + RT^* \ln p_s) - RT' \frac{\partial \ln p_s}{\partial x} + F_x \\ \text{or } \frac{Du}{Dt} + \frac{\partial P}{\partial x} &= -\sigma \frac{\partial u}{\partial \sigma} + v(f + \frac{u}{a} \tan\phi) - RT' \frac{\partial \ln p_s}{\partial x} + F_x \equiv s_1 \end{aligned} \quad (2.20)$$

Similarly we obtain,

$$\frac{Dv}{Dt} + \frac{\partial P}{\partial y} = -\dot{\sigma} \frac{\partial v}{\partial \sigma} - u(f + \frac{u}{a} \tan \phi) - RT' \frac{\partial \ln p_s}{\partial y} + F_y \equiv s_2 \quad (2.21)$$

$$\begin{aligned} \frac{DT}{Dt} + \sigma \frac{\partial T^*}{\partial \sigma} - \kappa T^* \left[\frac{\dot{\sigma}}{\sigma} + \frac{D \ln p_s}{Dt} \right] \\ = -\dot{\sigma} \frac{\partial T'}{\partial \sigma} + \kappa T' \left[\frac{\dot{\sigma}}{\sigma} + \frac{D \ln p_s}{Dt} \right] + \frac{H}{C_p} \end{aligned}$$

from a use of the mass continuity equation we obtain,

$$\begin{aligned} \frac{D}{Dt} (T - \kappa T^* \ln p_s) - \frac{\gamma^* \dot{\sigma} \sigma}{R} &= \dot{\sigma} \left[\frac{\kappa T'}{\sigma} - \frac{\partial T'}{\partial \sigma} \right] - \kappa T' \left[\frac{\partial \dot{\sigma}}{\partial \sigma} + \nabla \cdot \vec{V} \right] + \frac{H}{C_p} \\ \frac{D}{Dt} \left[-g \frac{\sigma}{R} \frac{\partial z}{\partial \sigma} - \kappa T^* \ln p_s \right] - \frac{\gamma^* \dot{\sigma} \sigma}{R} &= \dot{\sigma} \left[\frac{\kappa T'}{\sigma} - \frac{\partial T'}{\partial \sigma} \right] - \kappa T' \left[\frac{\partial \dot{\sigma}}{\partial \sigma} + \nabla \cdot \vec{V} \right] + \frac{H}{C_p} \\ -\frac{\sigma}{R} \frac{D}{Dt} \left[\frac{\partial P}{\partial \sigma} + \sigma \gamma^* \ln p_s \right] - \frac{\gamma^* \dot{\sigma} \sigma}{R} &= \dot{\sigma} \left[\frac{\kappa T'}{\sigma} - \frac{\partial T'}{\partial \sigma} \right] - \kappa T' \left[\frac{\partial \dot{\sigma}}{\partial \sigma} + \nabla \cdot \vec{V} \right] + \frac{H}{C_p} \\ \text{or } \frac{D}{Dt} \left[\frac{1}{\gamma^*} \frac{\partial P}{\partial \sigma} + \sigma \ln p_s \right] + \dot{\sigma} &= -\frac{\gamma' \dot{\sigma}}{\gamma^*} + \frac{\kappa R T'}{\sigma \gamma^*} \left[\frac{\partial \dot{\sigma}}{\partial \sigma} + \nabla \cdot \vec{V} \right] - \frac{R H}{C_p \sigma \gamma^*} \equiv s_3 \end{aligned} \quad (2.22)$$

$$\frac{Dq}{Dt} = -\dot{\sigma} \frac{\partial q}{\partial \sigma} + E \equiv s_4 \quad (2.23)$$

In equation (2.20)-(2.23) all the non-linear terms appear on the right hand side.

A few more definitions are required for the semi-Lagrangian formulation, these are given below

$$F = F(x, y, \sigma, t), \text{ a function at any point } x, y, \sigma \text{ and at current time step } t \quad (2.24)$$

$$F^+ = F(x, y, \sigma, t + \Delta t), \text{ a function at point } x, y, \sigma \text{ and at a future time step } t + \Delta t \quad (2.25)$$

$$F^\circ = F(x-a, y-b, \sigma, t), \text{ a function at time } t \text{ at a point } x-a, y-b \text{ from where the parcel arrives at } x, y \text{ at time } t + \Delta t \quad (2.26)$$

In semi-Lagrangian form DF/DT is expressed by

$$\frac{DF}{Dt} \equiv \frac{d_H F}{dt} = \frac{F^+ - F^\circ}{\Delta t} \quad (2.27)$$

A semi-Lagrangian time average denoted by overbar is defined as

$$\overline{F} = \frac{F^+ + F^0}{2} \quad (2.28)$$

Upon application of the semi-Lagrangian - semi-implicit operations the equations (2.20)-(2.23) and (2.6) are transformed into the following equations.

$$\frac{d_H u}{dt} + \frac{\partial \overline{P}}{\partial x} = S_1^0 \quad (2.29)$$

$$\frac{d_H v}{dt} + \frac{\partial \overline{P}}{\partial y} = S_2^0 \quad (2.30)$$

$$\frac{d_H}{dt} \left[\frac{1}{\gamma^*} \frac{\partial \overline{P}}{\partial \sigma} + \sigma \ln p_s \right] + \frac{\overline{\sigma}}{\sigma} = S_3^0 \quad (2.31)$$

$$\frac{d_H q}{dt} = S_4^0 \quad (2.32)$$

and

$$\frac{d_H \ln p_s}{dt} + \overline{\nabla \cdot \mathbf{v}} + \frac{\partial \sigma}{\partial \sigma} = 0 \quad (2.33)$$

Here the forcing terms on the right hand side of equations (2.20)-(2.23) are replaced by their values at the origin. Equations (2.29)-(2.33) can be expressed as a set of 5 symbolic algebraic equations

$$w_j^+ = x_j^0 \quad j = 1, 2, \dots, 5 \quad (2.34)$$

As described earlier, the superscript + refers to a future value at a grid point, ° refers to the current value at the point of origin. The subscript j indicates equations corresponding to equations (2.29)-(2.33).

The individual terms in the equation (2.34) may be identified as

w_j

$$w_1 = u + \frac{\Delta t}{2} \frac{\partial P}{\partial x} \quad (2.35)$$

$$w_2 = v + \frac{\Delta t}{2} \frac{\partial P}{\partial y} \quad (2.36)$$

$$W_3 = \frac{1}{\gamma^*} \frac{\partial P}{\partial \sigma} + \sigma \ln p_s + \frac{\Delta t}{2} \dot{\sigma} \quad (2.37)$$

$$W_4 = q \quad (2.38)$$

$$W_5 = \ln p_s + \frac{\Delta t}{2} \left[\nabla \cdot \vec{V} + \frac{\partial \dot{\sigma}}{\partial \sigma} \right] \quad (2.39)$$

X_j

$$X_1 = u - \frac{\Delta t}{2} \left[\frac{\partial P}{\partial x} - 2s_1 \right] \quad (2.40)$$

$$X_2 = v - \frac{\Delta t}{2} \left[\frac{\partial P}{\partial y} - 2s_2 \right] \quad (2.41)$$

$$X_3 = \frac{1}{\gamma^*} \frac{\partial P}{\partial \sigma} + \sigma \ln p_s - \frac{\Delta t}{2} (\dot{\sigma} - 2s_3) \quad (2.42)$$

$$X_4 = q + s_4 \times \Delta t \quad (2.43)$$

$$X_5 = \ln p_s - \frac{\Delta t}{2} \left[\nabla \cdot \vec{V} + \frac{\partial \dot{\sigma}}{\partial \sigma} \right] \quad (2.44)$$

By eliminating various quantities from equations (2.35)-(2.39) a single equation for the model parameter P is obtained

$$\frac{\Delta t^2}{4} \nabla^2 P + \frac{\partial}{\partial \sigma} \left[\frac{1}{\gamma^*} \frac{\partial P}{\partial \sigma} \right] = \frac{\Delta t}{2} \nabla \cdot \vec{W} + \frac{\partial W_3}{\partial \sigma} - W_5 \equiv Q \quad (2.45)$$

$$\text{where } \vec{W} = i_\lambda W_1 + i_\phi W_2 \quad (2.46)$$

Equation (2.45) is a three dimensional elliptic equation. This equation can be solved with appropriate boundary conditions for P. W^+ can be obtained from equation (2.34) making use of equations (2.40)-(2.44).

Equations (2.35)-(2.39) can then be used to give the prognostic variables. At upper and lower boundaries the vertical velocity $\dot{\sigma}=0$ (see section 2.5). At upper boundary, therefore, (2.37) becomes

$$\frac{1}{\gamma^*} \frac{\partial P}{\partial \sigma} = W_3 - \sigma \ln p_s$$

At lower boundary

$$\frac{1}{\gamma^*} \frac{\partial P}{\partial \sigma} = W_3 - \sigma \ln p_s \quad \text{where } \sigma=1$$

From the vertical structure of the model, given in figure 1, we shall make the following definitions:

NP1: Number of σ layer boundaries

σ_k ($k=1(1)NP1$): σ at layer boundaries

$\tilde{\sigma}_k$ ($k=1(1)N$): σ at layer means

$$\Delta \sigma_k = \sigma_{k+1} - \sigma_k \quad k=1(1)N \quad (2.47)$$

$$\Delta \tilde{\sigma}_k = \tilde{\sigma}_{k+1} - \tilde{\sigma}_k \quad k=1(1)NMI \quad (2.48)$$

$$P_k = gz_k + RT_k^* \ln p_s \quad (2.49)$$

$$P_{NP1} = gz_s + RT_s^* \ln p_s \quad (2.50)$$

or

$$\ln p_s = \frac{P_{NP1}}{RT_s^*} - \frac{gz_s}{RT_s^*} \quad (2.51)$$

In writing the equations in finite difference form, the following boundary conditions are used (see section 2.5):

Top of the model

$$\sigma = \sigma_T, \quad \sigma = 0 \quad (2.52)$$

Bottom of the model

$$\sigma = 1, \quad \sigma = 0 \quad (2.53)$$

The left hand side terms (W_j) of equation (2.34) are written in finite difference form as follows:

Starting from the expressions for W_1 and W_2 from (2.35) and (2.36)

For any layer k we can write,

$$\tilde{W}_{1k} = \tilde{u}_k + \frac{\Delta t}{2} \left[\frac{\frac{\partial P_{k+1}}{\partial x} + \frac{\partial P_k}{\partial x}}{2} \right], \quad (2.54)$$

and

$$\tilde{w}_{2k} = \tilde{v}_k + \frac{\Delta t}{2} \left[\frac{\frac{\partial P_{k+1}}{\partial y} + \frac{\partial P_k}{\partial y}}{2} \right] \quad (2.55)$$

(2.54) and (2.55) can be expressed as a single vector equation, i.e.,

$$\begin{aligned} \vec{\tilde{w}}_k &= i_\lambda \vec{\tilde{w}}_{1k} + i_\phi \vec{\tilde{w}}_{2k} \\ &= \vec{\tilde{v}}_k + \frac{\Delta t}{2} \left[\frac{\nabla P_{k+1} + \nabla P_k}{2} \right] \end{aligned} \quad (2.56)$$

The divergence of (2.56) is expressed by,

$$\nabla \cdot \vec{\tilde{w}}_k = \nabla \cdot \vec{\tilde{v}}_k + \frac{\Delta t}{2} \left[\frac{\nabla^2 P_{k+1} + \nabla^2 P_k}{2} \right]. \quad (2.57)$$

From (2.57) by replacing k by $k-1$ we obtain

$$\nabla \cdot \vec{\tilde{w}}_{k-1} = \nabla \cdot \vec{\tilde{v}}_{k-1} + \frac{\Delta t}{2} \left[\frac{\nabla^2 P_k + \nabla^2 P_{k-1}}{2} \right] \quad (2.58)$$

adding (2.57) and (2.58) and dividing by 2 we obtain,

$$\frac{1}{2} (\nabla \cdot \vec{\tilde{w}}_k + \nabla \cdot \vec{\tilde{w}}_{k-1}) = \frac{(\nabla \cdot \vec{\tilde{v}}_k + \nabla \cdot \vec{\tilde{v}}_{k-1})}{2} + \frac{\Delta t}{2} \left[\frac{\nabla^2 P_{k+1} + 2\nabla^2 P_k + \nabla^2 P_{k-1}}{4} \right] \quad (2.59)$$

For the top layer ($k=1$) equation (2.57) takes the form

$$\nabla \cdot \vec{\tilde{w}}_1 = \nabla \cdot \vec{\tilde{v}}_1 + \frac{\Delta t}{2} \left[\frac{\nabla^2 P_2 + \nabla^2 P_1}{2} \right] \quad (2.60)$$

For the lowest layer ($k=N$) equation (2.57) takes the form

$$\nabla \cdot \vec{\tilde{w}}_N = \nabla \cdot \vec{\tilde{v}}_N + \frac{\Delta t}{2} \left[\frac{\nabla^2 P_{N+1} + \nabla^2 P_N}{2} \right] \quad (2.61)$$

We shall next examine the expression for w_3 :

At general levels k and $k-1$

$$\tilde{w}_{3k} = \frac{1}{\gamma_k^*} \left[\frac{P_{k+1} - P_k}{\Delta \sigma_k} \right] + \delta_{k \ln p_s} + \frac{\Delta t}{2} \left[\frac{\dot{\sigma}_{k+1} + \dot{\sigma}_k}{2} \right] \quad (2.62)$$

$$\tilde{w}_{3k-1} = \frac{1}{\gamma_{k-1}^*} \frac{P_k - P_{k-1}}{\Delta \sigma_{k-1}} + \delta_{k-1 \ln p_s} + \frac{\Delta t}{2} \left[\frac{\dot{\sigma}_k + \dot{\sigma}_{k-1}}{2} \right] \quad (2.63)$$

From equations (2.62) and (2.63) we obtain,

$$\begin{aligned} \frac{\tilde{W}_{3k} - \tilde{W}_{3k-1}}{\Delta\sigma_k} &= \frac{1}{\Delta\sigma_k} \left[\frac{1}{\tilde{\gamma}_k^*} \left[\frac{P_{k+1} - P_k}{\Delta\sigma_k} \right] - \frac{1}{\tilde{\gamma}_{k-1}^*} \left[\frac{P_k - P_{k-1}}{\Delta\sigma_{k-1}} \right] \right] \\ &\quad + \ln p_s + \frac{\Delta t}{2} \left[\frac{\dot{\sigma}_{k+1} - \dot{\sigma}_{k-1}}{2\Delta\sigma_k} \right] \end{aligned} \quad (2.64)$$

For the top layer equation (2.62) takes the form

$$\begin{aligned} \tilde{W}_{31} &= \frac{1}{\tilde{\gamma}_1^*} \left[\frac{P_2 - P_1}{\sigma_2 - \sigma_1} \right] + \sigma_1 \ln p_s + \frac{\Delta t}{2} \frac{\dot{\sigma}_2}{2} \\ \text{or } \tilde{W}_{31} &= \frac{1}{\gamma_2^*} \left[\frac{P_2 - P_1}{\sigma_2 - \sigma_1} \right] + \left[\sigma_1 + \frac{\Delta\sigma_1}{2} \right] \ln p_s + \frac{\Delta t}{2} \frac{\dot{\sigma}_2}{2} \\ \frac{\tilde{W}_{31}}{\Delta\sigma_1} &= \frac{1}{\tilde{\gamma}_1^*} \frac{1}{\Delta\sigma_1} \left[\frac{P_2 - P_1}{\sigma_2 - \sigma_1} \right] + \frac{\sigma_1}{\Delta\sigma_1} \ln p_s + \frac{1}{2} \ln p_s + \frac{\Delta t}{2} \frac{\dot{\sigma}_2}{2\Delta\sigma_1} \end{aligned} \quad (2.65)$$

For the lowest layer we obtain,

$$\frac{\tilde{W}_{3N}}{\Delta\sigma_{NM1}} = \frac{1}{\tilde{\gamma}_N^*} \frac{1}{\Delta\sigma_{NM1}} \left[\frac{P_{NP1} - P_N}{\sigma_{NP1} - \sigma_N} \right] + \sigma_{NP1} \frac{\ln p_s}{\Delta\sigma_{NM1}} - \frac{1}{2} \ln p_s + \frac{\Delta t}{2} \frac{\dot{\sigma}_N}{2\Delta\sigma_{NM1}} \quad (2.66)$$

At general levels W_5 is written as:

$$\tilde{W}_{5k} = \ln p_s + \frac{\Delta t}{2} \nabla \cdot \vec{V}_k + \frac{\Delta t}{2} \left[\frac{\dot{\sigma}_{k+1} - \dot{\sigma}_k}{\Delta\sigma_k} \right] \quad (2.67)$$

$$\tilde{W}_{5k-1} = \ln p_s + \frac{\Delta t}{2} \nabla \cdot \vec{V}_{k-1} + \frac{\Delta t}{2} \left[\frac{\dot{\sigma}_k - \dot{\sigma}_{k-1}}{\Delta\sigma_{k-1}} \right] \quad (2.68)$$

In the present case $\Delta\sigma_k = \Delta\sigma_{k-1}$, combining equations (2.67) and (2.68) we obtain,

$$\frac{\tilde{W}_{5k} + \tilde{W}_{5k-1}}{2} = \ln p_s + \frac{\Delta t}{2} \left(\frac{\nabla \cdot \vec{V}_k + \nabla \cdot \vec{V}_{k-1}}{2} \right) + \frac{\Delta t}{2} \left[\frac{\dot{\sigma}_{k+1} - \dot{\sigma}_{k-1}}{2\Delta\sigma_k} \right] \quad (2.69)$$

combining equations (2.59), (2.69) we obtain

$$\begin{aligned} \frac{\tilde{W}_{5k} + \tilde{W}_{5k-1}}{2} &= \ln p_s + \frac{\Delta t}{2} (\nabla \cdot \vec{W}_k + \nabla \cdot \vec{W}_{k-1}) \\ &\quad - \left[\frac{\Delta t}{2} \right]^2 \left[\frac{\nabla^2 P_{k+1} + 2\nabla^2 P_k + \nabla^2 P_{k-1}}{4} \right] \\ &\quad + \frac{\Delta t}{2} \left[\frac{\dot{\sigma}_{k+1} - \dot{\sigma}_{k-1}}{\Delta\sigma_k} \right] \end{aligned} \quad (2.70)$$

For the top layer combining equations (2.60), (2.67) we obtain

$$\tilde{W}_{51} = \ln p_s + \frac{\Delta t}{2} \left[\nabla \cdot \tilde{W}_1 - \frac{\Delta t}{2} \left[\frac{\nabla^2 P_2 + \nabla^2 P_1}{2} \right] \right] + \frac{\Delta t}{2} \frac{\dot{\sigma}_2}{\Delta \sigma_1} \quad (2.71)$$

or

$$\ln p_s + \frac{\Delta t}{2} \frac{\dot{\sigma}_2}{\Delta \sigma_1} = \tilde{W}_{51} - \frac{\Delta t}{2} \nabla \cdot \tilde{W}_1 + \left[\frac{\Delta t}{2} \right]^2 \left[\frac{\nabla^2 P_2 + \nabla^2 P_1}{2} \right] \quad (2.72)$$

For the lowest layer combining equations (2.61), (2.67) we obtain

$$\tilde{W}_{5N} \ln p_s + \frac{\Delta t}{2} \left[\nabla \cdot \tilde{W}_N - \frac{\Delta t}{2} \left[\frac{\nabla^2 P_{NP1} + \nabla^2 P_N}{2} \right] \right] - \frac{\Delta t}{2} \frac{\sigma_N}{\Delta \sigma_N} \quad (2.73)$$

or

$$\ln p_s - \frac{\Delta t}{2} \frac{\sigma_N}{\Delta \sigma_N} = \tilde{W}_{5N} - \frac{\Delta t}{2} \nabla \cdot \tilde{W}_N + \left[\frac{\Delta t}{2} \right]^2 \left[\frac{\nabla^2 P_{NP1} + \nabla^2 P_N}{2} \right] \quad (2.74)$$

Upon elimination of various terms from the finite difference forms of the equations of motion, thermodynamic energy and mass continuity one obtains a single three-dimensional Helmholtz equation

$$\left[\frac{\Delta t}{2} \right]^2 \nabla^2 P + \frac{\partial}{\partial \sigma} \left[\frac{1}{\gamma^*} \frac{\partial P}{\partial \sigma} \right] = \frac{\Delta t}{2} \nabla \cdot \tilde{W} + \frac{\partial W_3}{\partial \sigma} - W_5 \equiv Q \quad (2.75)$$

Its finite difference form is obtained by combining equations (2.64), and (2.70), i.e.,

$$\begin{aligned} & \frac{1}{\Delta \sigma_k} \left[\frac{1}{\tilde{\gamma}_k^*} \left[\frac{P_{k+1} - P_k}{\Delta \sigma_k} \right] - \frac{1}{\tilde{\gamma}_{k-1}^*} \left[\frac{P_k - P_{k-1}}{\Delta \sigma_{k-1}} \right] \right] \\ & + \left[\frac{\Delta t}{2} \right]^2 \left[\frac{\nabla^2 P_{k+1} + 2\nabla^2 P_k + \nabla^2 P_{k-1}}{4} \right] \\ & = \frac{\Delta t}{2} \frac{(\nabla \cdot \tilde{W}_k + \nabla \cdot \tilde{W}_{k-1})}{2} + \left[\frac{\tilde{W}_{3k} - \tilde{W}_{3k-1}}{\Delta \sigma_k} \right] - \left[\frac{\tilde{W}_{5k} + \tilde{W}_{5k-1}}{2} \right] \end{aligned} \quad (2.76)$$

For the top layer, substituting for the last two terms in equation

(2.65) from equation (2.72), we obtain,

$$\begin{aligned} & \frac{\Delta t}{2} \frac{\nabla \cdot \tilde{W}_1}{2} + \frac{\tilde{W}_{31}}{\Delta \sigma_1} - \frac{\tilde{W}_{51}}{2} \\ & = \frac{1}{\tilde{\gamma}_1^*} \frac{1}{\Delta \sigma_1} \left[\frac{P_2 - P_1}{\sigma_2 - \sigma_1} \right] + \frac{\sigma_1}{\Delta \sigma_1} \ln p_s + \left[\frac{\Delta t}{2} \right]^2 \left[\frac{\nabla^2 P_2 + \nabla^2 P_1}{4} \right] \end{aligned} \quad (2.77)$$

Substituting for $\ln p_s$ in equation (2.77) from equation (2.51), we

obtain,

$$\begin{aligned} & \frac{1}{\tilde{\gamma}_1^*} \frac{1}{\Delta\sigma_1} \left[\frac{P_2 - P_1}{\sigma_2 - \sigma_1} \right] + \frac{\sigma_1}{\Delta\sigma_1} \frac{P_{NP1}}{RT_S^*} + \left[\frac{\Delta t}{2} \right]^2 \left[\frac{\nabla^2 P_2 + \nabla^2 P_1}{4} \right] \\ &= \frac{\Delta t}{2} \frac{\nabla \cdot \tilde{W}_1}{2} + \frac{\tilde{W}_{31}}{\Delta\sigma_1} - \frac{\tilde{W}_{51}}{2} + \frac{gz_S}{RT_S^*} \frac{\sigma_1}{\Delta\sigma_1} \end{aligned} \quad (2.78)$$

Similarly, at the lowest layer from equations (2.66), (2.74) and (2.51) we obtain

$$\begin{aligned} & - \frac{1}{\tilde{\gamma}_N^*} \frac{1}{\Delta\sigma_N} \left[\frac{P_{NP1} - P_N}{\sigma_{NP1} - \sigma_N} \right] - \frac{P_{NP1}}{RT_{NP1}^*} \frac{1}{\Delta\sigma_N} + \left[\frac{\Delta t}{2} \right]^2 \left[\frac{\nabla^2 P_{NP1} + \nabla^2 P_N}{4} \right] \\ &= - \frac{\tilde{W}_{3N}}{\Delta\sigma_N} - \frac{\tilde{W}_{5N}}{2} + \frac{\Delta t}{2} \frac{\nabla \cdot \tilde{W}_N}{2} - \frac{gz_S}{RT_{NP1}^*} \frac{1}{\Delta\sigma_N} \end{aligned} \quad (2.79)$$

Thus equation (2.75) is written in a finite difference form as follows:

$$\begin{aligned} & \frac{1}{\Delta\sigma_k} \left[\frac{1}{\tilde{\gamma}_k^*} \left[\frac{P_{k+1} - P_k}{\Delta\sigma_k} \right] - \frac{1}{\tilde{\gamma}_{k-1}^*} \left[\frac{P_k - P_{k-1}}{\Delta\sigma_{k-1}} \right] \right] \\ &+ \left[\frac{\Delta t}{2} \right]^2 \left[\frac{\nabla^2 P_{k+1} + 2\nabla^2 P_k + \nabla^2 P_{k-1}}{4} \right] \\ &= \frac{\Delta t}{2} \frac{(\nabla \cdot \tilde{W}_k + \nabla \cdot \tilde{W}_{k-1})}{2} + \frac{\tilde{W}_{3k} - \tilde{W}_{3k-1}}{\Delta\sigma_k} - \frac{\tilde{W}_{5k} + \tilde{W}_{5k-1}}{2} \end{aligned} \quad (2.80)$$

$k=2(1)N$

For the top layer ($k=1$) its form is,

$$\begin{aligned} & \frac{1}{\tilde{\gamma}_1^*} \frac{1}{\Delta\sigma_1} \left[\frac{P_2 - P_1}{\sigma_2 - \sigma_1} \right] + \frac{\sigma_1}{\Delta\sigma_1} \frac{P_{NP1}}{RT_S^*} + \left[\frac{\Delta t}{2} \right]^2 \left[\frac{\nabla^2 P_2 + \nabla^2 P_1}{4} \right] \\ &= \frac{\Delta t}{2} \frac{(\nabla \cdot \tilde{W}_1)}{2} + \frac{\tilde{W}_{31}}{\Delta\sigma_1} - \frac{\tilde{W}_{51}}{2} + \frac{gz_S}{RT_S^*} \frac{\sigma_1}{\Delta\sigma_1} \end{aligned} \quad (2.81)$$

and at the lowest layer ($k=NP1$) its form is,

$$- \frac{1}{\tilde{\gamma}_N^*} \frac{1}{\Delta\sigma_N} \left[\frac{P_{NP1} - P_N}{\sigma_{NP1} - \sigma_N} \right] - \frac{P_{NP1}}{RT_{NP1}^*} \frac{1}{\Delta\sigma_N} + \left[\frac{\Delta t}{2} \right]^2 \left[\frac{\nabla^2 P_{NP1} + \nabla^2 P_N}{4} \right]$$

$$= -\frac{\tilde{W}_{3N}}{\Delta\sigma_N} - \frac{\tilde{W}_{5N}}{2} + \frac{\Delta t}{2} \left[\frac{\nabla \cdot \tilde{W}_N}{2} \right] - \frac{gz_s}{RT_{NP1}^*} \frac{1}{\Delta\sigma_N} \quad (2.82)$$

It follows from equations (2.80) to (2.82) that equation (2.75) can be represented by a set of NP1 Helmholtz equations. However, these equations are coupled and need to be made linearly independent before a two dimensional direct solver could be applied for their solution.

The set of linear equations (2.80) to (2.82) can be represented by a single matrix equation

$$\underline{A}\underline{P} + \nabla^2 \underline{B}\underline{P} = \underline{F} \quad (2.83)$$

A and B are (NP1xNP1) matrices, \underline{P} is a column vector of length NP1. \underline{F} is also a column vector of length NP1. Equation (2.83) can be written as

$$\underline{P} + \nabla^2 \underline{A}^{-1} \underline{B}\underline{P} = \underline{A}^{-1} \underline{F} \quad (2.84)$$

$$\text{Let } \underline{A}^{-1} \underline{B} = \underline{C} \quad (2.85)$$

Thus equation (2.84) becomes

$$\underline{P} + \nabla^2 \underline{C}\underline{P} = \underline{A}^{-1} \underline{F} \quad (2.86)$$

Matrix \underline{C} can be diagonalized using a similarity transformation.

If two matrices \underline{T} and \underline{T}^{-1} can be determined such that

$$\underline{T} \underline{C} \underline{T}^{-1} = \underline{\epsilon} \quad (2.87)$$

then

$$\underline{C} = \underline{T}^{-1} \underline{\epsilon} \underline{T} \quad (2.88)$$

$$\text{where } \underline{\epsilon} = \begin{vmatrix} \epsilon_1 & & \\ & \epsilon_2 & \\ & & \epsilon_{NP1} \end{vmatrix}$$

is a diagonal matrix representing eigen values of a matrix \underline{C} .

Substituting equation (2.88) in equation (2.86) we obtain,

$$\underline{P} + \nabla^2 \underline{T}^{-1} \underline{\epsilon} \underline{T} \underline{P} = \underline{A}^{-1} \underline{F} \quad (2.89)$$

Operating equation (2.89) by \underline{T} , we obtain

$$\underline{TP} + \nabla^2 \underline{\epsilon} \underline{T} \underline{P} = \underline{T} \underline{A}^{-1} \underline{F}$$

$$\text{Let } \underline{T} \underline{P} = \underline{R} \quad \text{and} \quad \underline{T} \underline{A}^{-1} = \underline{E} \quad (2.90)$$

$$\underline{R} + \nabla^2 \underline{\epsilon} \underline{R} = \underline{EF} \quad (2.91)$$

Equation (2.91) is a matrix representation for a set of linearly independent Helmholtz equations. Solution of equation (2.91) by the direct method provides \underline{R} . Thus values of \underline{P} can be obtained by using (2.90).

Let \underline{V} be the matrix of eigen-vectors of matrix \underline{C} corresponding to eigen values $\underline{\epsilon}$ i.e.

$$\underline{C} \underline{V} = \underline{V} \underline{\epsilon} \quad (2.92)$$

$$\text{or} \quad \underline{C} = \underline{V} \underline{\epsilon} \underline{V}^{-1} \quad (2.93)$$

$$\text{But} \quad \underline{C} = \underline{T}^{-1} \underline{\epsilon} \underline{T}$$

therefore $\underline{T}^{-1} = \underline{V}$ = Eigen vector matrix

For finding the eigen values ($\underline{\epsilon}$) and eigen vectors (\underline{T}^{-1}) of matrix \underline{C} ($=\underline{A}^{-1}\underline{B}$), the elements of matrices \underline{A} and \underline{B} are required. These can be written from equations (2.80), (2.81), (2.82) as follows.

Matrix A.

$$A_{1,1} = -\frac{1}{\tilde{\gamma}_1^*} \frac{1}{\Delta \tilde{\sigma}_1} \frac{1}{\Delta \sigma_1} \quad (2.94-a)$$

$$A_{1,2} = \frac{1}{\tilde{\gamma}_1^*} \frac{1}{\Delta \tilde{\sigma}_1} \frac{1}{\Delta \sigma_1} \quad (2.94-b)$$

$$A_{1,NP1} = \frac{\sigma_1}{\Delta \tilde{\sigma}_1} \frac{1}{RT_{NP1}^*} \quad (2.94-c)$$

$$A_{i,i-1} = \frac{1}{\tilde{\gamma}_{i-1}^*} \frac{1}{\Delta\sigma_{i-1}} \frac{1}{\Delta\sigma_i} \quad (2.94-d)$$

$$A_{i,i} = - \frac{1}{\tilde{\gamma}_i^*} \frac{1}{\Delta\sigma_i} \frac{1}{\Delta\sigma_i} - \frac{1}{\tilde{\gamma}_{i-1}^*} \frac{1}{\Delta\sigma_{i-1}} \frac{1}{\Delta\sigma_i} \quad (2.94-e)$$

$$A_{i,i+1} = \frac{1}{\tilde{\gamma}_i^*} \frac{1}{\Delta\sigma_i} \frac{1}{\Delta\sigma_i} \quad (2.94-f)$$

$$A_{NP1,N} = \frac{1}{\tilde{\gamma}_N^*} \frac{1}{\Delta\sigma_{N-1}} \frac{1}{\Delta\sigma_N} \quad (2.94-g)$$

$$A_{NP1,NP1} = - \frac{1}{\tilde{\gamma}_N^*} \frac{1}{\Delta\sigma_N} \frac{1}{\Delta\sigma_N} - \frac{1}{RT_{NP1}} \frac{1}{\Delta\sigma_N} \quad (2.94-h)$$

Matrix B

$$B_{1,1} = 0.25 (\Delta t/2)^2 \quad (2.95-a)$$

$$B_{1,2} = 0.25 (\Delta t/2)^2 \quad (2.95-b)$$

$$B_{i,i-1} = 0.25 (\Delta t/2)^2 \quad (2.95-c)$$

$$B_{i,i} = 0.50 (\Delta t/2)^2 \quad (2.95-d)$$

$$B_{i,i+1} = 0.25 (\Delta t/2)^2 \quad (2.95-e)$$

$$B_{NP1,N} = 0.25 (\Delta t/2)^2 \quad (2.95-f)$$

$$B_{NP1,NP1} = 0.25 (\Delta t/2)^2 \quad (2.95-g)$$

Equation (2.91) can be written for each component, as the following

$$R_k(x,y,t) + \epsilon_k \nabla^2 R_k(x,y,t) = G_k(x,y,t) \quad k = 1(1)NP1 \quad (2.96)$$

Here each k represents one vertical mode. It is seen that the original three-dimensional elliptic equation has been decoupled in the vertical and transformed into a set of two-dimensional Helmholtz equations.

The finite difference form of equation (2.96) consistent with the horizontal discretization is

$$R_{ij} + \epsilon \nabla^2 R_{ij} = G_{ij} \quad i = 2(1)L-1, j = 2(1)M-1 \quad (2.97)$$

where

$$\nabla^2 R_{ij} = \frac{R_{i+1,j} - 2R_{ij} + R_{i-1,j}}{\Delta x_j^2} + \frac{R_{i,j+1} - 2R_{ij} + R_{i,j-1}}{\Delta y^2} - \frac{R_{i,j+1} - R_{i,j-1}}{2\Delta y} \frac{\tan \phi_j}{a} \quad (2.98)$$

For simplicity, subscript k is omitted. The values of R_{ij} at the horizontal boundaries are known from the boundary conditions.

The solution of equation (2.97) requires the following steps :

- (i) The introduction of a variable S_{ij} , defined by,

$$S_{ij} = R_{ij} - R_{1j} - (R_{L,j} - R_{1,j})(i-1)/(L-1) \quad (2.99)$$

This converts equation (2.97) into one with homogeneous boundary condition at the east-west boundaries, i.e.

$$S_{ij} + \epsilon \nabla^2 S_{ij} = H_{ij} \quad i=2(1)L-1, j=2(1)M-1 \quad (2.100)$$

$$S_{1j} = S_{L,j} = 0 \quad j=1(1)M \quad (2.101)$$

Here $S_{i,1}$, and $S_{i,M}$ are to be prescribed.

$$\text{and} \quad H_{ij} = G_{ij} - (1+\epsilon \nabla^2) [R_{1j} - (R_{L,j} - R_{1,j})(i-1)/(L-1)] \quad (2.102)$$

- (ii) The variable S_{ij} and the forcing function H_{ij} are extended in the x -direction anti-symmetrically about the eastern boundary $i=L$,

$$SS_{ij} = \begin{array}{ll} S_{ij} & i=1(1)L-1 \\ -S_{2L-1,j} & i=L(1)2L-2 \end{array} \quad (2.103)$$

$$HH_{ij} = \begin{array}{ll} H_{ij} & i=1(1)L-1 \\ -H_{2L-i,j} & i=L(1)2L-1 \end{array} \quad (2.104)$$

The Helmholtz equation for SS_{ij} thus reads

$$SS_{ij} + \epsilon \nabla^2 SS_{ij} = HH_{ij} \quad i=1(1)2L-2, j=2(1)M-1 \quad (2.105)$$

SS_{ij} is periodic in the x-direction and SS_{i1} and SS_{iM} are prescribed at the boundaries

(iii) A discrete Fourier transform in x-direction is applied to equation (2.105),

$$\epsilon \left[\frac{1}{\Delta y^2} + \frac{\tan \phi_j}{2a\Delta y} \right] \bar{\bar{SS}}_{j-1}^l + \left[\frac{1-4\epsilon \sin^2 \frac{l\pi}{2(L-1)}}{\Delta x^2} - \frac{2\epsilon}{\Delta y^2} \right] \bar{\bar{SS}}_j^l + \epsilon \left[\frac{1}{\Delta y^2} - \frac{\tan \phi_j}{2a\Delta y} \right] \bar{\bar{SS}}_{j+1}^l = \bar{\bar{HH}}_j^l$$

$$l=1(1)2L-3, j=2(1)M-1 \quad (2.106)$$

Here the Fourier transform is defined by

$$\bar{\bar{FF}}_j^l = \frac{1}{2L-2} \sum_{i=1}^{2L-2} e^{-\sqrt{-1} \frac{2li\pi}{2L-2}} FF_{ij} \quad (2.107)$$

It can be shown that the inverse transform gives

$$FF_{ij} = \sum_{l=1}^{2L-3} e^{\sqrt{-1} \frac{2li\pi}{2L-2}} \bar{\bar{FF}}_j^l \quad (2.108)$$

(iv) Equation (2.106) represents a set of $M-2$ linear algebraic equations with $M-2$ unknowns, i.e., $\bar{\bar{SS}}_2^l, \bar{\bar{SS}}_3^l, \dots, \bar{\bar{SS}}_{M-1}^l$, which can be solved by standard inversion methods. In fact, the matrix of equation (2.106) is tridiagonal, and is solved by a Forward-Backward iteration.

(v) After solving $\bar{\bar{SS}}_j^l$ from equation (2.106), one obtains SS_{ij} from

equation (2.108).

(vi) Next we calculate R_{ij} from equation (2.99).

(vii) Finally we calculate P_{ijk} from equation (2.90).

We shall next address the Lagrangian interpolation.

The semi-Lagrangian advective scheme was first proposed by Krishnamurti (1962). A linear stability analysis of this scheme was carried out by Mathur (1970). A multi-level formulation of the semi-Lagrangian advection scheme explored the formation of an intertropical convergence zone, Krishnamurti (1969). In these studies an Euler-backward time differencing scheme was used. An excellent review of the aforementioned efforts was presented by Haltiner (1971). Rapid further developments on the formulation of semi-Lagrangian - semi-implicit versions of primitive equation models emerged from a series of recent studies, Robert et al. (1985), Ritchie (1986), Bates and McDonald (1982). In these studies the use of semi-implicit time differencing and long local trajectories for the horizontal advection resulted in a drastic reduction of the computation time. Proposals for the removal of the Helmholtz equation for the pressure via a transformation of variables was made by Tanguay and Robert (1986). This can, in principle, provide a further reduction in the computational time. A local analytical representation of the basic variables and forcing functions is normally done via use of local interpolation surfaces. Ritchie (1986) proposed yet another improvement in the mathematical formulation of the semi-Lagrangian advection, that permits the removal of such an interpolation phase. A proposal to cast this as a spectral-semi-Lagrangian - semi-implicit problem was recently suggested by Ritchie (1987). Many of these newer methods

remain to be tested at the present time for possible implementation in multi-level models. Mathur (1983) proposed a one-step semi-Lagrangian model that utilizes an explicit time differencing scheme. The present study utilizes a one-step semi-Lagrangian advection with a semi-implicit formulation for the time differencing scheme.

For any variable A, the general time dependent problem can be written as:

$$\frac{dA}{dt} = F \quad (2.109)$$

where F is the forcing function and

$$\frac{d}{dt} = \frac{\partial}{\partial t} + u \frac{\partial}{\partial x} + v \frac{\partial}{\partial y}$$

The numerical integration of equation (2.109) by the semi-Lagrangian advective scheme is carried out in the following manner:

- (a) over the time Δt the origin of a parcel reaching a certain grid point is traced.
- (b) The value of A at the new location is advected from its place of origin.
- (c) an average forcing \bar{F} is obtained over the period Δt and is added to the advected value of A.

Mathematically this is expressed by

$$A_Q(t+\Delta t) = A_P(t) + \bar{F}\Delta t \quad (2.110)$$

i.e. the air parcel starting at point P in time Δt reaches the point Q and the average forcing in the time Δt is \bar{F} .

where

$$\bar{F} = \frac{1}{\Delta t} \int_t^{t+\Delta t} F dt \quad (2.111)$$

To numerically integrate equation (2.109) in order to obtain equation (2.110) certain approximations have to be made. Given the velocity fields at the time t and assuming that the forcing over the

period t to $t+\Delta t$ is constant the distance travelled in time Δt is given by

$$\Delta x = u(t)\Delta t + \frac{1}{2}F_u(\Delta t)^2 \quad (2.112)$$

$$\Delta y = v(t)\Delta t + \frac{1}{2}F_v(\Delta t)^2$$

Where Δx and Δy are the distances travelled along the x and y directions respectively. This approximately gives us the location of the point P . Using an interpolation technique the value $A_p(t)$ is obtained. To obtain an average value of \bar{F} (equation (2.111)) we assume that this forcing is also constant and is equal to the forcing at the parcel at point P . i.e.

$$\bar{F} = F_p(t) \quad (2.113)$$

A second order Lagrangian interpolation scheme is used in this model. This scheme uses a nine point stencil. Higher order schemes, at the expense of considerable increase in computational time could be designed. The accuracy of a given scheme depends upon the order of interpolation used, both to find position of, and the value of the fields, at the departure points. McDonald (1987, 1984) has analyzed the accuracy associated with the different spatial interpolation schemes. More recently McDonald and Bates (1987), Temperton and Staniforth (1987) have suggested the way to improve the estimate of the departure point positions. In general these schemes require information from more than two time levels.

In the x -momentum equation the grid point values of the meridional velocity v are staggered with respect to the points that carry the zonal velocity u , hence certain averaging procedures are required. The velocity component v at u_{ijk} grid point is obtained as follows:

$$\tilde{v}_{ijk} = \frac{1}{4}(v_{i-1jk} + v_{ijk} + v_{i-1j+1k} + v_{ij+1k}) \quad (2.114)$$

and a forcing function corresponding to the v component is averaged from:

$$\tilde{F}_{ijk}^v = \frac{1}{4}(F_{i-1jk}^v + F_{ijk}^v + F_{i-1j+1k}^v + F_{ij+1k}^v) \quad (2.115)$$

Since the u_{ijk} and F_{ijk}^u are known the distance travelled in time Δt are given by:

$$\Delta x = u_{ijk}\Delta t + \frac{1}{2}F_{ijk}^u(\Delta t)^2 \quad (2.116)$$

$$\Delta y = \tilde{v}_{ijk}\Delta t + \frac{1}{2}\tilde{F}_{ijk}^v(\Delta t)^2 \quad (2.117)$$

This gives us the location of point P for the semi-Lagrangian form of x-momentum.

For y-momentum equation since the grid points with values of u are not located at the V points, certain averaging is again required. The velocity component u at v_{ijk} grid point is obtained as follows:

$$\tilde{u}_{ijk} = \frac{1}{4}(u_{ij-1k} + u_{i+1j-1k} + u_{ijk} + u_{i+1jk}) \quad (2.118)$$

and the forcing function corresponding to the u component is averaged by:

$$\tilde{F}_{ijk}^u = \frac{1}{4}(F_{ij-1k}^u + F_{i+1j-1k}^u + F_{ijk}^u + F_{i+1jk}^u) \quad (2.119)$$

again the distance travelled are given by:

$$\Delta x = \tilde{u}_{ijk}\Delta t + \frac{1}{2}\tilde{F}_{ijk}^u(\Delta t)^2 \quad (2.120)$$

$$\Delta y = v_{ijk}\Delta t + \frac{1}{2}F_{ijk}^v(\Delta t)^2 \quad (2.121)$$

This gives us the location of point P for the semi-Lagrangian form of y-momentum equation.

We shall next address the thermodynamic, continuity and moisture conservation equations.

Since the temperature, surface pressure and the moisture variables are carried at the same grid point a general procedure for all three equation is given here.

Again since for these variables the u and v do not fall on their grid points, the following averaging procedures are employed.

$$\tilde{u}_{ijk} = \frac{1}{2}(u_{ijk} + u_{i+1jk}) \quad (2.122)$$

$$\tilde{F}_{ijk}^u = \frac{1}{2}(F_{ijk}^u + F_{i+1jk}^u) \quad (2.123)$$

$$\tilde{v}_{ijk} = \frac{1}{2}(v_{ijk} + v_{ij+1k}) \quad (2.124)$$

$$\tilde{F}_{ijk}^v = \frac{1}{2}(F_{ijk}^v + F_{ij+1k}^v) \quad (2.125)$$

Knowing these values of above variables the distance travelled can be obtained as:

$$\Delta x = \tilde{u}_{ijk}\Delta t + \frac{1}{2}\tilde{F}_{ijk}^u(\Delta t)^2 \quad (2.126)$$

$$\Delta y = \tilde{v}_{ijk}\Delta t + \frac{1}{2}\tilde{F}_{ijk}^v(\Delta t)^2 \quad (2.127)$$

This gives the location of point P, for the semi-Lagrangian form for the respective equations.

The integration involves the following steps:

1. The forcing, s_j are calculated at grid points and are stored in S_j .
2. Δx and Δy are calculated using the procedure discussed above.
3. Forcings s_j , at the grid points, are interpolated to the origin of the parcel using Δx , Δy by a similar interpolation scheme and stored in s_j° .
4. Forcings for the elliptic equation are calculated using X_j 's and stored in Q .
5. The three dimensional elliptic equation is transformed into a set of 2 dimensional linearly independent Helmholtz equations and these

are solved by direct method to obtain P^+ .

6. Given P^+ and W^+ , the prognostic and diagnostic variables are calculated as follows:

u-component of wind

$$u^+ = W_1^+ - \frac{\Delta t}{2} \frac{\partial P^+}{\partial x} \quad (2.128)$$

v-component of wind

$$v^+ = W_2^+ - \frac{\Delta t}{2} \frac{\partial P^+}{\partial y} \quad (2.129)$$

Surface pressure

$$\ln p_s^+ = \frac{1}{RT_s^*} (P_s^+ - g z_s) \quad (2.130)$$

Moisture Variable

$$q^+ = W_4^+ \quad (2.131)$$

Geopotential Height

$$Z^+ = \frac{1}{g} (P^+ - RT^* \ln p_s) \quad (2.132)$$

Temperature

$$T^+ = -\frac{\sigma g}{R} \frac{\partial Z^+}{\partial \sigma} \quad (2.133)$$

Vertical velocity σ

$$\dot{\sigma}^+ = \frac{2}{\Delta t} \int_{\sigma_T}^{\sigma} \left[w_5^+ - \ln p_s^+ - \frac{\Delta t}{2} \nabla \cdot \tilde{v}^+ \right] d\sigma \quad (2.134)$$

These steps are repeated to obtain the forecast.

2.4 Initialization:

Sugi (1986) proposed a dynamic normal mode initialization procedure that utilizes a forward backward iteration (around the first

time step). In this method the forward-backward iterations are carried out with the linear terms, while keeping the physical and nonlinear effects fixed. After every 100 iterations the physical and nonlinear terms are updated and this process is continued until roughly 5 iterations are completed. Sugi has demonstrated a rapid damping of high frequency modes with a solution which corresponds closely to that obtained from nonlinear normal mode initialization with physics. Sugi also demonstrated a rapid convergence in the time history of mean square surface pressure, mean square divergence and grid point values of surface pressure. Sugi's study was carried out within a global spectral model at a resolution of 42 waves (triangular). The transform grid at the resolution corresponds approximately to 250 km². When the Sugi iteration is carried out in regional grid point models at a resolution of roughly 50 km² or higher a rapid damping of the gravitational high frequency modes occurs. However in mesoscale models with still higher resolutions this iteration scheme appears to fail and requires a reformulation. The present study utilizes grid sizes of the order of 50 km or higher and this method appears to converge quite rapidly.

2.4.1 Formulation:

The linear and nonlinear terms in the model equations are separated for the Sugi initialization as shown below:

(a) X-momentum equation

$$\frac{Du}{Dt} = -\sigma \frac{\partial u}{\partial \sigma} + v \left[f + \frac{u}{a} \tan \phi \right] - RT' \frac{\partial}{\partial x} \ln p_s + F_x - \frac{\partial p}{\partial x} \quad (2.135)$$

where
$$\frac{D}{Dt} = \frac{\partial}{\partial t} + u \frac{\partial}{\partial x} + v \frac{\partial}{\partial y} \quad (2.136)$$

equation (2.135) can be rewritten as:

$$\begin{aligned} \frac{\partial u}{\partial t} &= -\frac{\partial P}{\partial x} + vf + \left[-\sigma \frac{\partial u}{\partial \sigma} - u \frac{\partial u}{\partial x} - v \frac{\partial u}{\partial y} + \frac{vu}{a} \tan\phi - RT' \frac{\partial}{\partial x} \ln p_s + F_x \right] \\ &= F_u^l + F_u^n \end{aligned} \quad (2.137)$$

where F_u^l and F_u^n are the linear and nonlinear parts of the equation respectively and are given by:

$$F_u^l = -\frac{\partial P}{\partial x} + vf \quad (2.138)$$

$$F_u^n = -\sigma \frac{\partial u}{\partial \sigma} - u \frac{\partial u}{\partial x} - v \frac{\partial u}{\partial y} + \frac{vu}{a} \tan\phi - RT' \frac{\partial}{\partial x} \ln p_s + F_x \quad (2.139)$$

(b) Y-momentum equation

$$\frac{Dv}{Dt} = -\sigma \frac{\partial v}{\partial \sigma} - u \left[f + \frac{u}{a} \tan\phi \right] - RT' \frac{\partial}{\partial y} \ln p_s + F_y - \frac{\partial P}{\partial y} \quad (2.140)$$

following the same procedure we can write equation (2.140) as:

$$\frac{\partial v}{\partial t} = -\frac{\partial P}{\partial y} - uf + \left[-\sigma \frac{\partial v}{\partial \sigma} - u \frac{\partial v}{\partial x} - v \frac{\partial v}{\partial y} - \frac{uu}{a} \tan\phi - RT' \frac{\partial}{\partial y} \ln p_s + F_y \right] \quad (2.141)$$

or
$$\frac{\partial v}{\partial t} = F_v^l + F_v^n \quad (2.142)$$

where

$$F_v^l = -\frac{\partial P}{\partial y} - uf \quad (2.143)$$

$$F_v^n = -\sigma \frac{\partial v}{\partial \sigma} - u \frac{\partial v}{\partial x} - v \frac{\partial v}{\partial y} - \frac{uu}{a} \tan\phi - RT' \frac{\partial}{\partial y} \ln p_s + F_y \quad (2.144)$$

are the linear and nonlinear terms respectively.

(c) Continuity Equation:

In the Eulerian form, the continuity equations can be written as:

$$\left[\frac{\partial}{\partial t} + \vec{v} \cdot \nabla \right] \ln p_s = -\frac{\partial \dot{\sigma}}{\partial \sigma} - \nabla \cdot \vec{v} \quad (2.145)$$

where
$$\vec{v} = iu + jv \quad (2.146)$$

and
$$\nabla = i \frac{\partial}{\partial x} + j \frac{\partial}{\partial y} \quad (2.147)$$

integrating equation (2.145) with respect to σ from $\sigma=1$ to $\sigma=\sigma_T$ we get:

$$\int_{\sigma_T}^1 \frac{\partial}{\partial t} \ln p_S d\sigma + \int_{\sigma_T}^1 \vec{v} \cdot \nabla \ln p_S d\sigma = - \int_{\sigma_T}^1 \frac{\partial \sigma}{\partial \sigma} d\sigma - \int_{\sigma_T}^1 \nabla \cdot \vec{v} d\sigma \quad (2.148)$$

defining $\hat{v} = \frac{1}{(1-\sigma_T)} \int_{\sigma_T}^1 \vec{v} d\sigma \quad (2.149)$

Using the boundary conditions $\int_{\sigma_T}^1 \frac{\partial \sigma}{\partial \sigma} d\sigma = \dot{\sigma}_1 - \dot{\sigma}_T = 0$

we can write equation (2.148) in the form

$$\frac{\partial}{\partial t} \ln p_S = - \hat{v} \cdot \nabla \ln p_S - \nabla \cdot \hat{v} \quad (2.150)$$

or

$$\frac{\partial}{\partial t} \ln p_S = F_{ps}^l + F_{ps}^n \quad (2.151)$$

where

$$F_{ps}^l = - \nabla \cdot \hat{v} \quad (2.152)$$

$$F_{ps}^n = - \hat{v} \cdot \nabla \ln p_S \quad (2.153)$$

are the linear and nonlinear terms respectively.

Subtracting equations (2.145) and (2.150) we can derive a diagnostic equation giving

$$\frac{\partial \sigma}{\partial \sigma} = (\hat{v} - \vec{v}) \cdot \nabla \ln p_S + \nabla \cdot (\hat{v} - \vec{v}) \quad (2.154)$$

(d) Thermodynamic equation:

$$\frac{D}{Dt} \left[\frac{1}{\gamma^*} \frac{\partial P}{\partial \sigma} + \sigma \ln p_S \right] + \dot{\sigma} = - \frac{\gamma' \dot{\sigma}}{\gamma^*} + \frac{\kappa R T'}{\sigma \gamma^*} \left[\frac{\partial \sigma}{\partial \sigma} + \nabla \cdot \vec{v} \right] + \dot{Q} \quad (2.155)$$

let $X = \frac{1}{\gamma^*} \frac{\partial P}{\partial \sigma}$ we can write (2.155) as:

$$\frac{DX}{Dt} + \sigma \frac{D}{Dt} \ln p_s + \dot{\sigma} = - \frac{\gamma' \dot{\sigma}}{\gamma^*} + \frac{\kappa R T'}{\sigma \gamma^*} \left[\frac{\partial \sigma}{\partial \sigma} + \nabla \cdot \vec{v} \right] + \dot{Q} \quad (2.156)$$

substituting for $\frac{\partial}{\partial t} \ln p_s$ from equation (2.150):

$$\frac{DX}{Dt} + \sigma \left[\frac{\partial}{\partial t} \ln p_s + \vec{v} \cdot \nabla \ln p_s \right] + \dot{\sigma} = - \frac{\gamma' \dot{\sigma}}{\gamma^*} + \frac{\kappa R T'}{\sigma \gamma^*} \left[\frac{\partial \sigma}{\partial \sigma} + \nabla \cdot \vec{v} \right] + \dot{Q} \quad (2.157)$$

$$\begin{aligned} \text{or } \frac{DX}{Dt} + \sigma (-\hat{v} \cdot \nabla \ln p_s - \nabla \cdot \hat{v} + \vec{v} \cdot \nabla \ln p_s) + \dot{\sigma} \\ = - \frac{\gamma' \dot{\sigma}}{\gamma^*} + \frac{\kappa R T'}{\sigma \gamma^*} \left[\frac{\partial \sigma}{\partial \sigma} + \nabla \cdot \vec{v} \right] + \dot{Q} \end{aligned} \quad (2.158)$$

$$\text{or } \frac{DX}{Dt} = \sigma \nabla \cdot \hat{v} + \left[\sigma (\hat{v} - \vec{v}) \cdot \nabla \ln p_s - \frac{\gamma' \dot{\sigma}}{\gamma^*} + \frac{\kappa R T'}{\sigma \gamma^*} \left[\frac{\partial \sigma}{\partial \sigma} + \nabla \cdot \vec{v} \right] + \dot{Q} \right] - \dot{\sigma} \quad (2.159)$$

$$\text{or } \frac{DX}{Dt} = \sigma \nabla \cdot \hat{v} - \dot{\sigma} + \left[\sigma (\hat{v} - \vec{v}) \cdot \nabla \ln p_s - \frac{\gamma' \dot{\sigma}}{\gamma^*} + \frac{\kappa R T'}{\sigma \gamma^*} \left[\frac{\partial \sigma}{\partial \sigma} + \nabla \cdot \vec{v} \right] + \dot{Q} \right] \quad (2.160)$$

$$\text{or } \frac{DX}{Dt} = F_x^l + F_x^n \quad (2.161)$$

where

$$F_x^l = \sigma \nabla \cdot \hat{v} - \dot{\sigma} \quad (2.162)$$

$$F_x^n = - \sigma (\hat{v} - \vec{v}) \cdot \nabla \ln p_s - \frac{\gamma' \dot{\sigma}}{\gamma^*} + \frac{\kappa R T'}{\sigma \gamma^*} \left[\frac{\partial \sigma}{\partial \sigma} + \nabla \cdot \vec{v} \right] + \dot{Q} \quad (2.163)$$

are the linear and nonlinear terms respectively.

(e) Moisture conservation equation:

Since the dynamic initialization procedure does not effect the moisture variable in a direct way, no attempt is made to separate the

moisture equation into linear and nonlinear parts.

2.4.2 Procedure:

First the model is run in the complete form and updated fields are obtained at first time step. From the fields stored at the time zero, the total tendencies are obtained. The nonlinear tendencies can be readily obtained by subtracting the linear tendency from the total tendency. Following Sugi (1986) these nonlinear tendencies are held fixed through the forward-backward integration. This forward-backward integration is performed for n times, after which the updated initial fields are used to run the model for one time step. This rerun of the model gives a new set of nonlinear tendencies, which are again held fixed through n forward-backward integrations. This procedure is repeated for several times. Fig. 3 gives a flow diagram for the entire procedure.

The linear integration scheme is different from that used in the model. In the model a semi-Lagrangian, semi-implicit scheme is used for the spatial and temporal time differencing. The linear forward-backward steps are performed in the Eulerian sense using the selective damping scheme proposed by Okamura (see Haltiner and Williams page 387). The Okamura scheme consists of a forward followed by a backward step and averaging.

$$F_{n+1}^1 = F_n + \Delta t \left[\frac{\partial F}{\partial t} \right]_{n-} \quad (2.164)$$

$$F_n^{\text{new}} = F_{n+1}^1 - \Delta t \left[\frac{\partial F^1}{\partial t} \right]_{n+1} \quad (2.165)$$

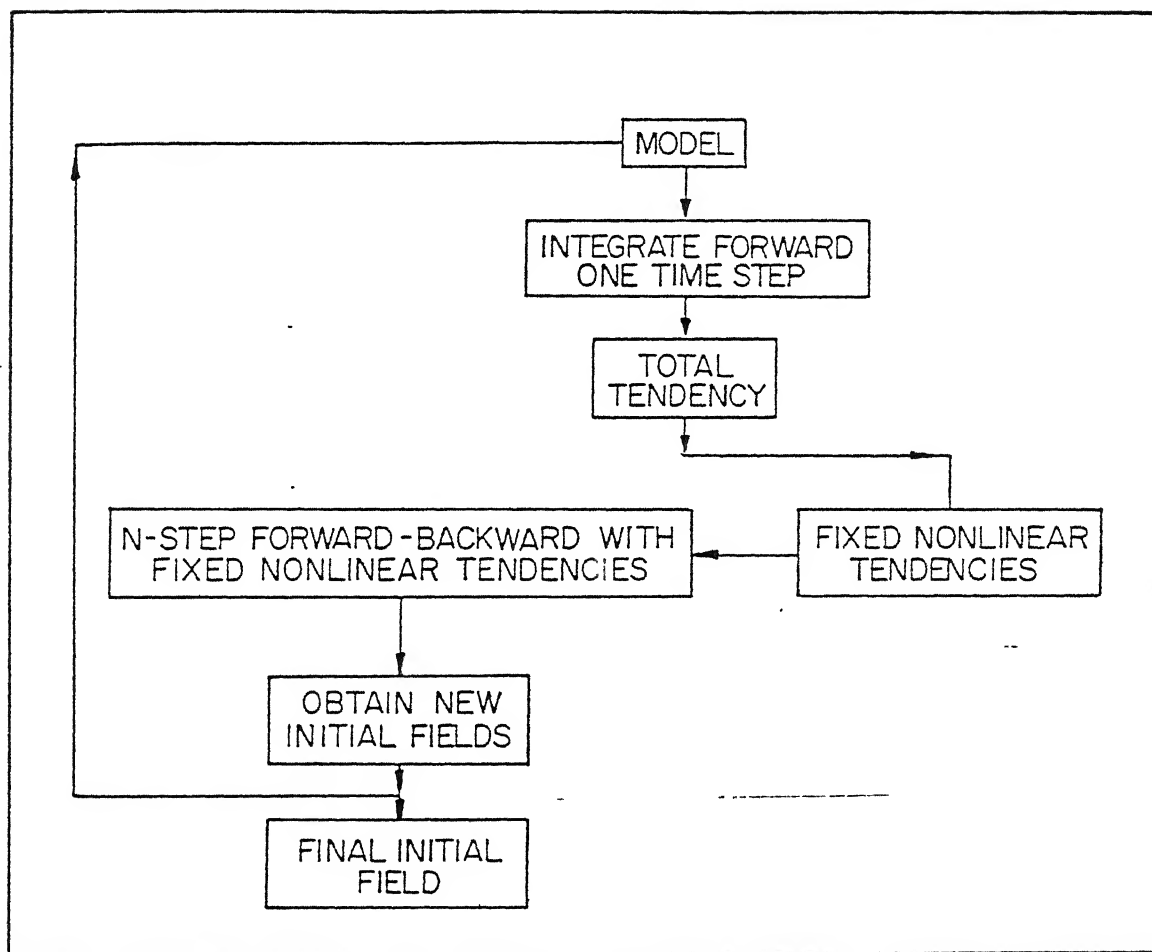


Figure 3: Flow diagram of the initialization procedure.

$$\bar{F}_n = 3F_n - 2F_n^{\text{new}} \quad (2.166)$$

where F maybe u , v , $\ln p_s$ or x and n stands for the time step.

The variable x is calculated in the very beginning of the procedure from its definition.

2.5 Boundary Conditions:

a) Vertical:

In the vertical $\dot{\sigma}$ is set to zero at model top and bottom for all the times t . The lowest level of model follows the surface terrain.

These conditions can be represented as:

$$\dot{\sigma} = 0 \quad \text{at} \quad \sigma = 0.1$$

$$\text{and} \quad \sigma = 1.0$$

$$\text{and at} \quad \sigma = 1.0$$

$$Z(x, y, \sigma=1) = Z_s(x, y)$$

where Z_s is the surface terrain field and is function of x and y .

b) Horizontal:

Numerical treatment of lateral boundary is a difficult but a very important aspect of limited area modelling. The flow in the interior of the domain is sensitive to the specification of the lateral boundary conditions, even for the short range forecasts.

An excellent review of commonly used lateral boundary conditions for the limited area models is given by Davis (1983), Sundstorm and Elvins (1979). The necessarily limited domain introduces the lateral boundary conditions within the atmosphere whose physical interpretation is obscure. Further incorrect specification of lateral boundary

conditions itself can generate local unstable modes even if the basic finite difference approximations used in the interior are stable. The uniqueness and well-posedness of lateral boundary conditions of a limited area model are still open questions. However over the years many pragmatic approaches have been successfully developed and applied towards the short range forecasting. These could be broadly put in the two categories. The first approach is so called grid nesting where a much larger domain is also modelled using a coarser resolution, and the evolving fields are then used to determine the boundary conditions for the smaller domain (Chen and Miyakoda 1974, Miyakoda and Rosati 1977, Leslie et al. 1981). The second approach is to formulate open boundary conditions which allow the disturbances to radiate out of the modelled domain with minimum boundary reflections. The most used procedures under this category are diffusive damping schemes in which the boundary noise problem is dealt by introducing a marginal zone of large diffusion (Mesinger, 1977), tendency modification schemes in which the time tendencies are assigned a weighted average of the externally specified fields and internally forecasted fields (Perkey and Kreitzberg 1976), relaxation or nudging schemes in which the flow near the boundary is relaxed towards a large scale analysis through the use of Newtonian or diffusion term (Kallberg and Gibson 1977, Tatsumi 1980). Apart from these many explicit radiation schemes based on outflow-inflow conditions have also been used (Williamson and Browning 1974, Okamura 1975, Orlanski 1976, Miller and Thorpe 1981, Kurihara 1983).

A similar pragmatic approach has been used in the present model. Two such options of the boundary conditions are currently available:

I. Fixed boundary conditions: In this case all the prognostic variables i.e u, v, p, lnps and q are held fixed in time. To avoid the wave reflection, caused by such a boundary condition, a Laplacian type smoother near the boundary is applied. The same smoother is also applied in the interior of the domain to suppress the noise. However, as the lateral boundaries are approached, the smoothing coefficient increases. For the 1.875 lat/long grid the smoothing coefficient nearest to the boundary is 16 times its value in the interior of the domain. This increase is a function of grid resolution. For smaller grid resolutions this multiplying factor has a smaller value.

II. Time dependent boundary conditions: Here the prognostic variables are allowed to change with time. The future values of the prognostic variables can be obtained either from a global forecast or from the observations. These specified values then are merged with the forecast produced by the model. In the present study we use time dependent boundary conditions based on future observations. If at any time t the model forecast is x_f and the externally specified value is x_s , where x is any prognostic variable, then the following expression is used to give the merged forecast

$$x_c = (1-\alpha) x_f + \alpha x_s$$

where α is a constant and equal to 1.0 at the boundary. Away from lateral boundary it decreases and becomes zero in the interior. The specific values for α are 1.0, 0.45339, 0.20556, 0.09320, 0.01916, and 0.0 for grid points, 0, 1, 2, 3, 4, 5 and more, distance away from the boundary.

The above procedure is carried out for u, v, z, lnps and q on the σ surfaces and is repeated at each time step of the model

integration. The specified value X_s is obtained through a linear interpolation between two observation times.

CHAPTER 3

PARAMETERIZATION OF PHYSICAL PROCESSES

Apart from the dynamical aspects, the model also includes a number of physical processes. These comprise of:

- Large scale condensation,
- Shallow moist convection,
- Deep cumulus convection,
- Planetary boundary layer,
 - a) Surface fluxes
 - b) Fluxes above the surface layer.
- Radiative Processes
 - a) Short wave radiative processes,
 - b) Long wave radiative processes,
- Surface energy balance,
- Orography.

A fairly accurate parameterization of the above mentioned physical processes in an NWP model is very essential to capture the various details of importance in a forecast. Following is a brief description of the parameterization schemes used in the model for all individual processes. Numerical algorithms are written in a modular form for

each of these physical processes. These parameterizations provide the physical forcing terms for the previously discussed equations of motion.

3.1 Parameterization of Large Scale Condensation:

Large scale condensation within the model is essentially the removal of supersaturation at any grid point of the model. This excess moisture develops due to the other dynamical or physical processes such as vertical advection of moisture fluxes and radiative cooling, etc.

Super saturation at each time step at a given grid point is defined by

$$\Delta q = q - q_s \quad (3.1)$$

where q and q_s are the specific humidity and saturation specific humidity at that point.

If $\Delta q > 0$, then at that level of atmosphere the excess humidity is precipitated out. The heating due to the precipitation ($L\Delta q/\Delta t$) is computed and added as a source term in the thermodynamic equation.

$$C_p \frac{T}{\theta} \frac{\partial \theta}{\partial t} = \dots + \frac{L\Delta q}{\Delta t} \quad (3.2)$$

Similarly change in moisture due to supersaturation is also added to the moisture continuity equation.

$$\frac{\partial q}{\partial t} = \dots - \frac{\Delta q}{\Delta t} \quad (3.3)$$

Thus the supersaturation is simply condensed out with an equivalent heat released at that level of the atmosphere.

Calculation of the saturation specific humidity q_s is usually carried out from the use of various approximations such as the Tetens formulae,

$$q_s(T) = \frac{0.622 e_s(T)}{p - 0.378 e_s(T)} \quad (3.4)$$

vapor pressure
$$e_s = 6.11 \exp \left[\frac{a(T-273.16)}{(T-b)} \right] \quad (3.5)$$

where the constants a and b in the expression for vapor pressure are defined in terms of saturation over water ($a = 17.26$, $b = 35.86$) or over ice ($a = 21.87$, $b = 7.66$). The Tetens formulae have been tested and found to be reasonable for the construction of moist adiabats in the troposphere.

3.2 Parameterization of Shallow Convection:

Following Tiedke (1984) we assume a simple diffusive form for the parameterization of shallow convection. Shallow convection is invoked over conditionally unstable undisturbed situation (rainfall rate < 5 mm/day) via a K theory. The humidity and the thermal equations are expressed by,

$$\frac{\partial \bar{q}}{\partial t} = \dots \frac{\partial}{\partial p} K_Q \frac{\partial \bar{q}}{\partial p} \quad (3.6)$$

and

$$\frac{\partial \bar{\theta}}{\partial t} = \dots \frac{\partial}{\partial p} K_\theta \frac{\partial \bar{\theta}}{\partial p} \quad (3.7)$$

Furthermore, following Tiedke (1984), we set, $K_Q = K_\theta = K g^2 \rho^2$, the coefficient varies with height as the square of the density. Based on numerous studies with the GATE, ATEX and AMTEX data sets Tiedke suggests a value of $K = 25 \text{ m}^2 \text{ s}^{-1}$. However, setting a constant value of K does not provide a smooth continuity with the fluxes at the

lifting condensation level. It is desirable that $Kg^2\rho^2 \frac{\partial \bar{q}}{\partial p}$ at the lifting condensation level be consistent with the planetary boundary layer flux at that level. If we define:

$$K = \frac{F_q(LCL)/L}{\rho^2 g \frac{\partial \bar{q}}{\partial p}_{LCL}} \quad (3.8)$$

then the humidity flux in the subcloud layer and the shallow convective cloud layer are smoothly connected. A similar definition of K_θ is also used for the same reasons. Above the lifting condensation level in the cloud layer $K_\theta \frac{\partial \bar{\theta}}{\partial p}$ is negative, implying a downward eddy flux of sensible heat from the base of inversion to the cloud base. On the other hand $K_Q \frac{\partial \bar{q}}{\partial p}$ is essentially positive in the shallow convective cloud layer. Since the humidity flux is small both at the cloud base and at the cloud top, over the lower half of the clouds $\frac{\partial}{\partial p} K_Q \frac{\partial \bar{q}}{\partial p}$ is negative and is positive over the upper half of the clouds. Thus these shallow convective clouds tend to moisten the layers of the atmosphere over the upper half of the clouds. Heckley (1984) has summarized the results of recent numerical predictions made with the ECMWF model. The experience at ECMWF shows that the inclusion of shallow convection improves the overall tropical forecasts slightly. In its absence the planetary boundary layer tends to be too moist and the region below the inversion layer tends to be too dry. Although the present formulation is very simple it is shown to provide an overall improvement of the thermodynamical structure over the undisturbed areas. In the present formulation the vertical eddy flux of momentum is included in the planetary boundary layer; however, it is not included within the cloud layer.

It is easy to see that moisture is conserved by this parameterization of shallow convection. The total convergence of flux of humidity in the cloud layer is equal to $Fq(LCL)$, i.e. the flux at the cloud base.

It is important to assure that these shallow clouds are nonprecipitating and do not systematically produce saturation on the large scale. To assure that it is desirable to set an upper limit on the final specific humidity q_F produced by the process,

$$\text{i.e.} \quad q_F/q_s \leq 0.8$$

This is easy to implement formally although it violates the conservation slightly. However, this is necessary in order to avoid the eventual formation of layer clouds and associated large scale condensation.

The present formulation of shallow convection is very simplistic, and deserves to be investigated in further detail.

3.3 Parameterization of deep moist convection:

The procedure followed here is identical to that used in Krishnamurti et al. (1983a). Deep convective parameterization is invoked if the atmosphere is conditionally unstable and if a net supply of moisture convergence is available. The existence of conditional instability is determined from vertical gradient of moist static energy i.e.,

$$\frac{\partial}{\partial p} (gz + C_p T + Lq) < 0 \quad (3.9)$$

The large scale moisture supply is expressed by

$$I_L = - \frac{1}{g} \int_{P_T}^{P_B} \omega \frac{\partial q}{\partial p} dp \quad (3.10)$$

The horizontal advection of moisture is used in the large scale dynamics as a moisture advection term.

Krishnamurti et al. (1980), suggest that the large scale supply of moisture, I_L , is a close measure of the rainfall rate. In order to provide sufficient moisture for moistening of the vertical columns and to account for the observed rainfall on the large scale, two parameters are introduced following Krishnamurti et al. (1980). One of these is a mesoscale moisture convergence parameter η and the other a moistening parameter b . The total moisture supply is now expressed by,

$$I = I_L(1+\eta) \quad (3.11)$$

Furthermore, the rainfall rate R and the moistening rate M are accordingly partitioned, i.e.,

$$R = I(1-b) = I_L(1+\eta)(1-b) \quad (3.12)$$

$$M = Ib = I_L(1+\eta)b \quad (3.13)$$

Following Kanamitsu (1975) the supply of moisture required to produce a cloud over a unit area is expressed by,

$$Q = \frac{1}{g} \int_{P_T}^{P_B} \frac{(q_s - q)}{\Delta \tau} dp + \frac{1}{g} \int_{P_T}^{P_B} \left[\frac{C_p T (\theta_s - \theta)}{L \theta \Delta \tau} + \omega \frac{C_p T}{L \theta} \frac{\partial \theta}{\partial p} \right] dp \quad (3.14)$$

Here $\Delta \tau$ denotes a cloud time scale and is set to 30 minutes. The subscript s denotes the variables along a moist adiabat which is obtained by raising the surface air upwards. The two terms in the above equation are expressed by,

$$Q = Q_q + Q_\theta \quad (3.15)$$

The total supply I may likewise be split into the moistening and heating parts by the relation,

$$I_q = I_b = I_L b(1+\eta) \quad (3.16)$$

and
$$I_\theta = I(1-b) = I_L(1-b)(1+\eta) \quad (3.17)$$

The thermal and the humidity equations are expressed by:

$$\frac{\partial \theta}{\partial t} + \mathbf{v} \cdot \nabla \theta + \frac{\omega \partial \theta}{\partial p} = a_\theta \left(\frac{\theta_s - \theta}{\Delta \tau} + \frac{\omega \partial \theta}{\partial p} \right) \quad (3.18)$$

$$\frac{\partial q}{\partial t} + \mathbf{v} \cdot \nabla q = a_q \left(\frac{q_s - q}{\Delta \tau} \right) \quad (3.19)$$

Where a_θ and a_q are defined by the relations,

$$a_\theta = \frac{I_\theta}{Q_\theta} = \frac{I(1-b)}{Q_\theta} = \frac{I_L(1+\eta)(1-b)}{Q_\theta} \quad (3.20)$$

$$a_q = \frac{I_q}{Q_q} = \frac{I_b}{Q_q} = \frac{I_L b(1+\eta)}{Q_q} \quad (3.21)$$

The parameterization is closed if b and η are somehow determined then a_θ and a_q may be evaluated from the relations,

$$a_\theta = \frac{I_\theta}{Q_\theta} = \frac{I(1-b)}{Q_\theta} = \frac{I_L(1-b)(1+\eta)}{Q_\theta} \quad (3.22)$$

and

$$a_q = \frac{I_q}{Q_q} = \frac{I_b}{Q_q} = \frac{I_L b(1+\eta)}{Q_q} \quad (3.23)$$

Krishnamurti et al. (1983a) proposed a closure for b and η based on a screening multiregression analysis of GATE observations.

$$\frac{M}{I_L} = a_1 \zeta + b_1 \bar{\omega} + c_1 \quad (3.24)$$

$$\frac{R}{I_L} = a_2 \zeta + b_2 \bar{\omega} + c_2 \quad (3.25)$$

Where a_1 , b_1 , c_1 , a_2 , b_2 , and c_2 are regression constants whose magnitudes may be found in Krishnamurti et al. (1983a). ζ and $\bar{\omega}$ are respectively the relative vorticity and the vertically integrated vertical velocity.

Thus, in numerical weather prediction, ζ and ω determine M/I_L and

R/I_L ;

$$\text{since } \frac{M}{I_L} = b(1+\eta) \quad (3.26)$$

$$\text{and } \frac{R}{I_L} = (1+\eta)(1-b) \quad (3.27)$$

These two relations determine b and η .

We can find a_θ and a_q from the relations,

$$a_\theta = \frac{I_L(1-b)(1+\eta)}{Q_\theta} = \frac{R}{Q_\theta} \quad (3.28)$$

and

$$a_q = \frac{I_L b(1+\eta)}{Q_q} = \frac{M}{Q_q} \quad (3.29)$$

It is also of interest to note that the apparent heat source Q_1 and

the apparent moisture sink Q_2 , for this formulation, may be expressed

by:

$$Q_1 = a_\theta \left[c_p \frac{T}{\theta} \frac{(\theta_s - \theta)}{\Delta \tau} + \omega c_p \frac{T}{\theta} \frac{\partial \theta}{\partial p} \right] + c_p \frac{T}{\theta} [H_R + H_S] \quad (3.30)$$

$$Q_2 = -L \left[a_q \frac{(q_s - q)}{\Delta \tau} + \omega \frac{\partial q}{\partial p} \right] \quad (3.31)$$

The code monitors the apparent heating and moistening for output

purposes. The total convection precipitation is given by,

$$P_T = \frac{1}{g} \int_{P_T}^{P_B} a_\theta c_p \frac{T}{\theta} \frac{(\theta_s - \theta)}{\Delta \tau} dp \quad (3.32)$$

3.4 Parameterization of surface fluxes

Surface fluxes in the model are calculated following the formulation of Chang (1978). The formulation is based upon the assumption of the existence of a constant flux layer of about 50 meters depth near the earth surface in which the fluxes of momentum, sensible heat and latent heat (moisture flux) are constant with height.

The surface fluxes of momentum, heat and moisture are given as

$$F_M = -\rho \langle u'w' \rangle_s \quad (3.33)$$

$$F_S = -\rho c_p \langle \theta'w' \rangle_s \quad (3.34)$$

and
$$F_L = -\rho L \langle q'w' \rangle_s \quad (3.35)$$

where u' , w' , θ' and q' are the deviations of horizontal velocity, vertical velocity, potential temperature and specific humidity from their large scale values. Thus these are associated with the turbulent eddies. The $\langle \rangle$ is a large scale time average. Subscript s denotes the surface layer. The computation of these surface fluxes is based on similarity theory described by Chang (1978).

The basis of the similarity analysis are the planetary boundary layer observations, e.g. Businger, et al. (1971). According to these observations, nondimensionalized vertical gradients of large-scale

quantities such as the wind (\bar{u}), potential temperature ($\bar{\theta}$) and specific humidity (\bar{q}) in the surface layer can be expressed as universal functions of a nondimensional height (z/L) where z is the height above the earth's surface and L is the Monin-Obukhov length.

Monin-Obukhov length is defined by,

$$L = u_*^2 / \kappa \beta \theta_* \quad (3.36)$$

Here $\beta = g/\theta_0$ where θ_0 is the mean potential temperature in the constant flux layer. u_* and θ_* are related to the surface momentum flux and surface sensible heat flux by

$$u_*^2 = - \langle u'w' \rangle_s \quad (3.37)$$

$$\text{and} \quad u_* \theta_* = - \langle \theta'w' \rangle_s \quad (3.38)$$

We express the nondimensional wind shear, potential temperature gradient and moisture gradient by the relations,

$$\frac{\kappa z}{u_*} \frac{\partial \bar{u}}{\partial z} = \phi_m(z/L) \quad (3.39)$$

$$\frac{\kappa z}{\theta_*} \frac{\partial \bar{\theta}}{\partial z} = \phi_h(z/L) \quad (3.40)$$

$$\text{and} \quad \frac{\kappa z}{q_*} \frac{\partial \bar{q}}{\partial z} = \phi_q(z/L) \quad (3.41)$$

The empirical fits of the boundary layer observations are usually separated in terms of stability. Stability is expressed in terms of the sign of the Monin-Obukhov length L or that of the Bulk Richardson Number R_{iB} .

$$R_{iB} = \beta \frac{\frac{d\bar{\theta}}{dz}}{\left[\frac{d\bar{u}}{dz} \right]^2} \quad (3.42)$$

For the stable surface layer

$$L > 0 \quad (3.43)$$

$$\text{or } R_{iB} > 0 \quad (3.44)$$

For the unstable surface layer

$$L < 0 \quad (3.45)$$

$$\text{or } R_{iB} < 0 \quad (3.46)$$

Since, apriori the Monin Obukhov length is an unknown quantity, stability is assessed from the sign of the Bulk Richardson Number R_{iB} .

Empirical fits on the boundary layer observations (Businger et al., 1971) for wind shear and potential temperature gradient for stable and unstable cases, are expressed, following Chang (1978), by the following nondimensional relations,

a) Stable case

$$kz/u_* \frac{\partial \bar{u}}{\partial z} = 1.0 + 4.7 z/L \quad (3.47)$$

$$kz/\theta_* \frac{\partial \bar{\theta}}{\partial z} = 0.74 + 4.7 z/L \quad (3.48)$$

and

b) Unstable case

$$kz/u_* \frac{\partial \bar{u}}{\partial z} = (1 - 15 z/L)^{-\frac{1}{4}} \quad (3.49)$$

$$kz/\theta_* \frac{\partial \bar{\theta}}{\partial z} = 0.74(1 - 9 z/L)^{-\frac{1}{2}} \quad (3.50)$$

u_* and θ_* within the constant flux layer are constant with height since fluxes are constant. Using this fact and the definition of Monin-Obukov length given by (3.36) we can integrate the equations (3.47) and (3.48) to provide u_* and θ_* for stable case as:

$$u_* = \frac{k(u_2 - u_1)}{\ln(z_2/z_1) + 4.7 \frac{\Delta z}{L}} \quad (3.51)$$

and

$$\theta_* = \frac{k(\theta_2 - \theta_1)}{0.74 \ln(z_2/z_1) + 4.7 \frac{\Delta z}{L}} \quad (3.52)$$

where u_1 , u_2 and θ_1 , θ_2 are wind speeds and potential temperature at heights z_1 , z_2 in the constant flux layer. Δz is equal to $(z_2 - z_1)$. Using (3.36), (3.51) and (3.52) by eliminating u_* and θ_* a quadratic equation in $\Delta z/L$ is obtained. Its one solution which satisfies the physical constraint that $L > 0$ for the stable condition is

$$\frac{\Delta z}{L} = \ln \left(\frac{z_2}{z_1} \right) \left[\frac{9.4 R_{iB} - 0.74 + (4.88 R_{iB} + 0.5476)^{1/2}}{9.4 - 44.18 R_{iB}} \right] \quad (3.53)$$

where R_{iB} (Bulk Richardson Number)

$$= \frac{\beta (\theta_2 - \theta_1) \Delta z}{(u_2 - u_1)^2}$$

Equation (3.53) also requires that $0 < R_{iB} < 0.212$ to ensure $\Delta z/L > 0$ for $R_{iB} > 0$. For stable case $\Delta z/L$ is calculated from (3.53) and this in turn provides u_* and θ_* using (3.51) and (3.52). u_* and θ_* provide the momentum flux and sensible heat flux through the relations (3.37) and (3.38).

For unstable case the integration of (3.49) and (3.50) provides:

$$u_* = \frac{k(u_2 - u_1)}{\ln \left(\frac{z_2}{z_1} \right) - \psi_1 \left(\frac{z_2}{L}, \frac{z_2}{z_1} \right)} \quad (3.54)$$

and

$$\theta_* = \frac{k(\theta_2 - \theta_1)}{0.74 \left[\ln \left(\frac{z_2}{z_1} \right) - \psi_2 \left(\frac{z_2}{L}, \frac{z_2}{z_1} \right) \right]} \quad (3.55)$$

The functions ψ_1 and ψ_2 are given by

$$\psi_1\left(\frac{z_2}{L}, \frac{z_2}{z_1}\right) = \ln \left[\left\{ \frac{(1 + E_2)}{(1 + E_1)} \right\}^2 \left\{ \frac{(1 + E_2^2)}{(1 + E_1^2)} \right\} \right] - 2 \tan^{-1} E_2 + 2 \tan^{-1} E_1 \quad (3.56)$$

and

$$\psi_2\left(\frac{z_2}{L}, \frac{z_2}{z_1}\right) = 2 \ln \frac{(1 + \tau_2)}{1 + \tau_1} \quad (3.57)$$

where

$$E_1 = \left(1 - \frac{15z_2/L}{z_2/z_1}\right)^{1/4} \quad (3.58)$$

$$E_2 = \left(1 - 15 \frac{z_2}{L}\right)^{1/4} \quad (3.59)$$

$$\tau_1 = \left(1 - \frac{9z_2/L}{z_2/z_1}\right)^{1/2} \quad (3.60)$$

$$\tau_2 = \left(1 - 9 \frac{z_2}{L}\right)^{1/2} \quad (3.61)$$

Using (3.36), (3.54) and (3.55) we can get an expression for z_2/L . Chang (1978) has given a polynomial least square fit to obtain z_2/L from the modified bulk Richardson number R_{im} defined by

$$R_{im} = R_{iB} \frac{z_2}{\Delta z} \quad (3.62)$$

The equation is given by

$$\ln \left(\frac{-z_2}{L}\right) = a_0 + a_1 \ln(-R_{im}) + a_2 [\ln(-R_{im})]^2 + a_3 [\ln(-R_{im})]^3 \quad (3.63)$$

The regression coefficients a_0 , a_1 , a_2 and a_3 are functions of $\ln(z_2/z_1)$.

Thus, knowing z_2/L , u_* , θ_* , surface flux of momentum and surface flux of sensible heat can be obtained.

The fluxes can also be expressed in terms of bulk aerodynamic formulae i.e.

$$F_M = \rho C_D (u_2 - u_1)^2 \quad (3.64)$$

$$F_S = \rho C_p C_H (u_2 - u_1) (\theta_2 - \theta_1) \quad (3.65)$$

$$F_L = \rho L C_Q (u_2 - u_1) (q_2 - q_1) * GW \quad (3.66)$$

where C_D , C_H and C_Q are exchange coefficients for momentum, heat and moisture and GW is a ground wetness parameter. By comparing equations (3.64), (3.65) with equations (3.37), (3.38) using the definition of fluxes from (3.33) and (3.34) the expressions for the stability dependent exchange coefficients can be written down as:

a) Stable Case: $L > 0$,

Momentum:

$$C_D = \frac{k^2}{\left[\ln \frac{z_2}{z_1} + 4.7 \frac{\Delta z}{L} \right]^2} \quad (3.67)$$

Heat:

$$C_H = \frac{-k^2}{\left[\ln \frac{z_2}{z_1} + 4.7 \frac{\Delta z}{L} \right] \left[0.74 \ln \frac{z_2}{z_1} + 0.47 \frac{\Delta z}{L} \right]} \quad (3.68)$$

Moisture:

The exchange coefficient for moisture C_Q is simply defined by:

$$C_Q = 1.7 C_H \quad (3.69)$$

b) unstable case: $L < 0$,

The exchange coefficients are

Momentum:

$$C_D = \frac{k^2}{\left[\ln z_2/z_1 - \psi_1 \right]^2} \quad (3.70)$$

Heat:

$$C_H = \frac{-k^2}{0.74 [\ln z_2/z_1 - \psi_1] [\ln z_2/z_1 - \psi_2]} \quad (3.71)$$

Moisture:

$$C_Q = 1.7 C_H \quad (3.72)$$

Ground wetness parameter GW required for the calculation of moisture surface flux is defined by the following empirical relations :

$$GW = \left[\frac{\alpha_{\max} - \alpha}{\alpha_{\max} - \alpha_{\min}} \right] (1 - RH) \quad (3.73)$$

$$\text{or} \quad GW = 0.85 (1.0 - \exp(-200.0(0.25-\alpha)^2)) \quad (3.74)$$

Here RH denotes the relative humidity of air at level 2. α_{\max} , α and α_{\min} respectively denote the maximum surface albedo of the domain, local surface albedo and the minimum surface albedo of the domain. Over ocean GW is set to 1.0.

In practice the height z_1 is taken to be the roughness height z_0 .

Over the oceans we use Charnock's formula to define roughness height, i.e.

$$z_0 = 0.04 * u_*^2 / g \quad (3.75)$$

Since z_0 is a function of the momentum flux its value presupposes a knowledge of u_* . u_* is first calculated using constant exchange coefficient in the Bulk Aerodynamic formula. This provides a first guess value for z_0 . Later it is updated by iterating (3.75) with the stability dependent calculation for u_* in the similarity theory.

Over land areas the roughness height z_0 is determined using the formula given by Delsol et al., 1971.

$$z_0 = 0.15 + 0.2 (236.8 + 18.42*h)^2 * 10^{-8} \text{ m.} \quad (3.76)$$

Here h denotes the terrain height in meters. In our calculations we have set an upper limit for $z_0=1$ meter.

3.5 Parameterization of fluxes above the surface layer:

Above the surface layer the fluxes of heat, moisture and momentum are calculated following the K-theory (Louis, 1979) where the eddy diffusion coefficient K depends on the mixing length, the vertical wind shear and the stability of the atmosphere.

The convergence of flux at any level is calculated from a diffusion equation,

$$\frac{\partial Q}{\partial t} = \frac{1}{\rho} \frac{\partial}{\partial z} \left[\rho K_Q \frac{\partial Q}{\partial z} \right] \quad (3.77)$$

where Q stands for u , v , θ or q . At the upper boundary flux is assumed to be zero and at the lower boundary it is equal to the surface fluxes as calculated in section 3.4. We define the eddy diffusion coefficients for heat (K_θ), moisture (K_q) and momentum (K_m) by the relations,

$$K_\theta = K_q = l^2 \left| \frac{\partial \vec{V}}{\partial z} \right| S_1(R_i) \left[\frac{m^2}{s} \right] \quad (3.78)$$

$$\text{and} \quad K_m = l^2 \left| \frac{\partial \vec{V}}{\partial z} \right| S_2(R_i) \left[\frac{m^2}{s} \right] \quad (3.79)$$

l = mixing length

S_1 and S_2 express the dependence on Richardson number R_i , and are expressed by the following empirical relations :

$$S_1, S_2 = \frac{1.0}{(1 + 5R_i)^2} \text{ for } R_i \geq 0 \quad \begin{matrix} \text{(heat, moisture, and} \\ \text{momentum)} \end{matrix} \quad (3.80)$$

$$S_1 = \frac{(1.0 + 1.286 |R_i|^{\frac{1}{2}} - 8R_i)}{(1 + 1.286 |R_i|^{\frac{1}{2}})} \quad R_i < 0 \quad \begin{matrix} \text{(heat, moisture)} \end{matrix} \quad (3.81)$$

and
$$S_2 = \frac{(1.0 + 1.746|R_i|^{\frac{1}{2}} - 8R_i)}{(1 + 1.746|R_i|^{\frac{1}{2}})} \quad R_i < 0 \quad (\text{momentum}) \quad (3.82)$$

$$R_i = \frac{\frac{g}{\theta_v} \left[\frac{\partial \theta_v}{\partial z} \right]}{\left| \frac{\partial V}{\partial z} \right|^2} \quad (3.83)$$

where θ_v is virtual potential temperature.

l denotes the mixing length and is defined (following Blackadar, 1962) by

$$l = \frac{kz}{1 + \frac{kz}{l_{\text{inf}}}} ; \quad \begin{array}{l} l_{\text{inf}} = 150\text{m (momentum)} \\ \quad \quad = 450\text{m (heat, moisture)} \end{array} \quad (3.84)$$

$k = 0.35$ Von Karman constant

3.6 Shortwave Radiation

Solar radiation absorbed at the earth's surface and in the atmosphere is the initial source of energy causing atmospheric motions. A reliable treatment of solar radiation in numerical models of the atmospheric circulation is required.

The main absorbers of the solar radiation in the earth's atmosphere are water vapor in the troposphere and ozone in the stratosphere. Water vapor absorbs primarily in the near-infrared region, $0.7 \mu\text{m} < \lambda < 4 \mu\text{m}$. Ozone (O_3) is effective in the ultraviolet ($\lambda < 0.35 \mu\text{m}$) and in the visual ($0.5 \mu\text{m} < \lambda < 0.7 \mu\text{m}$). Fig. 4, taken from Pettit (1951) is representative of the spectral absorption for clear sky conditions.

The present parameterization in the model is based on the UCLA/GLAS GCM scheme and is described by Davies (1982). It includes a

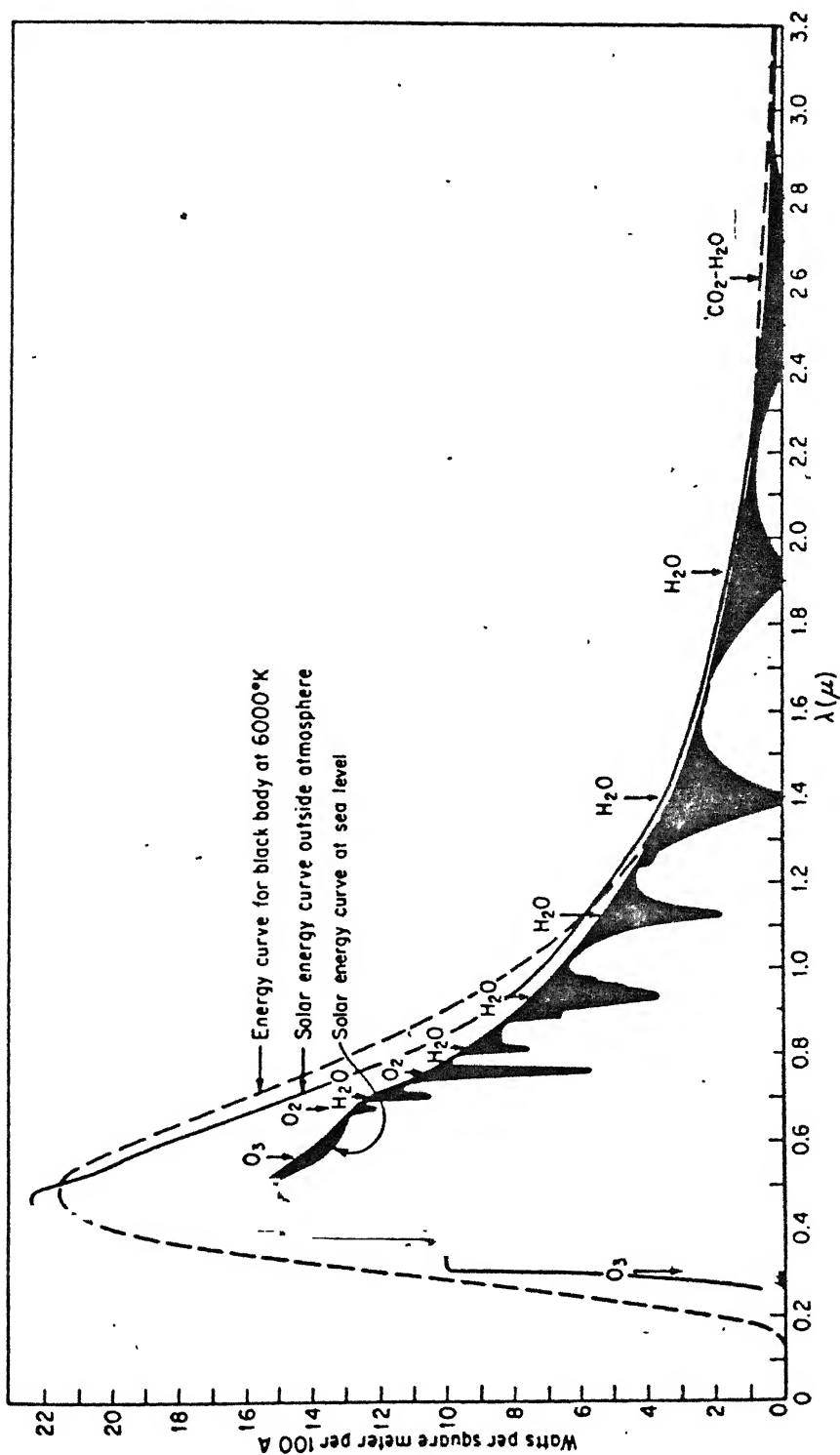


Figure 4: Spectral energy curve of solar radiation at sea level and extrapolated outside the atmosphere, as given by Pettit (1951). The darkened areas represent gaseous absorption in the atmosphere.

parameterization for the major absorption processes in the stratosphere, in the troposphere and at the earth's surface. The parameterization is a function of the water vapor distribution, the cloud coverage, the zenith angle of the sun, the albedo of the earth's surface and the ozone distribution. In this scheme ozone absorption and water vapor absorption are assumed to be in above mentioned separable spectral regions. Multiple scattering is taken into account whenever it is significant. Following is the brief description of these absorption processes.

a) Water Vapor Absorption

According to Lacis and Hansen (1974) absorption by water vapor is the major source of solar radiative heating in the atmosphere. However, parameterizing water vapor absorption is difficult for three reasons. These reasons are:

- i. The absorption coefficient of water vapor is highly frequency-dependent and accurate monochromatic values are not available for the entire spectrum.
- ii. Significant scattering and absorption can occur in the same part of the atmosphere.
- iii. The absorption coefficient has a significant dependence on pressure.

For clear skies the effect of scattering in the spectral region of significant water vapor absorption is negligible. The absorption due to water vapor is obtained directly from empirical absorption functions. The total fractional absorption as a function of water

vapor amount is given by (Yamamoto, 1962)

$$A_{wv}(y) = \frac{2.9y}{(1+141.5y)^{0.635} + 5.925y} \quad (3.85)$$

where

y = centimeters of precipitable water vapor.

An approximate correction is made for the pressure (p) and temperature (T) dependence of the absorption by using an effective water vapor amount in place of y as:

$$y^{eff} = y \left(\frac{p}{p_0} \right)^n \left(\frac{T_0}{T} \right)^{\frac{1}{2}} \quad (3.86)$$

where n = pressure scaling taken to be 1.

p₀ = reference pressure (1013 mb)

T₀ = reference temperature (273 K)

The absorption by water in the lth layer of the clear atmosphere is given by

$$A_{l,wv} = \mu_0 S_0 \{ A_{wv}(My_{l+1}) - A_{wv}(My_l) + R_g [A_{wv}(My_l^*) - A_{wv}(My_{l+1}^*)] \} \quad (3.87)$$

S₀ = solar influx at the top of the atmosphere

μ₀ = cosine of the solar zenith angle (θ₀)

R_g = ground albedo

y_l = effective water vapor amount traversed by the direct solar beam in reaching the top of the lth layer

$$= \frac{1}{g} \int_0^{p_l} q \left(\frac{p}{p_0} \right) \left(\frac{T_0}{T} \right)^{\frac{1}{2}} dp \quad (3.88)$$

q = specific humidity

M = magnification factor (Rodgers, 1967) accounting for the slant path and refraction.

$$= 35/(1224\mu_0^2 + 1)^{\frac{1}{2}}$$

My^*_l = effective water vapor amount traversed by the reflected radiation in reaching the l th layer from below

$$= \frac{M}{g} \int_0^{p_g} q \left(\frac{p}{p_0} \right) \left(\frac{T_0}{T} \right)^{\frac{1}{2}} dp + \frac{5}{3g} \int_{p_{l+1}}^{p_g} q \left(\frac{p}{p_0} \right) \left(\frac{T_0}{T} \right)^{\frac{1}{2}} dp \quad (3.89)$$

where p_l , p_{l+1} and p_g are the pressure at the top of the l th layer, at the bottom of the l th layer and at the ground.

For cloudy sky multiple scattering is the principal factor affecting the absorption; in this case the parameterization is based on a discrete probability distribution for the absorption coefficient derived from measured absorptivities.

The absorptivity is expressed by:

$$A_{wv}(y) = 1 - \int_0^{\infty} p(k) e^{-ky} dk \quad (3.90)$$

where

$p(k)dk$ = fraction of the incident flux that is associated with the absorption coefficient between k and $k + dk$.

A_{wv} is approximated by the following finite sum

$$A_{wv}(y) = 1 - \sum_{i=1}^5 p(k_i) e^{-k_i y} \quad (3.91)$$

where only 5 significant absorption coefficients are considered. Davies (1982) has calculated values for $p(k_i)$ and k_i . These values are given in Table 2.

Table 2

Discrete probability distribution of water vapor
absorption coefficients

From Davies, 1982

i	k_i	$p(k_i)$
1	0.005	0.107
2	0.041	0.104
3	0.416	0.073
4	4.752	0.044
5	72.459	0.025

The radiative transfer problem including multiple scattering for cloudy sky is solved as discussed by Davies (1982). The optical properties of each layer associated with each k_i are specified by the total optical thickness ζ of the layer and by the single scattering albedo $\tilde{\omega}$.

$$\zeta_{l,i} = \zeta_l^C + k_i(y_{l+1} - y_l) \quad (3.92)$$

$$\tilde{\omega}_{l,i} = \zeta_l^C / \zeta_{l,i} \quad (3.93)$$

where ζ_l^C is the optical thickness due to cloud particles in the l th layer.

b) Ozone Absorption

According to Lacis and Hansen (1974) the major source of stratospheric heating is the absorption of solar radiation by ozone. The absorption due to ozone occurs at the wavelengths where the Rayleigh scattering is significant. But, the absorption by ozone can be accurately parameterized because the significant absorption takes place very high in the atmosphere where there is little scattering. Most of the Rayleigh scattering takes place below the ozone layer, so the lower atmosphere acts mainly as a reflecting layer. On the other hand, the temperature and pressure dependence of the absorption coefficient are not very large, and can be neglected if the coefficients are chosen for a temperature representative of the ozone layer.

The absorption due to the ozone amount is different in the weak visual bands (Chapuis band) versus the ultraviolet bands (Hartley and Huggins bands). Figure 5 shows the percent of the solar flux absorbed

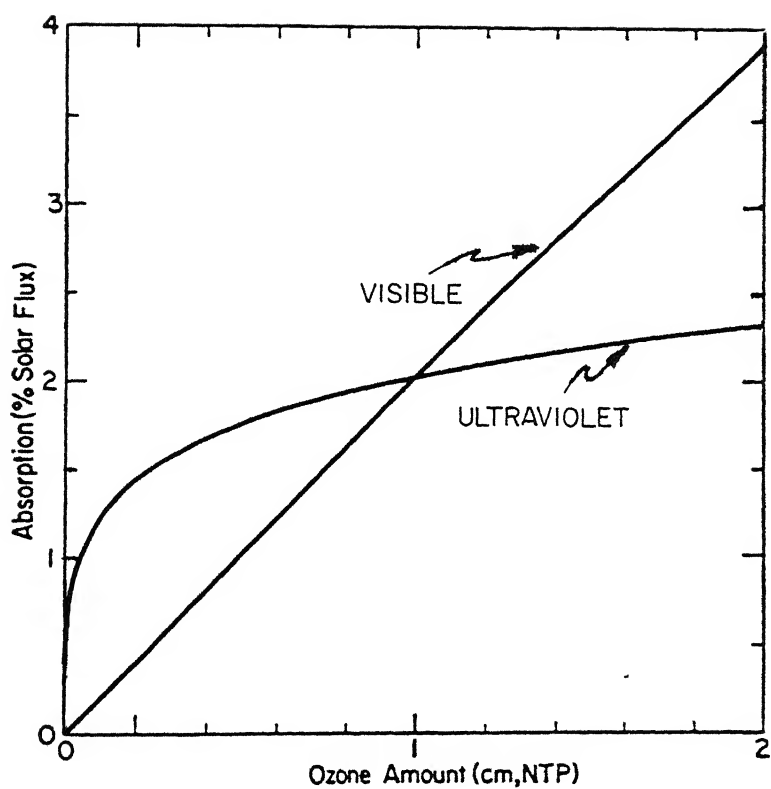


Figure 5: Percent of the solar flux absorbed as a function of ozone amount for two spectral regions.

as function of ozone amount for the two spectral regions. The ultraviolet bands are practically saturated at 0.5 cm of ozone, while the visual bands remain nearly proportional to the ozone amount. The parameterization of absorption due to ozone must accurately portray these different bands. The total fractional ozone absorption as a function of ozone amount (X) is expressed as follows:

$$A_{OZ}(X) = A_{OZ}^{uv}(X) + A_{OZ}^{vis}(X) \quad (3.94)$$

where:

$A_{OZ}^{uv}(X)$ = the fraction of incident solar flux that is absorbed in the ultraviolet bands as a function of ozone amount,

$A_{OZ}^{vis}(X)$ = the fraction of incident solar flux that is absorbed in the visual bands as a function of ozone amount.

Lacis and Hansen (1974) have fitted the frequency-integrated absorption curves for ozone to the following expressions.

$$A_{OZ}^{vis}(X) = \frac{0.02118X}{1.0 + 0.42X + 0.000323X^2} \quad (3.95)$$

$$A_{OZ}^{uv}(X) = \frac{1.082X}{(1.0 + 138.6X)^{0.805}} + \frac{0.0658X}{1.0 + (103.6X)^3} \quad (3.96)$$

The ozone amount traversed by the direct solar beam in reaching the l th layer of the atmosphere is:

$$X_l = u_l M \quad (3.97)$$

where:

u_l = the amount of ozone in cm in a vertical column above the l th layer,

M = magnification factor accounting for the slant path and refraction, as defined earlier.

$$M = \frac{35}{(1224 \mu_o^2 + 1)} \quad (3.98)$$

The ozone path traversed by the diffuse radiation illuminating the l th layer from below is:

$$X_l^* = u_t M + 1.9(u_t - u_l) \quad (3.99)$$

where:

u_t = the total ozone amount in a vertical path above the main reflecting layer (i.e., the ground for clear skies or the cloud-top for cloudy skies).

The total absorption of shortwave radiation in l th layer due to ozone is therefore:

$$A_{l,oz} = \mu_0 S_0 [\{A_{oz}(X_{l+1}) - A_{oz}(X_l)\} + \bar{R}(\mu_0) \{A_{oz}(X_l^*) - A_{vz}(X_{l+1}^*)\}] \quad (3.100)$$

where:

$\bar{R}(\mu_0)$ = the albedo of the reflecting region, including the effective albedo of the lower atmosphere and the ground reflectivity; for cloudy skies it is determined by a multi-layer solution. For clear skies it is given by the expression of Lacis and Hansen (1974):

$$\bar{R}(\mu_0) = \bar{R}_a(\mu_0) + [1 - \bar{R}_a(u_0)](1 - \bar{R}_a^*)R_g / (1 - \bar{R}_a^*R_g) \quad (3.101)$$

where:

$\bar{R}_a(\mu_0)$ = effective albedo of the lower atmosphere. For clear skies is given by $0.219/(1.0 + 0.816\mu_0)$,

R_g = ground reflectivity,

\bar{R}_a^* = the spherical albedo of the reflecting region. For clear sky it is given by 0.144.

$\bar{R}_a(\mu_0)$ and \bar{R}_a^* were determined by least squares fit.

c) Earth's Surface Absorption

The shortwave absorption at earth's surface is treated

differently for cloudy and clear skies.

The surface absorption is divided into two parts. One part ($A_{g,1}$) is for the wavelength regions where the absorption coefficient of water is significant. Second part ($A_{g,2}$) is for the absorption in remaining wavelengths. Approximately 35% of the solar flux is contained in the spectral regions of significant water vapor absorption.

$$A_g = A_{g,1} + A_{g,2} \quad (3.102)$$

where A_g = total surface absorption.

I. Clear Sky:

Lacis and Hansen (1974) define the surface absorption for clear sky in the spectral regions associated with significant water vapor absorption as:

$$A_{g,1} = \mu_0 S_0 [0.353 - A_{wv}(My_t)](1 - R_g) \quad (3.103)$$

where:

$\mu_0 S_0 A_{wv}(My_t)$ = absorbed direct solar flux by water vapor in a vertical column above the ground,

R_g = ground albedo.

The surface absorption in the spectral regions of negligible water vapor absorption is defined as:

$$A_{g,2} = \mu_0 S_0 [0.647 - \bar{R}_R(\mu_0) - A_{Oz}(Mu_t)](1 - R_g)/(1 - \bar{R}_R^* R_g) \quad (3.104)$$

where:

$\mu_0 S_0 A_{Oz}(Mu_t)$ = absorbed direct solar flux by ozone in a vertical path above the ground.

$\bar{R}_R(\mu_0)$ = the atmospheric albedo due to Rayleigh scattering, and

$$\text{is given by: } \bar{R}_r(\mu_0) = \frac{0.28}{1 + 6.43\mu_0}$$

\bar{R}_r^* = the spherical albedo of the Rayleigh atmosphere for illumination from below.

$$= 0.0685$$

II. Cloudy Sky:

For cloudy sky $A_{g,1}$ is obtained by multiplying the total transmission at the ground for each value of k_i (absorption coefficient) by the factor $(1-R_g) p(k_i)$ and summing over i for the discrete distribution of absorption coefficients given in Table 2.

$A_{g,2}$ is computed from the expression given below where Rayleigh scattering is neglected.

$$A_{g,2} = \mu_0 [0.647 - A_{OZ}(\mu_t)] [1 - \bar{R}_a(\mu_0)](1 - R_g)/(1 - \bar{R}_a^* R_g) \quad (3.105)$$

where u_t is the ozone amount in a vertical path above the highest cloud layer, and $\bar{R}_a(\mu_0)$ and \bar{R}_a^* refer to the visual cloud albedo.

This completes the procedure for calculating the short wave absorption in the atmosphere and at the earth's surface which provides the heating rates due to short wave absorption. There are several limitations of this scheme. For instance, it ignores the effects of aerosols and the spectral nature of the surface albedo.

3.7 Longwave radiation:

The longwave radiation scheme of the model is also based on the UCLA/GLAS GCM scheme and is described by Harshvardhan and Corsetti (1984). The basic equations for the longwave upward and downward

fluxes are:

$$F_{\text{clr}}^{\uparrow}(p) = \int_{\Delta\nu} d\nu [B_{\nu}(T_s)\tau_{\nu}(p, p_s) + \int_{p_s}^p B_{\nu}(T(p')) \frac{d\tau_{\nu}(p, p')}{dp'} dp'] \quad (3.106)$$

$$F_{\text{clr}}^{\downarrow}(p) = \int_{\Delta\nu} d\nu \left[\int_{p_t}^p B_{\nu}(T(p')) \frac{d\tau_{\nu}(p, p')}{dp'} dp' \right] \quad (3.107)$$

This is for a clear sky case, integrated over the spectral range $\Delta\nu$.

Here the individual variables are:

$B_{\nu}(T_s)$ = blackbody flux at the surface temperature T_s ,

p_s = surface pressure

T_s = surface temperature,

$T(p')$ = air temperature at pressure p' ,

p_t = pressure at the top of the atmosphere,

$\tau_{\nu}(p, p')$ = diffuse transmittance between the levels p and p' ,

ν = spectral wavenumber.

The diffuse transmittance in above equations is not only a function of temperature and pressure but it varies very rapidly with wavenumber ν , therefore rendering the computation of fluxes difficult and computationally inefficient. In practice, models avoid this problem by resorting to certain assumptions regarding the distribution of spectral lines in the various absorption bands and constructing approximate band models. A fast method of computing the transmittance functions over the spectral bands of interest has been developed by Chou and Peng (1983) and Chou (1984).

The thermal infrared spectrum of interest is shown in figure 6. The molecular line absorption due to the water vapor stretches from 0 cm^{-1} to 3000 cm^{-1} . Where 0-340 cm^{-1} , 1380-1900 cm^{-1} are water vapor band centers (regions of strong absorption) and 340-1380 cm^{-1} ,

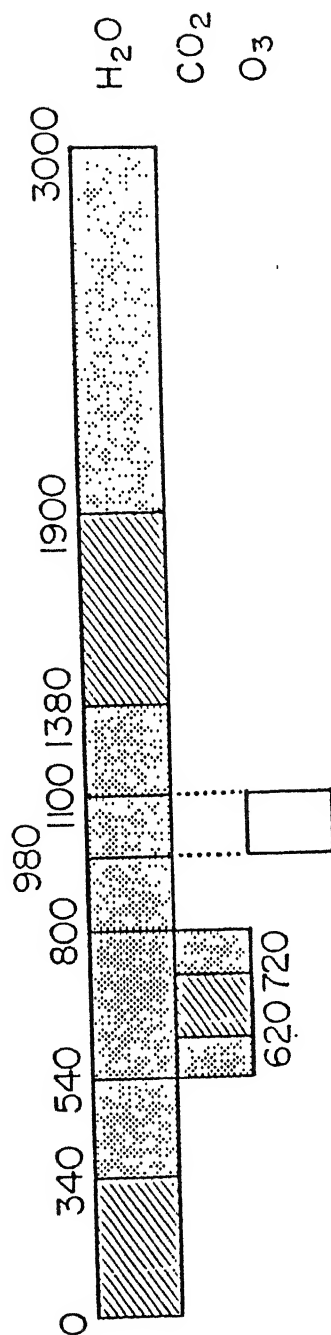


Figure 6: IR spectral ranges for H₂O, CO₂ and O₃ parameterized in the radiation code. Dashed area represents the band centers (for the H₂O and CO₂) and shaded areas are the band wings. Note that CO₂ (15 μm band) and O₃ (9.6 μm band) overlap with the H₂O.

1900-3000 cm^{-1} are water vapor wings (regions of moderate absorption). Apart from the molecular line absorption there is continuum absorption (e-type) due to water vapor. This e-type absorption is also assumed to extend from 0-3000 cm^{-1} . Absorption due to CO_2 is from 580 to 800 cm^{-1} where 620 to 720 cm^{-1} is the band center and 580-620, 720-800 cm^{-1} are the band wings for CO_2 . O_3 absorption is from 980 to 1100 cm^{-1} . The spectral ranges 540-800 cm^{-1} and 980-1100 cm^{-1} are known as 15 μm band and 9.6 μm band respectively. Spectral range 0-3000 cm^{-1} , excluding the 15 μm band and the 9.6 μm band, is termed as water vapor band.

An alternate form of the flux equations is obtained through integration by parts of (3.106) and (3.107).

$$F_{\text{clr}\uparrow}(p) = \Delta\nu B(T(p)) + G(p, p_s, T_s) - G(p, p_s, T(p_s)) + \int_{T(p)}^{T(p_s)} \frac{\partial G(p, p', T(p'))}{\partial T} dT(p') \quad (3.108)$$

$$F_{\text{clr}\downarrow}(p) = \Delta\nu B(T(p)) - G(p, p_t, T(p_t)) + \int_{T(p)}^{T(p_t)} \frac{\partial G(p, p', T(p'))}{\partial T} dT(p') \quad (3.109)$$

where:

$$B(T, (p)) = \frac{1}{\Delta\nu} \int B_\nu(T) d\nu, \quad (3.110)$$

$$G(p, p', T) = \int_{\Delta\nu} \tau_\nu(p, p') B_\nu(T) d\nu, \quad (3.111)$$

$$\frac{\partial G(p, p', T)}{\partial T} = \int_{\Delta\nu} \tau_\nu(p, p') \frac{\partial B_\nu(T)}{\partial T} d\nu. \quad (3.112)$$

and $T(p_s)$ = air temperature at the surface pressure p_s .

In the above $\tau(p, p)$ is set to 1 by the definition of transmittance. If the spectral width $\Delta\nu$ of the band is sufficiently narrow

$B_\nu(T)$ is replaced by $B(T)$, a mean value of the planck function. The equation for G becomes:

$$G(p, p', T) = B(T) \int_{\Delta\nu} \tau_\nu(p, p') d\nu \quad (3.113)$$

The radiative cooling rate, or the divergence of net flux is the final output of the radiation scheme. It is given by:

$$\frac{dT}{dt} = - \frac{g}{C_p} \frac{d(F\downarrow - F\uparrow)}{dp} \quad (3.114)$$

The model uses the above equations to calculate the longwave radiative cooling/heating rate of the atmosphere. Special considerations are given for cloudy skies, either overcast or partial cloud cover. The longwave surface flux is also calculated.

To evaluate the G functions for the fluxes given by (3.108, 109) the knowledge of the transmittance function is required. The diffuse transmittance function associated with molecular line absorption between the pressure levels p and p' at the wave number ν can be defined as (Chou, 1984).

$$\tau_\nu(p, p') = 2 \int_0^1 \exp(-d_\nu(p, p')/\mu) \mu d\mu \quad (3.115)$$

where $\mu = \cos\theta$; θ is the zenith angle
and d_ν is the optical thickness given

$$\text{by } d_\nu(p, p') = \int_{p'}^p c(p'') k_\nu(p'', T(p'')) \frac{dp''}{g} \quad (3.116)$$

where c is the absorber concentration and k is the absorption coefficient which is a function of wavenumber, pressure and temperature.

For computational efficiency k is taken to be the absorption coefficient at a reference pressure p_r and temperature T_r scaled by a factor depending on pressure and temperature.

$$k_p(p, T) = k_p(p_r, T_r) f(p, T) \quad (3.117)$$

therefore equation (3.116) can be written as

$$d_p(p, p') = k_p(p_r, T_r) w(p, p') = d_p(w) \quad (3.118)$$

$$\text{where } w(p, p') = \int_{p'}^p c(p'') f(p'', T(p'')) \frac{dp''}{g} \quad (3.119)$$

With the above definitions the molecular diffuse transmittance can be written as

$$\tau_p(p, p') = \tau_p(w) \quad (3.120)$$

The scaling factor $f(p, T)$ for different absorbers in different spectral bands are specified by Chou (1984) as:

$$f(p, T) = \left(\frac{p}{p_r}\right)^m \exp [r(T - T_r)] \text{ for water vapor and CO}_2 \text{ molecular absorption.} \quad (3.121)$$

$$f(p, T) = 1 \text{ for O}_3 \text{ molecular absorption.} \quad (3.122)$$

Where parameters m , r , reference temperature (T_r) and reference pressure (p_r) are also taken from Chou (1984). For water vapor absorption these parameters are given in table 3 and for CO₂ absorption they are given in table 4.

For water vapor, diffuse transmittance associated with e-type absorption is given by

$$\tau_p(p, p') = 2 \int_0^1 \exp [-\sigma_p(T_0)u(p, p')] \mu \, d\mu \quad (3.123)$$

where σ_p is the e-type absorption coefficient and is given by Roberts et al. (1976).

$$T_0 = 296^\circ\text{K}$$

Table 3

Parameters for the absorption due to
water vapor molecular lines

From Chou, 1984

	H ₂ O band-center	H ₂ O band-wing	15 μ m band	9.6 μ m band
Spectral range (cm ⁻¹)	0 - 340 1380 - 1900	340 - 540 800 - 980 1100 - 1380 1900 - 3000	540 - 800	980 - 1100
P _r (mb)	275	550	550	550
T _r (K)	225	256	256	256
r(K ⁻¹)	0.005	0.016	0.016	0.016
m	1	1	1	1

Table 4
Parameters for the band-center region and the
band-wing regions for CO₂ (15 μ m band)

	Band-center	Band wings	
		Narrow	Wide
$\Delta\nu(\Delta\nu^{-1})$	620 - 720	580 - 620 720 - 760	540 - 620 720 - 800
Pr(mb)	30	300	300
Pc(mb)	1	1	1
m	0.85	0.85	0.50
n	0.56	0.55	0.57
a	3.1	0.08	0.04
b	15.1	0.9	0.9
T _r (K)	240	240	240
r(K ⁻¹)	0.0089	0.025	0.025

u is the scaled water vapor amount and is given by:

$$u(p, p') = \int_p^{p'} e(p'') \exp \left[1800 \left(\frac{1}{T(p'')} - \frac{1}{296} \right) \right] q(p'') * \frac{dp''}{g} \quad (3.124)$$

where e is the water vapor pressure and q is water vapor mixing ratio.

Similar to equation (3.120) for molecular diffuse transmittance we can write transmittance for e-type absorption as

$$\tau_p(p, p') = \tau_v(u) \quad (3.125)$$

For water vapor, broad transmission function is given by $\tau_p(w) \tau_p(u) \equiv \tau_p(w, u)$.

With the above expressions of the transmittance functions the function G and its derivative $\partial G / \partial T$ required to estimate the IR fluxes can be computed. The expression for G given by equation 3.113 is

$$G = B(T) \int_{\Delta\nu} \tau_p(p, p') d\nu \quad (3.126)$$

G can be rewritten as

$$G = B(T) \int_{\Delta\nu} \tau_p(z) d\nu \text{ or } G = B(T) \tau(z) \quad (3.127)$$

where

$$\tau(z) = \int_{\Delta\nu} \tau_p(z) d\nu \quad (3.128)$$

$\tau_p(z)$ is $\tau_p(w)$ for molecular absorption and $\tau_p(u)$ for e-type absorption. In the regions of overlapping absorption due to different absorbers or overlapping molecular and e-type absorption $\tau_p(z)$ is the product of the respective transmittance functions.

Similarly $\frac{\partial G}{\partial T}$ is given by $\frac{\partial G}{\partial T} = \frac{\partial B(T)}{\partial T} \tau(z)$ (3.129)

Given the absorber amounts $\tau(z)$ for a given band $\Delta\nu$ can be evaluated using line by calculation with the knowledge of the respective absorber coefficients. Using such line by line calculations some

regression equations can be developed to provide transmittance τ as a function of absorber amounts. In the model the following regression relations for $\tau(z)$ for the various bands are used:

a) Water vapor band

In the band centers the molecular absorption is much stronger than e-type absorption, therefore e-type absorption is neglected for band centers. For the band wings both types of absorptions are included.

$$\tau(w;T) = \tau(w;250) [1 + \alpha(w)(T-250) + \beta(w)*(T-250)^2] \quad (3.130)$$

---for band centers

$$\tau(w,u;T) = \tau(w,u;250) [1 + \alpha(w,u)(T-250) + \beta(w,u)*(T-250)^2] \quad (3.131)$$

---for band wings

where

$\alpha(w,u), \alpha(w)$ = regression coefficients, listed in Table 5,

$\beta(w,u), \beta(w)$ = regression coefficients, listed in Table 6,

and

$\tau(w,u;250), \tau(w;250)$ = standardized transmission functions, listed in Table 7.

The G function for the water vapor band can be evaluated as

$$G_{WPB} = B_{WPC}(T)\tau(w;T) + B_{WPW}(T)\tau(w,u;T) \quad (3.132)$$

where $B_{WPC}(T)$ and $B_{WPW}(T)$ are respectively the average Plank functions over the band centers and band wings.

b) 15 μm band

In the 15 μm band CO_2 , water vapor molecular absorption and water vapor e-type absorption are present. The transmittance in this region is given by

TABLE 5 The regression coefficient, $10^4 \times \alpha(w, u)$, for computing the transmission functions

$\log_{10} w$	u (Band-Wing Region)																	Band-Center Region
	.0	.003	.006	.009	.012	.015	.018	.021	.024	.027	.030	.033	.036	.039	.042	.045	.048	
-6.0																		0
-5.7																		0
-5.4																		0
-5.1	0	1	2	2	2	1	1	0	0	0	0	-1	-1	-2	-2	-3	-4	1
-4.8	0	1	2	2	2	1	1	0	0	0	0	-1	-1	-1	-2	-3	-4	1
-4.5	0	2	2	2	2	2	1	1	0	0	0	-1	-1	-1	-2	-3	-4	1
-4.2	1	2	2	2	2	2	2	1	1	0	0	0	-1	-1	-1	-2	-3	2
-3.9	1	2	3	3	3	2	2	1	1	0	0	0	-1	-1	-1	-2	-3	2
-3.6	2	3	3	4	3	3	2	2	1	0	0	0	-1	-1	-1	-2	-3	3
-3.3	2	4	4	4	4	4	3	3	2	1	1	0	0	0	0	-1	-1	4
-3.0	3	5	5	5	5	5	5	4	4	3	3	2	2	1	1	0	0	5
-2.7	5	6	7	7	7	6	6	6	5	5	4	4	3	3	2	2	1	8
-2.4	6	8	9	9	9	8	8	8	7	7	6	6	5	5	4	4	3	10
-2.1	8	10	11	11	11	11	11	10	10	10	9	8	8	8	7	7	6	14
-1.8	11	13	14	14	14	14	14	14	13	13	12	12	11	11	10	10	9	19
-1.5	14	16	17	18	18	18	18	17	17	17	16	16	15	15	14	14	13	25
-1.2	19	21	22	23	23	23	23	23	22	22	22	21	21	21	20	20	19	36
-0.9	24	26	28	29	29	29	29	29	29	28	28	28	28	27	27	27	26	56
-0.6	31	33	35	36	36	36	37	37	37	37	36	36	36	36	36	36	35	97
-0.3	38	41	42	43	44	45	45	45	45	46	46	46	46	46	46	46	46	164
0.0	46	48	49	50	51	52	52	53	53	54	54	55	55	55	56	56	56	218
0.3	51	53	54	56	56	57	58	59	59	60	61	62	62	63	63	64	64	238
0.6	55	56	57	58	59	60	61	62	63	63	64	65	66	66	67	68	68	
0.9	56	57	58	59	60	61	62	63	63	64	65	66	66	67	68	69	70	

TABLE 6 The regression coefficient, $10^4 \times \beta(w, u)$, for computing the transmission functions

$\log_{10} w$	u (Band-Wing Region)																	Band-Center Region
	.0	.003	.006	.009	.012	.015	.018	.021	.024	.027	.030	.033	.036	.039	.042	.045	.048	
-6.0																		0
-5.7																		0
-5.4																		0
-5.1	0	1	1	2	3	3	4	4	5	5	6	6	7	7	8	8	9	0
-4.8	0	1	1	2	3	3	4	4	5	5	6	6	7	7	8	8	9	0
-4.5	0	1	1	2	3	3	4	4	5	5	6	6	7	7	8	8	9	0
-4.2	0	1	1	2	3	3	4	4	5	5	6	6	7	7	8	8	9	1
-3.9	0	0	1	2	3	3	4	4	5	5	6	6	7	7	8	8	9	1
-3.6	0	0	1	1	2	3	3	4	4	5	5	6	6	7	7	8	9	1
-3.3	0	0	1	1	2	3	3	4	4	5	5	6	6	7	7	8	9	1
-3.0	0	0	0	1	1	2	3	3	4	4	5	5	6	6	7	7	8	2
-2.7	-1	0	0	0	1	1	2	2	3	4	4	5	5	6	6	7	8	2
-2.4	-1	-1	0	0	0	1	1	2	2	3	4	4	5	5	6	6	7	3
-2.1	-2	-2	-1	0	0	0	0	1	2	2	3	4	4	5	5	6	6	4
-1.8	-3	-3	-2	-2	-1	0	0	0	1	1	2	2	3	3	4	4	5	5
-1.5	-5	-4	-4	-3	-2	-2	-1	-1	0	0	1	1	2	2	3	3	4	8
-1.2	-6	-6	-5	-5	-4	-3	-3	-2	-2	-1	-1	0	0	0	1	1	2	12
-0.9	-8	-8	-7	-7	-6	-5	-4	-4	-3	-3	-2	-2	-1	-1	0	0	1	23
-0.6	-11	-10	-10	-9	-9	-8	-8	-7	-6	-6	-5	-5	-4	-4	-3	-2	-1	46
-0.3	-13	-13	-13	-12	-11	-11	-10	-10	-9	-9	-8	-7	-7	-6	-6	-5	-4	87
0.0	-16	-16	-15	-15	-14	-14	-13	-13	-12	-11	-10	-10	-9	-9	-8	-7	-6	128
0.3	-18	-18	-17	-17	-16	-16	-15	-15	-14	-14	-13	-13	-12	-11	-11	-10	-9	151
0.6	-20	-19	-19	-18	-18	-17	-17	-16	-16	-15	-15	-14	-13	-13	-12	-12	-11	
0.9	-20	-20	-20	-19	-18	-18	-17	-16	-16	-15	-15	-14	-13	-13	-12	-12	-11	

TABLE 7 The "Planck weighted" transmission function, $10^3 \times \tau(w, u; 250 \text{ K})$, in the water vapor spectral regions. The units of w and u are g cm^{-2} .

$\log_{10} w$	u (Band-Wing Region)																	Band-Center Region
	.0	.003	.006	.009	.012	.015	.018	.021	.024	.027	.030	.033	.036	.039	.042	.045	.048	
-6.0																		996
-5.7																		992
-5.4																		987
-5.1	998	937	893	863	842	823	808	794	782	771	761	751	742	734	726	718	711	993
-4.8	997	936	892	862	840	822	806	793	780	770	759	750	741	733	725	717	710	969
-4.5	995	933	890	859	838	820	804	790	778	767	757	748	739	731	723	715	708	954
-4.2	991	930	886	856	835	817	801	787	775	764	754	744	735	727	719	711	704	933
-3.9	985	924	881	851	829	811	795	782	770	759	749	739	730	722	714	706	699	905
-3.6	977	916	873	843	822	803	788	774	762	751	740	730	721	712	703	696	688	886
-3.3	966	905	862	832	811	793	777	763	751	741	731	723	714	706	698	691	685	867
-3.0	950	890	847	817	796	778	762	749	737	726	716	706	697	689	681	673	666	847
-2.7	929	870	828	798	777	759	743	730	718	707	697	687	678	670	662	655	647	817
-2.4	902	844	803	774	753	735	719	706	694	683	673	663	654	646	638	631	623	752
-2.1	869	813	772	744	723	706	690	677	664	654	643	634	625	617	609	601	594	673
-1.8	829	775	736	708	688	670	655	642	630	619	609	600	591	582	575	567	560	652
-1.5	781	730	693	666	646	629	614	601	589	578	568	559	550	542	534	526	519	621
-1.2	725	678	642	617	598	581	566	553	541	531	521	511	503	494	487	479	472	585
-0.9	660	617	585	561	543	527	512	500	488	478	468	458	448	442	434	426	419	547
-0.6	590	553	525	503	485	470	456	443	432	422	412	403	395	386	379	371	364	509
-0.3	522	491	466	446	429	415	402	390	379	369	359	350	342	334	326	319	312	471
0.0	461	435	414	396	381	367	354	343	332	323	313	305	297	289	281	274	268	431
0.3	411	390	371	355	342	329	317	306	296	287	278	269	262	254	247	240	233	391
0.6	371	354	338	324	311	299	288	278	268	259	251	243	235	228	221	214	208	351
0.9	338	323	309	296	285	274	264	254	245	237	229	221	214	207	200	194	188	311

$$\tau(w, u, w_1) = \tau(w)\tau(u)\tau(w_1) \quad (3.133)$$

where w , u and w_1 are scaled water vapor amount for molecular absorption, scaled water vapor amount for e-type absorption and scaled CO_2 amount respectively.

$$\tau(w) = \exp [-6.7w(1 + 16w^{0.6})] \quad (3.134)$$

$$\tau(u) = \exp (-274u^{.83}) \quad (3.135)$$

$$\tau(w_1) = \exp (-aw_1/(1 + bw_1^n)) \quad (3.136)$$

where a , b and n have different values for CO_2 band center and wings. These values are listed in table 4. The final value of $z(w_1)$ for the entire band is taken to be frequency weighted average of the transmittance $\tau_c(w_1)$ in the band center region and $\tau_w(w_1)$ in the band wing region, i.e.

$$\tau(w_1) = \frac{1}{\Delta\nu} [\tau_c(w_1)\Delta\nu_c + \tau_w(w_1)\Delta\nu_w] \quad (3.137)$$

where $\Delta\nu_c$, $\Delta\nu_w$ and $\Delta\nu$ are width of the band center, band wing and entire $15 \mu\text{m}$ band respectively.

The function G is given by

$$G_{15\mu\text{m}} = B_{15\mu\text{m}}(T)\tau(w)\tau(u)\tau(w_1) \quad (3.138)$$

where $B_{15\mu\text{m}}(T)$ is the average Plank function over the $15 \mu\text{m}$ band.

9.6 μm band

In the $9.6 \mu\text{m}$ band the water molecular absorption is neglected. Thus the total absorption is due to ozone and water vapor e-type absorption. Therefore the transmittance for this band is given by

$$\tau(u, w_2) = \tau(u)\tau(w_2) \quad (3.139)$$

where w_2 is the ozone amount and u is the scaled water vapor amount for e-type absorption.

$$\tau(u) = \exp (-9.79u) \quad (3.140)$$

and

$$\tau(w_2) = 1 - \frac{81.31}{120.0} \left[1 - \exp\left\{-4.398\tilde{p}\left((1 + 4\frac{345.28 w_2}{0.87\tilde{p}})^{\frac{1}{2}} - 1\right)\right\} \right] \quad (3.141)$$

$$\text{where } \tilde{p} = \frac{\int_{p_1}^{p_2} (O_3 \text{ concentration}) * dp}{\int_{p_1}^{p_2} q dp}$$

q is the mixing ratio of water vapor.

The corresponding G function for this band is given by

$$G_{9.6\mu m} = B_{9.6\mu m}(T)\tau(u)\tau(w_2) \quad (3.142)$$

where $B_{9.6\mu m}(T)$ is the average Plank function over 9.6 μm band.

Finally the Plank function in equations 3.108 and 3.109 for upward and downward longwave radiation flux is given by

$$B(T(p)) = B_{WPC}(T(p)) + B_{WPW}(T(p)) + B_{15\mu m}(T(p)) + B_{9.6\mu m}(T(p)) \quad (3.143)$$

The function G is given by

$$G(p, p', T) = G_{WPB} + G_{15\mu m} + G_{9.6\mu m} \quad (3.144)$$

A similar expression for $\frac{\partial G}{\partial T}$ can also be obtained.

The upward and downward flux defined earlier are only valid in the clear sky. To account for the effect of cloudy sky the equations are modified as described below.

For longwave radiation the clouds are assumed to be non-reflective. For cloudy sky the modified equations (3.108) and (3.109) for the fluxes are given by:

$$F_{\text{cldy}}^{\uparrow}(p) = \Delta \nu B(T(p)) + c(p, p_s) [G(p, p_s, T_s) - G(p, p_s, T(p_s))] + \int_{T(p)}^{T(p_s)} c(p, p') \frac{\partial G}{\partial T}(p, p', T(p')) dT(p') \quad (3.145)$$

$$F_{\text{Cldy}}^{\downarrow}(p) = \Delta \nu B(T(p)) - c(p, p_t) G(p, p_t, T(p_t)) \\ + \int_{T(p)}^{T(p_t)} c(p, p') \frac{\partial G}{\partial T}(p, p', T(p')) dT(p') \quad (3.146)$$

where $c(p, p')$ is the probability for clear line of sight from p to p' . $c(p, p')$ depends upon the kind of cloud overlap present between p and p' . For the downward flux $c(p, p')$ between two pressure levels p and p' ($p > p'$) designated by vertical indices i and j respectively is given by

$$c_{ij} = (1-N_j) (1-N_{j+1}) \text{-----} (1-N_{i-1}) \quad (3.147)$$

where N_j is the fractinal cloudiness at the level j . N_j lies between 0 and 1. For clear sky N_j is zero. Similarly for the upward flux between the pressure levels p and p' ($p' > p$) designated by the vertical indicies i and j $c(p, p')$ is given by

$$c_{ij} = (1-N_j) (1-N_{j-1}) \text{-----} (1-N_{i+1}) \quad (3.148)$$

After determining the probabilities for clear line of sight c_{ij} 's the radiative fluxes are calculated and then longwave radiation cooling rates are computed by equation (3.114). Finally both shortwave and longwave cooling rates are added to the thermodynamic equation.

3.8 Surface Energy Balance:

Over the oceans the prescribed sea surface temperature is used as the earth's surface temperature. Over land areas the solution of a surface energy balance equation is used to obtain the ground temperature T_g . The surface energy balance is expressed by,

$$(S_{w\downarrow} - S_{w\uparrow}) + (L_{w\downarrow} - L_{w\uparrow}) - F_{s\uparrow} - F_{L\uparrow} = 0 \quad (3.149)$$

i.e.,

net shortwave flux + net longwave flux - sensible heat flux - latent heat flux = 0. In this balance we ignore the flux into the ground and the heat capacity of the ground is assumed to be zero. If α denotes the surface albedo we express the above equation by,

$$(1-\alpha) S_{W\downarrow} + (L_{W\downarrow} - L_{W\uparrow}) - (F_{S\uparrow} + F_{L\uparrow}) = 0 \quad (3.150)$$

The surface albedo is specified from climatological tabulation of Posey and Clapp (1964) and Kondratyev (1972). Figure 7a illustrates the field of albedo for the summer season. We furthermore express the fluxes by the following expressions,

$$L_{W\uparrow} = \sigma T_g^4 \quad (3.151)$$

$$F_{S\uparrow} = \rho C_H C_p |\vec{V}_2| (\theta_2 - \theta_g) \quad (3.152)$$

$$F_{L\uparrow} = \rho C_q L \overset{\rightarrow}{|\vec{V}_2|} (q_2 - q_g) \text{ GW} \quad (3.153)$$

The above were discussed in the surface similarity theory.

The energy balance equation is coupled to the surface similarity theory and is solved by the Newtonian iteration scheme.

3.9 Orography:

The orography was extracted from a basic Navy data tape. The Navy tape contains global orography on a 10 x 10 minute area. This data was averaged at the respective resolution.

Another field of data that enters the regional model is the sea surface temperature (SST). Climatological mean in a current 10 day averaged SST are used to define this field. Fig. 7b illustrates a

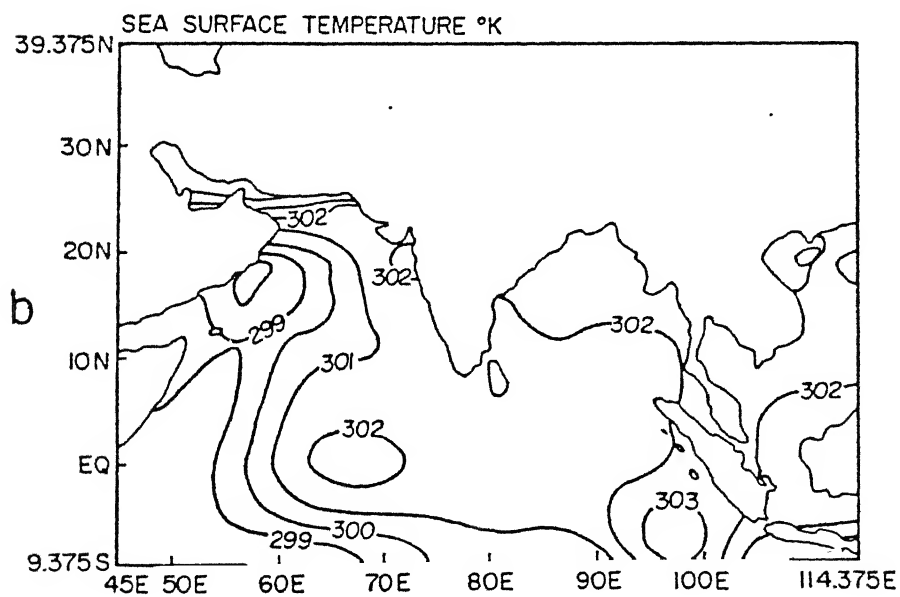
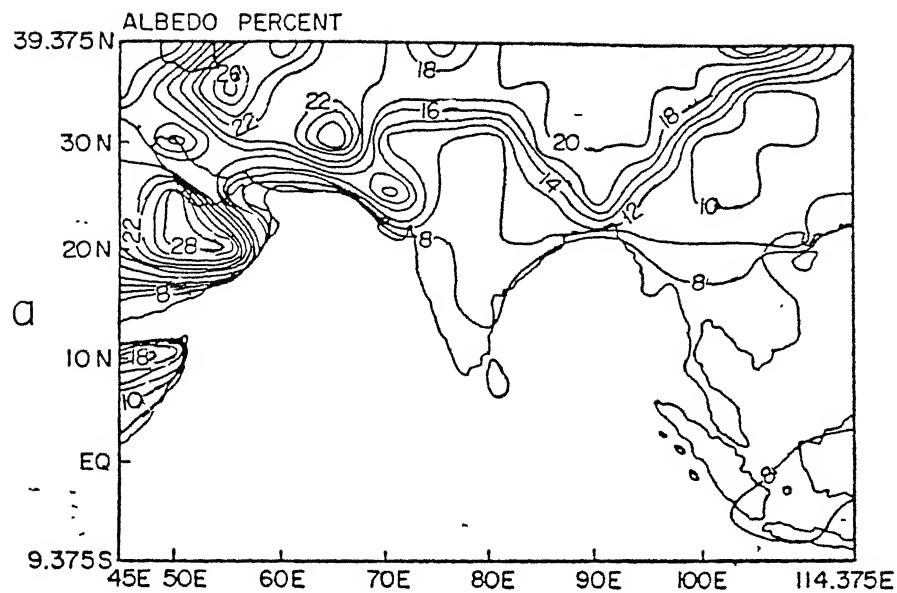


Figure 7: (a) Earth's albedo field for the summer season,
(b) Sea surface temperature used in the model.

typical field of SST over the monsoon oceans during the northern summer.

CHAPTER 4

PREDICTION OF THE LANDFALL OF A TROPICAL STORM

During May 1979 a major tropical cyclone formed in the southern Bay of Bengal and made a landfall over the east coast of southern India around the 12th of that month. This storm caused major destruction in life and property over Andhra Pradesh. Fig. 8, based on the Guam summaries, illustrates the observed track of this tropical cyclone.

The formative aspects of this tropical cyclone have been studied by Low Nam (1982). This storm formed along the lower tropospheric cyclonic shear zone of the Bay of Bengal monsoonal flows, that was well prior to the onset of monsoon over India. The formative period of this cyclone coincides with the onset of monsoon and heavy rain over Burma. An explosive growth of zonal flow accelerations in the monsoonal low level flows and rather marked divergent outflows over the southern Bay of Bengal were noted during the formative period.

The study, presented here, addresses the landfall of this tropical cyclone. The horizontal resolution is 1° lat/long grid. The multi-level regional model was initialized with the final FGGE IIb data sets for May 11 1979, 00 UTC. At this stage the tropical cyclone was located at 13° N and 82.5° E over the Bay of Bengal.

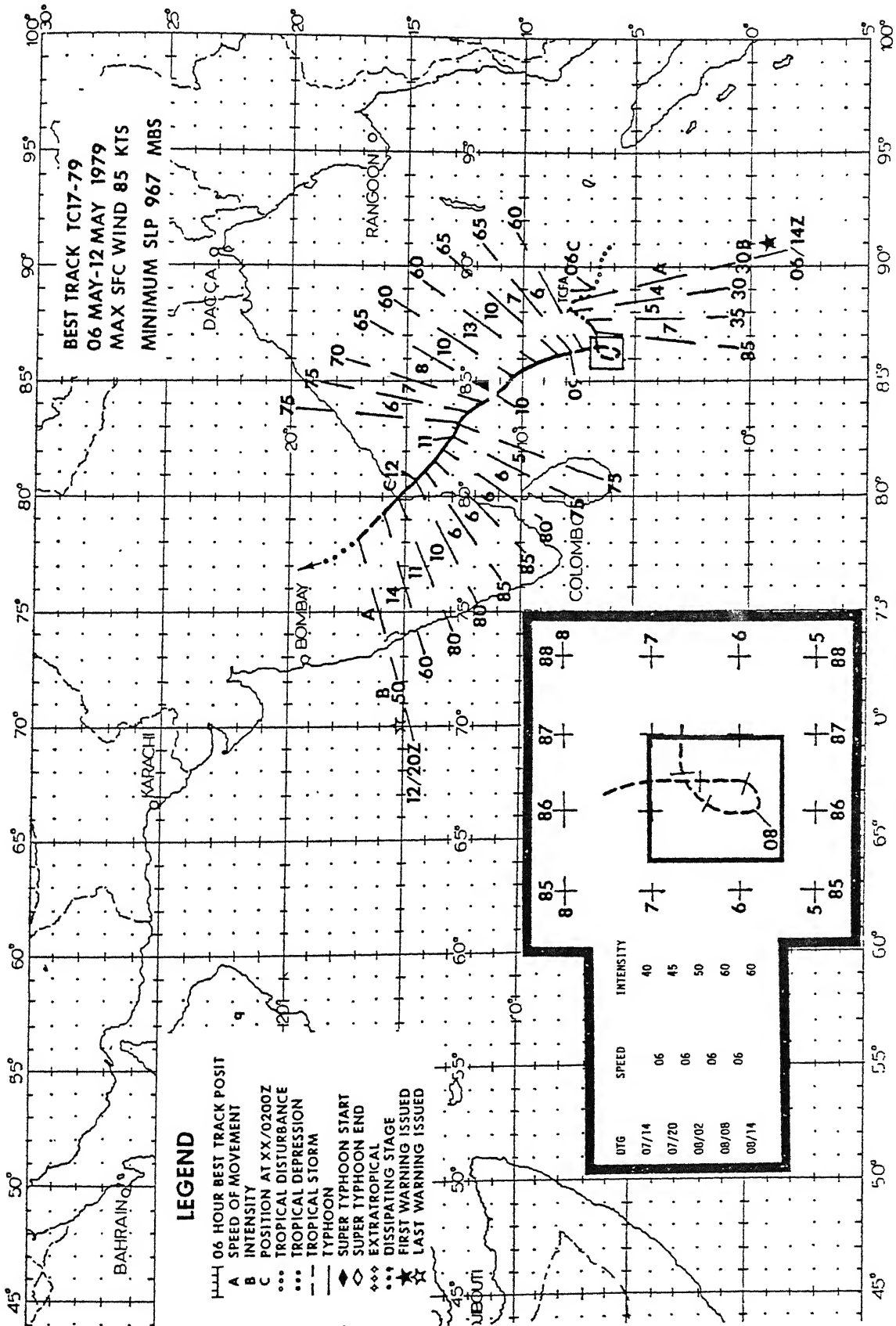


Figure 8: Observed track of the tropical cyclone based on the Guam summaries.

The ECMWF analysis describes a weaker storm than a typical tropical cyclone. The inner rain area of a tropical cyclone is usually confined to an area within the 150 km radius from the storm's center. The strongest winds are nearly always located within this radius from a tropical cyclone. At a horizontal resolution of 50 or 100 km an adequate description of the inner rain area is not possible since this region has to be described by only a few grid points. The ECMWF analysis incorporates high resolution cloud drift winds from the geostationary satellite (GOES Indian ocean). Those winds were almost the only observations over the open oceans in the initial data set. The horizontal resolution of these cloud winds were of the order of one wind every 200 km². Thus the initial data and the final ECMWF analysis were not capable of describing the structure of inner rain area adequately. In spite of the data deficiencies and coarse horizontal resolution the information content of the storm environment was somewhat reasonable. The model thus seems to describe a tropical storm rather than a tropical cyclone. It is the landfall of such a weaker disturbance that is possible to model in the present context.

4.1 Observational aspects of the landfall

Departing from a normal representation of flow fields on pressure surfaces we shall illustrate the horizontal motion field on the so called sigma surfaces. We simply want to look at results for one example of a forecast which are made on sigma surfaces without converting the results to the pressure surfaces, some of which lie below the earth's surface. The sigma to pressure conversion does smooth the

results to some extent and it is of considerable interest to see these uncontaminated results. Here we shall show the circulations at $\sigma = 0.85$, $\sigma = 0.5$ and $\sigma = 0.25$ surface, these closely correspond to the 850, 500 and 250 mb surfaces.

Fig. 9 (a, b, c, d, e, f and g) illustrates the horizontal motion field on the $\sigma = 0.85$ surface based on the observed wind analysis. The salient feature in these charts is the storm whose westward passage starting on May 11 1979 00 UTC through May 14 1979 00 UTC is illustrated here in steps of every 12 hours. The storm's maximum, based on the ECMWF analysis remains close to 20 ms^{-1} for the first 84 hours, thereafter a weakening in its intensity was noted as the storm passed over south-central India. The velocity maximum remains to the east and south-east of the storm center during its westward passage. A large scale counterclockwise circulation to the south of this storm denotes the southern-equatorial trough whose center was located close to 90°E and 10°S during this entire 4 day period. Southwesterly flows extended from the central Bay of Bengal towards Burma throughout this period and the Burmese monsoon had become fairly active. The low level flows over the Arabian sea were mostly from the North-Northwesterly direction, the dry Arabian air is a characteristic feature of the pre-onset (over India).

Of interest to the proposed prediction experiment is the westward motion and the landfall of the tropical cyclone which is reasonably described by these observations. The circulations based on the ECMWF analysis over the middle troposphere are described in the sequence of charts, Fig. 10 (a, b, c, d, e, f and g). These illustrations show

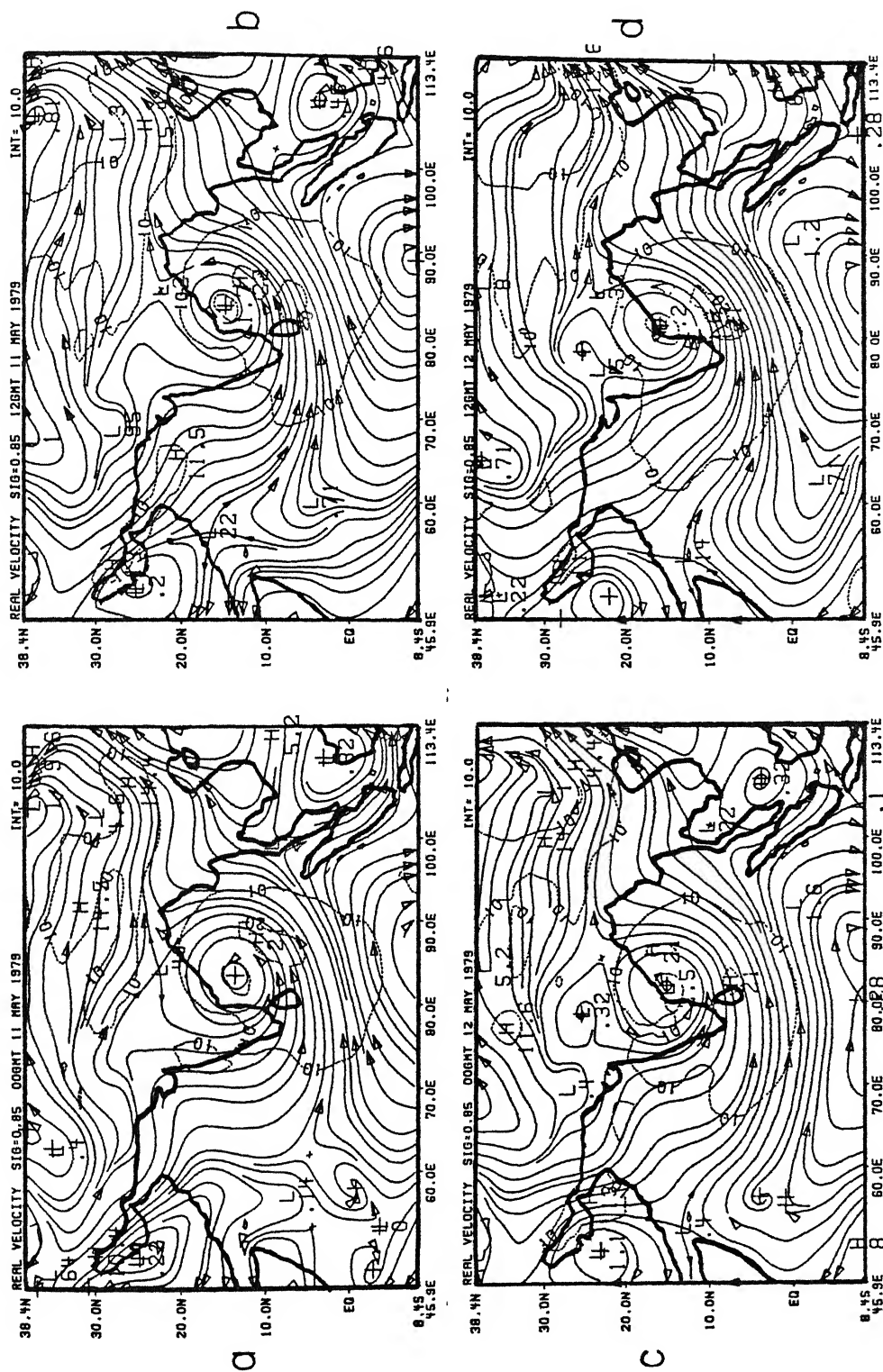
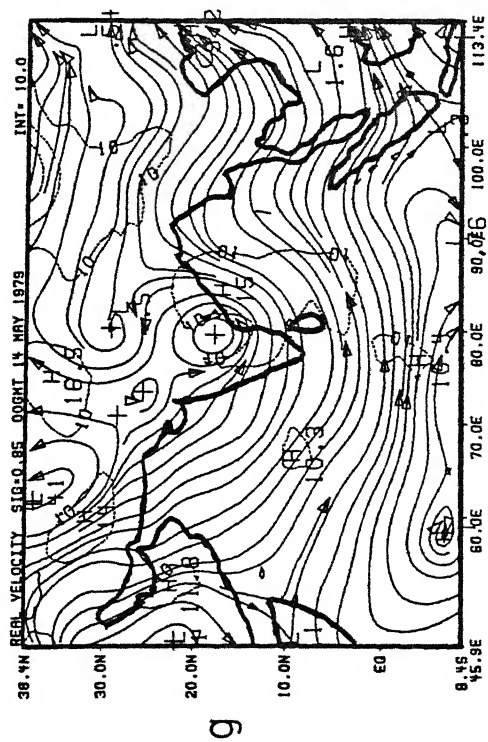
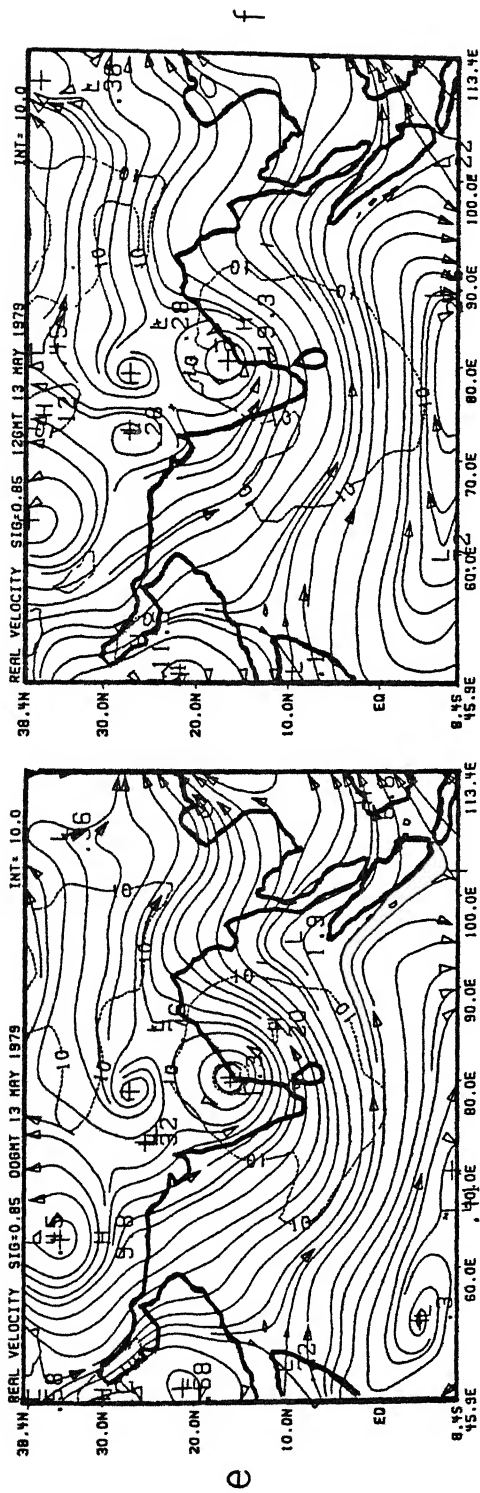


Figure 9 a, b, c, and d: Horizontal motion field on the $\sigma = 0.85$ surface based on the observed wind analysis starting May 11 1979 00 UTC to May 12 1979 1200 UTC.



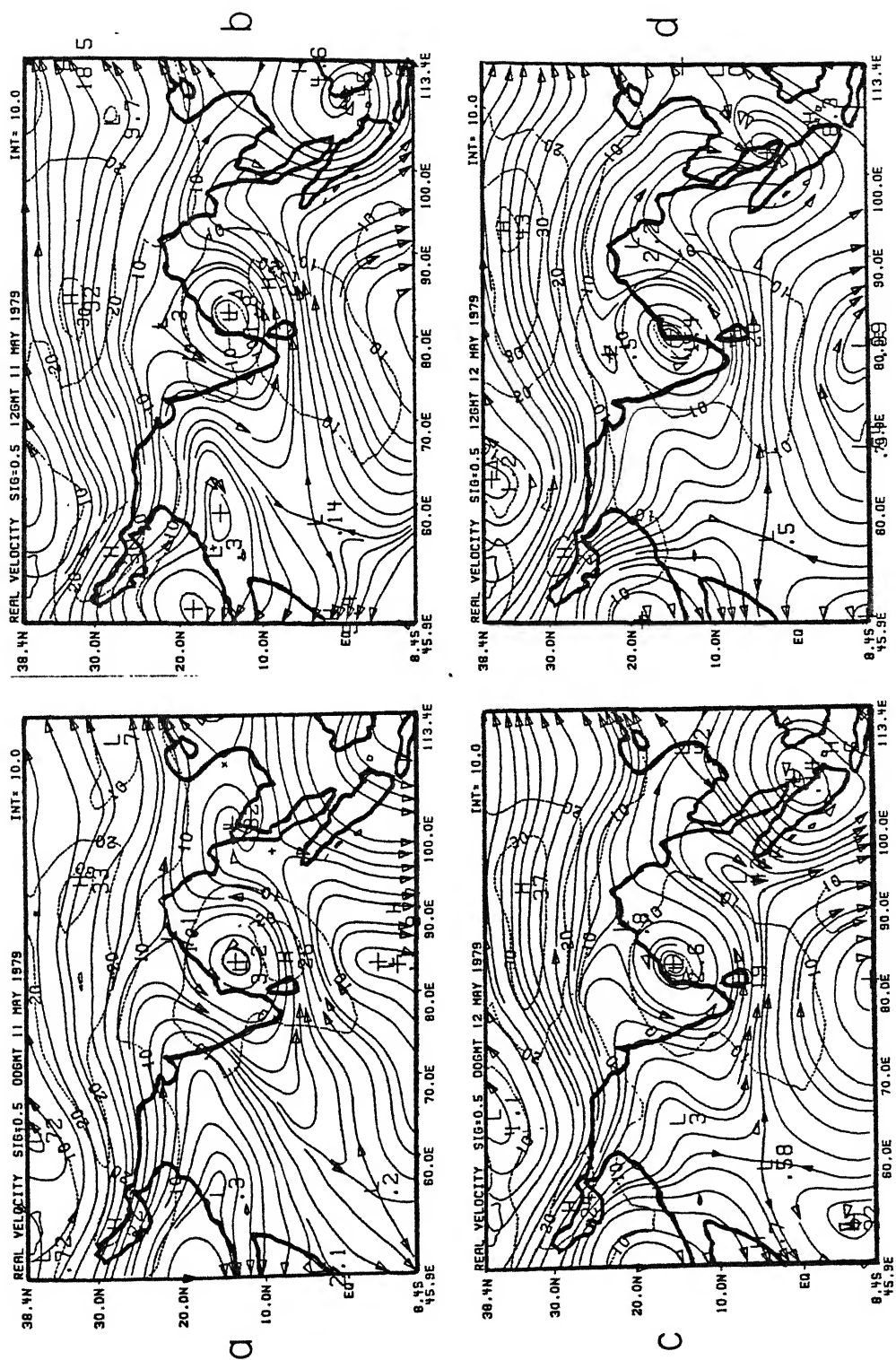


Figure 10 a, b, c and d: Horizontal motion field on the $\sigma = 0.5$ surface based on the observed wind analysis starting May 11 1979 00 UTC to May 12 1979 1200 UTC.

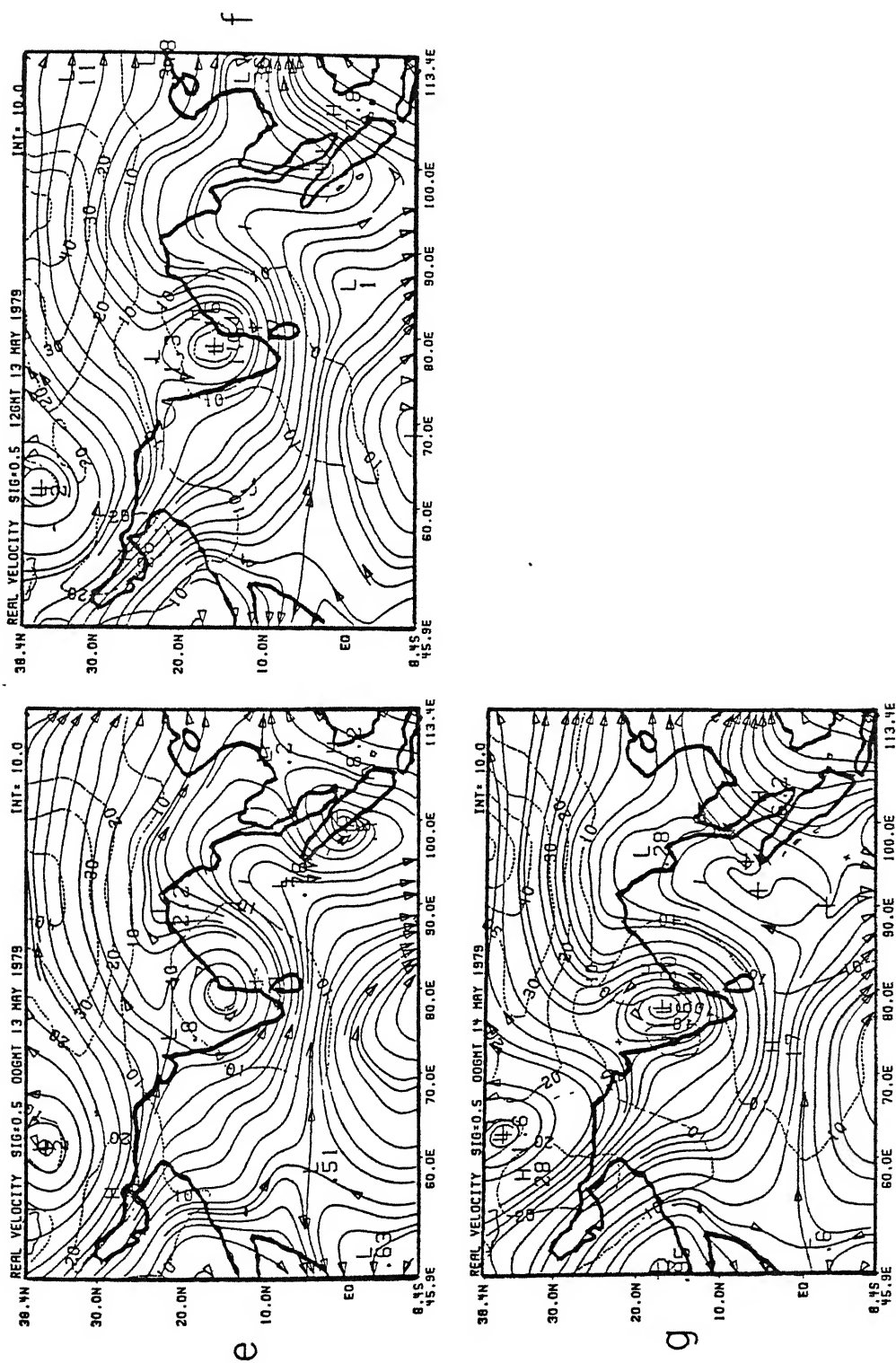


Figure 10 e, f and g: Horizontal motion field on the $\sigma = 0.5$ surface based on the observed wind analysis starting May 13 1979 00 UTC to May 14 1979 00 UTC.

the horizontal motion field on the $\sigma = 0.5$ surface for the period May 11 1979 00 UTC through May 14 1979 00 UTC in steps of 12 hours.

A major feature at the $\sigma = 0.5$ surface is the interaction of a so called westerly trough with the storm's upper level circulation. At the initial time this trough passes through 35N and 60E. It shows a steady eastward propagation and is located near 70E and 20N by the 14th of May. Subsequently this westerly trough axis merges with the upper circulation of the tropical cyclone. During this later stage considerable dry air enters the storm circulation as it weakens. The wind speed at the $\sigma = 0.5$ surface is generally less than 20 ms^{-1} , however the cyclonic circulation is quite well marked. A ridge extends northwards over Burma where the warm monsoonal air resides at this time.

The warm region is where the upper tropospheric anticyclonic circulation is found, which can be seen from the charts at the $\sigma = 0.25$ level after the initial date (see fig. 11a through g). This is the monsoonal upper anticyclone which makes its way to the Tibetan Plateau later in the summer season. The westerly upper trough which was noted at the $\sigma = 0.5$ surface has a stronger intensity at this level ($\sigma = 0.25$). Ahead of this upper trough strong winds of the order of 56 ms^{-1} were noted initially. These strong winds move well ahead of the trough in the subsequent 4-day period. A closer inspection of the flows over the tropical cyclone reveals a pronounced upper level diffluent geometry. That feature was present during this entire sequence. A part of the flow over the tropical cyclone moves northward and eventually eastwards around the upper anticyclone. Another part

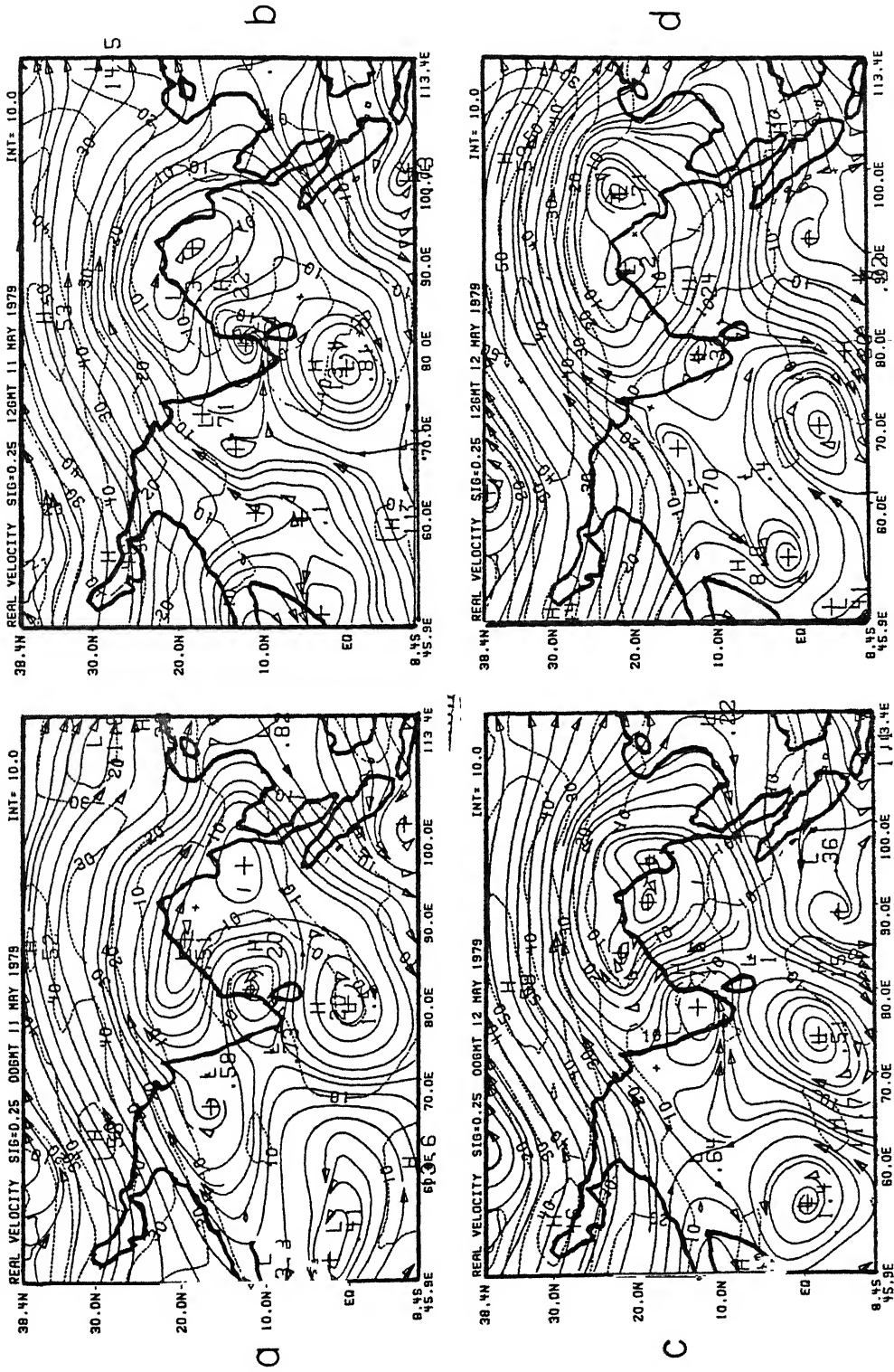
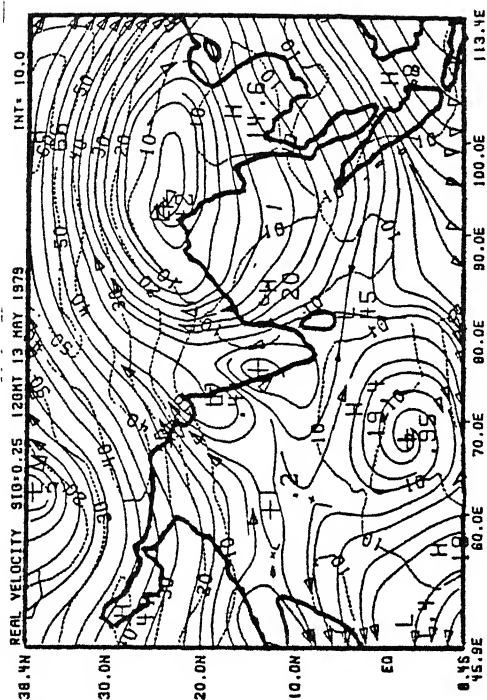
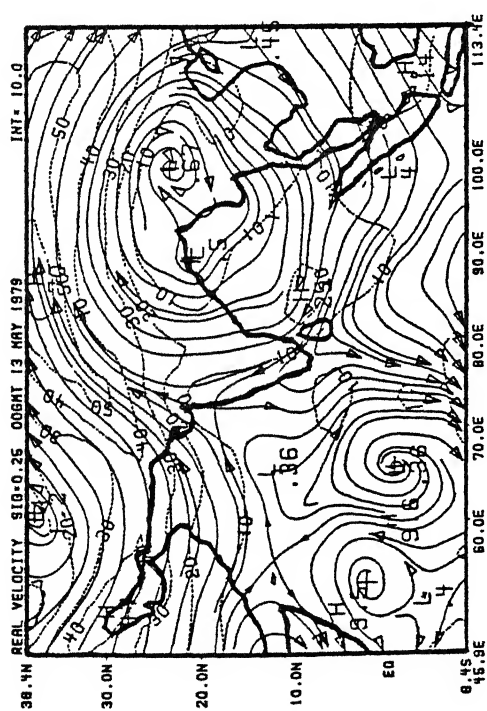


Figure 11 a, b, c and d: Horizontal motion field on the $\sigma = 0.25$ surface based on the observed wind analysis starting May 11 1979 00 UTC to May 12 1979 1200 UTC.



f



g

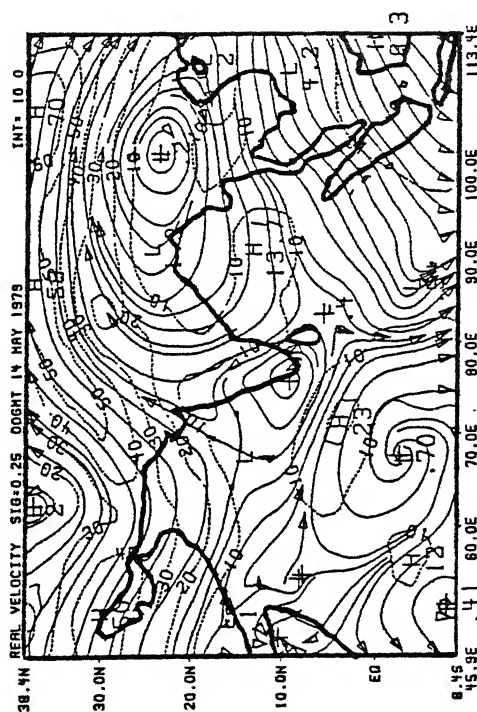


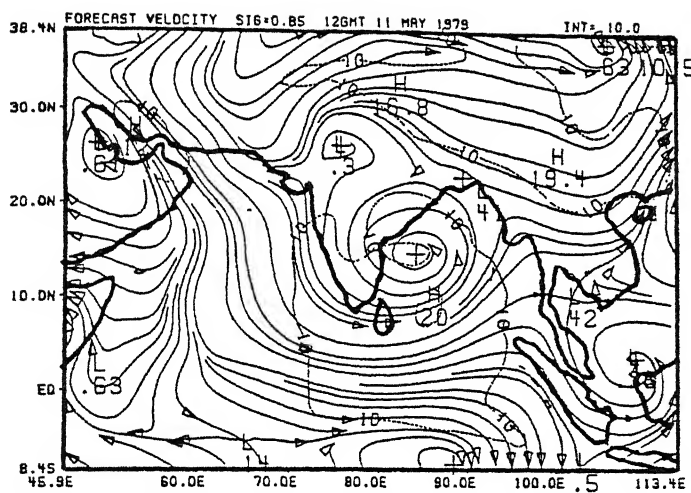
Figure 11 e, f and g: Horizontal motion field on the $\sigma = 0.25$ surface based on the observed wind analysis starting May 13 1979 00 UTC to May 14 1979 00 UTC.

of the same flow moves westwards and eventually southwards around an upper cyclonic circulation located over southern India. These two features i.e., the upper anticyclone over Burma (and Indochina) and the cyclonic circulation over southern India appear to be closely related to the upper circulation of the tropical cyclone.

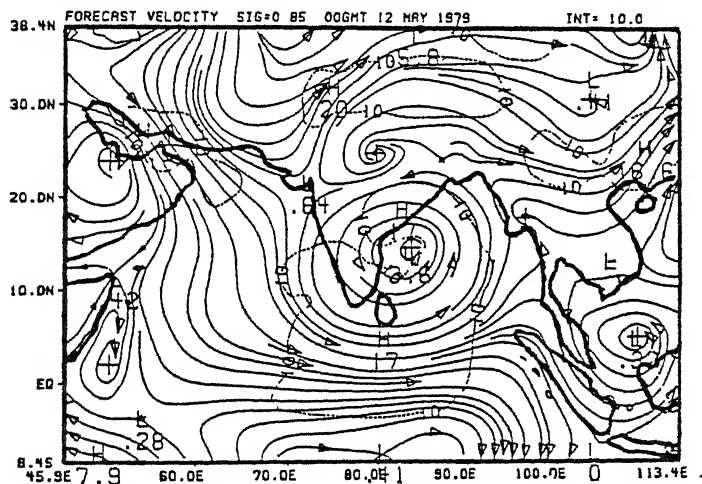
It is of interest to see if several of the aforementioned features can be predicted by the regional model.

4.2 Prediction of the landfall

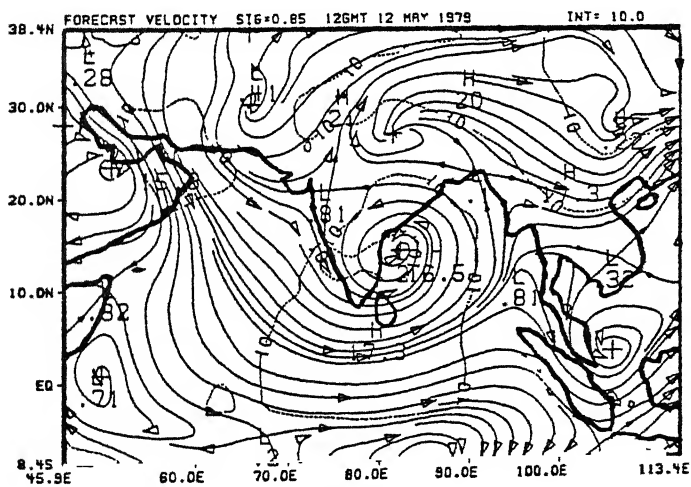
The predicted motion field showed very little error in the first 72 hours. The predicted flow fields closely paralleled those based on observations. We shall first illustrate the predicted fields at the $\sigma = 0.85$ surface (close to 850 mb). A sequence of predicted charts at hours 12, 24, 36, 48, 60 and 72 are shown in fig. 12 (a, b, c, d, e and f) respectively. Nearly all of the circulations features are reasonably placed in the prediction. The landfall of the tropical cyclone occurred 36 hours after the initial time along the southwest coast of India. The model predictions at hour 36 places the center of the storm's circulation at almost the same position on the east coast of India as was noted from the observed fields in fig. 9. The subsequent positions of the storm after landfall at hours 48, 60 and 72 show a remarkable agreement with the observed track. At hour 72 the observed center at $\sigma = 0.85$ was located at roughly 79E and 18N while the predicted position was roughly at 79E and 19N. When the storm was located over land (at hour 72) the strongest winds were located offshore. The observed (i.e., based on ECMWF analysis) wind maxima



a

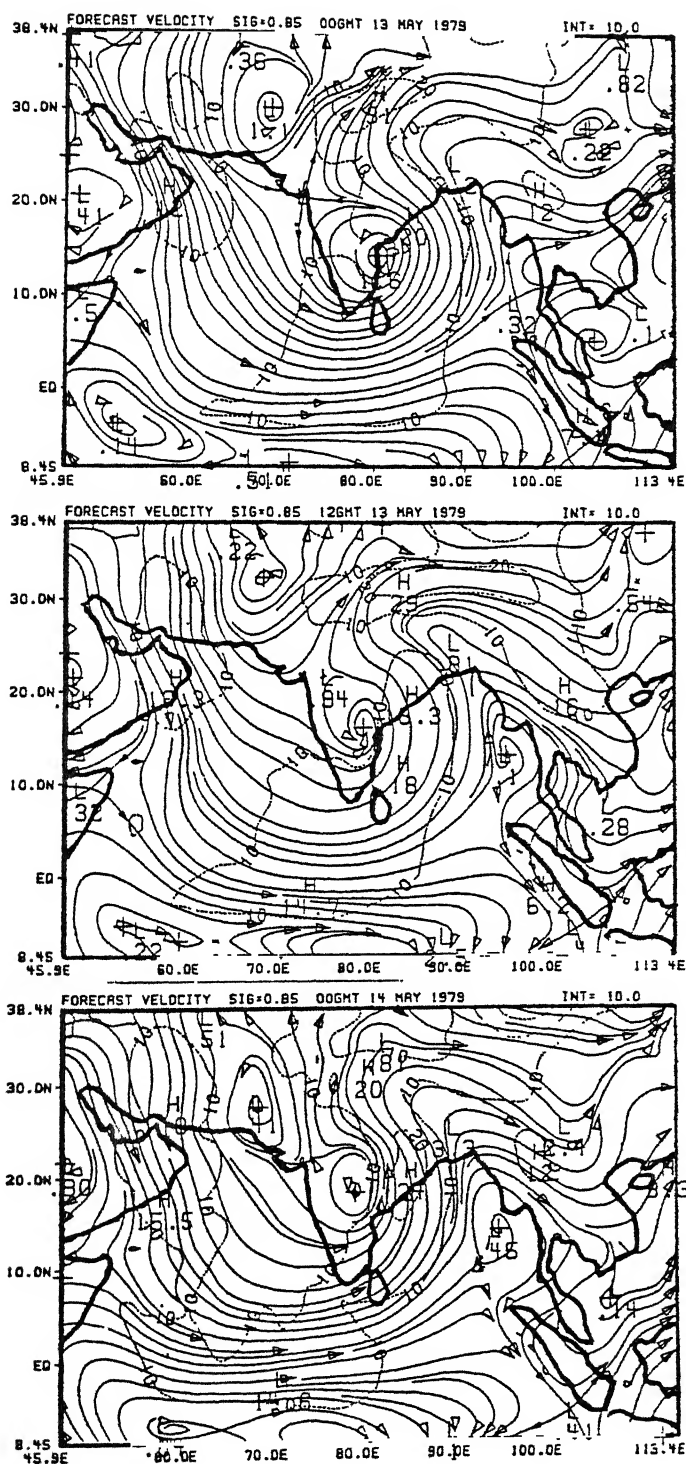


b



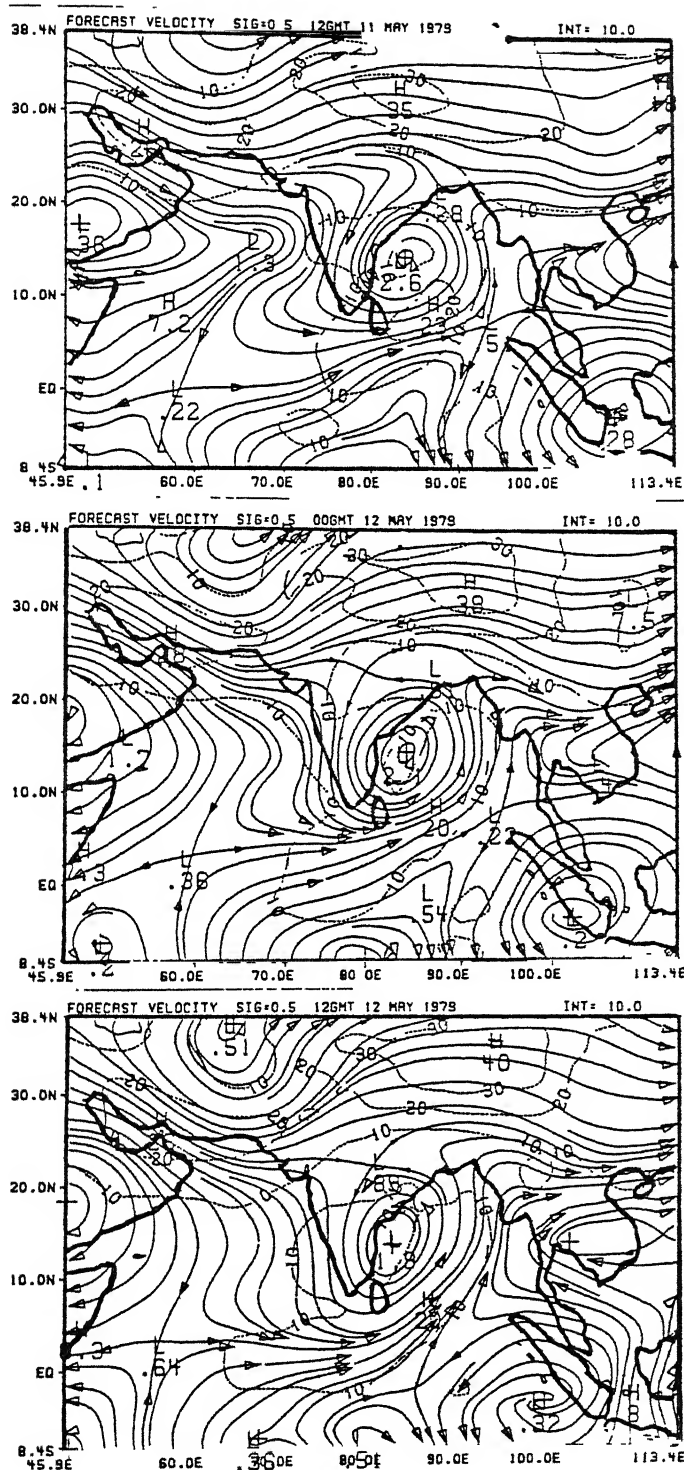
c

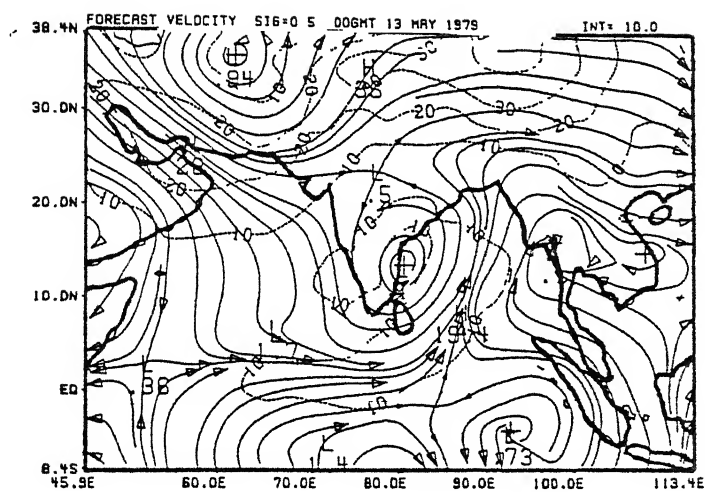
Figure 12 a, b and c: Predicted horizontal motion field on the $\sigma = 0.85$ surface starting May 11 1979 1200 UTC to May 12 1979 1200 UTC.



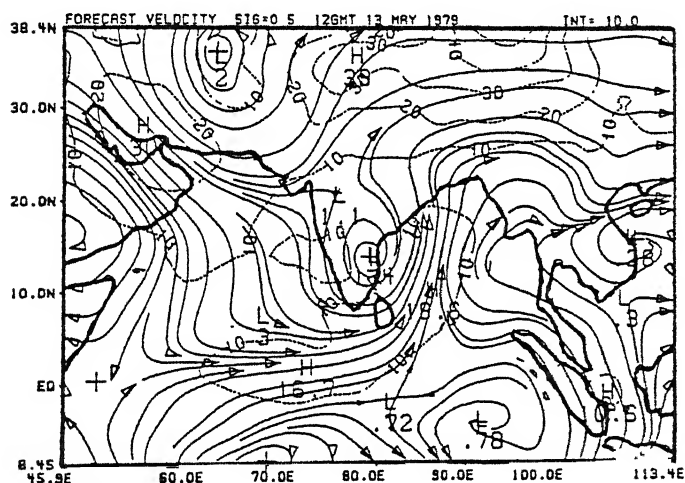
had an intensity around 15 ms^{-1} , the model results show stronger winds of the order of 24 ms^{-1} . The model winds over the ocean were in general stronger. This discrepancy in the intensity of winds may be due to a systematic error of the model. Alternatively, it is possible that the cloud drift winds were not assigned a correct level, thus the analysis may have a bias. The current numerical model does not include the vertical flux of momentum by shallow or deep cumulus clouds, which is another factor that is worthy of consideration.

At the middle troposphere ($\sigma = 0.5$) the storm (based on observed analysis) has a somewhat stronger intensity and is located somewhat westwards of the position at $\sigma = 0.85$. A westward tilt with height has been noted for such disturbance after landfall by Douglas 1987. The tilt is related to the increase of westerly wind with height in such hydrostatic systems. The model prediction at $\sigma = 0.5$ level are illustrated in fig. 13 (a, b, c, d, e and f) at intervals of every 12 hours. Again we note a remarkable success in the prediction of circulations through the 3 day period. The position of the storm at $\sigma = 0.5$ is nearly identical in the observed and the predicted panels at hour 72. The predicted winds are however weaker than the observed, around the storm. Thus it appears that the model prediction of the wind speeds are somewhat overestimated at $\sigma = 0.85$ and are underestimated at $\sigma = 0.5$. To the east of the storm the speed of the southerly flow, for both the observed and the predicted, are around 20 ms^{-1} . The major discrepancy is to the west of the storm where the model's underestimation is clearly apparent at the $\sigma = 0.5$ level. This region, over land does show the presence of many shallow and towering cumuli.

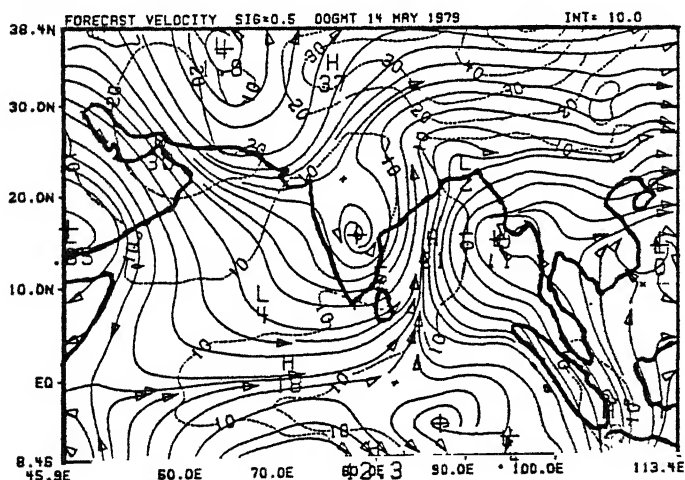




d



e



f

Figure 13 d, e and f: Predicted horizontal motion field on the $\sigma = 0.5$ surface starting May 13 1979 00 UTC to May 14 1979 00 UTC.

It is possible that the addition of cumulus momentum flux in the model might rectify this bias.

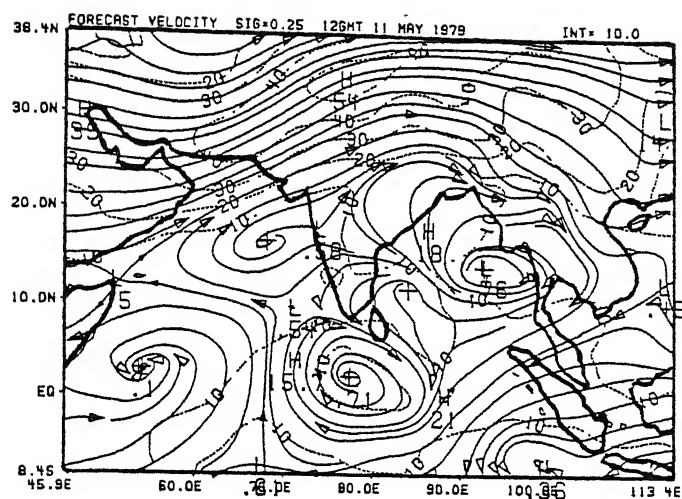
At the $\sigma = 0.25$ level, fig. 14 (a, b, c, d, e, and f), the model handles the eastward movement of the westerly trough remarkably well. The model also handles the strong winds ahead of the westerly trough quite well; the model's maximum winds over this region lie between 40 to 50 ms^{-1} during the first two days, thereafter the model exhibits a further strengthening of the winds reaching almost 66 ms^{-1} by 72 hours. Over this region near 35N and 75E, the observed winds at $\sigma = 0.25$ level were in excess of 50 ms^{-1} . The predicted winds at the jet stream level seem to be somewhat too high - although this region of the western Tibetan Plateau does not have adequate upper air observations. The upper anticyclone over Burma is very well represented by the predictions. The strong westerly winds to its north around 110E and 37N compare very closely - the observed maximum wind is around 70 ms^{-1} while the predicted value is around 69 ms^{-1} .

Overall, the predicted flow fields at all of these levels show a marked agreement with observations.

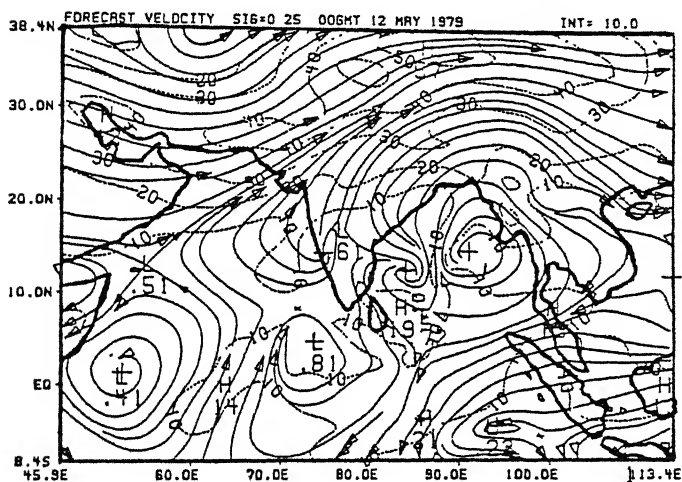
4.3 Rainfall prediction:

The total precipitation in the model comes from the parameterization of cumulus convection and from the disposition of super-saturation. The latter is here identified as the non-convective contribution.

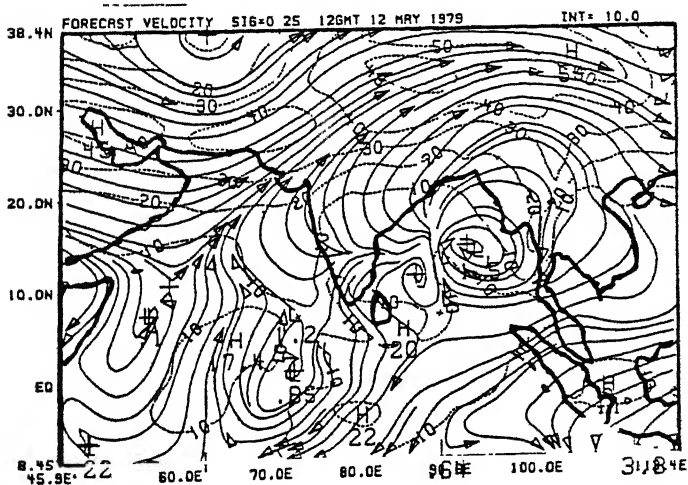
A recent atlas of daily rainfall rates, Krishnamurti et al.



a

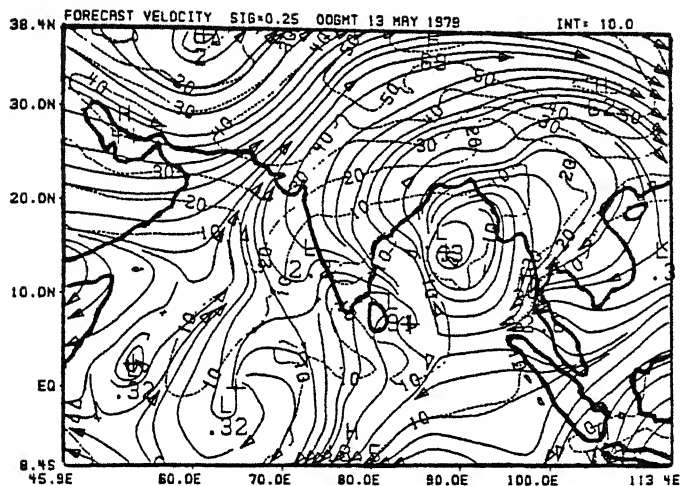


b

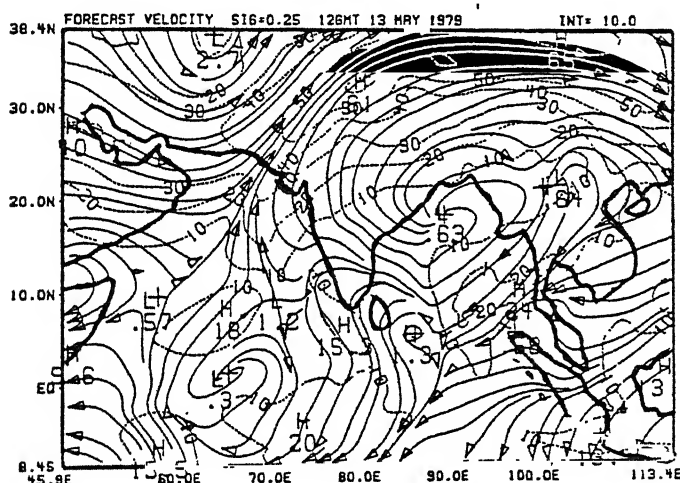


c

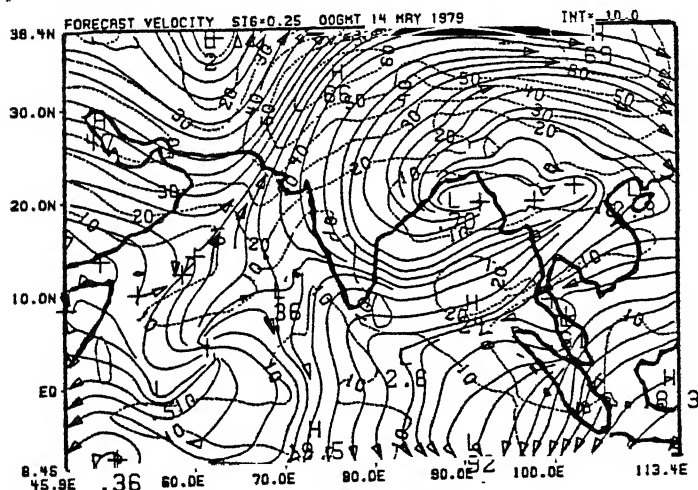
Figure 14 a, b and c: Predicted horizontal motion field on the $\sigma = 0.25$ surface starting May 11 1979 1200 UTC to May 12 1979 1200 UTC



d



e



f

Figure 14 d, e and f: Predicted horizontal motion field on the $\sigma = 0.25$ surface starting May 13 1979 00 UTC to May 14 1979 00 UTC.

(1983c), describes a procedure for the estimation of rainfall rates from a mix of satellite and raingauge observations. The FGGE IIc data collection includes a very large archive of raingauge observations. Well over 3,000 observations/day provide daily rainfall totals over a MONEX domain (30E to 150E, 30S to 40N). In view of these practical limitations, TIROS N infrared radiance data was used. This is a polar orbiting sun synchronous satellite which makes roughly 2 local passes a day with an equator crossing around 3AM and 3PM local time. The raingauge data are available on 24 hourly intervals at 00 UTC each day. The method of analysis consisted in first performing a statistical regression among the satellite radiances, its time rate of change and the raingauge rainfall totals over 24 hourly periods. For this purpose all of the satellite observations were collocated onto the raingauge sites via a space-time interpolation. The time synchronization required the use of cubic splines, and thus the time rate of change of radiances for this resolution represents an integrated representation of the growth (or decay) of large cloudy areas. Although such a use of data sets from polar orbiting satellites has not been made previously, it appears quite promising for NWP because of the space-time scales. The next step in this analysis is the construction of a first guess rainfall field for objective analysis from the aforementioned regression coefficients. This is done using the daily grid point values of the radiances and their time rate of change. The next step is an objective analysis of the raingauge rainfall field. This makes full use of all available raingauge data sets from the FGGE IIc data.

A comparison of the 24 hour precipitation amounts based on the satellite and raingauge with those obtained from the two versions of the model are presented in figs. 15, 16 and 17 (a, b, c). In each of these figures panel (a) shows the 'observed' 24 hourly total and the other two panels show the predicted estimates. In all of these charts the interval of analysis is 10 mm/day. The respective totals in figs. 15, 16 and 17 (a, b, c) are for the hours 0-24, 24-48 and 48-72. The panels (b) in these illustrations are based on a terrain tabulation that was obtained on a 2.5° latitude/longitude grid and interpolated on to the model resolution of 0.9375° latitude/longitude. The panels (c) illustrate the results from using terrain tabulations from a high resolution U.S. Navy data set on the resolution of the model. In general the model-based rain fall rates during the landfall of the tropical cyclone are weaker and spread out over a larger horizontal area. This discrepancy is perhaps related to the resolution. Although the arrival of heavy rain is reasonably predicted the position errors are still somewhat too large. In the first 24 hours the 'observed' coastal rainfall over Tamil Nadu was quite large compared to the predicted estimates. The model places a center of heavy rain over the open ocean. Although the circulation forecasts seemed fairly accurate during this period. A number of factors can contribute to this discrepancy. We believe that the initial humidity analysis over the open oceans is based entirely on the analysis-forecast cycle of ECMWF. Use of satellite radiance data to improve the humidity analysis following Krishnamurti *et al.* (1984) and Cadet (1983) can provide some improvement. The model prediction overestimates the strong southerly flows to the east of the tropical cyclone. That may also

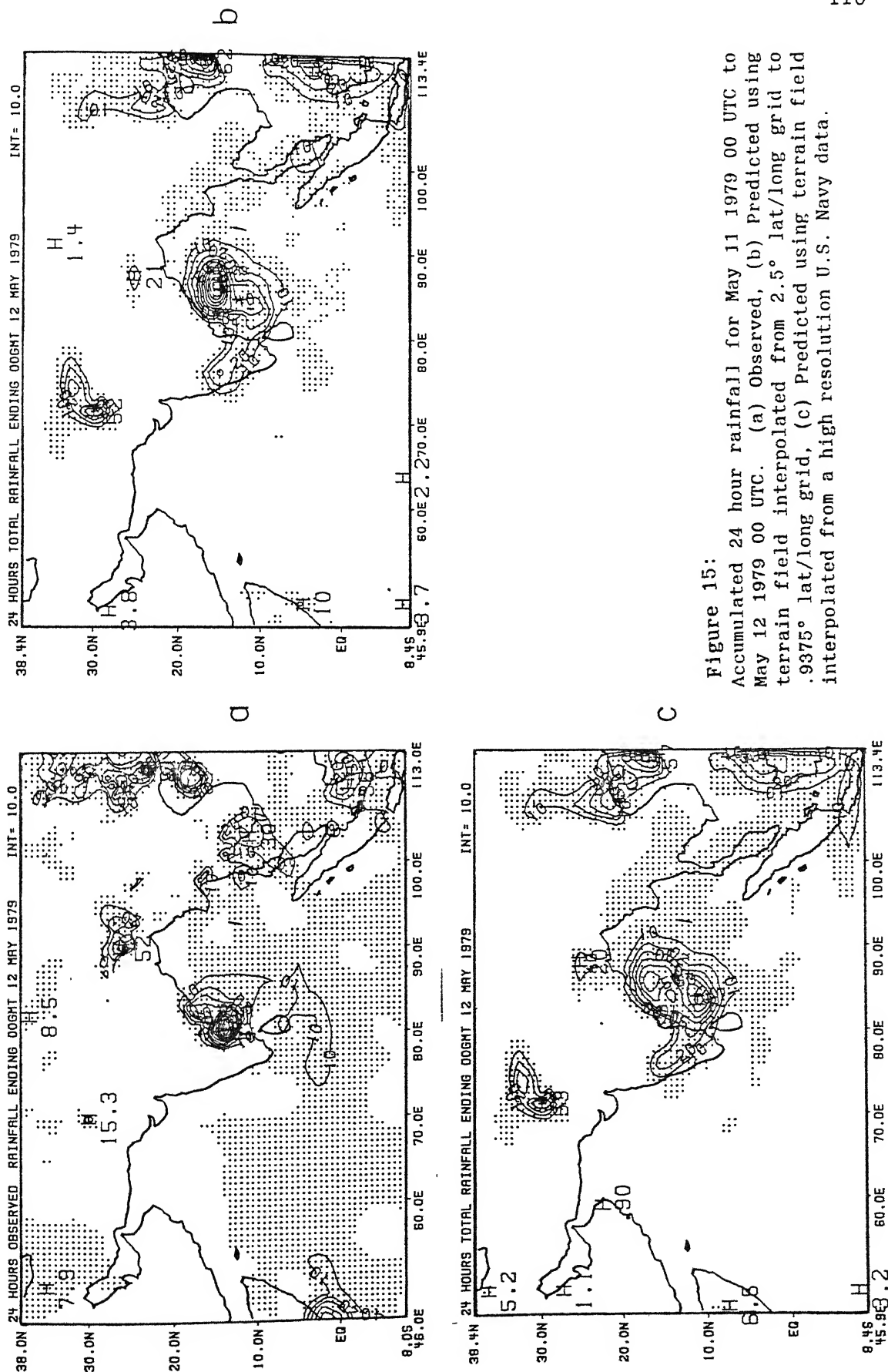
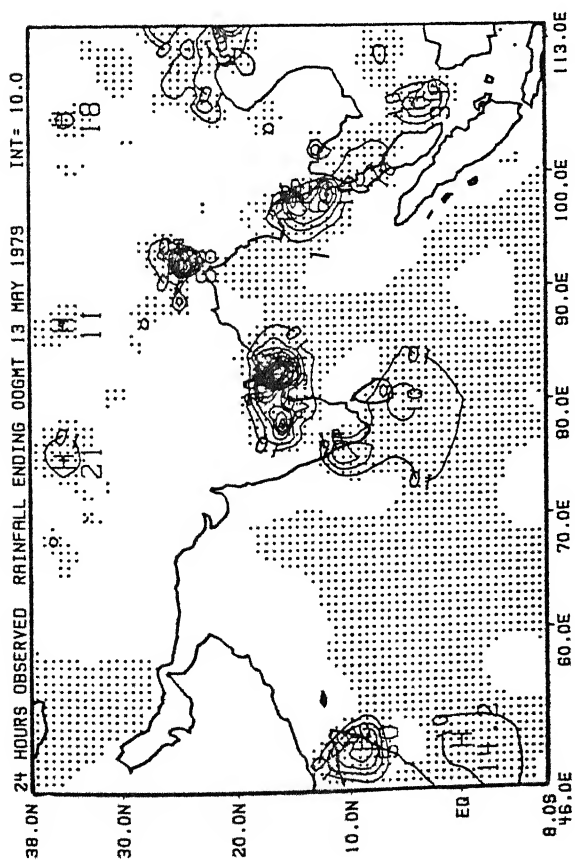


Figure 15:

Accumulated 24 hour rainfall for May 11 1979 00 UTC to May 12 1979 00 UTC. (a) Observed, (b) Predicted using terrain field interpolated from 2.5° lat/long grid to .9375° lat/long grid, (c) Predicted using terrain field interpolated from a high resolution U.S. Navy data.



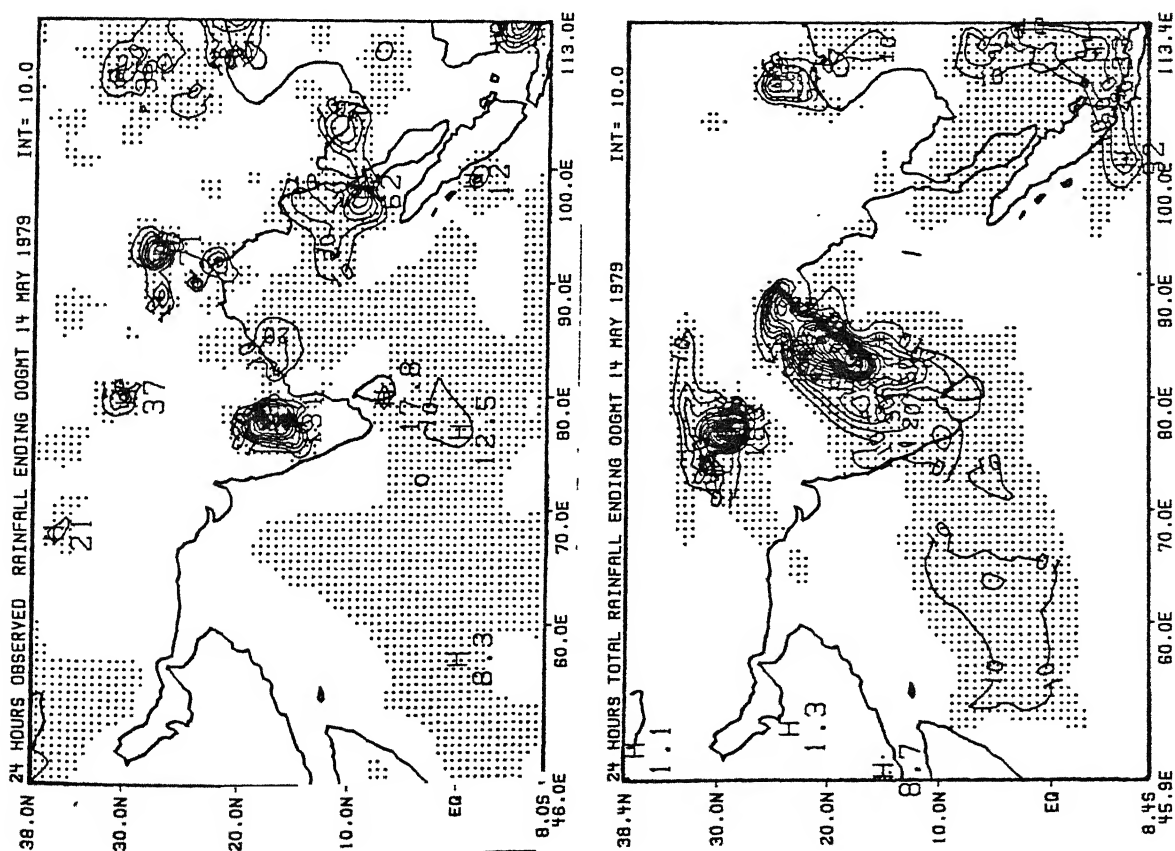


Figure 17:

Accumulated 24 hour rainfall for May 13 1979 00 UTC to May 14 1979 00 UTC. (a) Observed, (b) Predicted using terrain field interpolated from 2.5° lat/long grid to .9375° lat/long grid, (c) Predicted using terrain field interpolated from a high resolution U.S. Navy data.

have been an important factor for the discrepancy in the rainfall over the ocean. The cyclonic shear region is shifted eastward, although the circulation center is reasonably placed. The stronger convection on the cyclonic shear side of the predicted flows is a consistent computational result. This region also has stronger mass and moisture convergence. Better resolution and initialization procedures, such as dynamic relaxation (Nudging), may be needed to overcome some of these problems. The forecasts of the rainfall rates for hours 24-48 and 48-72 are quite reasonable, they show the landfall of a hurricane with heavy rain occurring over southern India, however as before the quality of forecast (district by district) still requires much improvement. The use of a finer resolution terrain (panels (c) of figs. 15, 16 and 17) appears to shift the rainfall maximum somewhat southwards initially when the storm center is over the open ocean. As the storm approached the Bay of Bengal Coast the interaction of the lower level circulations with the eastern Ghats results in an enhancement of rainfall total along the northern coasts of the peninsular.

CHAPTER 5

PARAMETERIZATION OF GROUND WETNESS

The interaction between the atmosphere, the land surface and the biosphere plays an important role in determining the weather through radiation, heat, moisture and momentum exchanges. For more than a decade, evidence has been accumulating from climate and forest model experiments that the atmosphere is sensitive to variations in processes at the land surface. The experiments of Charney (1975) and Charney et al. (1977) demonstrated considerable sensitivity to albedo and the parameterization of evaporation respectively. One essential factor in the surface evaporation estimation is the parameterization of soil moisture. Many soil moisture sensitivity experiments (Walker and Rountree, 1977; Shukla and Mintz, 1982; Yeh et al., 1984; Sud and Fennessy, 1984; Sud and Smith, 1985b; Kitch et al., 1988; Sud and Molod, 1988) have confirmed the importance of its parameterization in climate models. The general conclusion of these experiments is that a reduced soil moisture causes a reduction in evaporation which in turn decreases rainfall. Accurate initial conditions were shown to be important in the context of predictions on timescales from a few hours or days (Walker and Rountree, 1977; Rountree and Bolton, 1983) up to several months (Carson and Sangster, 1981). It is evidently important

to represent land surface processes realistically; this requires an adequate parameterization scheme, including specification of suitable data sets of vegetation, soil type and initial soil moisture.

At the earth's surface available (net radiative) energy is partitioned between three fluxes: 1. Surface soil heat flux, 2. Evaporative or latent heat flux and 3. Sensible heat flux. The balance of these fluxes with the net radiative fluxes determines the changes in surface temperature. To estimate the evaporative flux the knowledge of available soil moisture is necessary. Soil moisture also has a large impact on the thermal properties of land surface such as heat capacity and thermal conductivity.

Soil moisture/Ground wetness is a difficult parameter to estimate as it depends on the evaporation, rainfall, snowmelt, infiltration, surface runoff as well as vegetation. For a layer of ground between depths z and $z + \delta z$, neglecting horizontal sub-surface transfer of water the generalized equation for soil moisture change can be written as

$$\frac{\partial m^S(z)}{\partial t} = - \frac{\partial M(z)}{\partial z} + N(z) \quad (5.1)$$

where $m^S(z)$ = soil moisture at depth z

$M(z)$ = moisture flux at depth z

and $N(z)$ = source/sink term.

At the surface, moisture flux is given as

$$M(0) = -E(0) + (P + M_s - Y(0)) \quad (5.2)$$

where E = evapotranspiration

P = precipitation rate

M_s = snowmelt

and Y = surface runoff.

Ground wetness parameter can be defined as fractional soil moisture at the surface:

$$GW = \frac{m^s(0)}{m^s_{\max}} \quad (5.3)$$

where m^s_{\max} is the maximum value (field capacity) of $m^s(0)$.

To parameterize the above many simplifications are made in the present day models. One of the widely used methods in the climate models was first introduced by Manabe (1969a) resulting from Soviet observational studies by Romanova (1954). Romanova found that for plains and forest regions most of the moisture change takes place in the top one meter of soil, which usually encompasses the root zone of moist vegetation. Manabe's scheme uses one layer water budget equation which includes a simple parameterization for evaporation, precipitation, surface runoff and snowmelt. Field capacity is taken constant for all land points. The ground wetness sensitivity experiments mentioned earlier and others reviewed by Mintz (1984), use relatively simple parameterization schemes and lack geographical variations of most surface characteristics. More complex schemes have been developed in recent years which include the geographic variations of albedo, roughness length and root depth (Hansen et al., 1983; Dickinson, 1984; Sellers et al., 1986).

All leading numerical regional models use very simple parameterization for the ground wetness. NCAR/Penn State limited area model, JMA Tokyo regional spectral model and ECMWF limited area model use

climatological specified values for ground wetness. French weather service limited area model uses one layer predictive equation for soil moisture. In the present formulation of FSU regional model we use one of the following empirical relations for ground wetness.

$$GWM1 = \frac{(\alpha_{\max} - \alpha)}{(\alpha_{\max} - \alpha_{\min})} (1 - RH) \quad (5.4)$$

or

$$GWM2 = 0.85 [1.0 - \exp\{-200.0(0.25 - \alpha)^2\}] \quad (5.5)$$

where α is surface albedo and RH is relative humidity for the nearest layer to the ground. Climatological specified values of ground wetness or given by some empirical relations like equations (5.4) and (5.5) do not provide the change in soil moisture due to rainfall and other moisture fluxes at the surface. If a predictive equation is used for GW (Ground Wetness) as in French weather service model, one faces the problem of getting reliable initial values for the ground wetness besides the difficulties of parameterizing the various fluxes involved.

In the present chapter we propose a new scheme for ground wetness parameterization. The procedure can be used to obtain the initial values for the ground wetness to initialize the model. Further, it provides an expression for ground wetness which depends on the rainfall and other large scale surface parameters. The following section describes the proposed scheme. In the last section 5.3 some results of the new scheme are presented and the results are compared with the old scheme.

5.1 The Parameterization Scheme:

The scheme is based on the moisture budget analysis described by Haiyan He et al. (1987). First, the surface evaporation is estimated from vertically integrated apparent moisture sink (defined later in this section) and the rainfall rates. Using this evaporation rate surface energy balance is solved for the surface temperature. Thereafter surface evaporation and temperature provide ground wetness using similarity theory.

The moisture continuity equation in pressure coordinate system is given by:

$$\frac{\partial q}{\partial t} + \vec{V} \cdot \nabla q + \omega \frac{\partial q}{\partial p} = e - r \quad (5.6)$$

where q = specific humidity,

(\vec{V}, ω) = horizontal wind vector and vertical velocity $(\frac{\partial p}{\partial t})$

e = vertical diffusion of moisture flux

$$= g \frac{\partial F_Q(p)}{\partial p} \quad (5.7)$$

where $F_Q(p)$ = vertical moisture flux.

and r = moisture sink term due to rainfall.

Upon integrating equation (5.6) for the entire vertical column

and multiplying by L/g we obtain

$$\frac{L}{g} \int_{p_T}^{p_S} \left(\frac{\partial q}{\partial t} + \vec{V} \cdot \nabla q + \omega \frac{\partial q}{\partial p} \right) dp = L [F_Q(p_S) - F_Q(p_T)] - \frac{L}{g} \int_{p_T}^{p_S} r dp \quad (5.8)$$

$$\text{or} \quad - \frac{1}{g} \int_{p_T}^{p_S} Q_2 dp = LF_{QS} - LR \quad (5.9)$$

where

L = latent heat of vaporization

p_s = surface pressure

p_T = pressure at the top of the column taken as 125 mb

Q_2 = apparent moisture sink

$$= -L \left(\frac{\partial q}{\partial t} + \mathbf{V} \cdot \nabla q + \omega \frac{\partial q}{\partial p} \right) \quad (5.10)$$

R = Precipitation rate per unit area at the surface

F_{QS} = Surface evaporation per unit area

$$= F_Q(p_s)$$

$F_Q(p_T)$ = vertical moisture flux at the top of the atmosphere

which is assumed to be zero.

We define LF_{QS} = Surface latent heat flux

$$\equiv F_L^Q$$

Equation (5.9) can be rewritten to provide surface latent heat flux as:

$$F_L^Q = LR - \frac{1}{g} \int_{p_T}^{p_s} Q_2 dp \quad (5.11)$$

Equation (5.11) is used to calculate F_L . For computing Q_2 observed data for horizontal wind components (u, v) and specific humidity FGGE level II B data is used. The vertical p -velocity ω is obtained from the horizontal divergence by integrating the continuity equation

$$\frac{\partial u}{\partial x} + \frac{\partial v}{\partial y} + \frac{\partial \omega}{\partial p} = 0 \quad (5.12)$$

with the surface boundary condition on ω at $p = p_s$ expressed by:

$$\omega = \omega_s = -g \rho_s \left(\frac{u_s}{a \cos \phi} \frac{\partial H}{\partial \lambda} + \frac{v_s}{a} \frac{\partial H}{\partial \phi} \right) \quad (5.13)$$

This boundary condition implies that the surface flow is parallel

to the surface terrain.

$H = H(\lambda, \phi)$ surface terrain, where λ is the longitude and ϕ is the latitude.

u_s, v_s = surface zonal and meridional component of \vec{V}

Assuming that the motion is approximately adiabatic near the tropopause, an additional condition is imposed on the vertical velocity ω at p_T (≈ 125 mb) from the thermodynamic equation i.e.:

$$\omega = \omega_T = \frac{-\left(\frac{\partial \theta}{\partial t} + \vec{V} \cdot \nabla \theta\right)}{\frac{\partial \theta}{\partial p}} \quad (5.14)$$

where θ is the potential temperature. Using these constraints the horizontal divergence is corrected as:

$$D^{\text{corrected}} = D^{\text{original}} + \frac{\omega_T - \omega_s - \int_{p_T}^{p_s} D^{\text{original}} dp}{p_s - p_T} \quad (5.15)$$

After obtaining F_L , we make use of the surface energy balance and similarity theory to compute ground wetness parameter (GW). To improve the accuracy of the solution we adapt a soil-slab model for surface energy balance. Following Blackadar (1979) let us consider a thin surface soil layer at the surface temperature T_g^Q in thermal contact with the deeper layer, which is assumed to be acting as a heat reservoir at constant temperature T_m :

$$c_g \frac{\partial T_g^Q}{\partial t} = S_w^\downarrow (1-\alpha) + (L_w^\downarrow - \sigma T_g^Q) - F_s^\uparrow - F_L^\uparrow - c_g K_m (T_g^Q - T_m) \quad (5.16)$$

The first right hand side term of the above equation is the net short

wave radiation flux into the ground. The second term is the net longwave radiation flux into the ground. Third and fourth terms are the upward sensible heat and latent heat fluxes. The last term provides the flux due to conduction between the upper thin soil layer and the lower substrata.

α = surface albedo

C_g and K_m are given by the following expressions

$$C_g = 0.95 (\lambda c_s / 2\omega)^{1/2} \quad (5.17)$$

$$K_m = 1.18\omega \quad (5.18)$$

where

c_s = Heat capacity of the soil per unit volume

$$= \rho_g c_{sg}$$

c_{sg} is the specific heat capacity of the soil and ρ_g is the soil density.

ω = angular velocity of the earth's rotation

λ = thermal conductivity of the soil.

Heat capacity of the soil c_s and thermal conductivity of the soil λ are taken as functions of the moisture present in the soil.

For the present formulation, we have assumed c_s and λ to be linear functions of the soil moisture/ground wetness parameter GW as:

$$c_s = (1.42 + GW*1.68)*10^6 \text{ Jm}^{-3}\text{k}^{-1} \quad (5.19)$$

$$\lambda = (0.25 + GW*1.33) \text{ Wm}^{-1}\text{k}^{-1} \quad (5.20)$$

F_s (surface sensible heat flux) in equation (5.16) is calculated using the following expression

$$F_{s\uparrow} = \rho C_H C_P \left| \vec{V}_2 \right| (T_2 - T_g) \quad (5.21)$$

where T_2 is the temperature at a chosen level within the constant flux

layer at the surface. \vec{V}_2 is the horizontal wind vector at the same level. C_p is the specific heat. C_H is calculated using similarity theory discussed in section 3.4. The expression for C_H in stable and unstable surface layers are given by equations (3.53) and (3.62). From section 3.4 it is evident that for calculating C_H knowledge of surface temperature is required. Therefore equation (5.16) is solved iteratively along with the similarity theory. S_w and L_w are calculated using the radiation parameterization described in chapter 3. For F_L in equation (5.16) F_L^Q obtained by the expression (5.11) is used. Since c_s and λ depend on the ground wetness, climatological values for GW are used as a first guess. For the subsequent iterations GW is updated using the procedure given below.

Once the surface temperature (T_g^Q) is obtained surface saturation specific humidity q_{gs} is computed using Tetten's formula. Using this surface temperature stability dependent C_H and C_Q are calculated and ground wetness parameter GW is estimated using the following formula:

$$GW^Q = \frac{1}{q_{gs}} \left[q_2 - \frac{F_L^Q}{\rho C_{QL} |\vec{V}_2|} \right] \quad (5.22)$$

This expression for GW is obtained by writing latent heat flux F_L similar to the expression for F_s given by equation (5.21).

$$F_L = \rho C_{QL} |\vec{V}_2| (q_2 - GW * q_{gs}) \quad (5.23)$$

The above equation is solved for GW and F_L is replaced by F_L^Q given by equation (5.11). This generates a large data base for the ground wetness from the vertically integrated moisture budget. This GW is next expressed as a function of various large scale variables. A selective

second order regression scheme is used to provide GW as a function of average 24 hour accumulated rainfall rate, surface temperature, earth's surface albedo and terrain as

$$\begin{aligned} GW^{New} = & a_0 + a_1R + a_2T_g + a_3\alpha' + a_4H' + a_{11}R^2 + a_{22}T_g^2 \\ & + a_{33}\alpha'^2 + a_{44}H'^2 + a_{12}RT_g + a_{13}R\alpha' + a_{14}RH' \\ & + a_{23}T_g\alpha' + a_{24}T_gH' + a_{34}\alpha'H \end{aligned} \quad (5.24)$$

The regression coefficients are given in Table 8. In the above equation R is the 24 hour rainfall divided by 24. T_g is the surface temperature and α' and H' are scaled albedo and scaled terrain height given by:

$$\alpha' = \frac{(\alpha_{max} - \alpha)}{(\alpha_{max} - \alpha_{min})} \quad (5.25)$$

and

$$H' = \frac{(H_{max} - H)}{(H_{max} - H_{min})} \quad (5.26)$$

where α_{max} , H_{max} are the maximum values of albedo and terrain. Similarly α_{min} and H_{min} are the minimum values of albedo and terrain fields. As it is evident from Table 8 GW has a strong dependence on rainfall. The dependence on terrain field is mainly to account for the runoff due to slope of the ground. Ground wetness is closely related to the surface temperature also.

To carry out the above scheme FGGE data for 11 May 1979 to 16, May 1979 and 20 June 1979 to 28 June 1979 for horizontal winds, relative humidity, temperature geopotential height at all standard pressure levels is used. Daily rainfall rates for the above mentioned period are extracted from Summer Monex experiment data. The domain chosen is 2.8° - 38.4° N and 45.9° - 113.4° E. The above mentioned 15 days

Table 8

The regression for coefficients GW

a_0	3.131	a_4	-.329
a_1	0.484	a_{11}	-.130
a_2	-0.009	a_{33}	.162
a_3	0.143	a_{44}	.349

a_{12} , a_{13} , a_{14} , a_{23}

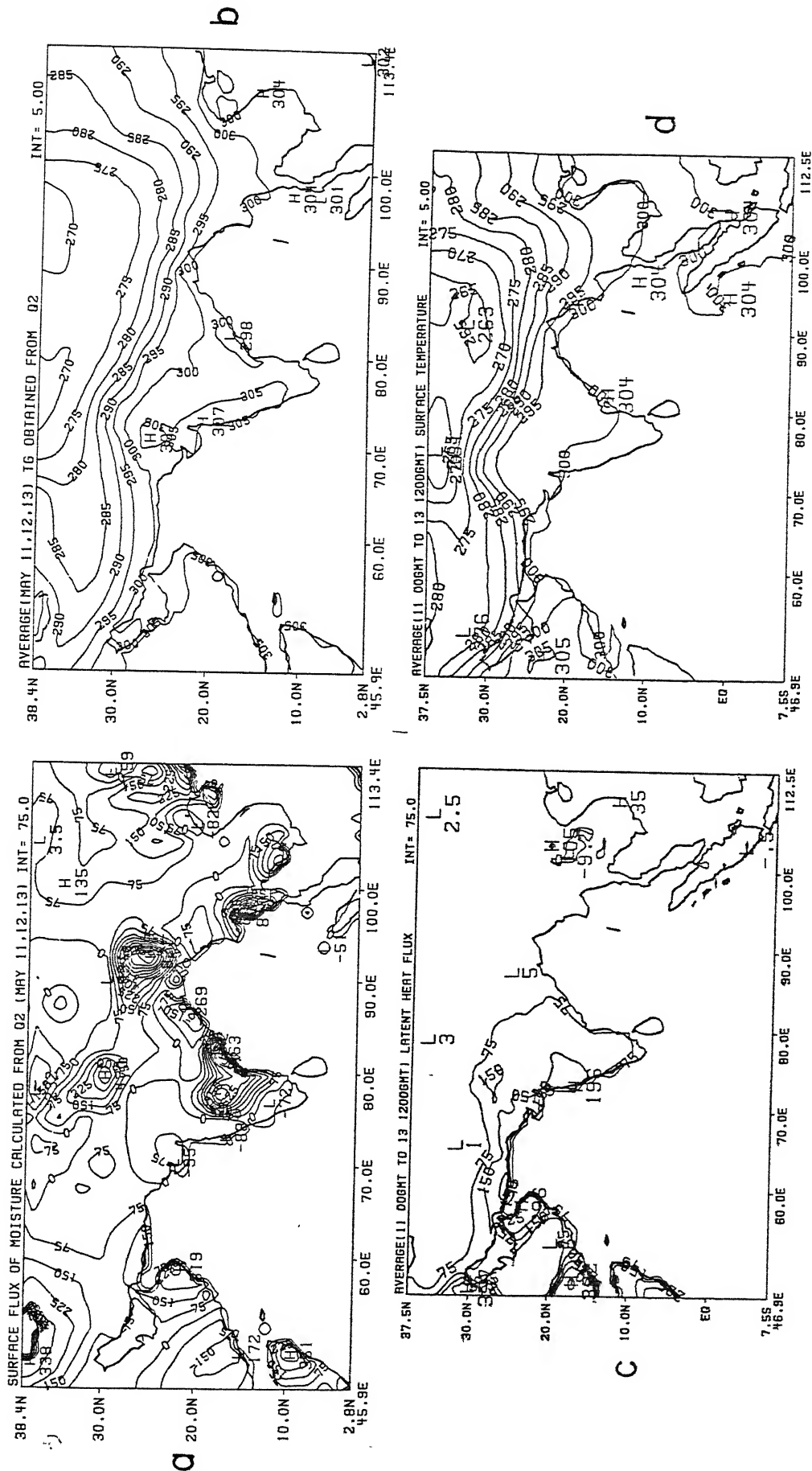
a_{24} and a_{34} are zero.

period is selected to include heavy rainfall as well as less rainfall over different regions of the domain. 15 days period is divided into 5 subperiods of 3 days each. The calculations are carried out over 3 day averages for the 5 sets.

5.2 Results and Discussion of the Parameterization:

Figure 18-a presents the average (11 May 1979 - 13 May 1979) surface latent heat flux F_L^Q (Watts/m²) as calculated from moisture budget analysis using equation 5.11. The four regions of large surface fluxes over Southeastern India, Bangladesh, Northern India and Southern Burma are regions that have experienced past rainfall. Figure 18-b shows the corresponding average surface temperature T_g^Q (°k) obtained by using the slab model for surface energy balance described by equation (5.16). The ground temperature largely reflects the colder temperatures to the North over regions of high elevation. Since F_L^Q is estimated directly from observed large scale fields u , v , q and rainfall rate and it does not involve the boundary layer parameterization i.e. similarity theory and GW parameterization it is considered a representation of the observed latent heat flux. In panels 18-c and 18-d the average surface latent heat flux and average surface temperature predicted by the model for the same period are compared with F_L^Q and T_g^Q . It is apparent that the model predicted ground wetness does not reflect the wet areas implied by the surface fluxes. The averaged ground temperature shown here reflects the high elevation. This field is quite similar to that of the topography.

The results of ground wetness (GW^Q) obtained by the new scheme



described above are presented in figures 19-23 in comparison with ground wetness (GWM1, GWM2) estimates from expressions (5.4) and (5.5). Figures 24 (a, b, c, d and e) show the average 24 hour rainfall (mm/day) for the five subperiods. The observed measures of rainfall, shown here, were derived from a mix of raingauge and satellite based estimates. Comparison of GW maps with the rainfall for the corresponding period reveals clearly that GW provided by the new scheme is in good agreement with the rainfall distribution, whereas GWM1 and GWM2 do not represent the soil moisture well. The ground wetness for the five subperiods, clearly illustrates the major deficiency of the specified ground wetness (shown in the bottom panel of each diagram). The ground wetness distribution from GWM2 is rather flat and exceeds 80% over most of India and Southeast Asia. The top panel on each of the figures 25-29 shows the latent heat flux F_L^Q over the land calculated from moisture budget analysis using expression (5.11) for 5 subperiods. The bottom two panels in these figures are the maps of latent heat flux ($F_L^{s_1}$, $F_L^{s_2}$) calculated using (5.4) and (5.5) expressions for GW, the similarity theory and surface energy balance as presently used in the model, discussed in Chapter 3. The second panels on these figures show $F_L^{s_{new}}$ which is also calculated by similarity dependent formula (5.23) but it uses ground wetness given by GW^Q and slab model for surface energy balance as discussed in section 5.2. It is clearly seen from the figures that $F_L^{s_{new}}$ is in close agreement with F_L^Q whereas the surface latent heat flux distributions given by $F_L^{s_1}$, $F_L^{s_2}$ are not very close to F_L^Q . The two older versions of ground wetness fail to represent the surface flux of latent heat. Similarly the next 30-34 figures show the corresponding

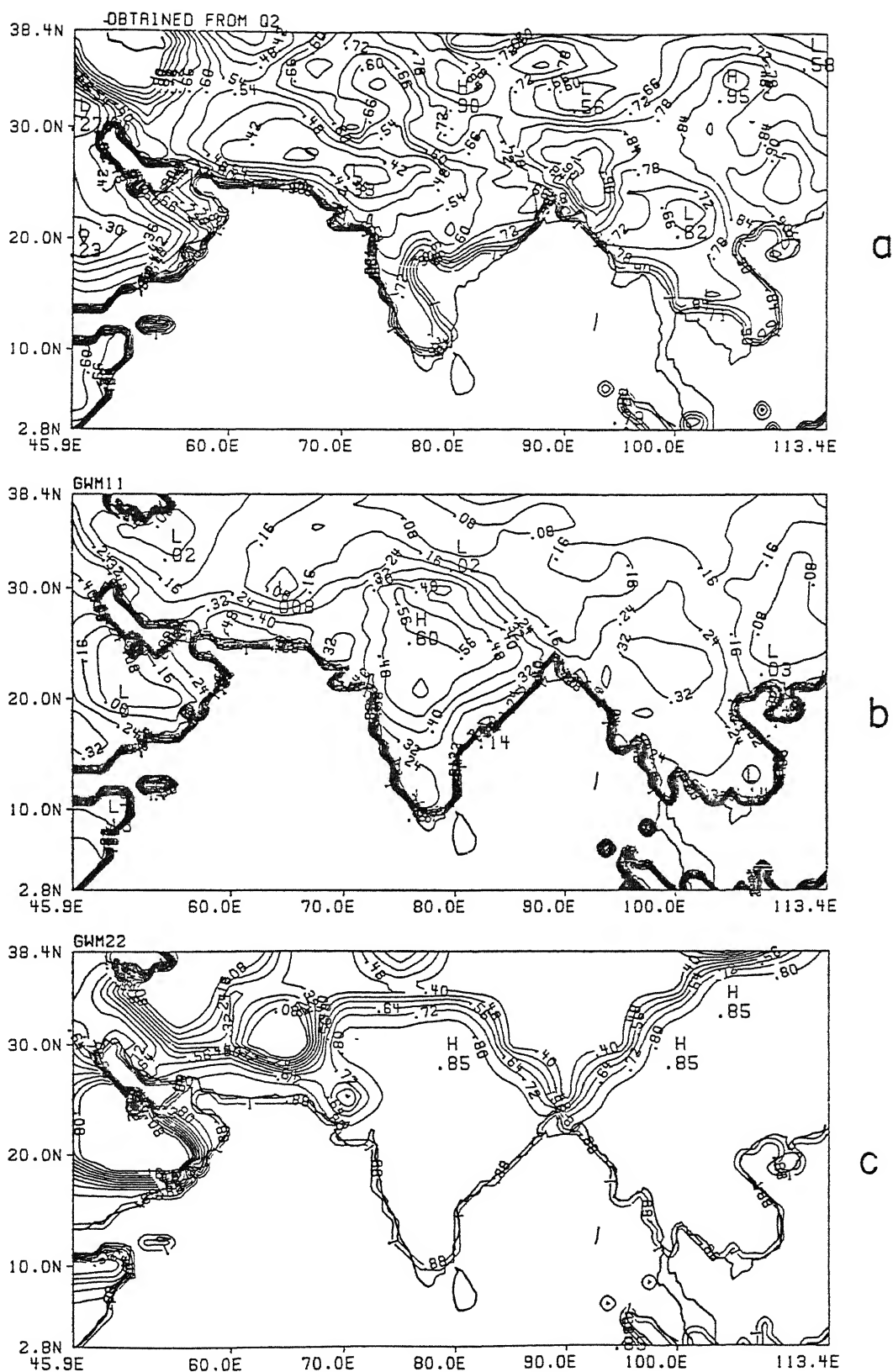


Figure 19 a, b and c: Average GW parameter maps for the subperiod 1 (May 11 1979 00 UTC - May 13 1979 12 UTC). It ranges from 0 for dry land to 1 for saturated land. (a) calculated from moisture budget analysis, (b) and (c) are calculated respectively by the expressions given by (5.4) and (5.5).

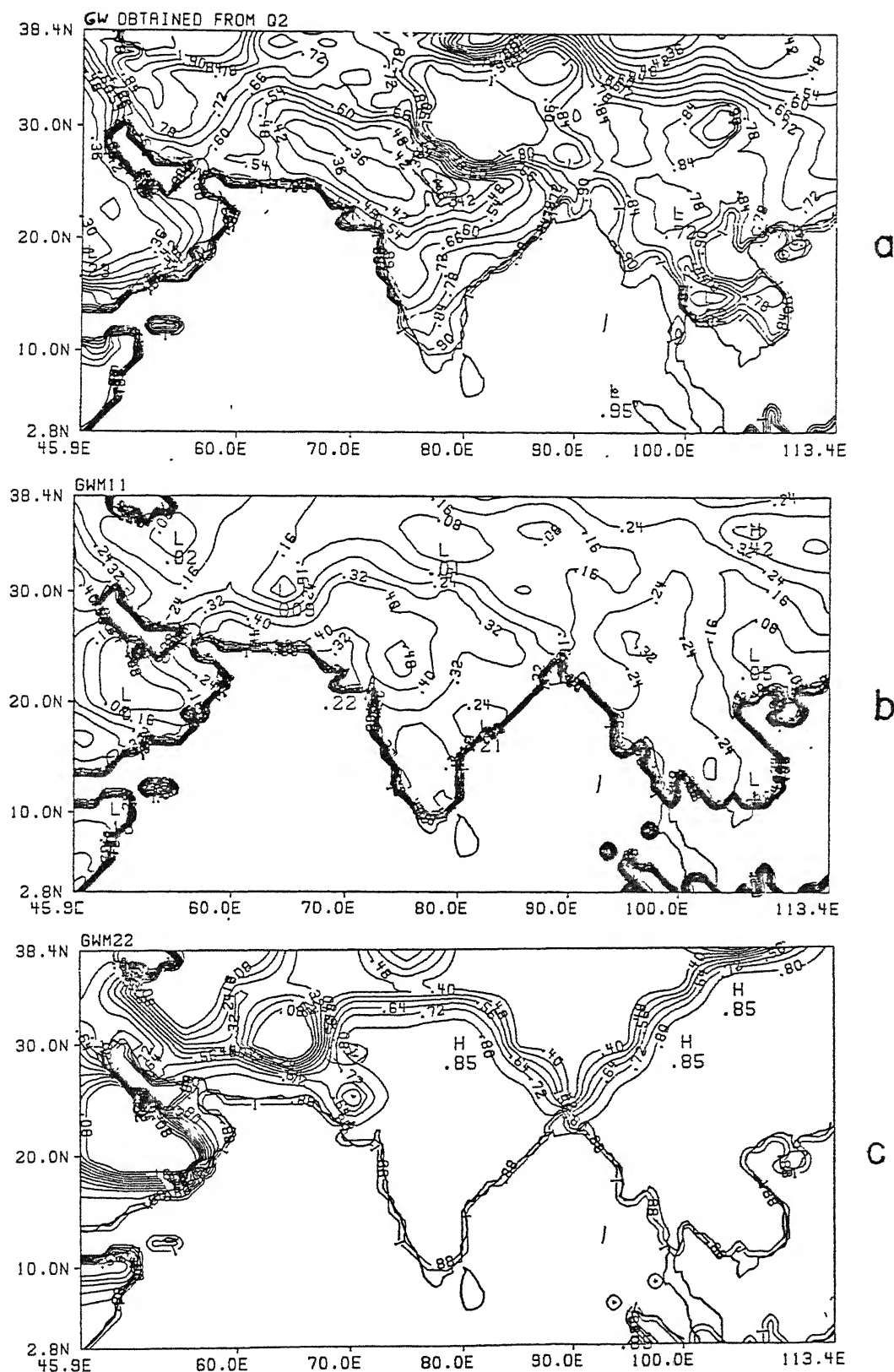


Figure 20 a, b and c: Average GW parameter maps for the subperiod 2 (May 14 1979 00 UTC - May 16 1979 12 UTC). It ranges from 0 for dry land to 1 for saturated land. (a) calculated from moisture budget analysis, (b) and (c) are calculated respectively by the expressions given by (5.4) and (5.5).

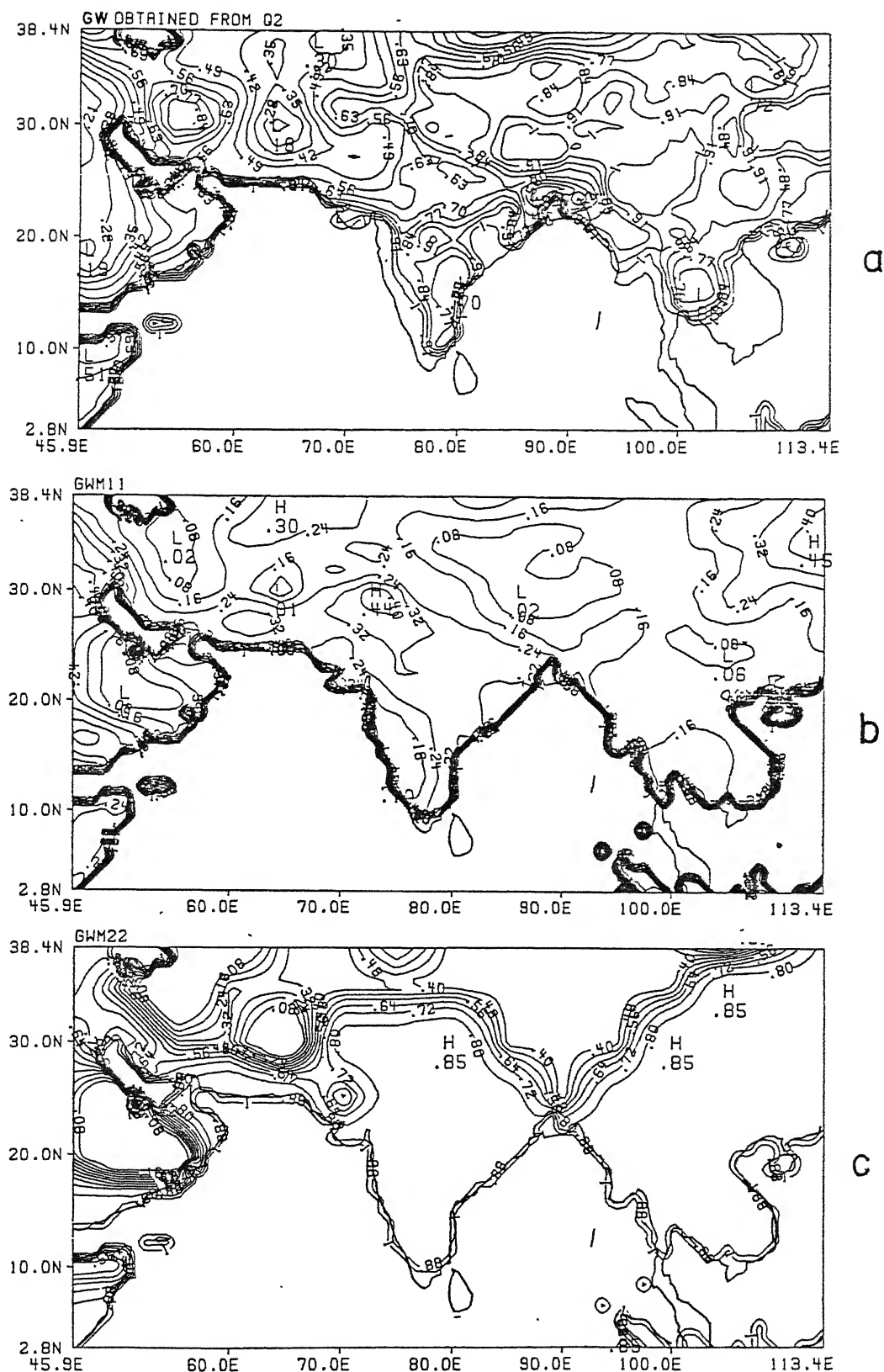


Figure 21 a, b and c: Average GW parameter maps for the subperiod 3 (June 20 1979 00 UTC - June 22 1979 12 UTC). It ranges from 0 for dry land to 1 for saturated land. (a) calculated from moisture budget analysis, (b) and (c) are calculated respectively by the expressions given by (5.4) and (5.5).

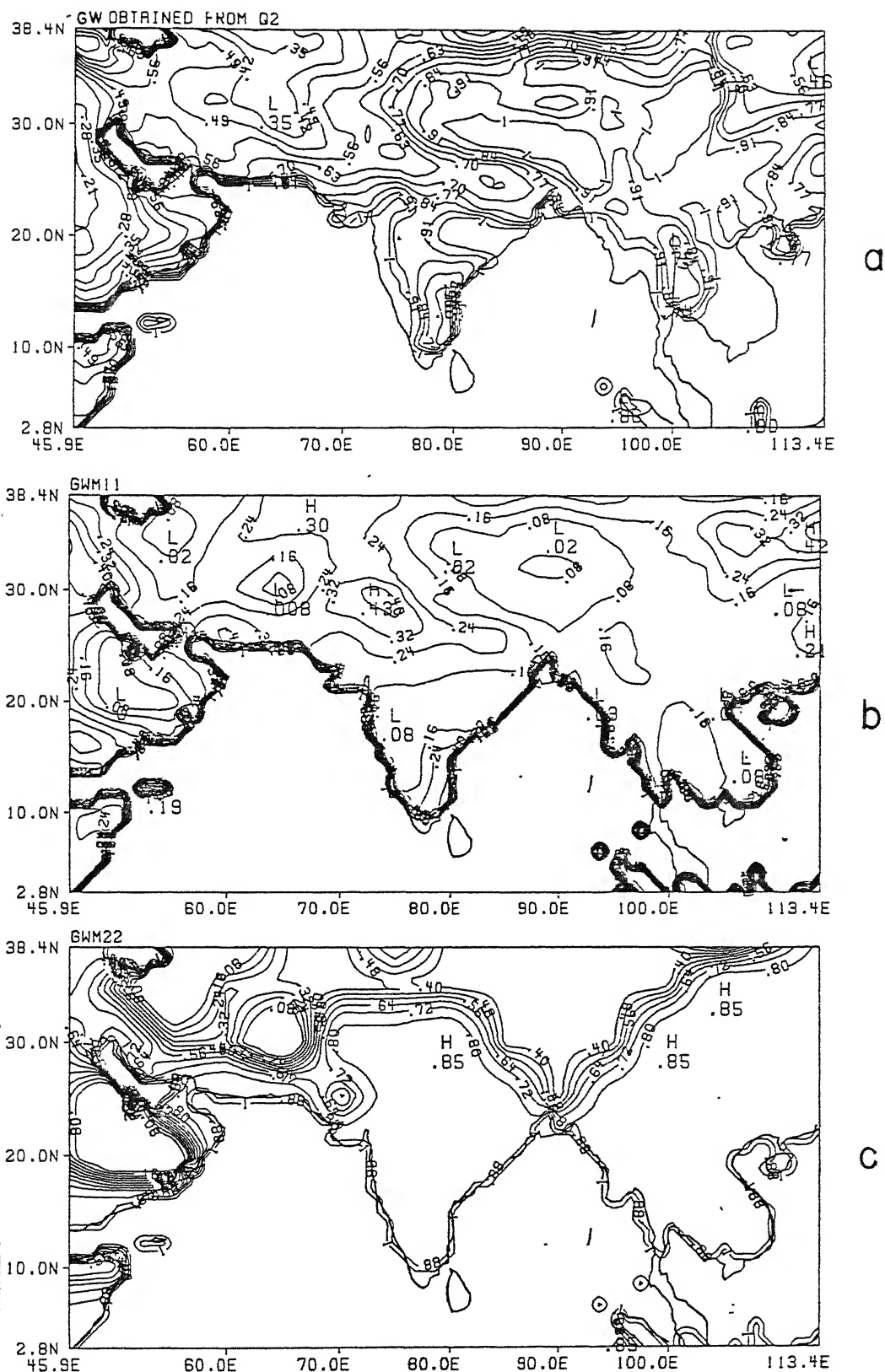


Figure 22 a, b and c: Average GW parameter maps for the subperiod 4 (June 23 1979 00 UTC - June 25 1979 12 UTC). It ranges from 0 for dry land to 1 for saturated land. (a) calculated from moisture budget analysis, (b) and (c) are calculated respectively by the expressions given by (5.4) and (5.5).

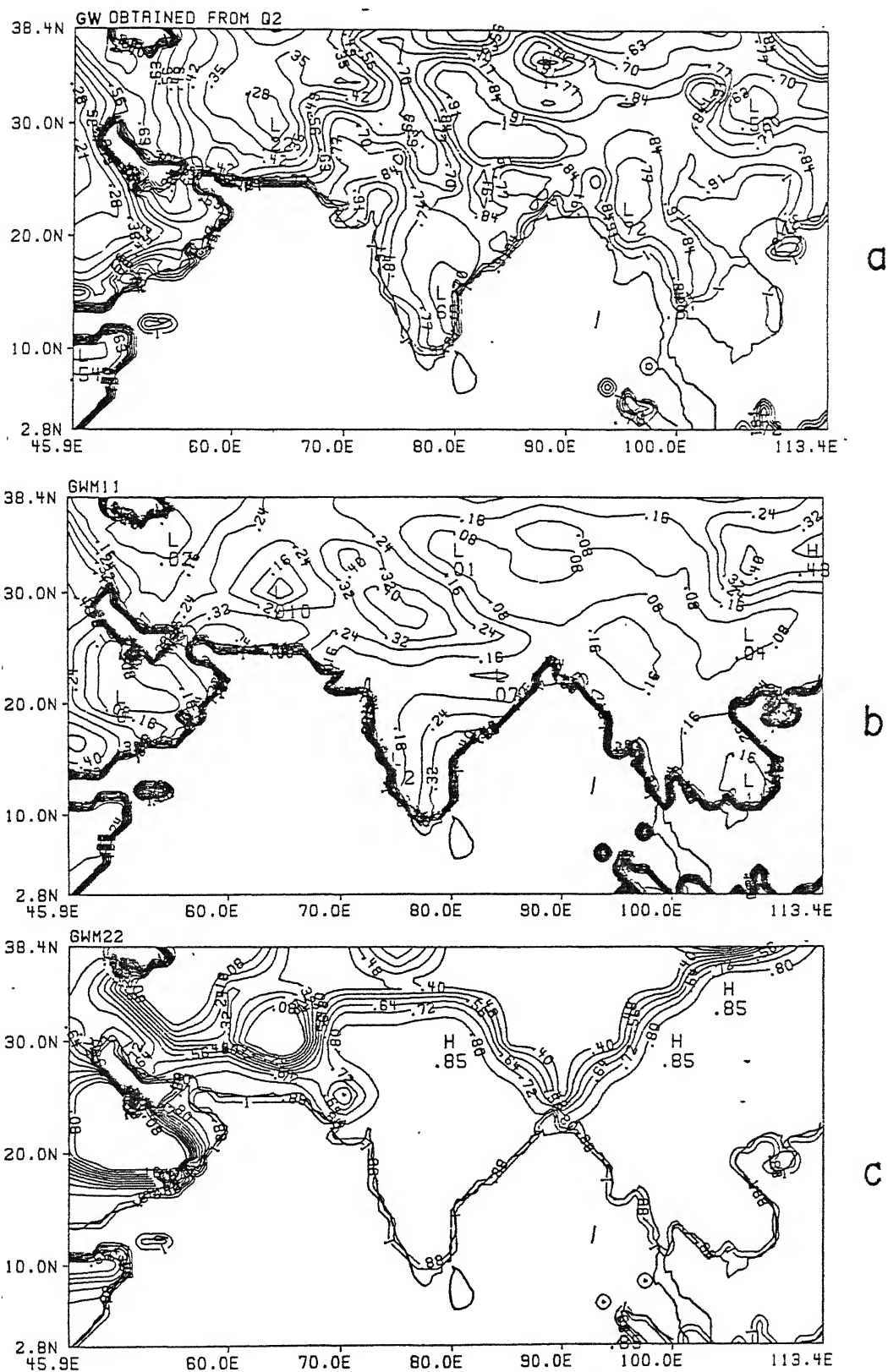


Figure 23 a, b and c: Average GW parameter maps for the subperiod 5 (June 26 1979 00 UTC - June 28 1979 12 UTC). It ranges from 0 for dry land to 1 for saturated land. (a) calculated from moisture budget analysis, (b) and (c) are calculated respectively by the expressions given by (5.4) and (5.5).

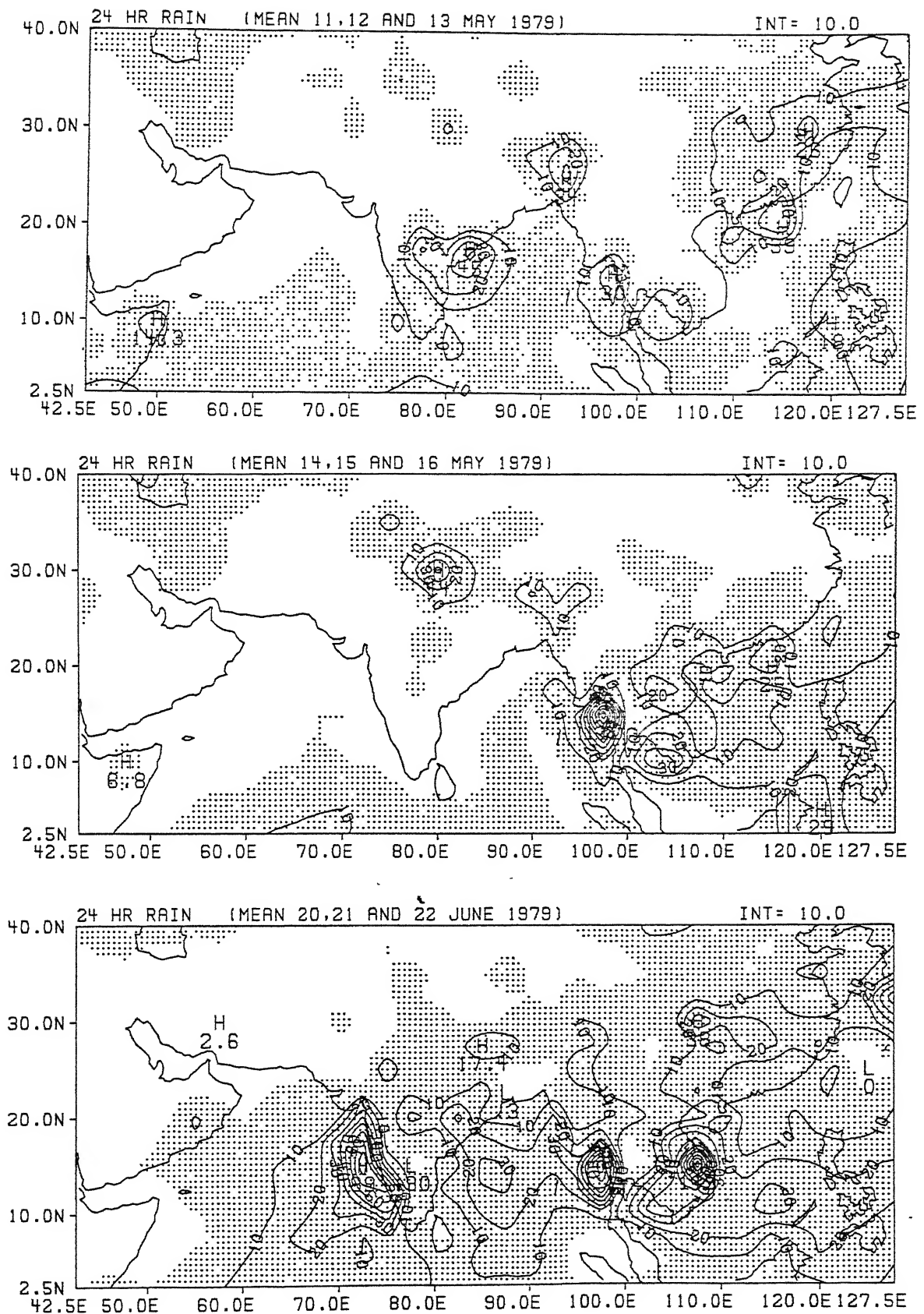


Figure 24 a, b and c: Three-day average observed rainfall rates (mm/day) derived from a mix of raingauge and satellite based estimates for the period (a) May 11 1979 00 UTC - May 14 1979 00 UTC, (b) May 14 1979 00 UTC - May 17 1979 00 UTC, (c) June 20 1979 00 UTC - June 23 1979 00 UTC.

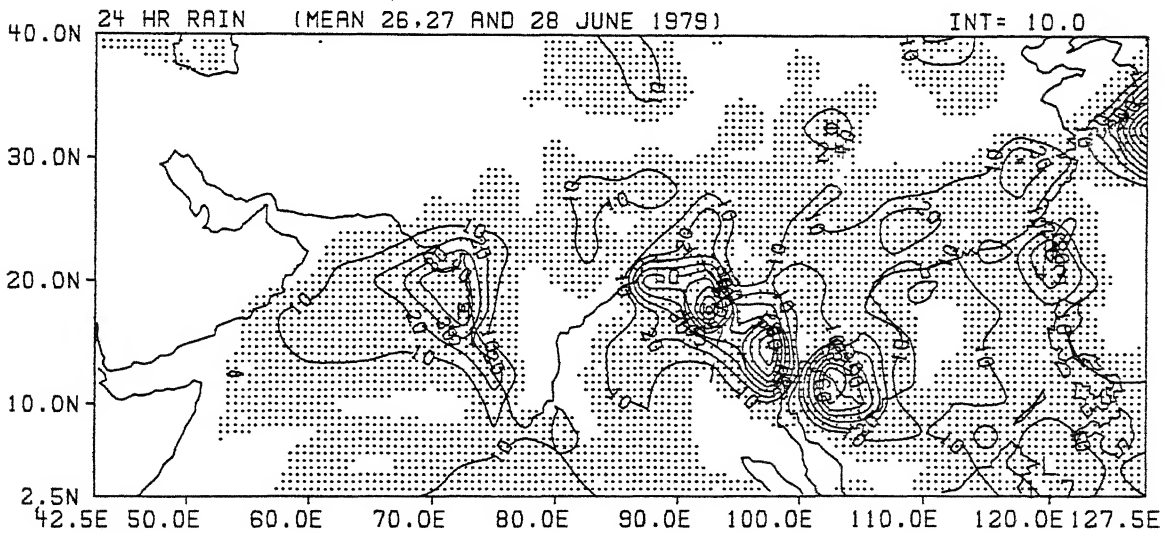
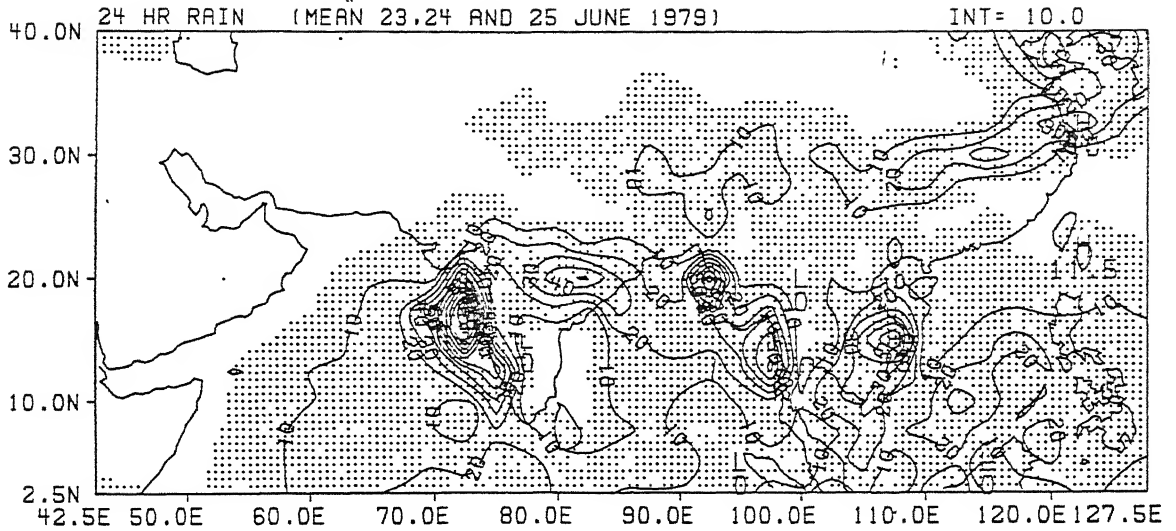
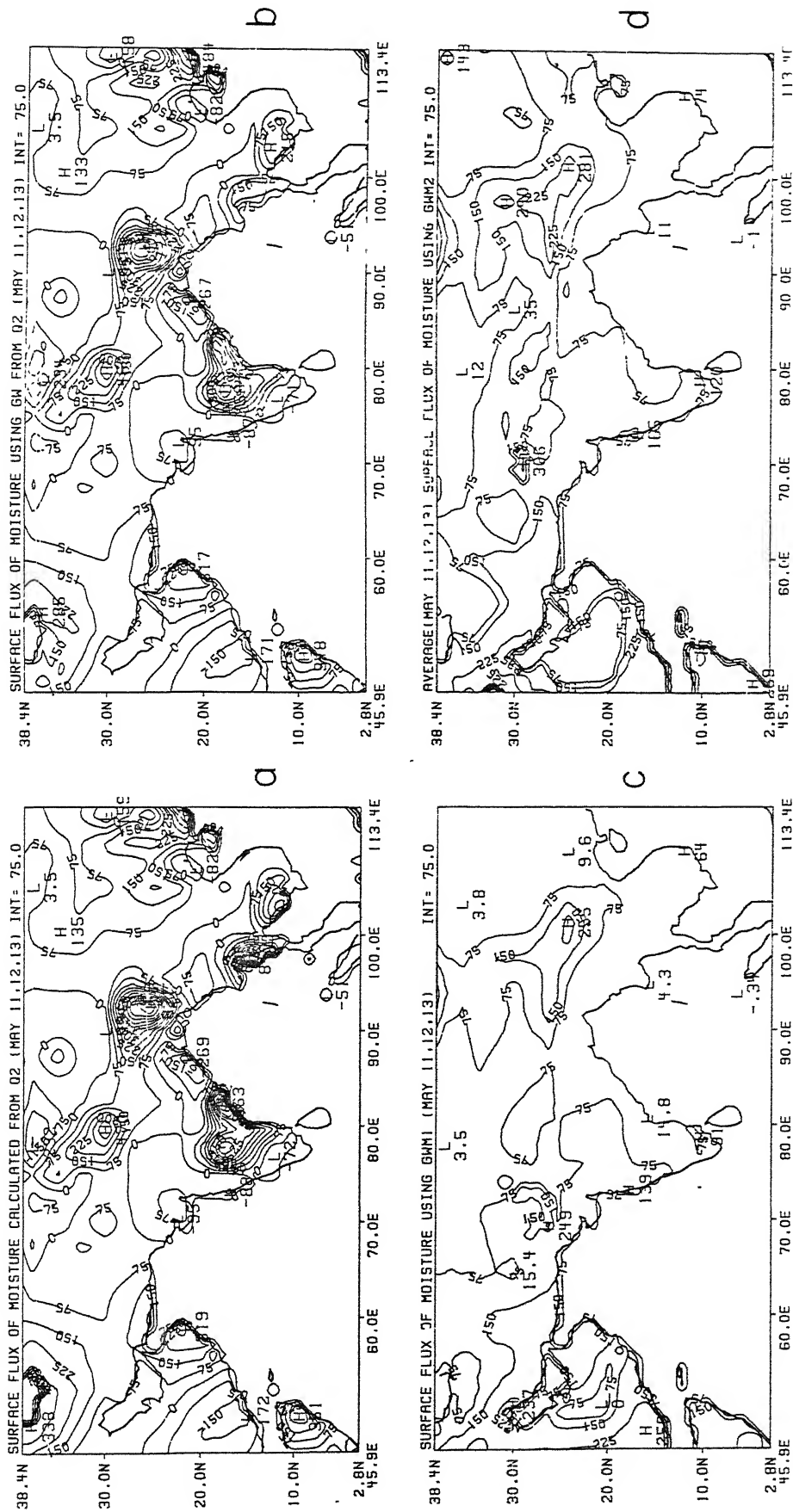


Figure 24 d and e: Three-day average observed rainfall rates (mm/day) derived from a mix of raingauge and satellite based estimates for the period (d) June 23 1979 00 UTC - June 26 1979 00 UTC, (e) June 26 1979 00 UTC - June 29 1979 00 UTC.



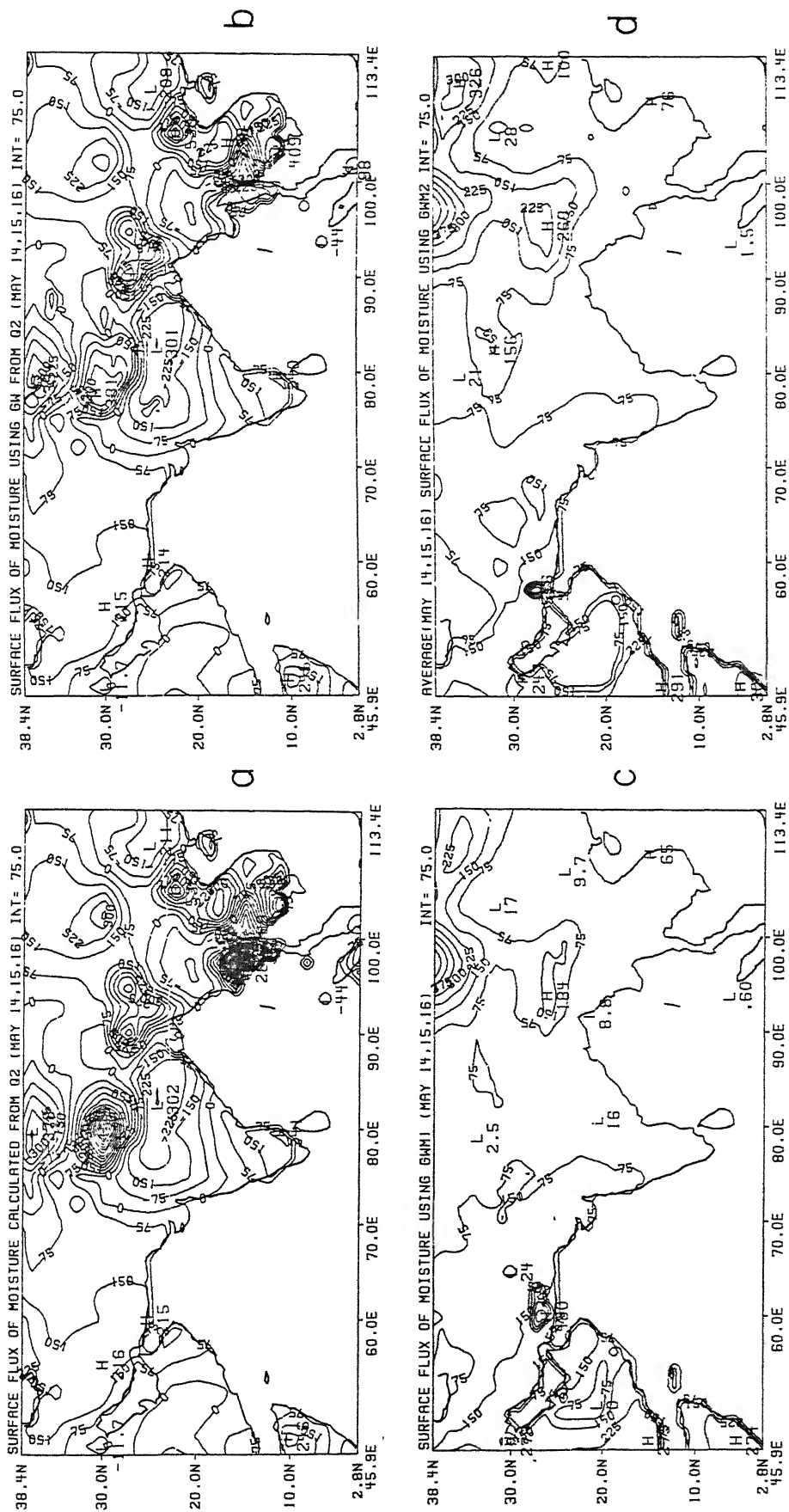


Figure 26 a, b, c and d: Average surface latent heat flux (watts/m²) for the subperiod 2 (May 14 1979 00 UTC - May 16 1979 12 UTC) calculated from (a) moisture budget analysis, (b) similarity theory and GW from moisture budget analysis, (c) similarity theory and GW from expression (5.4), (d) similarity theory and GW from expression (5.5).

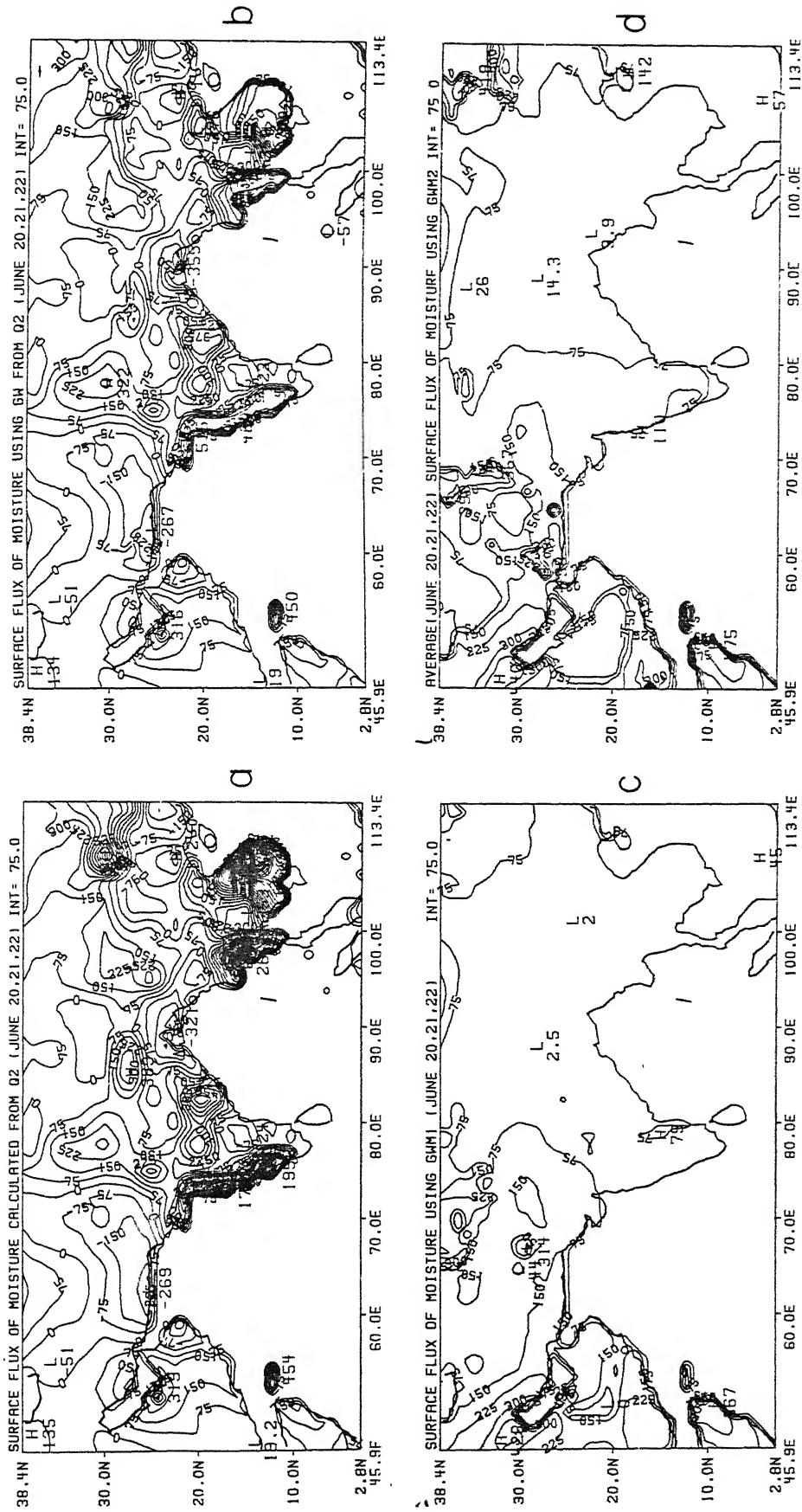


Figure 27 a, b, c and d: Average surface latent heat flux (watts/m^2) for the subperiod 3 (June 20 1979 00 UTC - June 22 1979 12 UTC) calculated from (a) moisture budget analysis, (b) similarity theory and GW from moisture budget analysis, (c) similarity theory and GW from expression (5.4), (d) similarity theory and GW from expression (5.5).

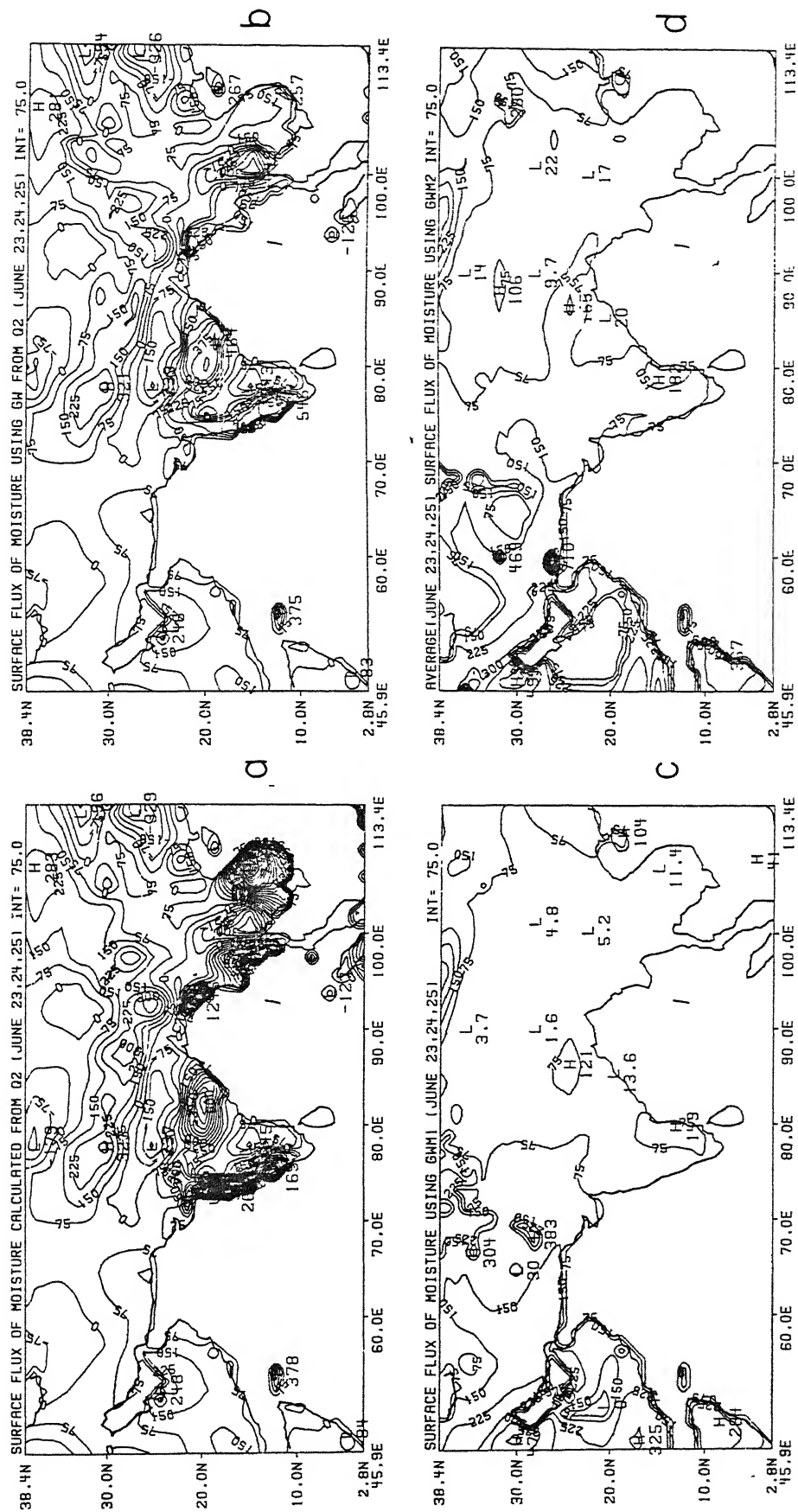


Figure 28 a, b, c and d: Average surface latent heat flux (watts/m²) for the subperiod 4 (June 23 1979 00 UTC - May 25 1979 12 UTC) calculated from (a) moisture budget analysis, (b) similarity theory and GW from moisture budget analysis, (c) similarity theory and GW from expression (5.4), (d) similarity theory and GW from expression (5.5).

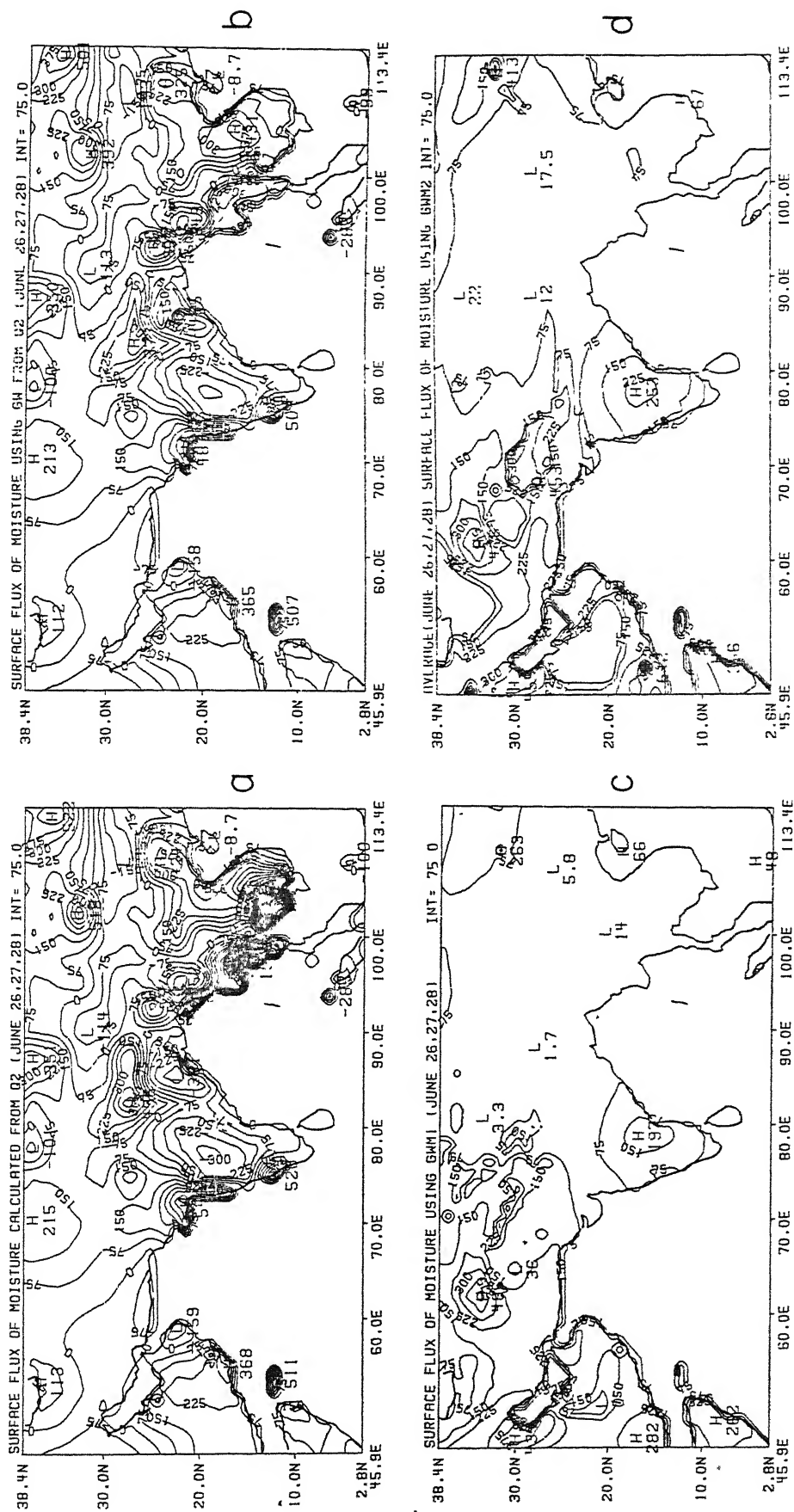


Figure 29 a, b, c and d: Average surface latent heat flux (watts/m²) for the subperiod 5 (June 26 1979 00 UTC - June 28 1979 12 UTC) calculated from (a) moisture budget analysis, (b) similarity theory and GW from moisture budget analysis, (c) similarity theory and GW from expression (5.4), (d) similarity theory and GW from expression (5.5).

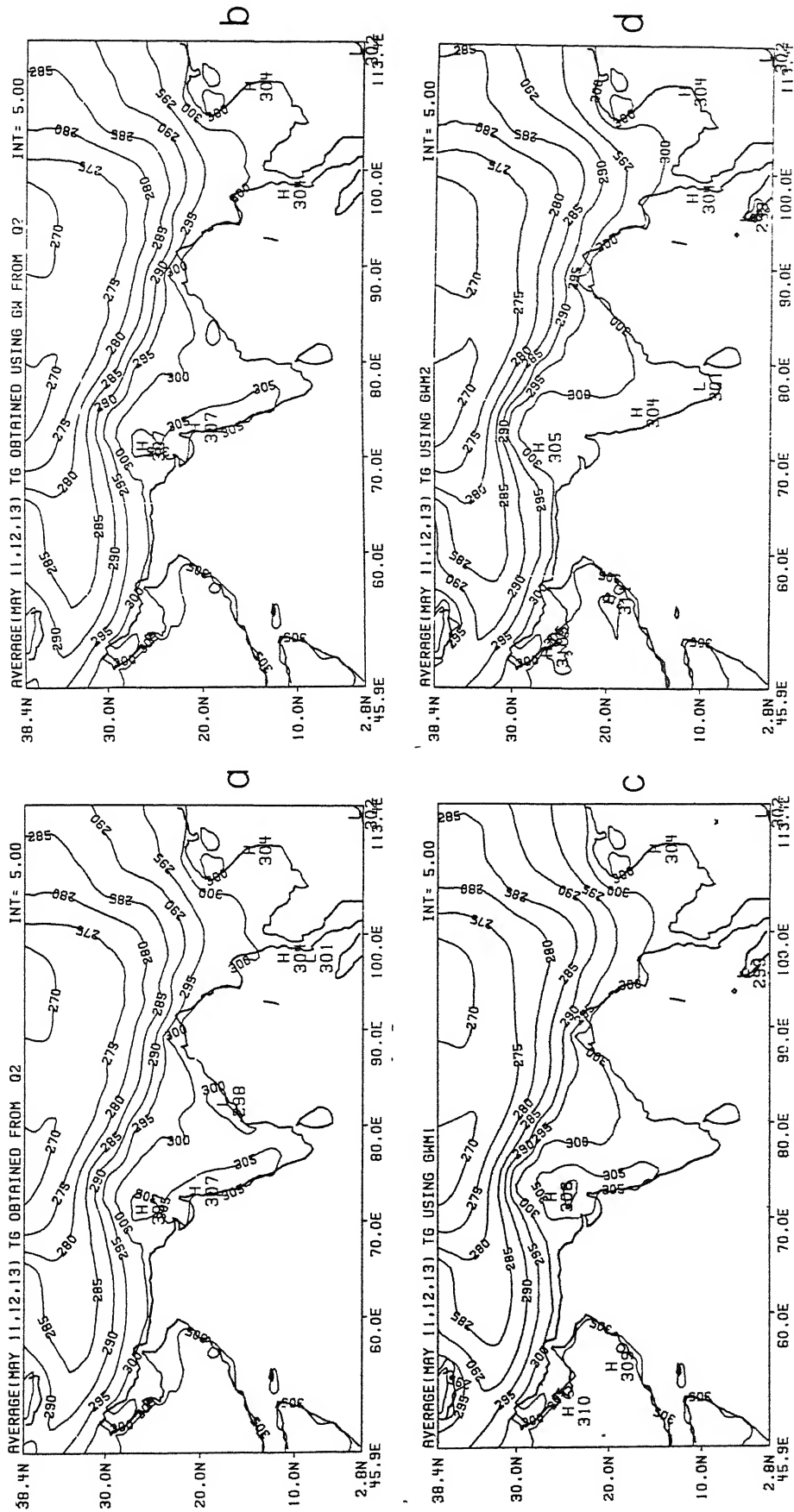


Figure 30 a, b, c and d: Average surface temperature ($^{\circ}\text{K}$) for the subperiod 1 (May 11 1979 00 UTC - May 13 1979 12 UTC). (a) Calculated from moisture budget analysis, (b) calculated using surface latent heat flux shown in figure 25 (b), (c) calculated using surface latent heat flux shown in figure 25 (c), (d) calculated using surface latent heat flux shown in figure 25 (d).

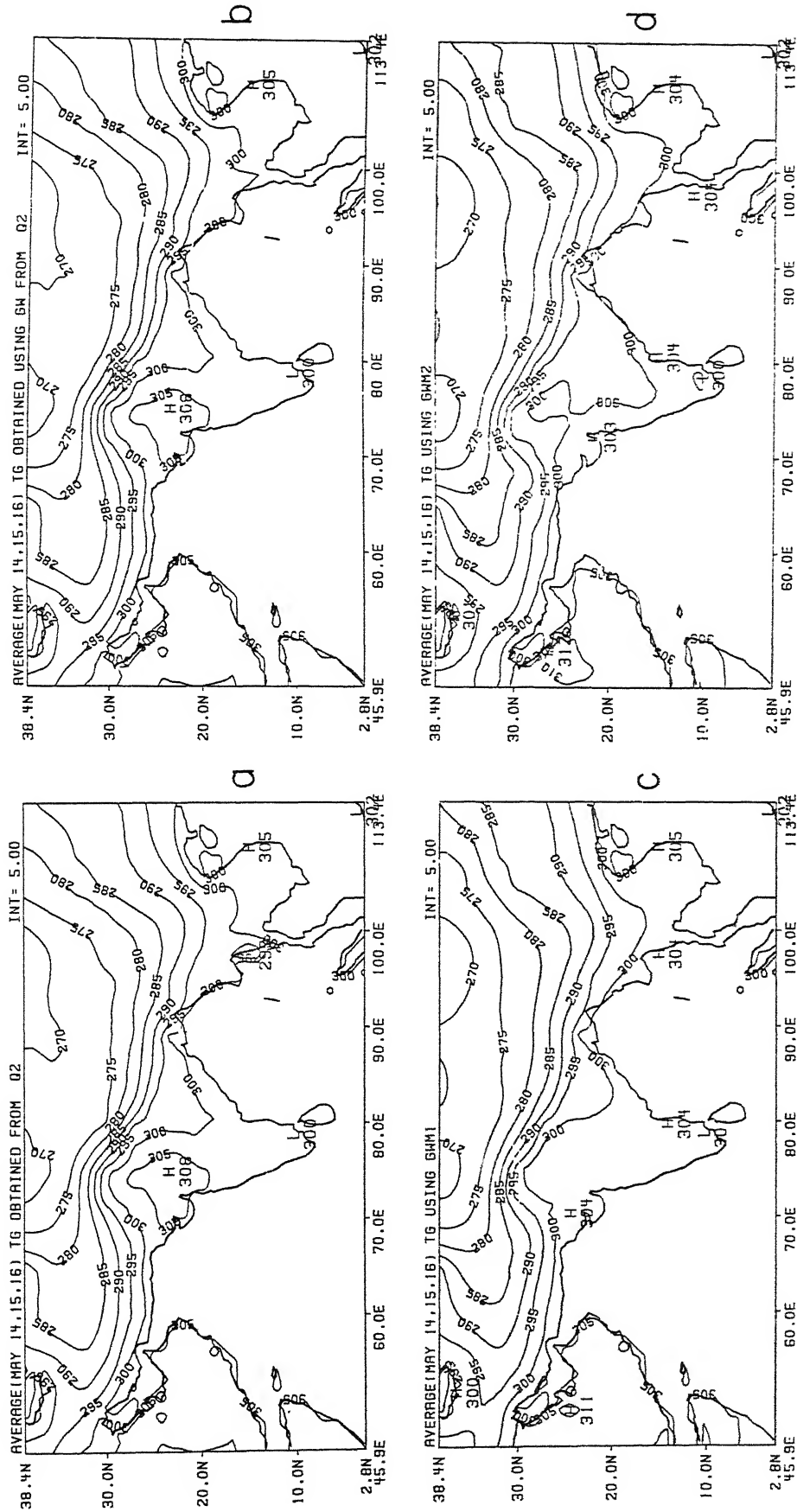


Figure 31 a, b, c and d: Average surface temperature (°K) for the subperiod 2 (May 14 1979 00 UTC - May 16 1979 12 UTC). (a) Calculated from moisture budget analysis, (b) calculated using surface latent heat flux shown in figure 26 (b), (c) calculated using surface latent heat flux shown in figure 26 (c), (d) calculated using surface latent heat flux shown in figure 26 (d).

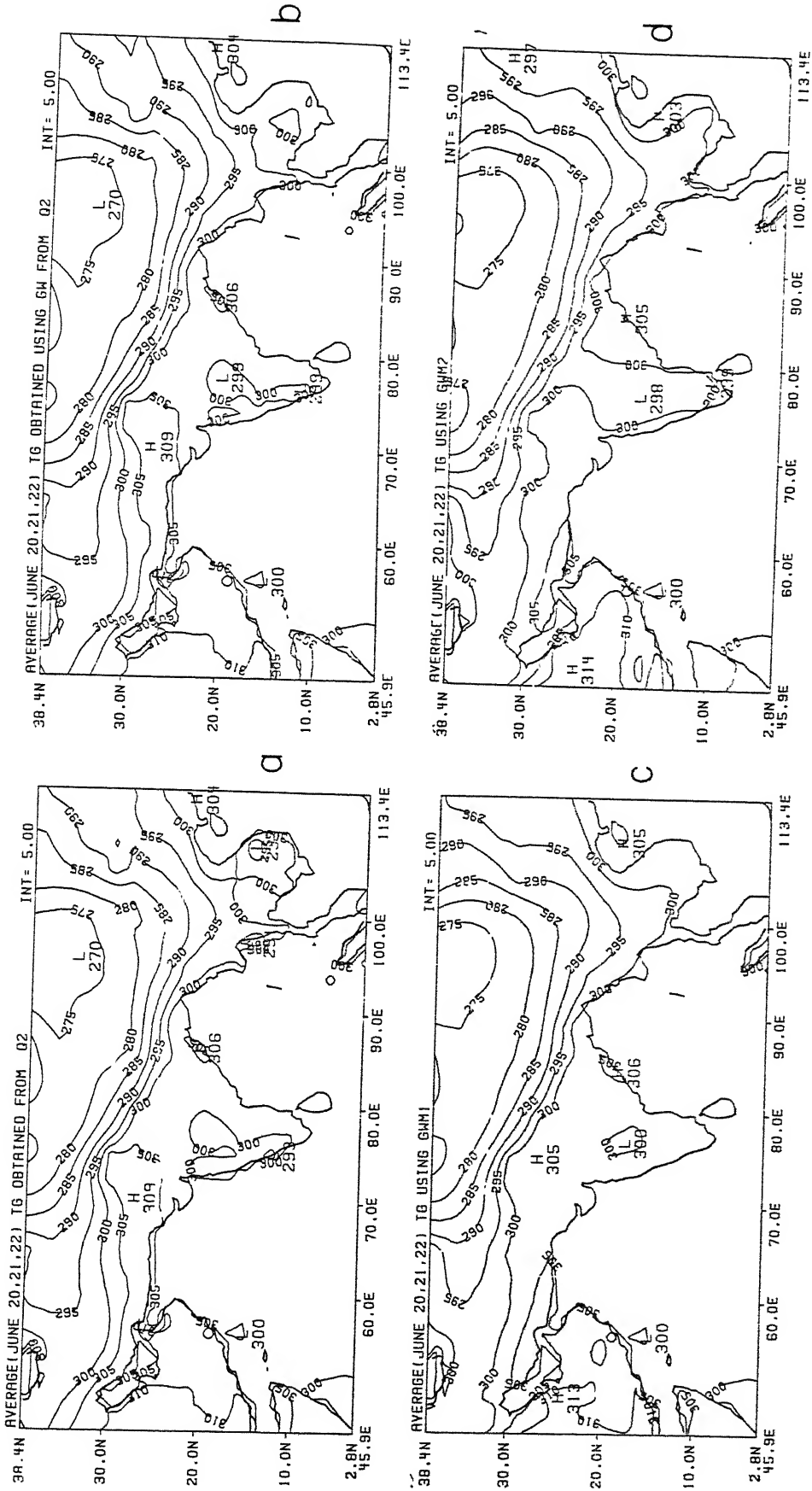


Figure 32 a, b, c, and d: Average surface temperature ($^{\circ}\text{K}$) for the subperiod 3 (June 20 1979 00 UTC - June 22 1979 12 UTC). (a) Calculated from moisture budget analysis, (b) calculated using surface latent heat flux shown in figure 27 (b), (c) calculated using surface latent heat flux shown in figure 27 (c), (d) calculated using surface latent heat flux shown in figure 27 (d).

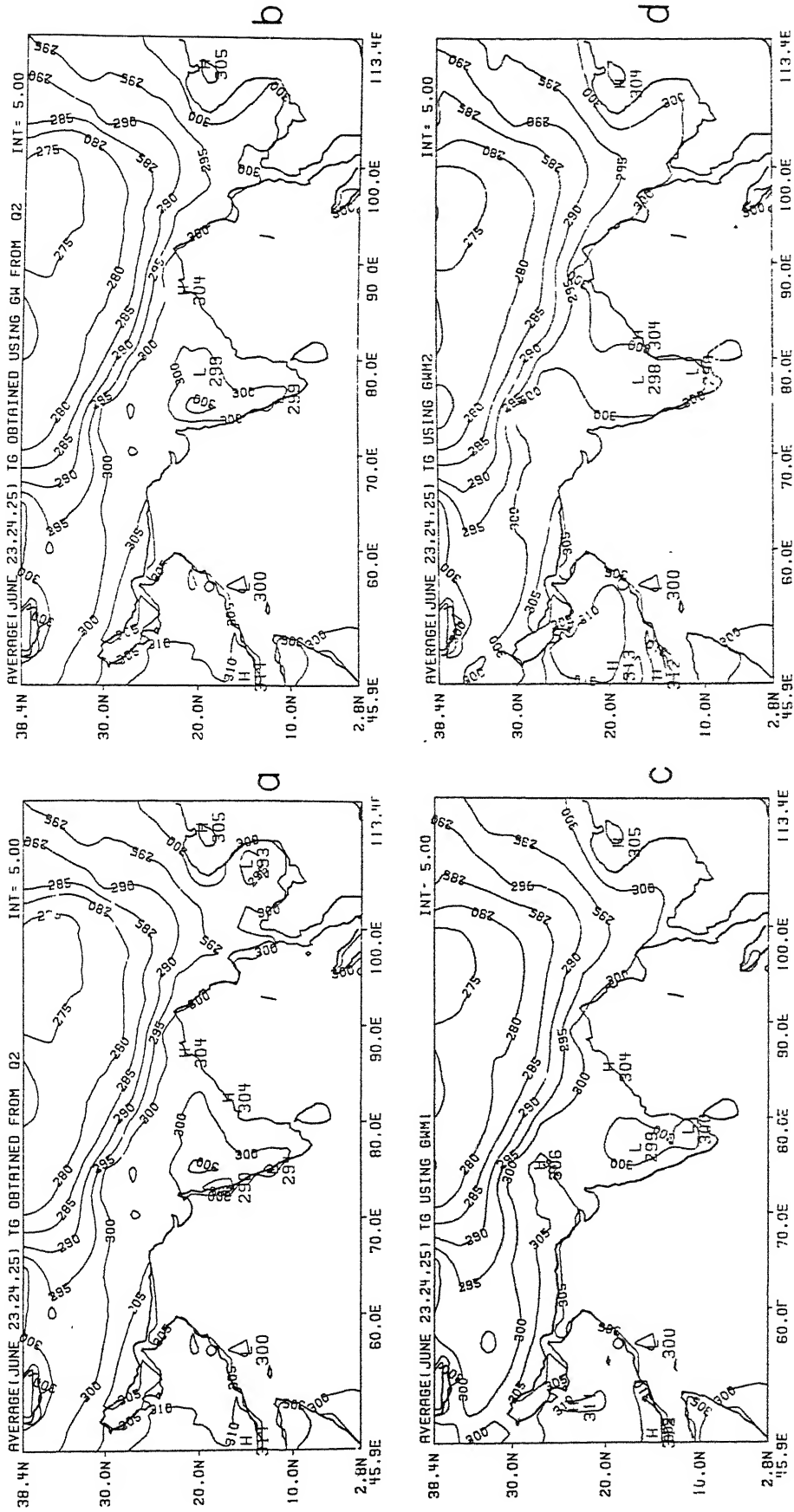


Figure 33 a, b, c and d: Average surface temperature ($^{\circ}\text{K}$) for the subperiod 4 (June 23 1979 00 UTC - June 25 1979 12 UTC). (a) Calculated from moisture budget analysis, (b) calculated using surface latent heat flux shown in figure 28 (b), (c) calculated using surface latent heat flux shown in figure 28 (c), (d) calculated using surface latent heat flux shown in figure 28 (d).

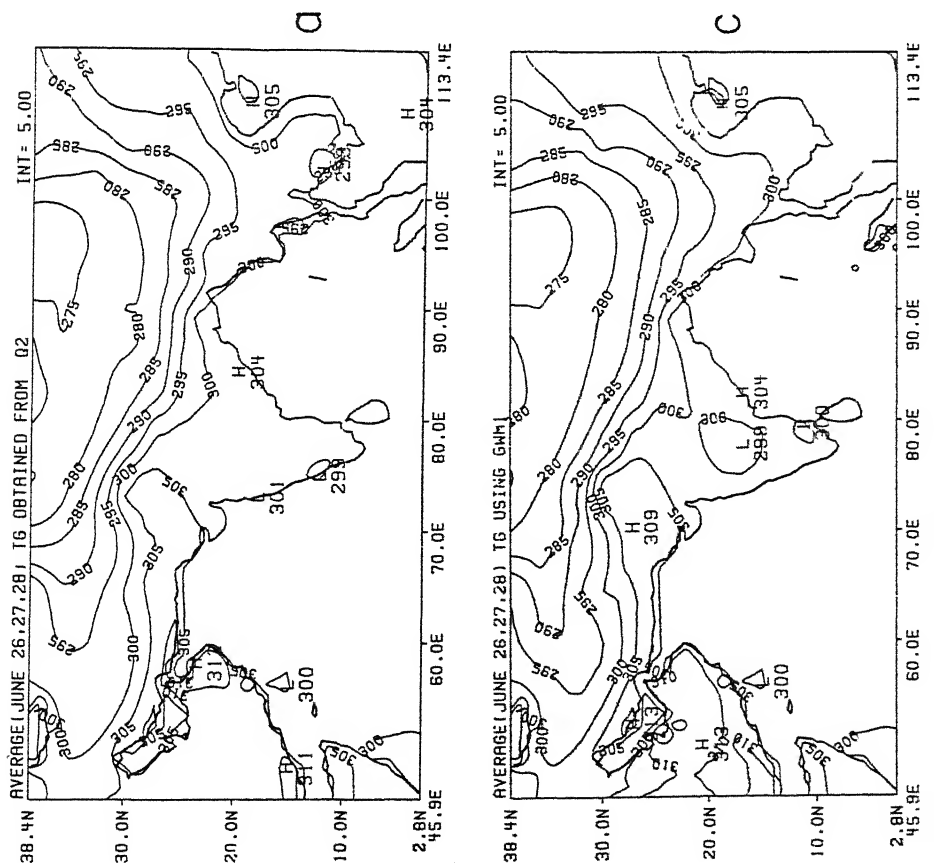


Figure 34 a, b, c and d: Average surface temperature (°K) for the subperiod 5 (June 26 1979 00 UTC - June 28 1979 12 UTC). (a) Calculated from moisture budget analysis, (b) calculated using surface latent heat flux shown in figure 29 (b), (c) calculated using surface latent heat flux shown in figure 29 (c), (d) calculated using surface latent heat flux shown in figure 29 (d).

surface temperatures calculated from each of the schemes for 5 subperiods.

Next, we shall divide the domain of interest into four subdomains; the averages of latent heat flux (F_L^Q , $F_L^{s_{new}}$, $F_L^{s_1}$, $F_L^{s_2}$) over the land are computed for each of these subdomains. These averages are compared in figures 35 and 36 for the five subperiods. The subdomains are defined as:

I 12.2° - 38.4°N, 45.9° - 66.6°E

II 2.8° - 21.6°N, 66.6° - 91.9°E

III 21.6° - 38.4°N, 66.6° - 91.9°E

and IV 12.2° - 38.4°N, 91.9° - 113.4°E

The figures 35-36 further confirm that for all the subdomains average flux calculated from the new parameterization of ground wetness is very close to the surface flux F_L^Q determined by large scale Q_2 and rainfall rate. The fluxes using GWM1 and GWM2 are not in good agreement with F_L^Q . Finally the figures 37 and 38 present the ground wetness (GW^{New}) given by expression (5.24). This is the final form of the ground wetness as function of rainfall, ground temperature, surface albedo and terrain height. GW^{New} has a correlation coefficient of 0.7 with GW^Q .

A 72 hour forecast of the tropical cyclone discussed in Chapter 4 is made to see the impact of improved parameterization of ground wetness. The model is initialized for May 11 1979, 00 UTC and a three day forecast is made. The figures 39 and 40 show the time evolution of the ground wetness as predicted in this experiment. Ground wetness

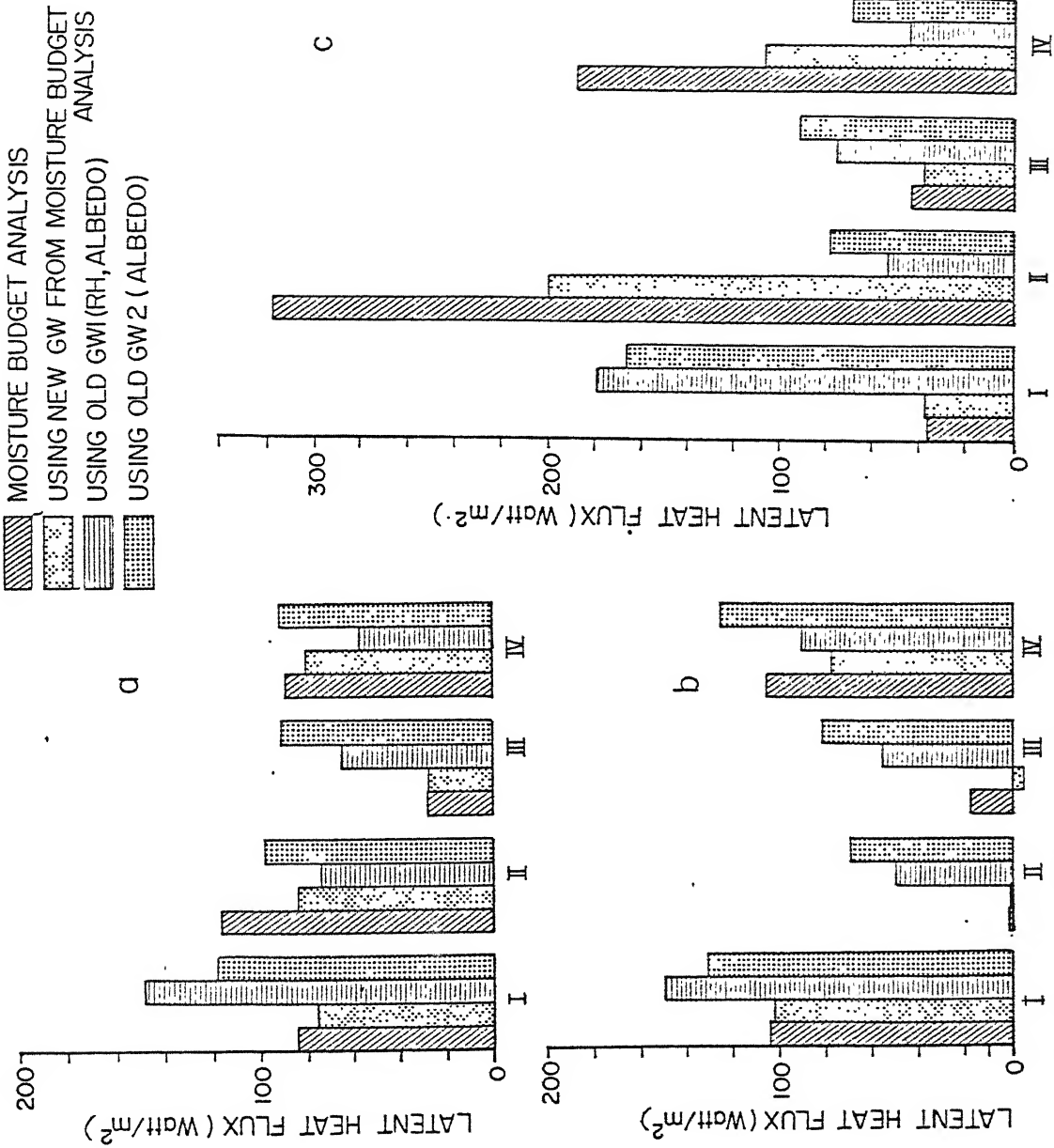


Figure 35 a, b, and c: Comparison of average surface latent heat flux (watts/m^2) calculated from 1. moisture budget analysis; 2. similarity analysis and GW from moisture budget analysis; 3. similarity analysis and GW from expression (5.4); 4. similarity analysis and GW from expression (5.5). These comparisons are for four domains defined as I. $12.2^\circ - 38.4^\circ\text{N}$, $45.9^\circ - 66.6^\circ\text{E}$, II. $2.8^\circ - 21.6^\circ\text{N}$, $66.6^\circ - 91.9^\circ\text{E}$ III. $21.6^\circ - 38.4^\circ\text{N}$, $66.6^\circ - 91.9^\circ\text{E}$ IV. $12.2^\circ - 38.4^\circ\text{N}$, $91.9^\circ - 113.4^\circ\text{E}$. (a) Subperiod 1, (b) Subperiod 2, (c) Subperiod 3.

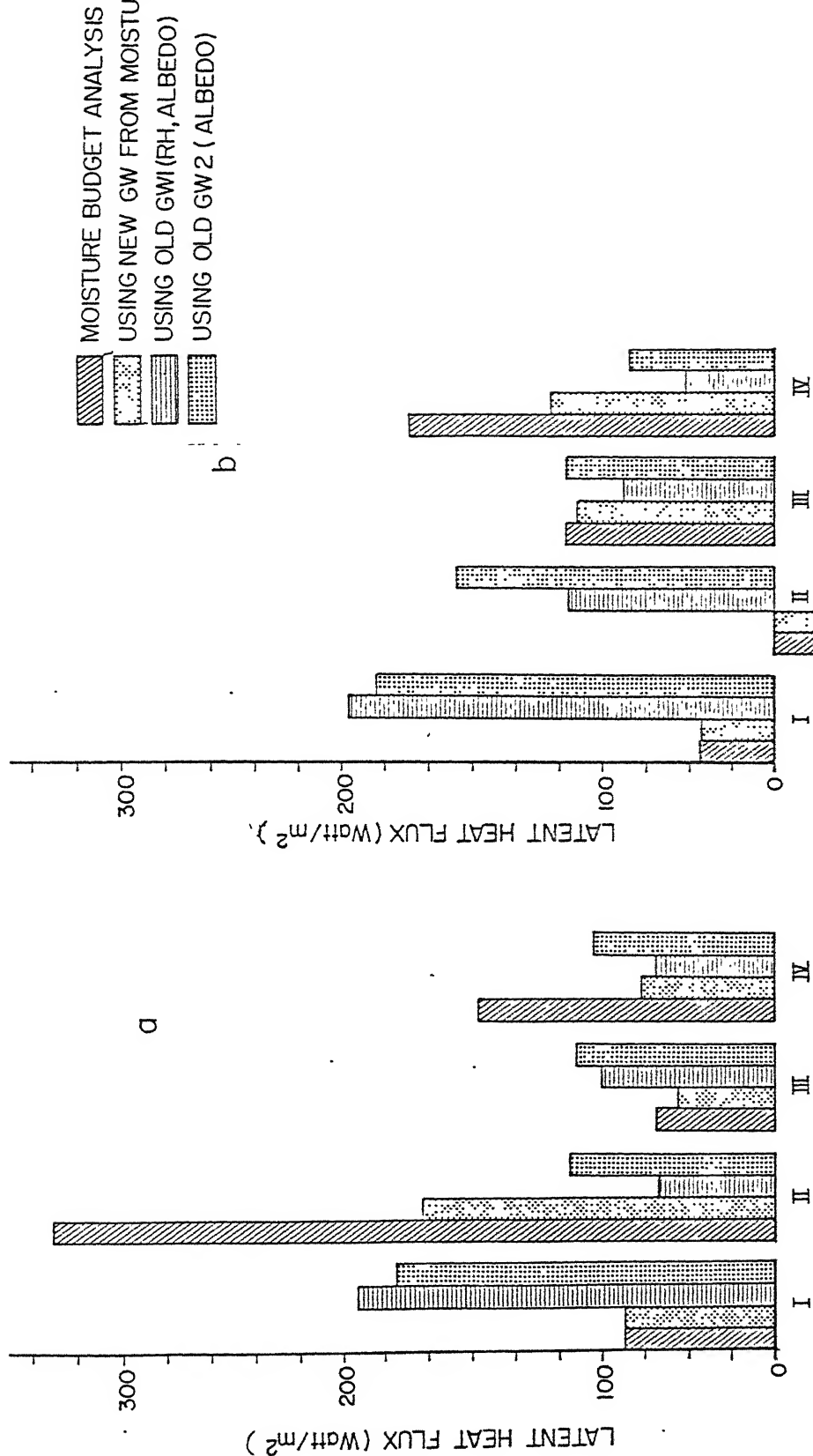
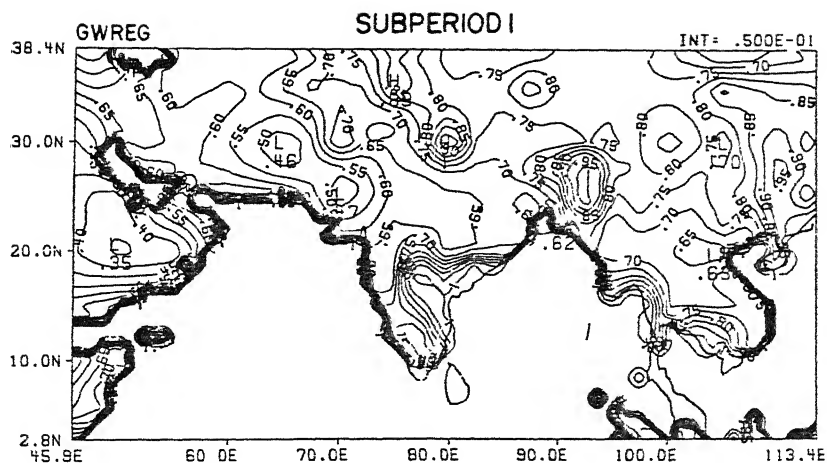
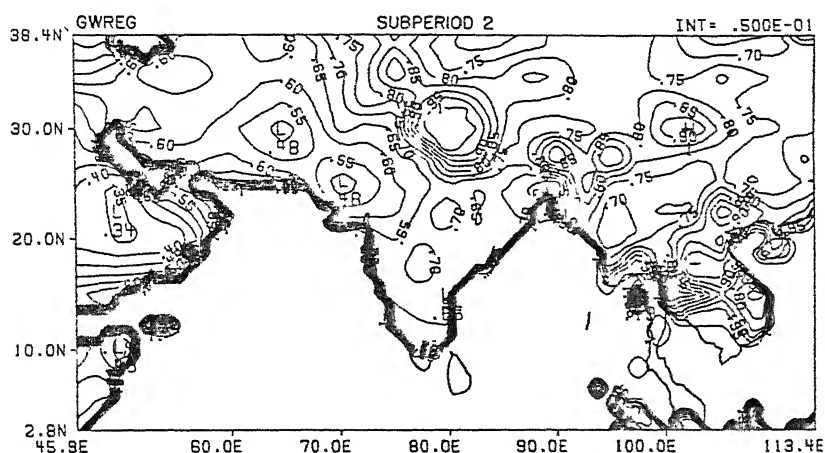


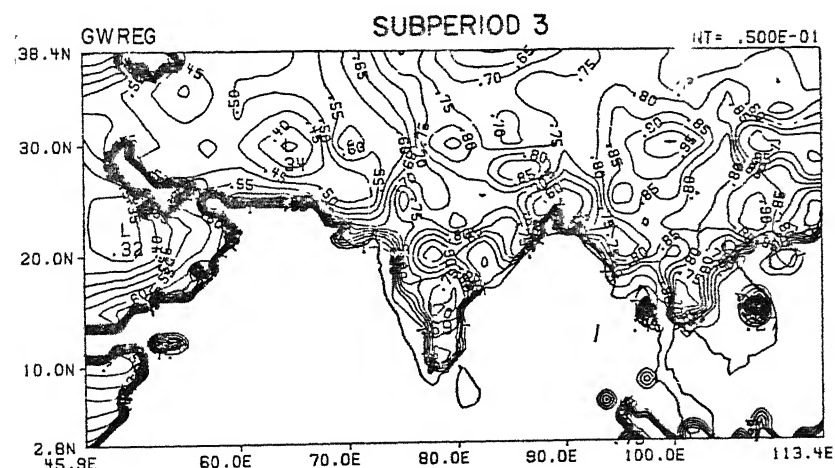
Figure 36 a and b: Comparison of average surface latent heat flux (watts/m²) calculated from 1. moisture budget analysis, 2. similarity analysis and GW from moisture budget analysis; 3. similarity analysis and GW from expression (5.4); 4. similarity analysis and GW from expression (5.5). These comparisons are for four domains defined as I. 12.2° - 38.4°N, 45.9° - 66.6°E, II. 2.8° - 21.6°N, 66.6° - 91.9°E III. 21.6° - 38.4°N, 66.6° - 91.9°E IV. 12.2° - 38.4°N, 91.9° - 113.4°E. (a) Subperiod 4, (b) Subperiod 5.



a



b



c

Figure 37 a, b and c: Average GW calculated from the GW expression given by (5.24). This is based on the regression analysis of GW estimates from moisture budget analysis with the parameters past 24 hour rainfall, surface temperature, albedo and terrain. (a) Subperiod 1 (May 11 1979 00 UTC - May 13 1979 12 UTC), (b) Subperiod 2 (May 14 1979 00 UTC - May 16 1979 12 UTC), (c) Subperiod 3 (June 20 1979 00 UTC - June 22 1979 12 UTC).

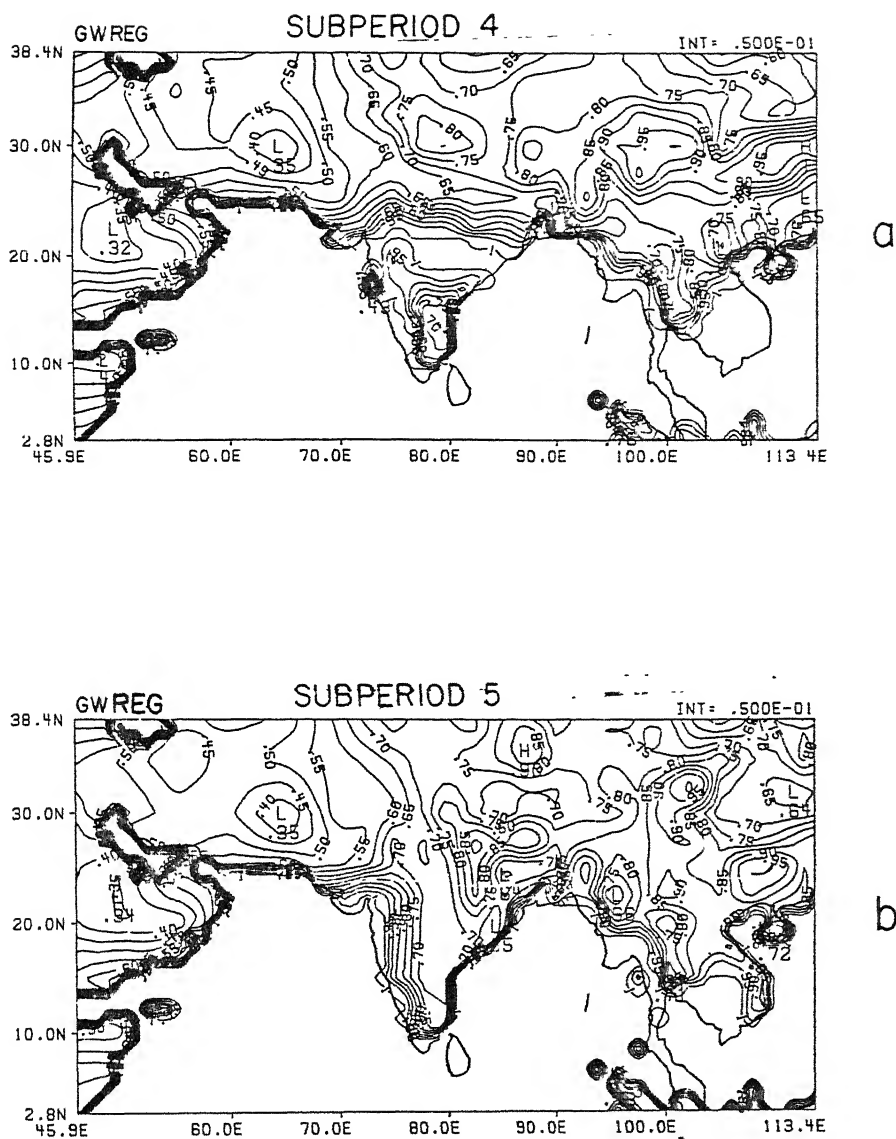


Figure 38 a and b: Average GW calculated from the GW expression given by (5.24). This is based on the regression analysis of GW estimates from moisture budget analysis with the parameters past 24 hour rainfall, surface temperature, albedo and terrain. (a) Subperiod 4 (June 23 1979 00 UTC - June 25 1979 12 UTC), (b) Subperiod 5 (June 26 1979 00 UTC - June 28 1979 12 UTC).

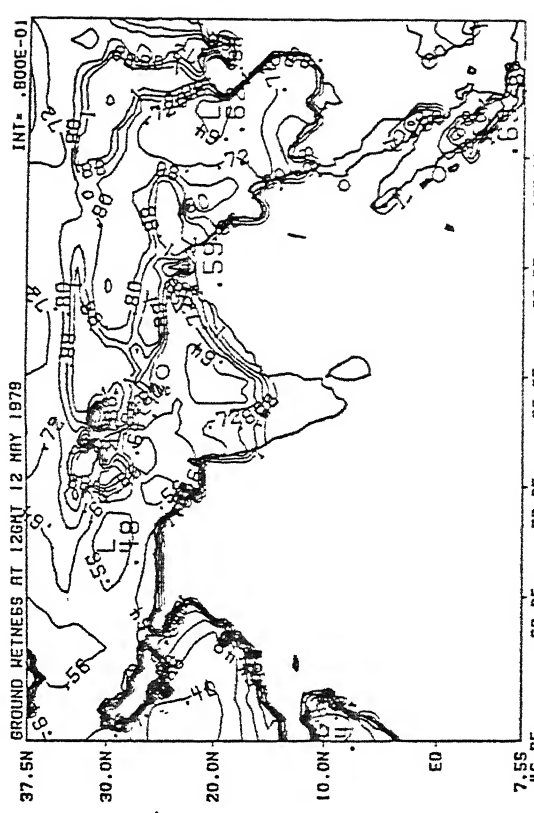
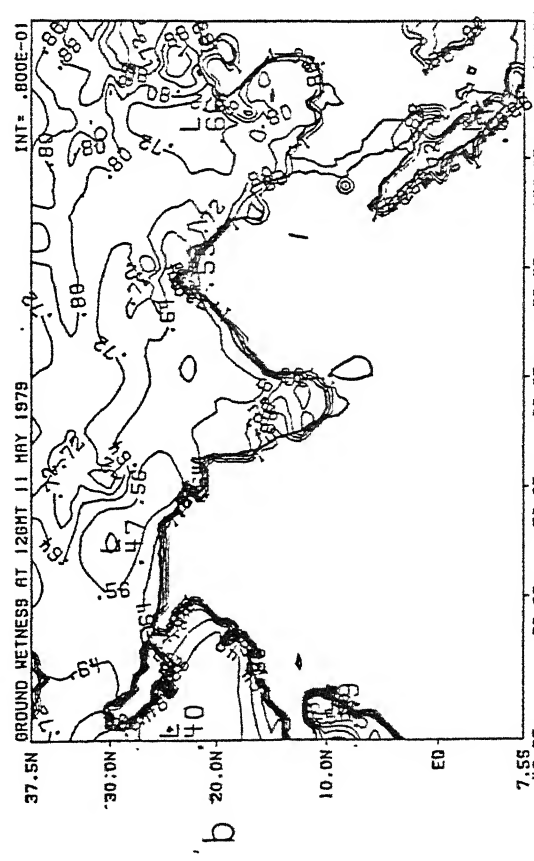
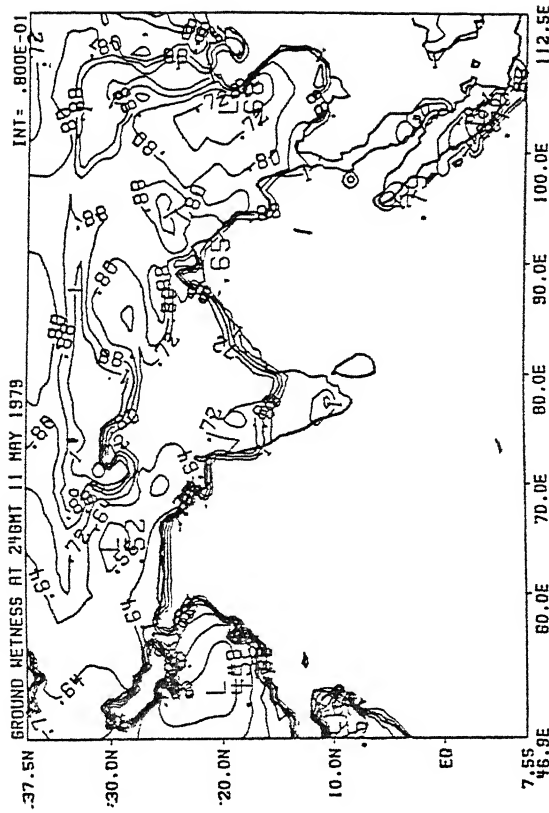
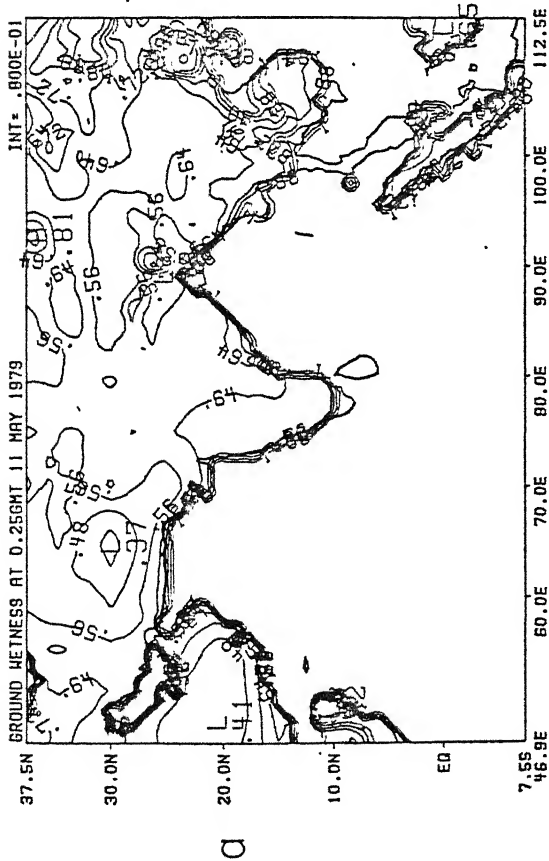
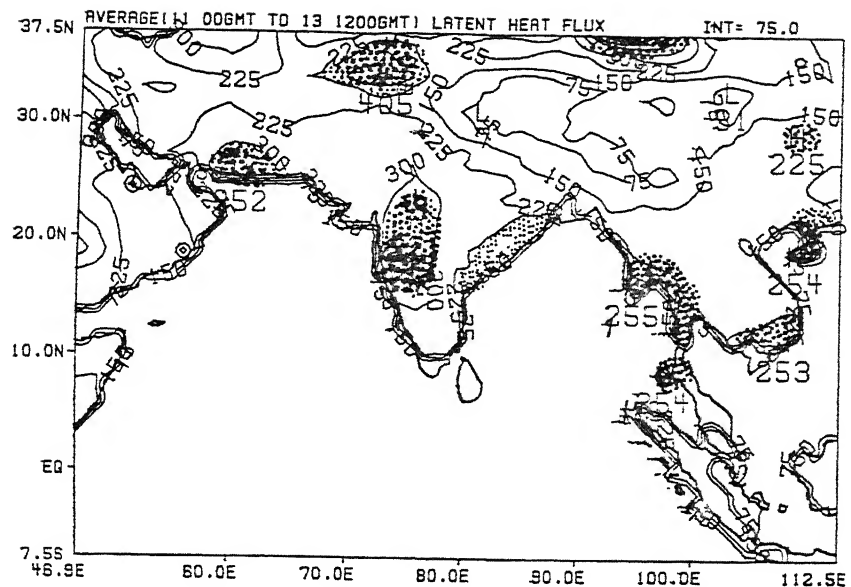
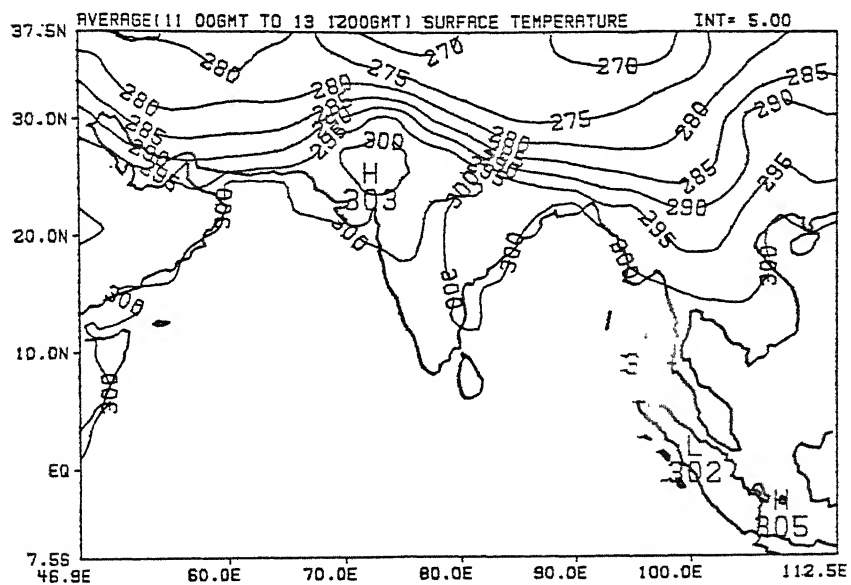


Figure 39 a, b, c and d: Maps showing GW at 12 hours interval as predicted by the model using new GW parameterization for (a) May 11 1979 00 UTC, (b) May 11 1979 12 UTC, (c) May 12 1979 00 UTC, and (d) May 12 1979 12 UTC.

maps are 12 hours apart. By referring to the observed rainfall shown earlier in figures 15a, 16a and 17a it can be inferred that soil moisture is very well predicted by the new scheme. Next figure 41 shows the predicted 3-day average surface temperature and latent heat flux. A comparison of figures 18-a, 18-c and 41-b shows that average latent heat flux using dynamic GW^{new} is enhanced compared to the predicted average F_L using specified ground wetness as GWM2 given by (5.5). Regions of high latent heat fluxes as seen in figure 18-a are better predicted with the new dynamic ground wetness compared to 18-c. Figure 42 shows the time series of predicted rainfall and ground wetness at two grid points located at 31.9 °N, 71.3 °E and 23.4 °N, 79.7 °E. In figures 43 and 44 time series of surface temperature and latent heat flux using old and new parameterization of GW are presented at the same grid points. The comparison shows that the diurnal changes in surface temperature and F_L are predicted better with the new parameterization scheme for GW. F_L with new scheme is enhanced for both the points. The results on the diurnal change of the ground temperature do not exhibit a sharp step function like behavior when the ground wetness is parameterized by the proposed regression approach. Two prominent features in these results are i) The amplitude of the latent heat fluxes from the regression based ground wetness parameterization are much larger in comparison to the estimate from the specific ground wetness: ii) The amplitude of the diurnal change is very well preserved cycle after cycle for the regression based ground wetness parameterization. The precipitation predictions using the new parameterization scheme are presented in the next chapter.



a



b

Figure 41: (a) Average latent heat flux (watts/m^2) for May 11 1979 00 UTC - May 13 1979 12 UTC predicted by the model using new GW parameterization. Shaded areas show the high values of latent heat flux. (b) Average (May 11 1979 00 UTC - May 13 1979 12 UTC) surface temperature ($^{\circ}\text{K}$) as predicted by the model in the above mentioned experiment.

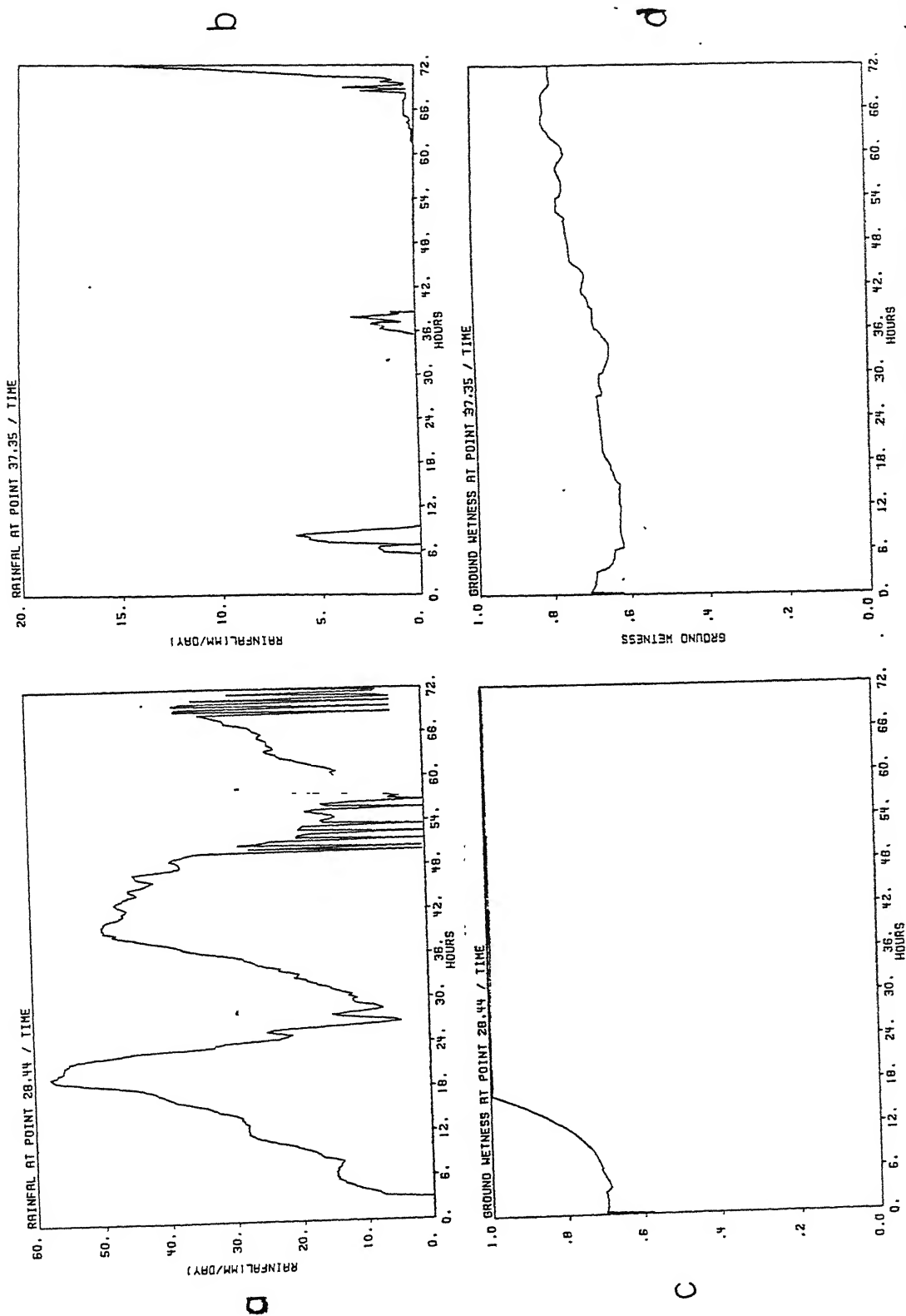


Figure 42: (a) and (b) are time series of model predicted rainfall using new GW parameterization for two grid points located at 31.9°N, 71.3°E and 23.4°N, 79.7°E respectively; (c) and (d) are the time series of model predicted GW for the above mentioned experiment at the same two grid points.

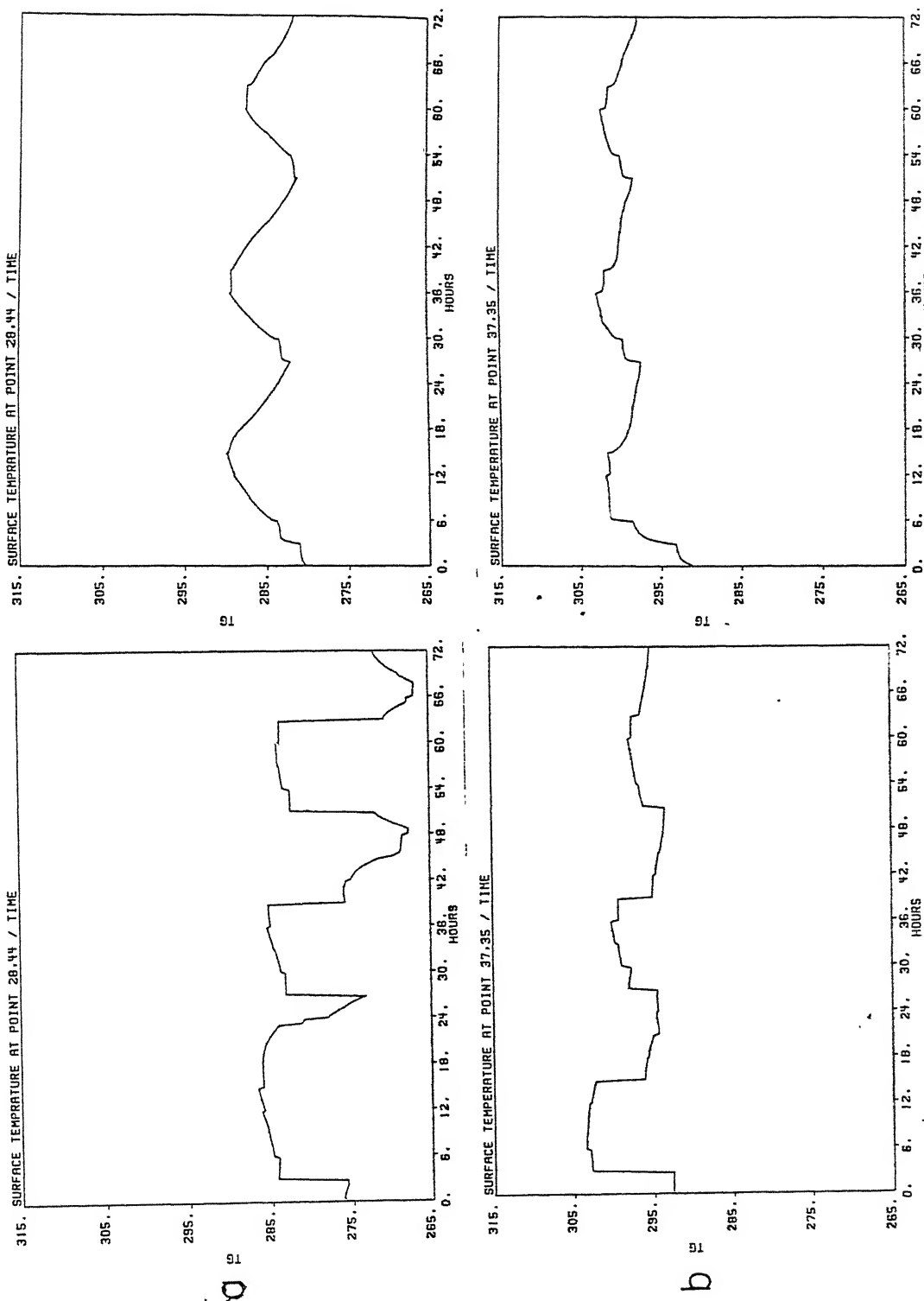


Figure 43: (a) and (b) are time series of model predicted surface temperature ($^{\circ}\text{K}$) using old GW parameterization for two grid points located at 31.9°N , 71.3°E and 28.4°N , 79.7°E respectively; (c) and (d) are the time series of model predicted surface temperature ($^{\circ}\text{K}$) using new GW parameterization for the above mentioned grid points.

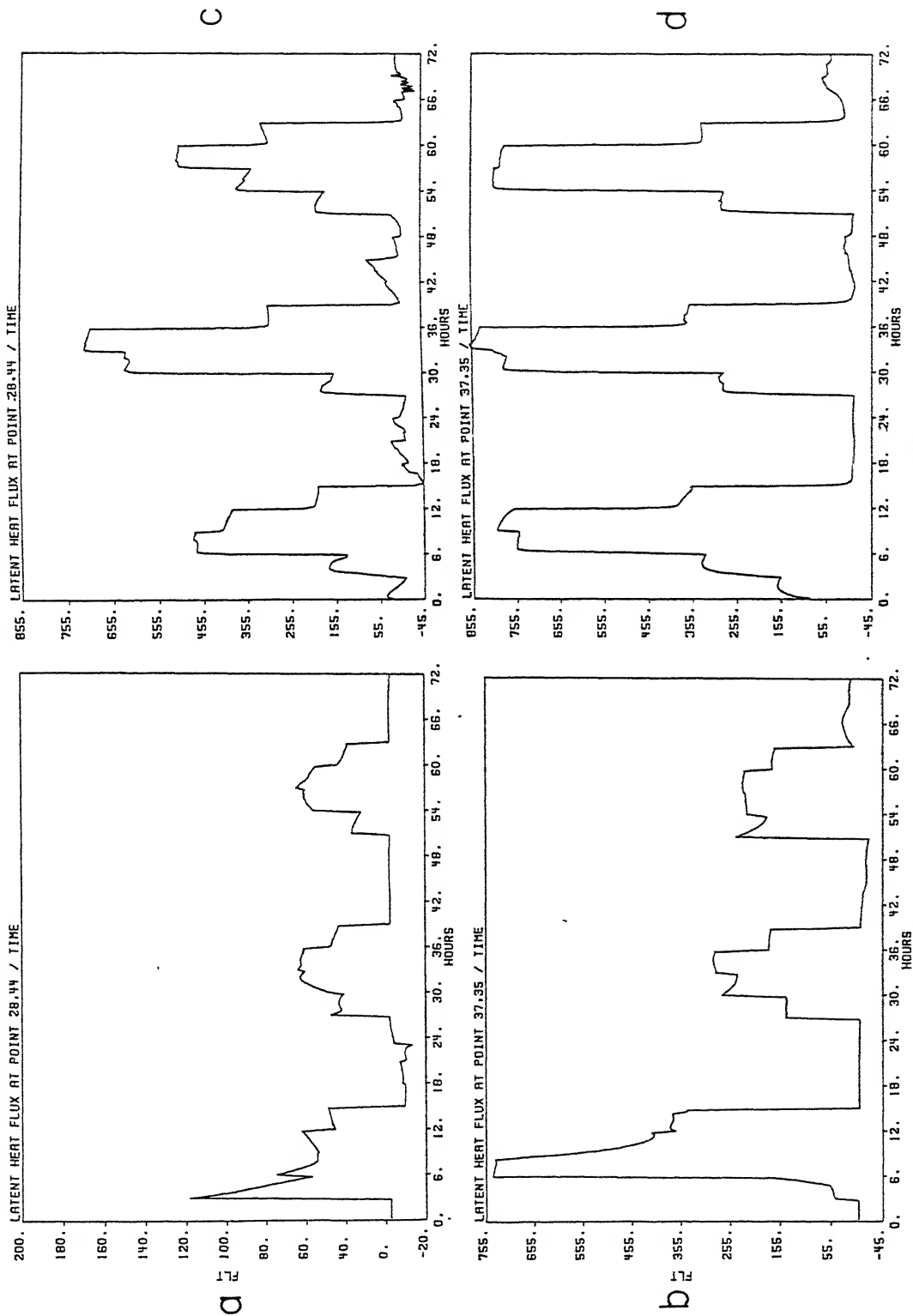


Figure 44: (a) and (b). Time series of surface latent heat flux (watts/m²) using old GW parameterization for two grid points located at 31.9°N, 71.3°E and 23.4°N, 79.7°E respectively, (c) and (d) are the time series of model predicted surface latent heat flux using new GW parameterization for the above mentioned grid points.

CHAPTER 6

SENSITIVITY OF RAINFALL PREDICTION TO GROUND

WETNESS AND RESOLUTION

In this Chapter we shall compare the results of forecasts on the sensitivity to the ground wetness parameterization, discussed in the previous Chapter, for two different horizontal resolutions. .

The specific example we explore here is the same case study that was discussed in Chapter 4 on the landfall of a tropical storm over southern India.

Two satellite photographs shown in figs. 45a and 45b illustrate the banded structure of the cloud cover of the tropical cyclone just prior to and after the landfall. These illustrations were obtained from the DMSP satellite. They describe the cloud cover at 10:00 am local time over India for May 12 and May 13, 1979, respectively. The cloud cover during these two days shows the typical structure of the tropical cyclone spiral rainbands. The dense cloud cover of the eye wall is also clearly portrayed by these illustrations. An open eye is also evident on the satellite picture of May 12th when the storm was over the ocean.

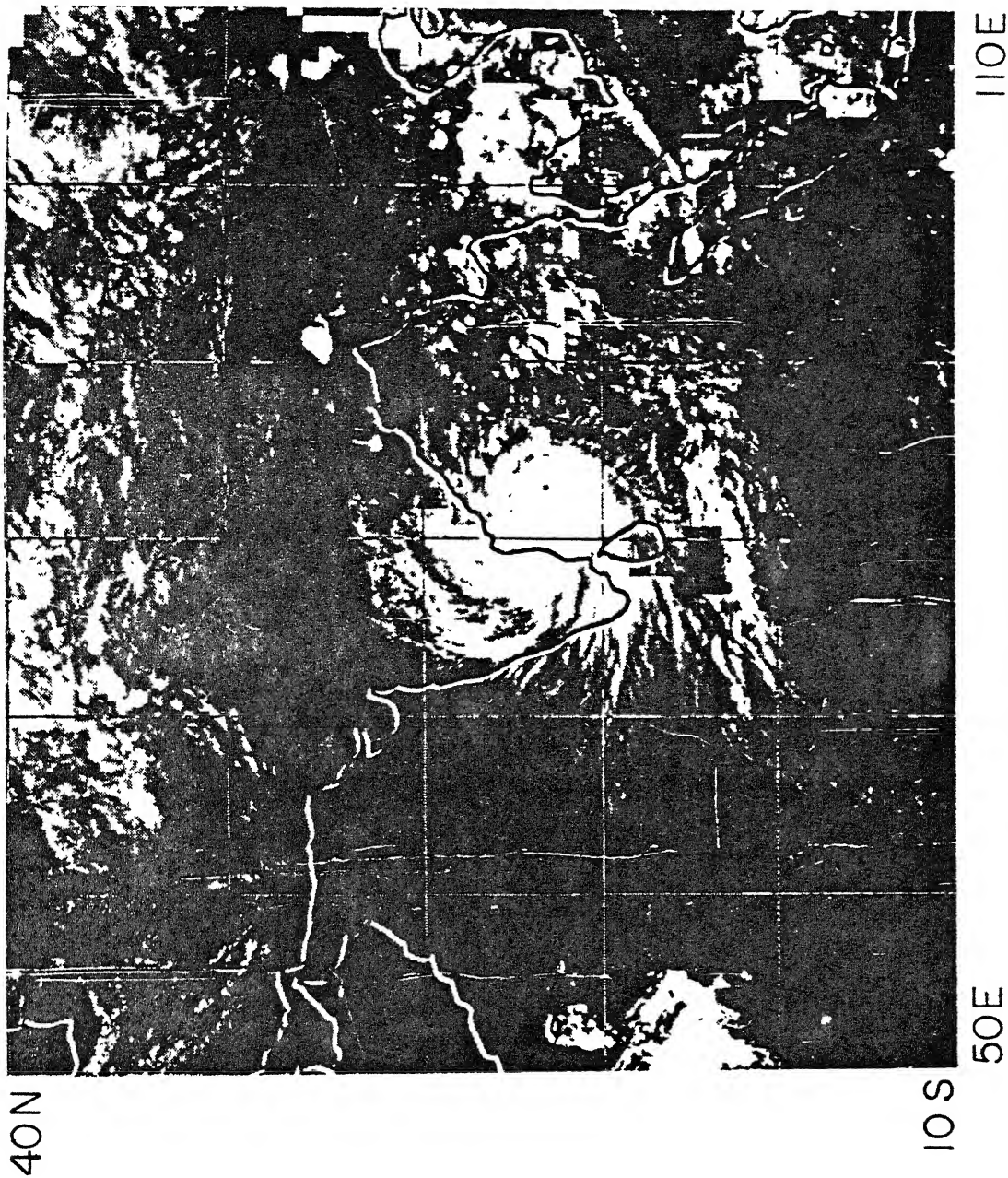


Figure 45a: Satellite photograph showing the cloud cover at 10:00 am local time over India for May 12, 1979.

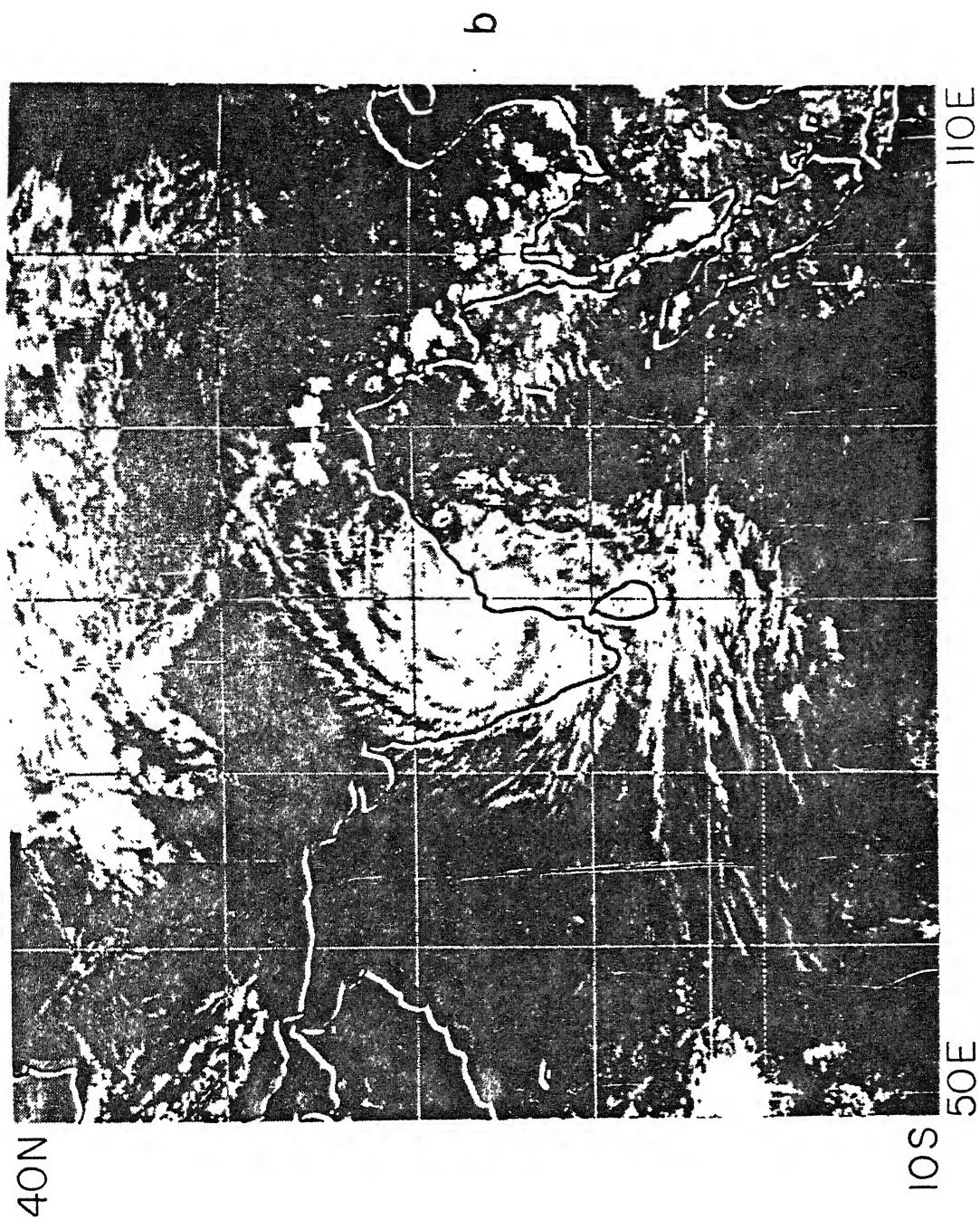


Figure 45b: Satellite photograph showing the cloud cover at 10:00 am local time over India for May 13, 1979.

It is of considerable interest to see the extent to which such features and details are revealed in the predicted rainfall fields. We shall next examine the 'observed' raingauge based rainfall records for these periods.

In figures 46a and 46b we show 24 hourly rainfall totals based on the FGGE data collections for the respective periods May 11 00 UTC to May 12 00 UTC and May 12 00 UTC to May 13 00 UTC. The observed rainfall amounts are derived from roughly 3000 raingauge sites over the domain illustrated here. The rainfall amounts were averaged over 1 degree latitude/longitude squares in order to smooth out local variability and to facilitate the illustration of this vast volume of data. A careful examination of these observed fields, shown in figures 46a and 46b clearly show a banded geometry in the rainfall distribution. The highest rainfall amounts are of the order of 100 to 160 mm/day in the near coastal regions of Madras and Andhra states.

In the control experiment the ground wetness was simply expressed as a function of the prescribed surface albedo. According to this formulation, the ground wetness has a strong inverse relationship to the surface albedo. In the parameterized ground wetness experiment the statistical relation, described in Chapter 5, was used. The remaining aspects of the model for these two sets of experiments were kept identically the same. Furthermore the data sets and the initial states were also identical. In a two to three day prediction experiment we do not expect a large impact from the parameterization of land surface processes. That is more of a climate issue; in climate modelling significant impact of surface wetness parameters have

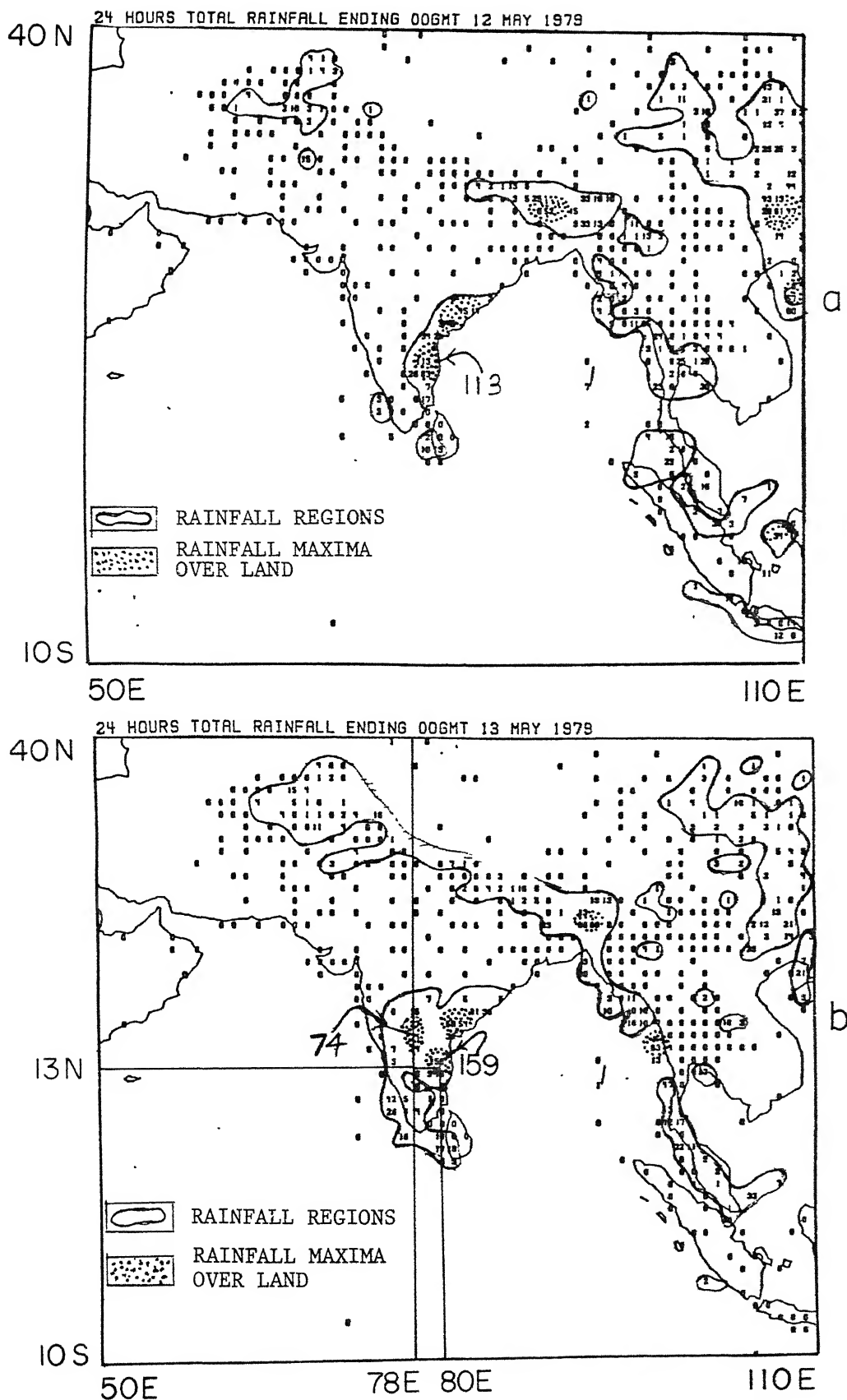


Figure 46: Accumulated 24 hour observed rainfall derived from raingauge data. Raingauge data has been averaged over 1 degree lat/long squares. (a) For the period May 11 1979 00 UTC to May 12 1979 00 UTC (b) For the period May 12 1979 00 UTC to May 13 1979 00 UTC.

been demonstrated by many investigators such as: Yamakazi (1989), Rind (1984) and several others mentioned in the previous chapter. Basically these studies show a major improvement in the climatological rainfall patterns with a time dependent modelling of the ground wetness. A reduced soil moisture causes a reduction in evaporation which in turn is shown to reduce the rainfall amounts in these studies. A motivation for carrying out the proposed present comparison study is to see if the parameterization scheme is stable and if it shows any measurable changes in the precipitation estimates within the considered time frame.

The other aspect of experimentation covered in this section is on the combined effects of resolution and ground wetness parameterization on the prediction. The increase of resolution does have a direct effect on the increase of vertical motion and rainfall rates. The increased rainfall provides an enhancement of the ground wetness parameterization and a positive feedback via latent heat fluxes towards further increase of rainfall can be expected.

The spiral rainbands in a hurricane have been studied for a number of years. In the context of numerical weather prediction models the simulation of the convection along the spiral rainbands and along the eye wall of a hurricane is recognized as a problem of major interest.

Three dimensional hurricane forecasting (or simulation) studies began with the efforts of Anthes et al. (1971) and Miller et al. (1972). In recent years Yamasaki (1986 and 1989) has reported on some

of the major developments in the simulation and prediction of hurricanes including their rainbands and the eye wall. These recent improvements included the development of a new cumulus parameterization scheme. Yamasaki (1975) developed a non-hydrostatic cloud ensemble model which was forced in a prescribed large scale environment. By carrying out three dimensional integration in such a model, Yamasaki generated the heating, moistening and rainfall rates by the cloud ensemble as functions of the prescribed large scale conditions. With the data sets thus generated, he developed a cumulus parameterization scheme for tropical numerical weather prediction. This led to the successful simulation of hurricanes with realistic structures, Yamasaki (1986, 1989). These studies basically showed a large frictional control in the formation of rainbands of a hurricane. The inflow angle of the spiral bands, and the number of bands seem to be controlled by the specification of the surface layer physics which were based in Yamasaki's studies on the conventional bulk-aerodynamic formulae. Our present modelling effort utilizes the similarity theory in the surface constant-flux layer. The surface exchange coefficients are stability dependent.

The results of our present study show a very reasonable prediction of the rainbands of the tropical cyclone that made its landfall over eastern India. The results of rainfall forecast for the control experiment and ground wetness parameterization experiment at two different resolutions are presented in the following sections.

6.1 Rainfall prediction at 1° latitude/longitude resolution:

The predicted rainfall rates for the first 24 hours and second 24 hours for 1° latitude/longitude resolution are respectively presented in figures (47 a,b) and (48 a,b). In both the figures, panel (a) is predicted rainfall from the forecast using simple ground wetness parameterization (based on surface albedo) and panel (b) shows predicted rainfall from the forecast using improved ground wetness parameterization (as discussed in chapter 4). By comparing the figures (47 a,b and 48 a,b) with the corresponding observed rainfall rates presented in figures (46 a,b) the sensitivity of the rainfall prediction to the ground wetness can be observed. It is clearly seen that rainfall rates over the land are enhanced in the new ground wetness experiment. For the first 24 hour rainfall, the rainfall over Bangladesh, South-East coast of India and Burma-Thailand coast is predicted better in the forecast using new ground wetness scheme. Similarly for the second 24 hours rainfall the position and intensity of rainfall maxima over land as shown by the shaded areas in these figures are better predicted by the new ground wetness forecast.

6.2 Rainfall prediction at 0.5° latitude/longitude resolution:

Figures (49 a,b) and (50 a,b) show respectively the first 24 hours and second 24 hours predicted rainfall for a forecast at horizontal resolution 0.5° latitude/longitude. Panel (a) in these diagrams shows the results for the simple representation of ground wetness while panel (b) shows the results for the improved ground wetness parameterization. At this horizontal resolution of the model

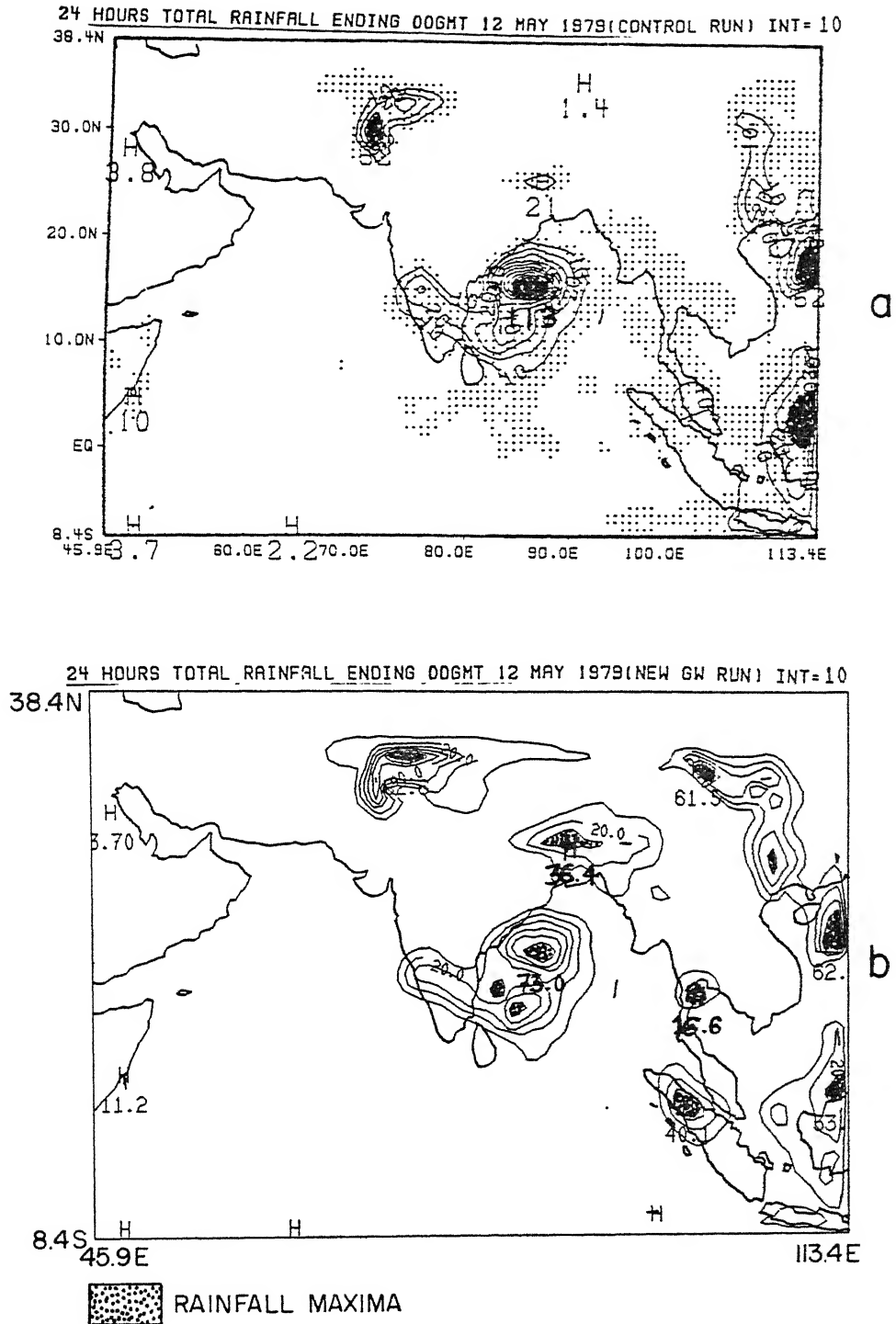


Figure 47: Accumulated 24 hour predicted rainfall for the period May 11 1979 00 UTC to May 12 1979 00 UTC. Model resolution is .9375° lat/long. (a) From a control experiment using old GW parameterization (b) From a sensitivity experiment using new GW parameterization.

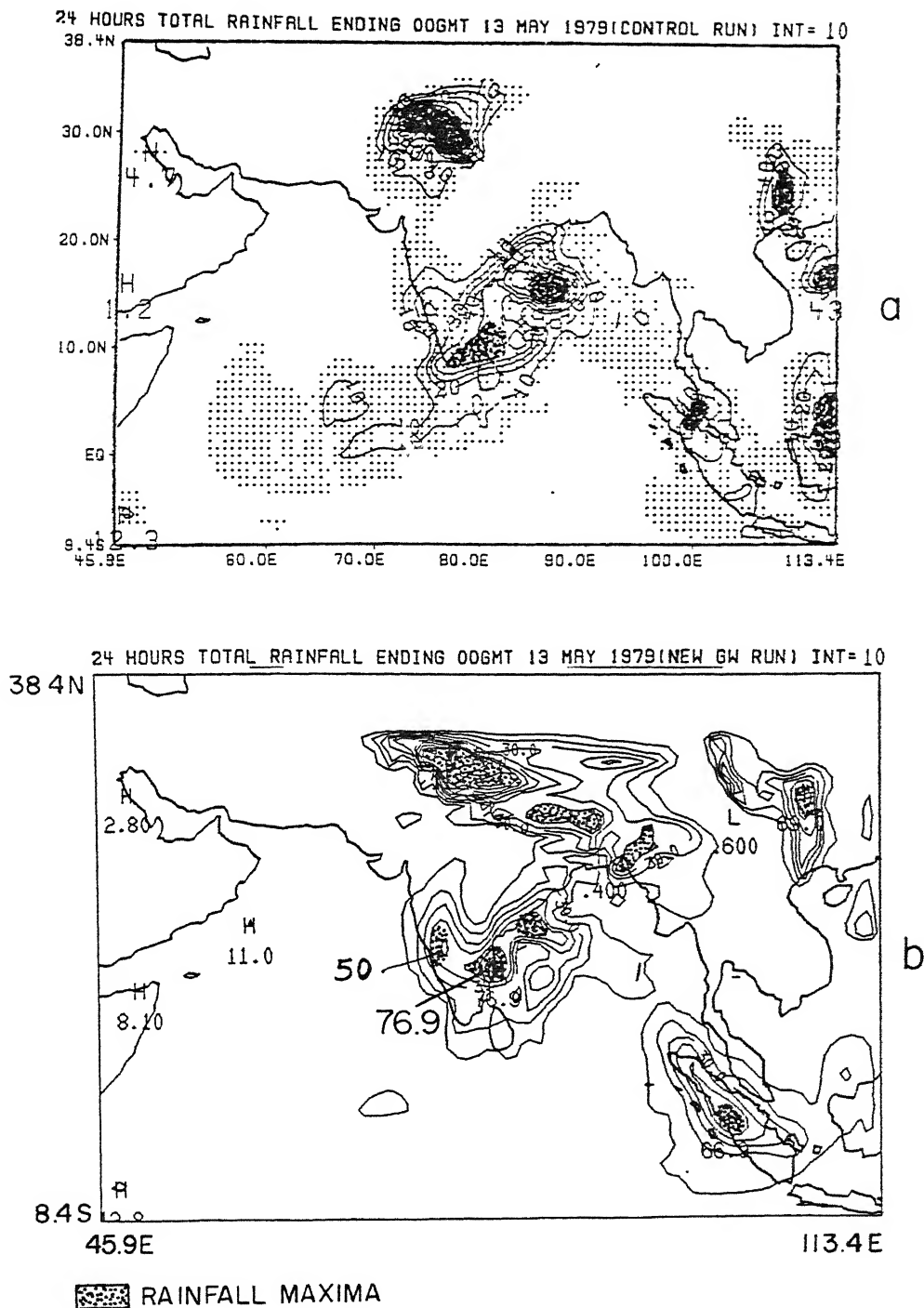
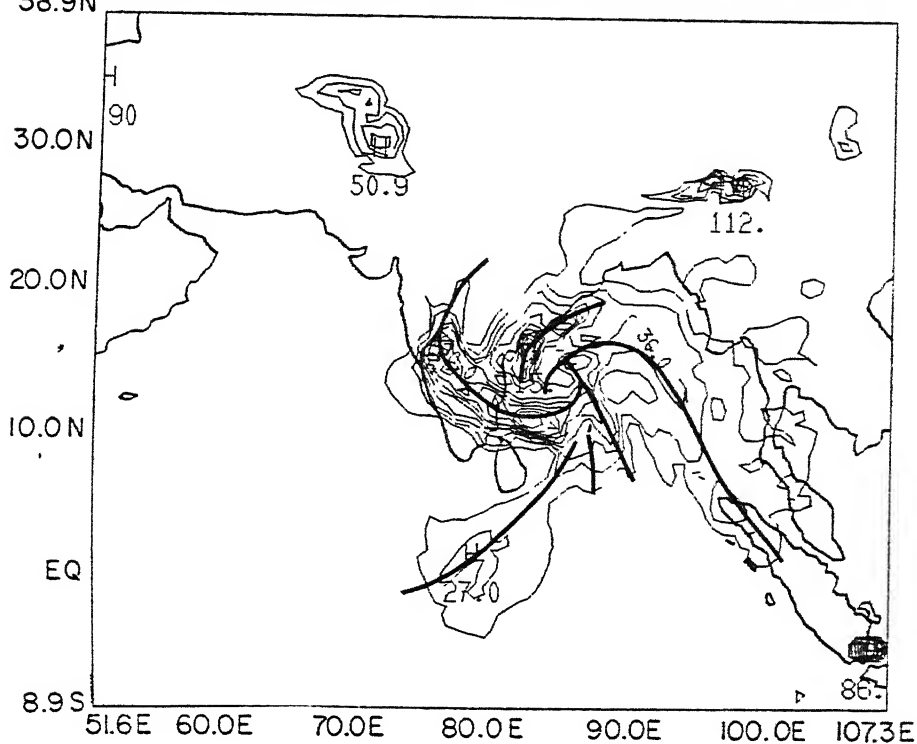


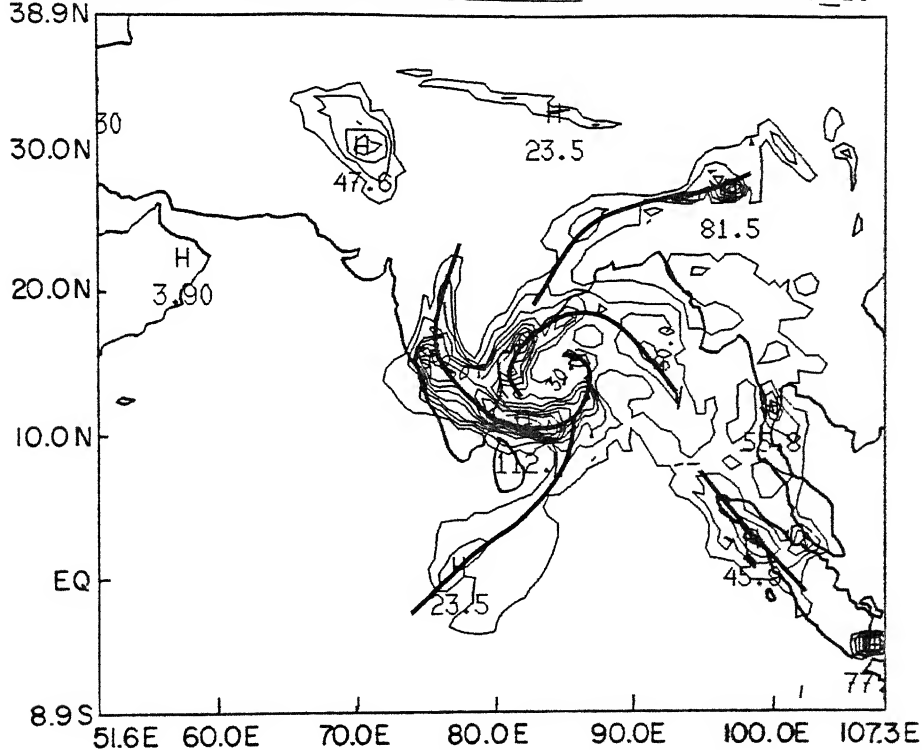
Figure 48: Accumulated 24 hour predicted rainfall for the period May 12 1979 00 UTC to May 13 1979 00 UTC. Model resolution is $.9375^\circ$ lat/long. (a) From a control experiment using old GW parameterization (b) From a sensitivity experiment using new GW parameterization.

24 HOURS TOTAL RAINFALL ENDING 00GMT 12 MAY 1979 (CONTROL RUN) INT=10
38.9N



a

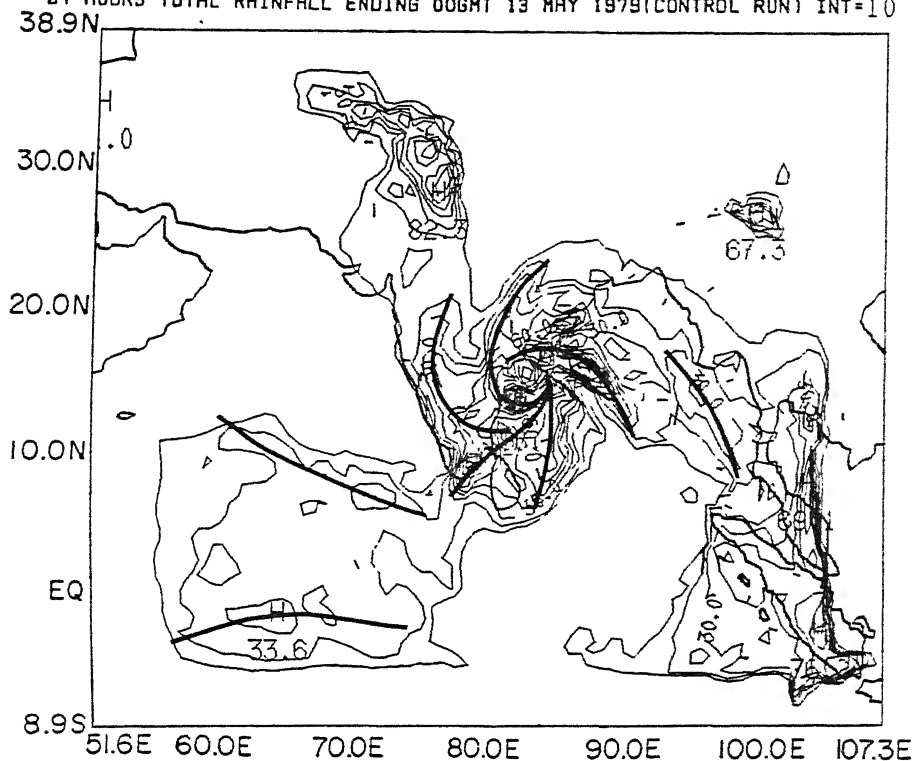
24 HOURS TOTAL RAINFALL ENDING 00GMT 12 MAY 1979 (NEW GW RUN) INT=10
38.9N



b

Figure 49: Accumulated 24 hour predicted rainfall for the period May 11 1979 00 UTC to May 12 1979 00 UTC. Model resolution is $.46875^\circ$ lat/long. Rainbands are highlighted by solid lines. (a) From a control experiment using old GW parameterization (b) from a sensitivity experiment using new GW parameterization.

24 HOURS TOTAL RAINFALL ENDING 00GMT 13 MAY 1979(CONTROL RUN) INT=10



24 HOURS TOTAL RAINFALL ENDING 00GMT 13 MAY 1979(NEW GW RUN) INT= 10

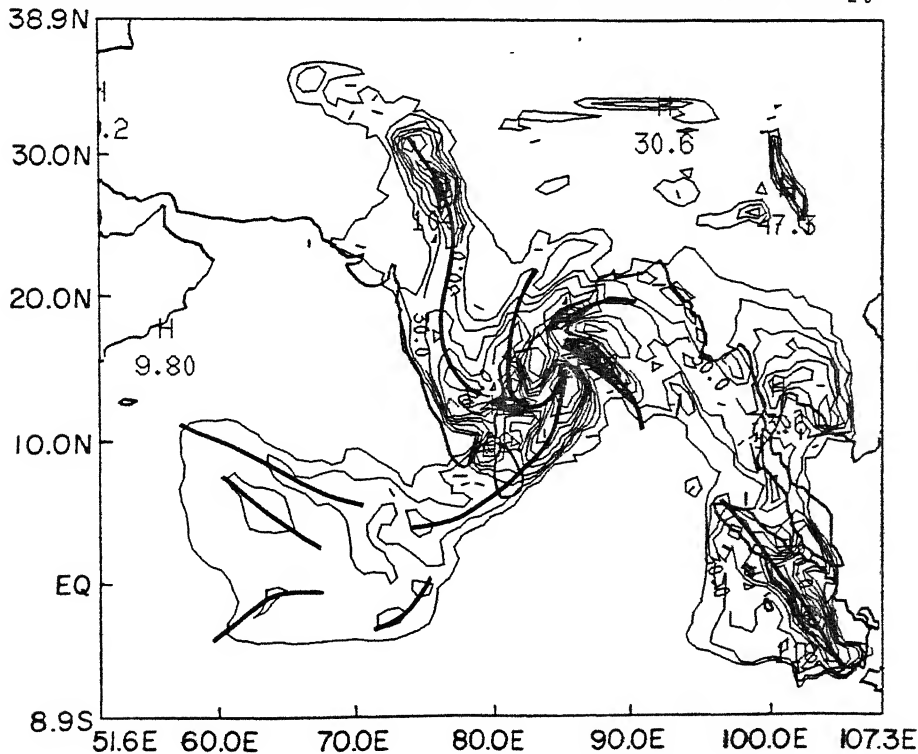


Figure 50: Accumulated 24 hour predicted rainfall for the period May 12 1979 00 UTC to May 13 1979 00 UTC. Model resolution is $.46875^\circ$ lat/long. Rainbands are highlighted by solid lines. (a) From a control experiment using old GW parameterization (b) From a sensitivity experiment using new GW parameterization.

both the experiments produce rainbands. However, there is an interesting and important positive impact from the improved ground wetness parameterization. The 0-24 and 24-48 hours rainfall rates shown in these figures bear a very strong resemblance to the banded structures of the satellite photographs shown in figures 45 (a,b). The location of the central areas of the spiralling predicted rainfall bands and the satellite cloud cover both converge to the same general storm center. The error in the location of the storm center is quite small at both the 24 and 48 hour panels in particular for the improved ground wetness parameterization experiment. A number of details of banded structure over south eastern Arabian sea, peninsular India, Bay of Bengal and Malay-Indonesia regions are very well represented. As stated earlier there are, however, some major differences in the predictions with the two representations of the ground wetness parameterization.

The differences between the rainfall estimates for the two ground wetness parameterization experiments are presented in figures 51 (a) and (b). Panel (a) shows the difference for first 24 hours rainfall and panel (b) shows the difference for second 24 hours rainfall. The shaded areas in these figures show the regions where the rainfall rates predicted by the new ground wetness experiment are higher compared to the control model run (using simple parameterization for GW). The banded structure of the rainfall is enhanced in the new ground wetness experiment. The rainfall over land is in general higher with the new GW scheme. In particular some major improvements in the second day rainfall prediction over Southern India with the new GW

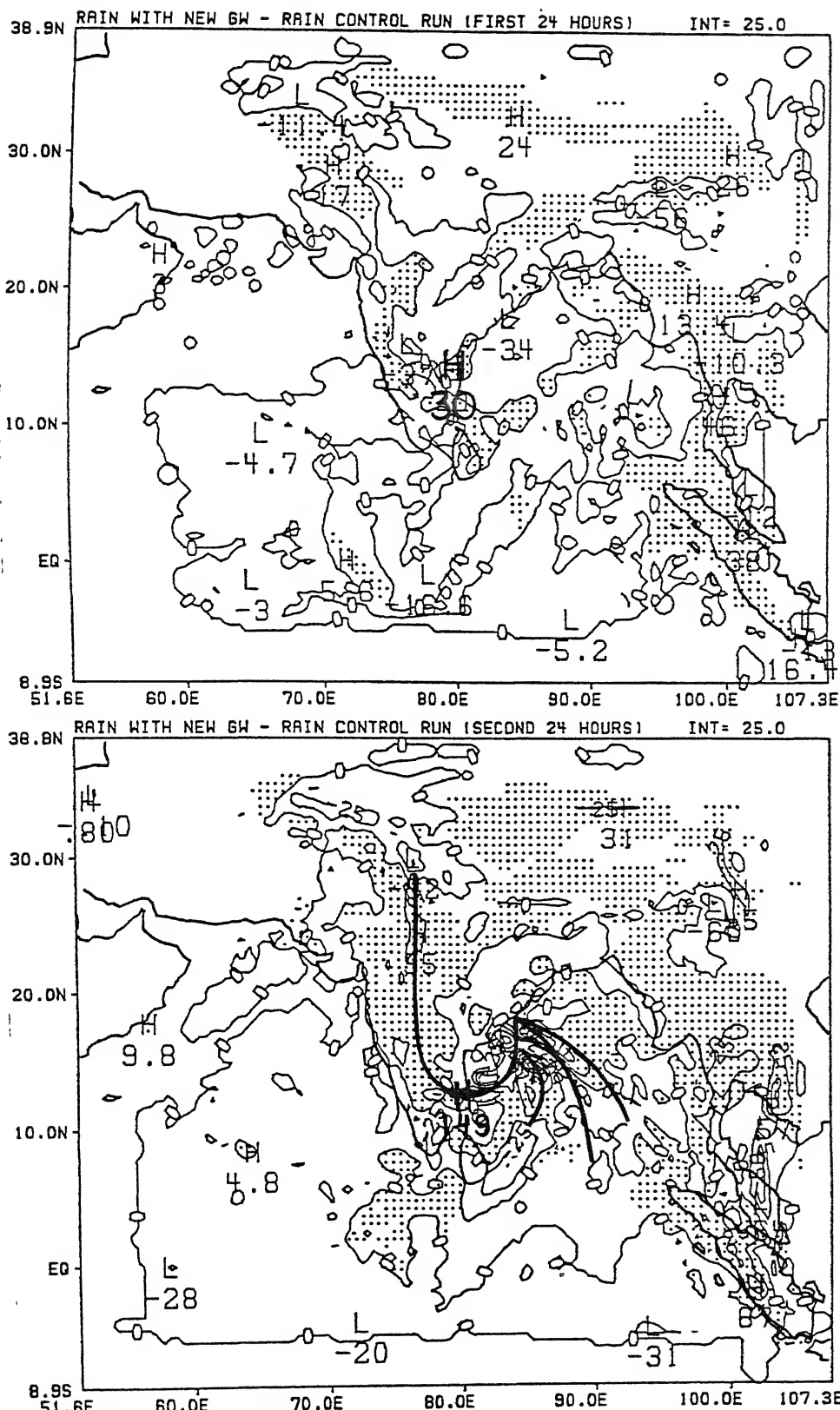


Figure 51: The difference in 24 hour predicted rainfall between model forecasts using old and new GW parameterization for .46875° lat/long resolution for the period (a) May 11 1979 00 UTC to May 12 1979 00 UTC and (b) May 12 1979 00 UTC to May 13 1979 00 UTC. The shaded regions indicate rainfall with new GW > rainfall with old GW.

scheme are shown in figures 52 (a) and (b). These figures are the same as figures 50 (a) and (b) but the contouring interval in these diagrams is 25 mm/day. On the South-East coast of India around 80° E and 13° N very heavy rainfall was observed as seen in figure 46 (b) for the period May 12 1979 00 UTC to May 13, 1979 00 UTC. The arrival of this heavy rainfall is very well predicted by the forecast using new GW scheme as seen in figure 52 (b). The position and magnitude of rainfall center over land is in very good agreement with the observed rainfall. In the control experiment there is a rainfall maximum over the ocean located at 82° E, 13° N and the rainfall over land around 80° E, 13° N is of the order of 50 mm/day, which is under predicted. Similarly the rainfall over South-Central India along the 78° E longitudinal line is very well predicted by the forecast using new GW scheme. The maximum rainfall along this line over Southern India is of the order of 75 mm/day from this forecast which is the same as raingauge observed rainfall. Whereas in the control run maximum rainfall along this line is of the order of 50 mm/day. Overall the precipitation pattern shows a closer agreement to the observed raingauge estimates for the prediction with the new ground wetness parameterization.

Finally, it is observed from these results that the impact of ground wetness parameterization is more on the second day rainfall forecasts. This confirms the fact that a realistic parameterization of ground wetness is very important for rainfall forecasts on larger time scales.

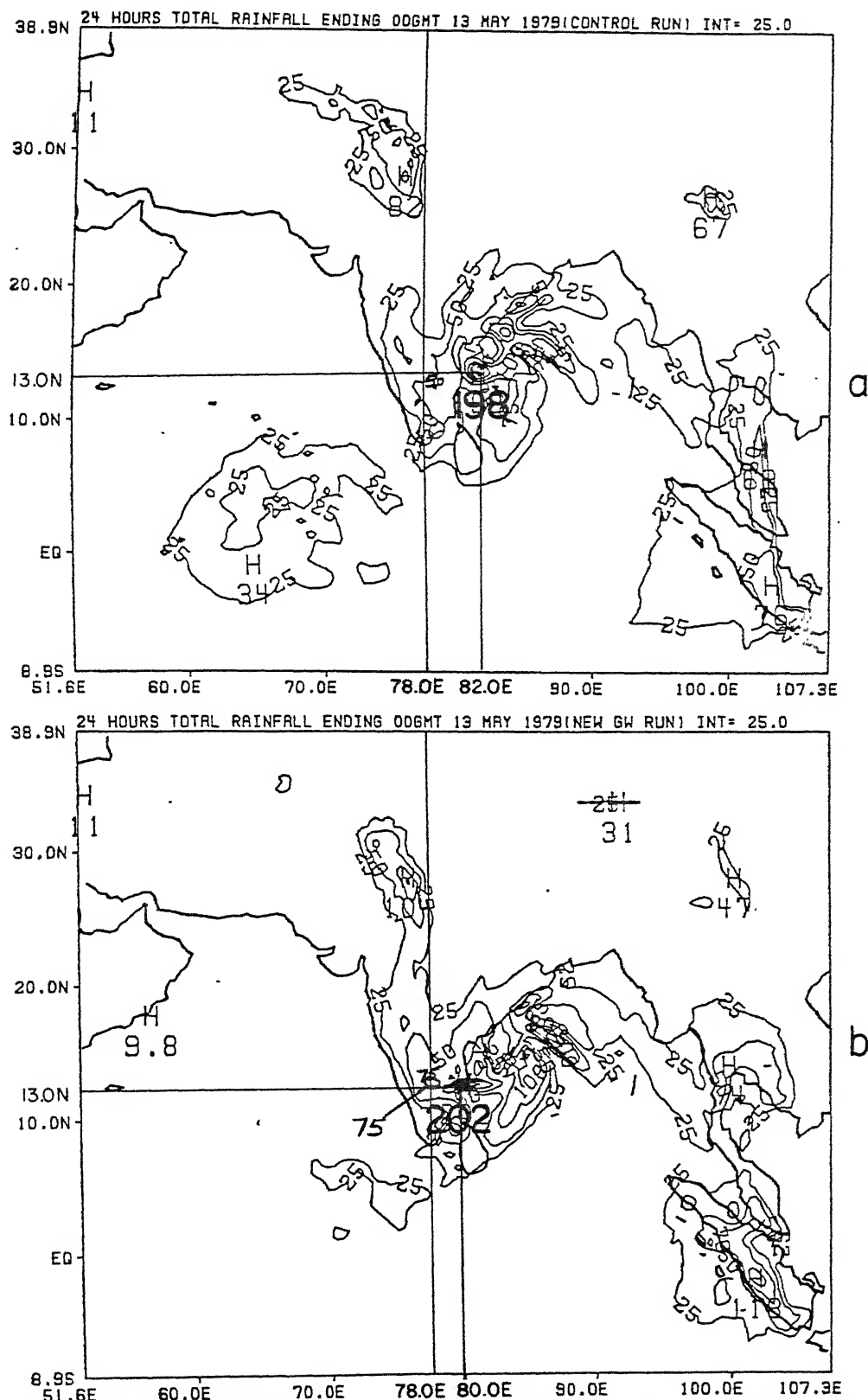


Figure 52: Accumulated 24 hour predicted rainfall for the period May 12 1979 00 UTC to May 13 1979 00 UTC. Model resolution is .46875° lat/long. (a) From a control experiment using old GW parameterization (b) From a sensitivity experiment using new GW parameterization. This figure is same as figure 50 a, b but the contouring interval is 25 mm/day.

CHAPTER 7

CONCLUSION

The most important results of this study are (1) the numerical prediction of the detailed rainbands of tropical cyclone as it made its landfall over India and (2) the improvement of rainfall rates prediction over the land using the new ground wetness parameterization scheme. The mechanism for the formation of rainbands are not addressed in this thesis. The high resolution model advects the cyclonic storm to nearly its correct position over southern India and the bands are nearly correctly located as compared to rather complex bands from a high resolution satellite photograph. These results pertain to roughly 48 hours after the initial state. The horizontal resolution of the model was roughly 50 km. At a resolution of approximately 100 km, these banded features were not adequately resolved. The impact of improved ground wetness was observed to be more on the second day rainfall prediction. The overall conclusion of the forecast experiment presented in chapter 4 is that the circulation forecasts made by the model are of quite high accuracy. However the details of the precipitation forecasts are reasonably good on the synoptic scale but require further improvements on the meso-scale.

The success of these results have a bearing on many aspects of the model development that are addressed in this thesis.

- The semi-Lagrangian advective scheme is shown to be a powerful method for the handling of the nonlinear advective terms. In the context of the shallow water equation this scheme has been shown to conserve the parcel and domain invariants very well to within 1% for periods of the order of 5 days.

- The computation time was saved by a factor of 4 to 5 from the use of a semi-implicit time differencing scheme. In comparison, the use of explicit time differencing, takes considerably more computer resources.

- The use of Arakawa c-grid with a staggering in the horizontal has enabled us to simplify the lateral boundary conditions for the pressure functions.

- The solution of a three dimensional Helmholtz equation was simplified from the use of a similarity transformation. This has enabled us to transform this problem into a series of two dimensional Helmholtz equations, these were solved from the use of a fast tri-diagonal matrix solver.

- The use of dynamic normal model initialization was found to adequately describe the initial divergence and precipitation fields. This scheme developed by Sugi (1981) seems to converge quite rapidly at the highest horizontal resolution (≈ 50 km) presented here.

- The use of steep mountains, called 'envelope orography' was incorporated into the prediction model. This has enabled the incorporation of steep mountains such as the Himalayas, the western Ghats and other orographic features around the Indian subcontinent.

- The modified Kuo's scheme, as used in the present study, was shown to handle precipitation rates that well exceed 100 mm/day.

- Although no sensitivity studies on the radiative transfer formulations are presented here, the model does include a state-of-the-art band model. This band model evaluates the transfer of short and longwave irradiances in the presence of modelled clouds, diurnal change and surface energy balance.

- An area where considerable research was carried out is the area of surface flux calculations of latent heat. Here a parameterization procedure for the ground wetness parameter was first developed. This required diagnostic calculations of moisture budget from atmospheric observations. Vertical integral of the moisture budget provided a data base for the surface flux of latent heat. These fluxes were incorporated into surface energy balance. Thereafter using surface similarity theory a data base for the ground wetness parameter was generated. The data for the ground wetness was next statistically regressed against a number of prediction model parameters and a parameterization of the ground wetness parameter was derived. This parameterization was next used in prediction experiments and compared with more conventional parameterization of the

ground wetness. The results of these experiments provided the best results at high resolution and from the use of the parameterized ground wetness parameter.

- The use of the parameterized ground wetness parameter was shown to provide a reasonable diurnal cycle of the ground temperature and surface fluxes. The later were in close agreement with values obtained from observed moisture budget estimates.

This study has several limitations. Perhaps the most obvious one is the lack of use of predicted boundary conditions. The specified boundary conditions used here are so called 'perfect values' based on observation. This seems to provide the best results. The forecasts were seen to degrade from the use of time invariant or global model forecast based boundary values. Further work is needed in this area. The model is quite sensitive to the use of various physical parameterizations such as cumulus convection and the planetary boundary layer. The ground wetness parameterization developed in this work does not make use of the vegetation cover over land. Further detailed sensitivity studies are required to provide a better understanding in these areas. In order to address the predictability over the monsoon region a larger number of experiments are needed.

REFERENCES

- Anthes, R.A., 1977: A cumulus parameterization scheme utilizing a one-dimensional cloud model. Mon. Wea. Rev., 105, 270-286.
- Anthes, R.A., S.L. Rosenthal, and J.W. Trout, 1971: Preliminary results from an asymmetric model of the tropical cyclone. Mon. Wea. Rev., 99, 744-758.
- Arakawa, A., and V.R. Lamb, 1977: Computational design of the basic dynamical process of the UCLA general circulation model. Methods in Computational Physics, 17, Academic Press, 173-265.
- Asselin, R., 1972: Frequency filter for time integrations. Mon. Wea. Rev., 100, 487-490.
- Bates, J.R. and A. McDonald, 1982: Multiply-upstream, semi-Lagrangian advective schemes: analysis and application to a multi-level primitive equation model. Mon. Wea. Rev., 110, 1831-1842.
- Benjamin, S.G., 1983: Some Effects of Surface Heating and Topography on the Regional Severe Storm Environment. Ph.D. thesis, Department of Meteorology, The Pennsylvania State University, 265 pp.
- Blackadar, A.K., 1962: The vertical distribution of wind and turbulent exchange in a neutral atmosphere, J. Geo. Res., 67, 3095-3102.
- Blackadar, A.K., 1979: High resolution models of the planetary boundary layer. Advances in Environmental Science and Engineering, 1, No. 1, Pfaffin and Ziegler, eds., Gordon and Breach Sci. Pub., New York, 50-85.
- Bougeault, P., 1985: A simple parameterization of the large-scale effects of deep cumulus convection. Mon. Wea. Rev., 113, 2108-2121.
- Brown, J. and K. Campana, 1978: An economical time-differencing system for numerical weather prediction. Mon. Wea. Rev., 106, 1125-1136.
- Burridge, D.M. and J. Haseler, 1977: A model for medium-range weather forecasting: adiabatic formulation. Technical report no. 4, ECMWF (available from ECMWF, Shinfield Park, Reading, Berkshire RG29AX, UK).
- Businger, J.A., J.C. Wyngaard, Y. Izumi and E.F. Bradley, 1971: Flux profile relationship in the atmospheric surface layer. J. Atmos. Sci., 28, 181-189.

- Cadet, D., 1983: Mean fields of precipitable water over the Indian Ocean during 1979 summer monsoon from TIROS-N soundings and FGGE data, Tellus, 35 B, 329-345.
- Carson, D.J. and A.B. Sangster, 1981: The influence of land-surface albedo and soil moisture on general circulation model simulations. Research activities in atmospheric and oceanic modelling (Ed. I.D. Rutherford). Numerical Experimentation Programme Report No. 2, pp. 5.14-5.21.
- Chang, L.W., 1978: Determination of surface flux of sensible heat, latent heat, and momentum utilizing the Bulk Richardson number. Papers in Meteor. Res., 1, 16-24.
- Charney, J.G., 1975: Dynamics of deserts and droughts in the Sahel. Quart. J. R. Met. Soc., 101, 193-202.
- Charney, J.G., W.J. Quirk, S.H. Chou, and J. Kornfield, 1977: A comparative study of the effects of albedo change on drought in semi-arid regions. J. Atmos. Sci., 34, 1366-1385.
- Chen, J.H. and K. Miyakoda, 1974: A nested grid computation for the barotropic free surface atmosphere, Mon. Wea. Rev., 102, 181-190.
- Chou, M.D., 1984: Broadband water vapor transmission functions for atmospheric IR flux computations. J. Atmos. Sci., 41.
- Chou, M.D. and L. Peng, 1983: A parameterization of the absorption in the 15 μm CO_2 spectral region with application to climate sensitivity studies. J. Atmos. Sci., 40, 2183-2192.
- Davies, H.C., 1976: A lateral boundary formulation for multi-level prediction models. Quart. J. Roy. Meteor. Soc., 102, 405-418.
- Davies, H.C., 1983: Limitations of some common lateral boundary schemes used in regional NWP models, Mon. Wea. Rev., 111, 1002-1112.
- Davies, R., 1982: Documentation of the solar radiation parameterization in the GLAS climate model. NASA Tech. Mem. 83961, Goddard Space Flight Center, Greenbelt, MD 20771.
- Deardorff, J.W., 1972: Parameterization of the planetary boundary layer for use in general circulation models. Mon. Wea. Rev., 100, 93-106.
- Del sol, F., K. Miyakoda and R. Clarke, 1971: Parameterized processes in the surface boundary layer of an atmospheric circulation model. Q.J. Roy. Met. Soc., 97, 181-208.
- Dickinson, R.E., 1984: Modelling evapotranspiration for three-dimensional global climate models. Geophysical Monograph, 29, A.G.U.

- Douglas, M.W., 1987: The Structure and Dynamics of Monsoon Depressions. Ph.D. thesis, Department of Meteorology, The Florida State University, 273 pp.
- Eliassen, A., 1956: A procedure for numerical integration of the primitive equations of the two-parameter model of the atmosphere. Sci. Rept. no. 4, Department of Meteorology, UCLA.
- Errico, R.M., 1986: Initialization of the FSU/NCAR Mesoscale Model. NCAR Technical Note, NCAR/TN-270+IA, 120 pp.
- Gadd, A.J. and J.F. Keers, 1970: Surface exchanges of sensible and latent heat in a 10-level model atmosphere. Quart. J. Roy. Meteor. Soc., 96, 297-308.
- Geleyn, J.-F. and Hollingsworth, A., 1979: An economical analytical method for the computation of the interaction between scattering and line absorption of radiation. Beitr. Phys. Atmos., 52, 1-16.
- Geleyn, J.F., 1985: On a simple, Parameter-free Partition between moistening and precipitation in the Kuo scheme. Mon. Wea. Rev., 43, 405-407.
- Haiyan He, J.W. McGinnis, Z. Song and M. Yanai, 1987: Onset of the Asian Summer Monsoon in 1979 and the effect of the Tibetan Plateau. Mon. Wea. Rev., 115, 1966-1995.
- Haltiner, G.J., 1971: Numerical weather prediction. John Wiley and Sons, 317 pp.
- Hansen, J. and others, 1983: Efficient three-dimensional global models for climate studies: Models I and II. Mon. Wea. Rev., 111, 609-662.
- Harshvardhan and T.G. Corsetti, 1984: Longwave parameterization for the UCLA/GLAS GCM. NASA Tech. Mem. 86072, Goddard Space Flight Center, Greenbelt, MD 20771.
- Heckley, W.A., 1984: A review of numerical experimentation at the ECMWF with emphasis on tropical prediction. GARP Special Report No. 44, WMO, Geneva, Chapter IV, 1-21. Available from World Meteorological Organization, Geneva, Switzerland.
- Kallberg, P.N. and J.K. Gibson, 1977: Lateral boundary conditions for limited area version of ECMWF model, WGNE Progress rep. no. 14, WMO, 103-105.
- Kanamitsu, M. 1975: On numerical prediction over a global tropical belt. Report No. 75-1, Dept. of Meteorology, Florida State University, Tallahassee, Florida, 32306, 282 pp.

- Kitoh, A., K. Yamazuki and T. Tokioka, 1988: Influence of soil moisture and surface albedo changes over the African tropical rain forest on summer climate investigated with the MRI.GCM-I. J. Meteor. Soc. Japan, 66, 65-86.
- Kondratyev, K. Ya., 1972: Radiation processes in the atmosphere. World Meteorological Organization Publication No. 309, Geneva, Switzerland, 214 pp.
- Krishnamurti, T.N., 1962: Numerical integration of primitive equations by quasi-Lagrangian advective scheme. J. Appl. Met., 1, 503-521.
- Krishnamurti, T.N., 1969: An experiment in numerical prediction in equatorial latitudes. Quart. J. Roy. Met. Soc., 95, 594-620.
- Krishnamurti, T.N., S. Cocke, R. Pasch and S. Low-Nam, 1983: Precipitation estimates from rain gauge and satellite observations summer MONEX, FSU Report No. 83-7, 373 pp.
- Krishnamurti, T.N., S. Low-Nam and R. Pasch, 1983a: Cumulus parameterization and rainfall rates II. Mon. Wea. Rev., 111, 815-828.
- Krishnamurti, T.N., K. Ingles, S. Cocke, T. Kitade and R. Pasch, 1984: Details of low latitude medium range numerical weather prediction using a global spectral model II. J. Met. Soc. Japan, 62, 613-649.
- Krishnamurti, T.N., Y. Ramanathan, H.-L. Pan, R.J. Pasch and J. Molinari, 1980: Cumulus parameterization and rainfall rates I, Mon. Wea. Rev., 108, 465-472.
- Kurihara, Y. and M.A. Bender, 1983: A numerical scheme to treat the open lateral boundary of a limited area model. Mon. Wea. Rev., 111, 445-459.
- Lacis, A.A. and J.E. Hansen 1974: A parameterization for the absorption of solar radiation in the earth's atmosphere. J. Atmos. Sci., 31, 118-133.
- Lax, P., and B. Wendroff, 1964: Difference schemes for hyperbolic equations with high order of accuracy. Communications on Pure and Applied Mathematics, 17, 381-398.
- Lepas, J., G. Le Goff, G. de Moor, L. Musson-Genon, M.C. Pierrard, J.P. Rocafort et D. Rousseau, 1979: Amethyste project report No. 2. EERM Internal Note No. 36 (in French).
- Leslie, L.M., G.A. Mills and D.J. Gauntlett, 1981: The impact of FGGE data coverage and improved numerical techniques in numerical weather prediction in the Australian region. Quart. J. Roy. Meteor. Soc., 107, 629-642.

- Louis, J.-F., 1979: A parametric model of vertical eddy fluxes in the atmosphere, Bound. Layer Meteo., 17, 187-202.
- Louis, J.F., M. Tiedtke, and J.F. Geleyn, 1981: A short history of the operational PBL-Parameterization at ECMWF. Workshop on Planetary Boundary Layer Parameterization, ECMWF, 25-27 November, 59-79 (available from ECMWF, Shinfield Park, Reading, Berkshire RG29AX, UK).
- Low-Nam, S.V., 1982: On the Impact of Data Sets in the Prediction of a Tropical Storm During Monex. M.S. thesis, Department of Meteorology, The Florida State University, 118 pp.
- Manabe, S., 1969a: Climate and the ocean circulation: I. The atmospheric circulation and the hydrology of the earth's surface. Mon. Wea. Rev., 97, 739-774.
- Mathur, M.B., 1970: A note on an improved quasi-Lagrangian advective scheme for primitive equations. Mon. Wea. Rev., 98, 214-219.
- Mathur, M.B., 1983: A quasi-Lagrangian regional model designed for operational weather prediction. Mon. Wea. Rev., 111, 2087-2098.
- McDonald, A., 1984: Accuracy of multiply-upstream, semi-Lagrangian advective schemes. Mon. Wea. Rev., 112, 1267-1275.
- McDonald, A., 1987: Accuracy of multiply-upstream, semi-Lagrangian advective scheme II. Mon. Wea. Rev., 115, 1446-1450.
- McDonald, A. and J.R. Bates, 1987: Improving the estimate of the departure point position in a two-time level semi-Lagrangian and semi-implicit scheme. Mon. Wea. Rev., 115, 737-739.
- McGregor, J.L. and L.M. Leslie, 1977: On the selection of grids for semi-implicit schemes. Mon. Wea. Rev., 105, 236-238.
- Mellor, G.L. and T. Yamada, 1974: A hierarchy of turbulence closure models for planetary boundary layers. J. Atmos. Sci., 34, 1791-1806.
- Mesinger, F. and A. Arakawa, 1976: Numerical methods used in atmospheric models. GARP Publication Series No. 14, WMO/ICSU Joint Organizing Committee, 64 pp.
- Mesinger, F., 1977: Forward-backward scheme and its use in a limited area model. Beitr. Phys. Atmos., 50, 200-210.
- Miller, B.I., P.P. Chase and B.R. Jarvinen, 1972: Numerical prediction of tropical weather systems. Mon. Wea. Rev., 100, 825-835.

- Miller, M.J. and A.J. Thorpe, 1981: Radiation conditions for the lateral boundaries of limited-area numerical models. Quart. J. Roy. Meteor. Soc., 107, 615-628.
- Mintz, Y., 1984: The sensitivity of numerically simulated climates to land-surface boundary conditions. The Global Climate, J.T. Houghton (ed.), Cambridge Univ. Press, 79-105.
- Miyakoda, K., and A. Rosati, 1977: One way nested grid models: The interface conditions and numerical accuracy, Mon. Wea. Rev., 105, 1092-1107.
- Okamura, Y., 1975: Computational design of a limited-area prediction model, J. Met. Soc. Japan, 43, 175-188.
- Orlanski, I., 1976: A simple boundary condition for unbounded hyperbolic flows. J. Comput. Phys., 21, 251-269.
- Perkey, D.J. and C.W. Kreitzberg, 1976: A time dependent lateral boundary scheme for limited area primitive equation models, Mon. Wea. Rev., 104, 744-755.
- Pettit, E., 1951: The Sun and Stellar Radiation in Astrophysics, J. Hynek, Ed. New York, McGraw - Hill, pp. 703.
- Phillips, N.A., 1962: Numerical integration of the hydrostatic system of equations with a modified version of the Eliassen finite-difference grid. Proc. Intern. Symp. Numer. Weather Pred. in Tokyo, 109-120.
- Posey, J.W. and P.F. Clapp, 1964: Global distribution of normal surface albedo. Geofisica Internacional (Mexico), 4, 33-48.
- Rind, D., 1984: The influence of vegetation on the hydrologic cycle in a general circulation model. Geophysical Monograph, 29, American Geophysical Union, 73-91.
- Ritchie, H., 1986: Eliminating the interpolation associated with the semi-Lagrangian scheme. Mon. Wea. Rev., 114, 135-146.
- Ritchie, H., 1987: Semi-Lagrangian advection on a gaussian grid. Mon. Wea. Rev., 115, 608-619.
- Robert, A.J., J. Henderson, and C. Turnbull, 1972: An implicit time integration scheme for baroclinic models of the atmosphere. Mon. Wea. Rev., 100, 329-335.
- Robert, A.J., I.L. Yee and H. Ritchie, 1985: A semi-Lagrangian and semi-implicit numerical integration scheme for multi-level atmospheric models. Mon. Wea. Rev., 113, 388-394.

- Roberts, R.E., J. E. A. Selby, L. M. Biberman, 1976: Infrared continuum absorption by Atmospheric Water Vapor in the 8-12 μm window. Appl. Opt., 15, 2085-2090.
- Romanova, E.N., 1954: The influence of forest belts on the vertical structure of the wind and on the turbulent exchange. Study of the Central Geophysical Observatory, No. 44 (106), Glavnaia Geofizicheskaya Observatoriya, Trudy, Leningrad, 80-90.
- Rowntree, P.R. and Bolton, J.A., 1983: Simulation of the atmospheric response to soil moisture anomalies over Europe. Quart. J. Roy. Met. Soc., 109, 501-526.
- Sadourny, R., 1975: The dynamics of finite difference models of the shallow-water equations. J. Atmos. Sci., 32, 680-689.
- Sellers, P.J., Y. Mintz, Y.C. Sud and A. Dalcher, 1986: A simple biosphere model (SiB) for use within general circulation models. J. Atmos. Sci., 43, 505-531.
- Sud, Y.C. and M. Fennessy, 1984: Influence of evaporation in semi-arid regions on the July circulation: A numerical study. J. Climatology, 4, 383-398.
- Sud, Y.C. and W.E. Smith, 1985b: Influence of local land-surface processes on the Indian monsoon: A numerical study. J. Climate Appl. Meteor., 24, 1015-1036.
- Sud, Y.C. and A. Molod, 1988: A GCM simulation study of the influence of Saharan evapotranspiration and surface-albedo anomalies on July circulation and rainfall. Mon. Wea. Rev., 116, 2388-2400.
- Sugi, M., 1986: Dynamic normal mode initialization. J. Met. Soc. Japan, 64, 623-636.
- Shukla, J. and Y. Mintz, 1982: The influence of land surface evapotranspiration on Earth's climate. Science, 215, 1498-1501.
- Sundström, A. and Elvius, T., 1979: Computational problems related to limited-area modelling. Numerical methods used in atmospheric models, 11, Chap. 7, GARP Series No. 17.
- Tanguay, M. and A. Robert, 1986: Elimination of Helmholtz equation associated with the semi-implicit scheme in a grid point model of the shallow water equations. Mon. Wea. Rev., 114, 2154-2162.
- Tatsumi, Y., 1980: Comparison of the time-dependent lateral boundary conditions proposed by Davis and Hovermale, WGENE Progress rep. no. 15, WMO, 93-94.

- Temperton, C. and A. Staniforth 1987: An efficient two time-level semi-Lagrangian semi-implicit integration scheme. Quart. J. Roy. Meteor. Soc., 113, 1025-1039.
- Tiedke, M., 1984: The sensitivity of the time-mean large-scale flow to cumulus convection in the ECMWF model. Workshop on convection in large-scale numerical models. ECMWF, 28 Nov. - 1 Dec. 1983, 297-316.
- Tuleya, Robert E., 1988: A numerical study of the genesis of tropical storms observed during the FGGE year. Mon. Wea. Rev., 116, 1188-1208.
- Walker, J. and Rowntree, P.R., 1977: The effect of soil moisture on circulation and rainfall in a tropical model. Quart. J.R. Met. Soc., 103, 29-46.
- Williamson, D.L. and G.L. Browning, 1974: Formulation of the lateral boundary conditions for the NCAR limited-area model. J. Appl. Meteor., 12, 8-16.
- Yamamoto, G., 1962: Direct absorption of solar radiation by atmospheric water vapor, carbon dioxide and molecular oxygen. J. Atmos. Sci., 19, 182-188.
- Yamasaki, M., 1975: A Numerical experiment of the interaction between cumulus convection and large-scale motion. Papers Meteor. Geophys., 26, 63-91.
- Yamasaki, M., 1986: A three-dimensional tropical cyclone model with parameterized cumulus convection. Pap. Met. Geophys., 37, 205-334.
- Yamasaki, M., 1989: Numerical experiments of tropical cyclones under observed situations with a new scheme of implicit representation of cumulus convection. 18th Conference on Hurricanes and Tropical Meteorology, May 16-19, San Diego, Calif., 172-173.
- Yamakazi, K., 1989: A study of the impact of soil moisture and surface albedo changes on global climate using the MRI. GCM-I. J. Met. Soc. Japan, 67, 123-146.
- Yeh, T.-C., R.T. Wetherrald and S. Manabe, 1984: The effect of soil moisture on the short-term climate and hydrology change - A numerical experiment. Mon. Wea. Rev., 112, 474-490.
- Zhang, D.L., and R.A. Anthes, 1982: A high-resolution model of the planetary boundary layer-sensitivity tests and comparisons with SESAME-79 data. J. Appl. Meteor., 21, 1594-1609.

